Measurements from Satellite Systems

Annual Scientific Report on NAS5-21798, 1973
Space Science and Engineering Center
The University of Wisconsin-Madison
Madison, Wisconsin, February 1974

METEOROLOGICAL MEASUREMENTS

FROM SATELLITE PLATFORMS

METEOROLOGICAL MEASUREMENTS FROM SATELLITE PLATFORMS

Annual Scientific Report on NAS5-21798

1972-1973

The research in this document has been supported in whole or in part by the National Aeronautics and Space Administration

Published for the
Space Science and Engineering Center
by the
University of Wisconsin Press

Published 1974

The University of Wisconsin Press

Box 1379, Madison, Wisconsin 53701

The University of Wisconsin Press, Ltd.

70 Great Russell Street, London

First printing

Printed in the United States of America

ISBN 0-299-97052-3

Correspondence concerning editorial matters should be addressed to

Space Science and Engineering Center

University of Wisconsin

1225 West Dayton Street

Madison, Wisconsin 53706

Orders for copies of this report should be addressed to

The University of Wisconsin Press

Principal Investigator: Verner E. Suomi

Contributors: A. Das

T. C. Huang

J. I. Kornfield

F. R. Mosher

L. A. Sromovsky

University of Wisconsin

CONTENTS

PREFACE

To obtain quantitative information from imaging sensors on geosynchronous satellites is a difficult, but highly rewarding research pursuit. The papers in this report are significant steps forward in this pursuit of operational applications of satellite data.

The first paper, by Kornfield, establishes a firm basis for proceeding with use of observations of sunglint on the ocean's surface to obtain measurements of surface winds. Mosher's and Sromovsky's contributions are valuable solutions to problems which have seriously handicapped users of ATS satellite data. The rest of this report is a set of six papers by Das and Huang which, taken together, constitute the final report of a two-year project to develop a flexible structural model to compare the attitude stability of different satellite configurations. The successful completion of the model and the results of the first analyses performed with it are noteworthy achievements.

With the authors, I wish to thank the many members of the Space Science and Engineering Center who have contributed to the work reported here. We sincerely appreciate the support of the National Aeronautics and Space Administration which has made our work possible.

Verner E. Suomi
Principal Investigator

ON THE DETERMINATION OF SEA SURFACE WIND OR STRESS FROM SUNGLINT OBSERVED BY AN EARTH SYNCHRONOUS SATELLITE

Jack I. Kornfield

ABSTRACT

Observations of the surface wind or stress are useful for measuring both oceanic and atmospheric circulations. One possible way to obtain measurements of the surface wind or stress over an ocean may be from the reflective characteristics of the ocean surface itself.

Mariners have long used the ocean's surface to indicate the wind speed in the form of the Beaufort scale. If the wind is weak (less than 1 kt) the sea's surface is likened to that of a mirror. As wind speed increases, sea surface roughness increases. This change in surface roughness with wind speed is displayed in the reflecting properties of the sea. The sun provides a tool with which to examine the reflecting properties of the sea and, by inference, the wind speed as well.

The reflection of the sun, known as sunglint or sun glitter, as seen by the Applications Technology Satellite spin scan cloud camera, is illustrated in Figure 1. The strength of the signal received from the sunglint areas depends primarily on the number of mirror-like facets which are tilted as the proper angle to reflect light from the sun to the satellite's spin scan camera. At a point on the ocean's surface, the number of reflecting facets tilted at the correct angle for such reflection form a statistic of the sea surface.

Although a relationship between slope distribution and surface stress has not been established theoretically or experimentally; Duntley (1954), Schooley (1954), and Cox and Munk (1956) have formulated empirical relationships between the distribution of slopes and the wind velocity above natural water surfaces.

Can the sunglint observed from a synchronous satellite in conjunction with these empirical relationships be used to measure the surface wind velocity or stress? A theoretical model through which the sunglint radiance may be made to yield the surface stress is formulated in this paper. Its development is divided into two parts; the first concerns itself with the relationship between the sea, its slope distribution, and the surface stress. The second part deals with the extraction of the sea surface slope distribution from the sunglint radiance. Estimates of the accuracy to which the surface wind velocity may be determined are obtained from the model and presented.

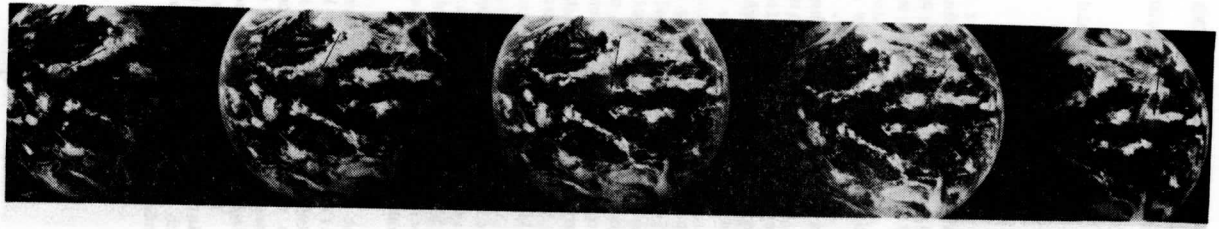

Figure 1

A sequence of Earth photographs taken from geosynchronous altitude
(arrows indicate sunglint)

SOME USEFUL PROPERTIES OF THE SLOPE DISTRIBUTION OF THE OCEAN SURFACE DUE TO WIND

> "There are many kinds of waves in the ocean. They differ greatly in form, velocity and origin. There are waves too long and low to see and waves that travel on density interfaces below the sea surface. Waves may be raised by ships, or landslides, or the passage of the moon, or earthquakes, or changes in atmospheric pressure. Probably there are kinds of waves that have not yet been discovered. But most waves, and the waves which are most important to mankind, are those raised by the wind."
>
> - Bascom, Waves and Beaches

INTRODUCTION

A manifestation of a wind generated wave on the ocean's surface is a distortion of the surface itself. In the absence of such waves, the ocean's surface is essentially horizontal and flat; in their presence, the ocean's surface is still essentially horizontal on a scale larger than the waves themselves but it is no longer flat. When a wave is present, some parts of the ocean surface are higher than others and the surface tilts. The slopes or the heights of the ocean surface may be used to describe the waves themselves. A description of ocean waves based on their slopes will be emphasized in this paper for these waves can be measured through their reflecting properties and can be related principally to wind as they are produced.

The response of the ocean surface to the winds is the production of capillary and gravity waves. The capillary waves rapidly set up by the wind are small and have rather short lifetimes (seconds). The gravity waves produced may be much larger, persist for days, and travel away from their area of generation to other parts of the ocean. Both slopes and heights are associated with these waves. In general, the smallest waves tend to have the steepest slopes.

A description of a disturbed water surface may be obtained in terms of the statistics of the surface. The distortions of the ocean due to waves will at any instant differ from area to area of the surface; in a fixed area the distortions will change in time. The ability of a statistic to describe the distortion of the ocean by the wind will depend on the response of the statistic to the wind. It will be shown that the wave slope statistics respond more rapidly to the wind than do the usual wave energy (height) statistics.

The probability that a particular slope occurs in an area at a particular moment may be used to describe the conditions in that area. The probability (p) that a particular slope occurs represents the fractional area of the horizontal covered by surfaces tilted to that slope at an instant of time. An observation made by Duntley (1954) indicates estimates of p obtained from time averages made at a point are equal to those obtained from aerial estimates of p at the same point.

Aerial Observations of the Slope Probability Function p

Schooley (1954) obtained estimates of p by photographing the reflection of a flash bulb from waves on a river from a bridge approximately 40 feet above its surface. The fractional area occupied by the sparkles was used as a measure of p. The results from a single photograph were approximated with a two dimensional normal distribution with principal axes in the upwind and cross wind direction. The probability p was represented by the standard deviations given along the principal axis as functions of wind speed. It was noted that the probability of slopes was slightly skewed upwind. However, the degree of skewness is lost in a Gaussian representation of p. It was also observed that the greatest slopes appeared on top of the larger waves.

Cox and Munk (1956) obtained an estimate of p by photographing the sun's reflection off the ocean's surface from an airplane flying at about two thousand feet. Clean and oil slicked surfaces were examined. Two types of cameras were used; one with a normal lens established the geometry for the other which photographed without a lens. Red filters were used to minimize the effects of ocean and sky background. The densities of the negatives from the lensless camera were directly related to the probability p after correction for background signal. Wind speeds were measured on a schooner with cup-type anemometers mounted on the bow sprit (9') and the foremast (41'). The probability distribution exhibited both skewness and peakedness (the solid lines in Figure 2), compared to a normal distribution (the dotted lines). The estimate of the probability function was fitted with the first few terms of Gram-Charlier series:

$$p(\zeta,\eta) = \frac{1 + t}{2\rho\sigma_u\sigma_c} \exp\left[-\frac{1}{2}\left[\zeta^2 + \eta^2\right]\right] \qquad (1)$$

where:

$$t = -\frac{1}{2} C_{21}(\zeta^2 - 1)\eta - \frac{1}{6} C_{03}(\eta^3 - 3\eta) + \frac{1}{24} C_{04}(\eta^4 - 6\eta^2 + 3)$$

$$+ \frac{1}{24} C_{40}(\zeta^4 - 6\zeta^2 + 3) + \frac{1}{4} C_{22}(\zeta^2 - 1)(\eta^2 - 1)$$

and:

$$\eta = \frac{\text{slope in the direction of the wind } (m_u)}{\text{standard deviation in the direction of the wind}}$$

$$\eta = \frac{m_u}{\sigma_u}$$

$$\zeta = \frac{\text{slope in the cross wind direction } (m_c)}{\text{standard deviation in the cross wind direction}}$$

$$\zeta = \frac{m_c}{\sigma_c}$$

The empirical values for the coefficients and variances for normal sea states were found to be (Figure 2):

$$\sigma_u^2 = (3.16 \cdot u \pm 4) \cdot 10^{-3}$$

Variances

$$\sigma_u^2 = (1.92 \cdot u + 3 \pm 2) \cdot 10^{-3}$$

$$C_{21} = (1 - .86 \cdot u \pm 3) \cdot 10^{-2}$$

Skewness Coefficients

$$C_{03} = (4 - 3.3 \cdot u \pm 12) \cdot 10^{-2}$$

$$C_{40} = .40 \pm .23$$

$$C_{22} = .12 \pm .06$$

Peakedness Coefficients

$$C_{04} = .23 \pm .41$$

for the wind speed u (meters/sec) measured at 41 feet.

The independent estimates of the slope probability function made by Schooley (1954) and Cox (1956) indicate that it may approach a unique limit. The values observed by each investigator for with-wind and cross-wind variances ($\sigma_u^2 \sigma_c^2$) are nearly the same for winds less than 10 m/sec (Figure 3), although the photographic technique of Cox and Munk (1956) covered an area some 2,500 times as large as the flash technique used by Schooley (1954). Also, both distributions were nearly Gaussian with a skewness in the same sense. Displaced downwind slopes with azimuths of accent in the direction of the wind were most probable.

The height and slope distribution of waves varies with the wind. As the wind changes, so will the height and slope distribution. An estimate of the response of the sea surface to the wind can be obtained.

The Response of the Slope Distribution to the Wind

The slope distribution, which may be viewed through the glitter pattern it produces, is expected to be useful in obtaining the local wind or stress. This is due to its rapid attainment of equilibrium with the local wind and its independence from gravity waves produced by distant storms.

Within an area of wave generation, the contribution of gravity waves to the total mean square slope and the energy (height) can be estimated through their respective spectra. These spectral estimates exhibit an equilibrium range (Philips, 1966; Barnet, 1969) and a sharp exponential cutoff. Typical of these spectra are the forms given by Cox (1956):

$$e(f,u) = g^2 c f^{-5} \exp(-2g^2/f^2u^2) \qquad (2)$$

$$s^2(f,u) = c f^{-1} \exp(-2g^2/f^2u^2) \qquad (3)$$

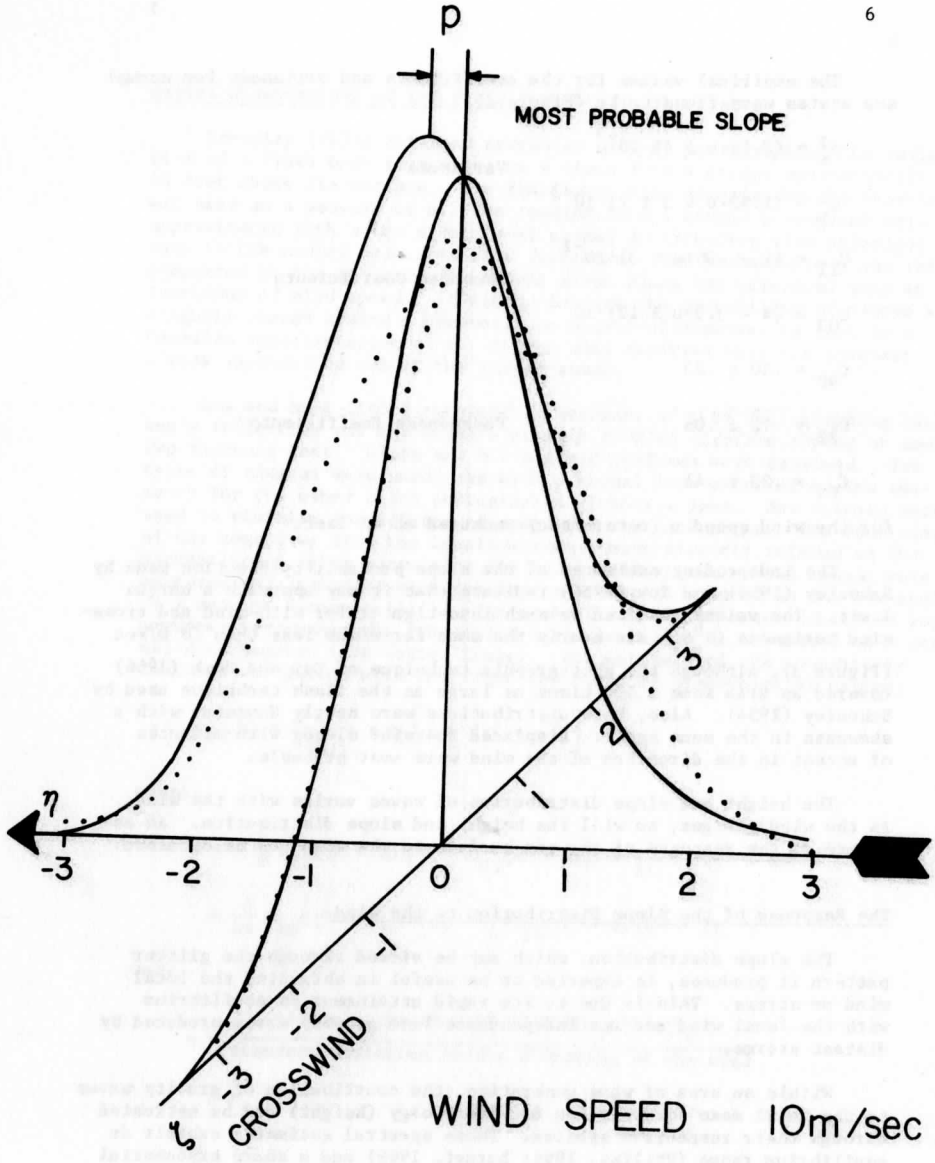
p
MOST PROBABLE SLOPE
η
-3
-2
-1
0
1
2
3
ζ
CROSSWIND
WIND SPEED 10m/sec

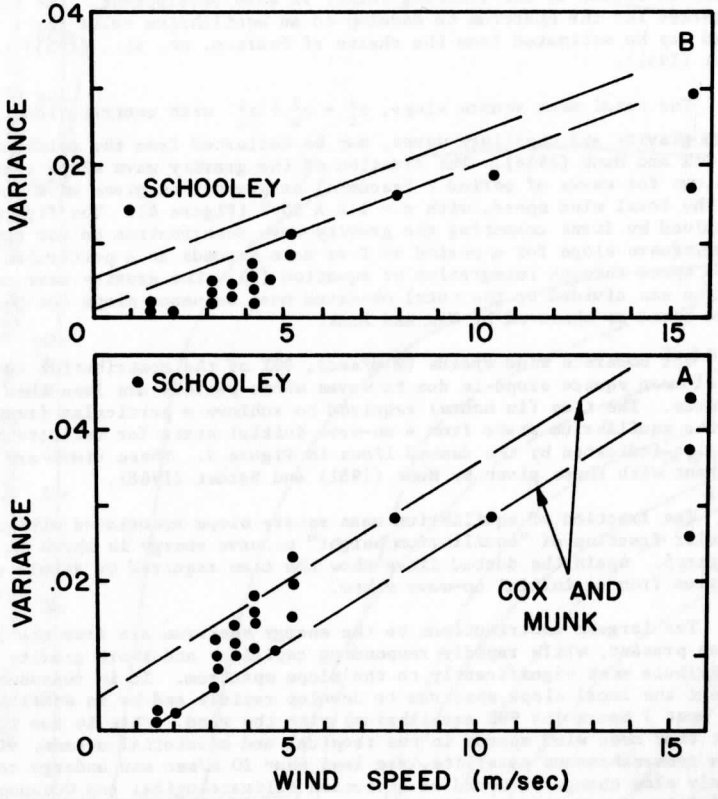

Figure 3

With wind variances, A, and cross wind variances,B, as functions of wind speed according to Schooley and Cox and Munk (after Cox and Munk).

where $e(f,u)$ and $s^2(f,u)$ are the contributions of energy per unit frequency band and the mean square slope per unit frequency band, respectively, at angular frequency f for a wind speed u. Also, c and g are constants; g is the acceleration of gravity and c the equilibrium range constant (Zaslavskiy and Kitaygorodskiy, 1971).

The degree of gravity wave development for a particular wind stress depends on the distance (fetch) and time (duration) over which the wind acts. For the large ("infinite") fetches typically found over the ocean, duration serves as the limiting factor in wave development. The time required for the spectrum to develop to an equilibrium value for a given wind may be estimated from the charts of Pearson, et. al., (1955) and Munk (1951).

The total mean square slope, $\sigma_t^2 = \sigma_u^2 + \sigma_c^2$, with contributions from both gravity and capillary waves, may be estimated from the calibration of Cox and Munk (1956). The fraction of the gravity wave slope contributions for waves of period T (seconds) or greater is given as a function of the local wind speed, with $c = 1.5 \times 10^{-2}$ (Figure 4). The figure was obtained by first computing the gravity wave contribution to the total mean square slope for a period of T or more seconds at a particular wind speed through integration of equation (3). The gravity wave contribution was divided by the total observed mean sequence slope for that wind speed as observed by Cox and Munk.

For moderate wind speeds (8 m/sec), 90% of the contribution to the total mean square slope is due to waves whose periods are less than 3 seconds. The time (in hours) required to achieve a particular fraction of the equilibrium state from a no-wave initial state for infinite fetch is also indicated by the dashed lines in Figure 4. These times are consistent with those given by Munk (1951) and Barnet (1968).

The fraction of equilibrium mean square slope associated with a particular fraction of "equilibrium height" or wave energy is shown in Figure 5. Again the dotted lines show the time required to attain equilibrium from an initial no-wave state.

The largest contributions to the energy spectrum are from the longest waves present, while rapidly responding capillary and short gravity waves contribute most significantly to the slope spectrum. It is reasonable to expect the local slope spectrum to develop rapidly and be in equilibrium (at most 7 hours for 99% equilibrium) with the wind. This is due to the fact that most wind speeds in the tropical and equatorial oceans, viewed by a geosynchronous satellite, are less than 10 m/sec and undergo relatively slow change in speed or direction (Climatological and Oceanographical Atlas for Mariners, 1960; Mintz and Dean, 1952).

Gravity waves produced by distant winds are called swell. They affect the portion of the ocean's surface for which the slope distribution is desired. The swell may have originated in regions of high winds (storms), or in broader regions of lighter winds. The utilization of a local slope distribution requires the effect of swell to be negligible. Observations of ocean swell (Snodgrass, et. al., 1966) indicate this may be the case. The total mean square slope of the observed

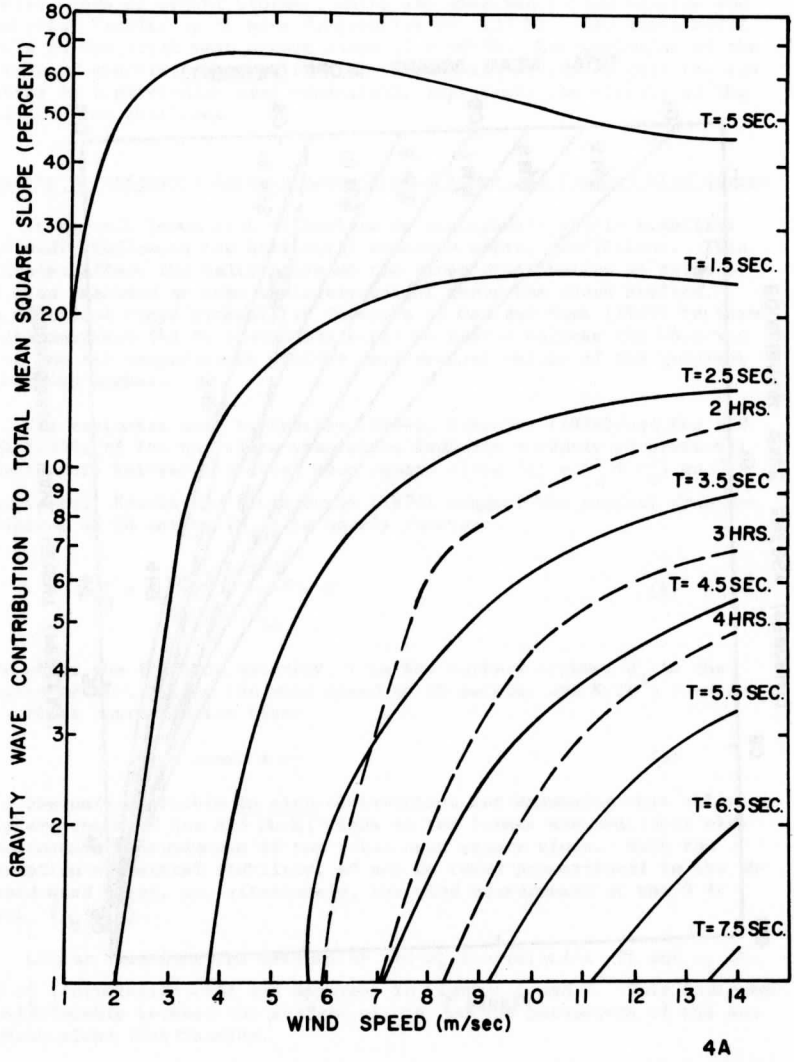
GRAVITY WAVE CONTRIBUTION TO TOTAL MEAN SQUARE SLOPE (PERCENT)
80
70
60
50
40
30
20
10
9
8
7
6
5
4
3
2
1
T=.5 SEC.
T=1.5 SEC.
T=2.5 SEC.
2 HRS.
T=3.5 SEC
3 HRS.
T= 4.5 SEC.
4 HRS.
T=5.5 SEC.
T=6.5 SEC.
T=7.5 SEC.
1 2 3 4 5 6 7 8 9 10 11 12 13 14
WIND SPEED (m/sec)
4A

Figure 4

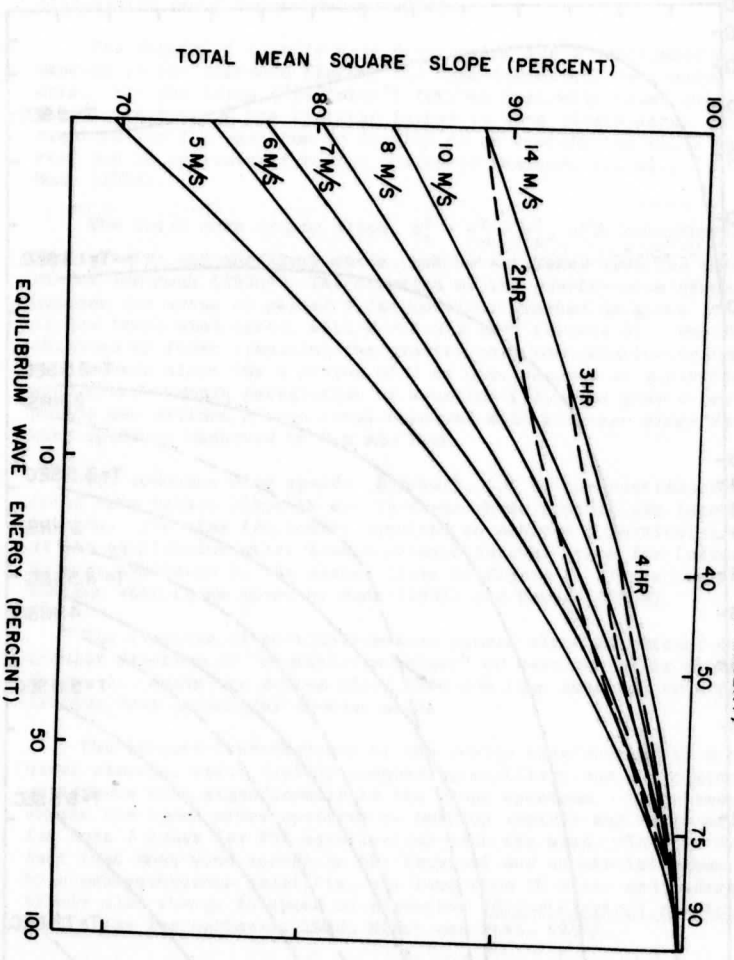
TOTAL MEAN SQUARE SLOPE (PERCENT)
EQUILIBRIUM WAVE HEIGHT (PERCENT)
EQUILIBRIUM WAVE ENERGY (PERCENT)
100
90
80
70
40
50
75
90
10
50
100
14 M/S
10 M/S
8 M/S
7 M/S
6 M/S
5 M/S
2HR
3HR
4HR
4B

Figure 5

storm swell outside its generating area at a distance of say 15° latitude is several orders of magnitude less than that expected from a sea raised by a 1 m/sec wind. This is brought about by the dispersive nature of ocean wave propagation and the rapid attenuation of high frequency waves above .08 Hz. The background swell (the swell produced by lighter winds or lesser storms), which was observed in the tropics and equatorial Pacific up to wave frequencies of .125 Hz, also contributes little to the total mean square slope (5×10^{-5}). Extrapolation of the background spectra, observed at Palmyra to 2 Hz, indicates that the sun glitter in a particular area essentially represents the effects of the wind local on that area.

Possible Relationship Between Mean Squared Slope and Surface Wind Stress

It is well known that variations in atmospheric static stability profoundly influence the horizontal momentum mixing coefficient. This will also affect the calibration of the slope distribution in terms of the wind measured at some arbitrary height above the ocean surface. The empirical slope probability function of Cox and Munk (1956) in terms of the masthead (41 ft.) wind may still be useful because the observed ocean and air temperatures yielded near neutral values of the gradient Richardson number.

The estimates made by Duntley (1954), Schooley (1954), and Cox and Munk (1966) of the sea slope statistics indicate a nearly proportional relationship between the total mean square slope ($\sigma_t^2 = \sigma_u^2 + \sigma_c^2$) and wind speed. Brocks and Krugermeyer (1970) suggest the neutral drag coefficient at 10 meters (D_{10}) is nearly constant.

$$D_{10} = \left(\frac{u^*}{u_{10}}\right)^2 = \frac{\tau/d_a}{u_{10}^2} = K \qquad (4)$$

Here u^* is the friction velocity, τ is the surface stress, d_a is the density of air, u_{10} is the wind speed at 10 meters, and K is a constant. To a first approximation then:

$$u^* = \text{const} \times \sigma_t^2 \qquad (5)$$

The only available *in situ* observations for examining this relationship are those of Cox and Munk; winds at two levels are available with simultaneous measurements of the total mean square slope. With the assumption of neutral stability, u^* may be taken proportional to the observed wind *shear*, or, alternately, the wind measurement at the 9 ft. level (u_9 ft.).

Linear relationships between u^* and σ_t^2 (correlation .9) and u_9 ft. and σ_t^2 (correlation .94) are apparent in Figures 6 and 7. This indicates a relationship between the surface stress and the parameters of the sea surface slope distribution.

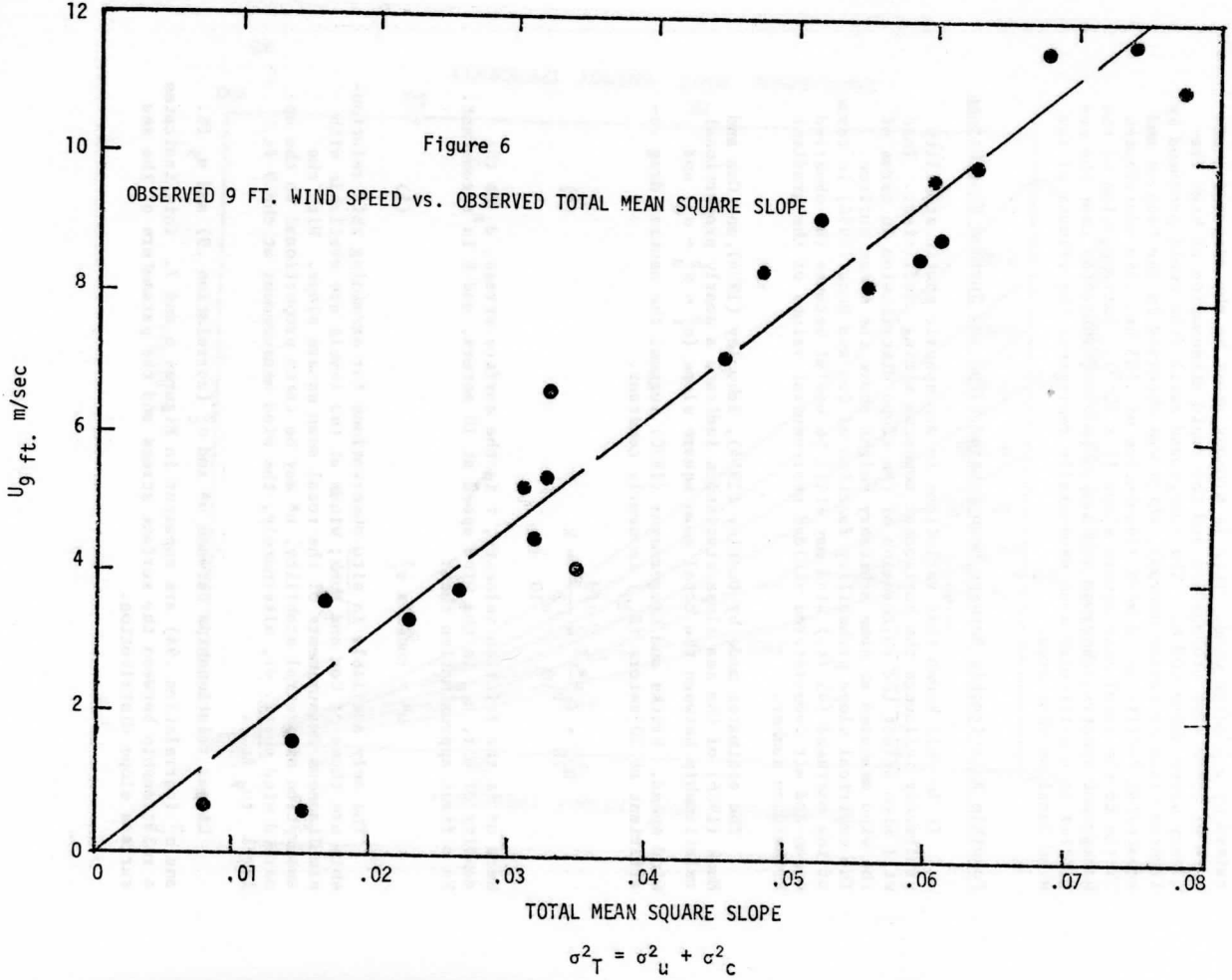

Figure 6

OBSERVED 9 FT. WIND SPEED vs. OBSERVED TOTAL MEAN SQUARE SLOPE

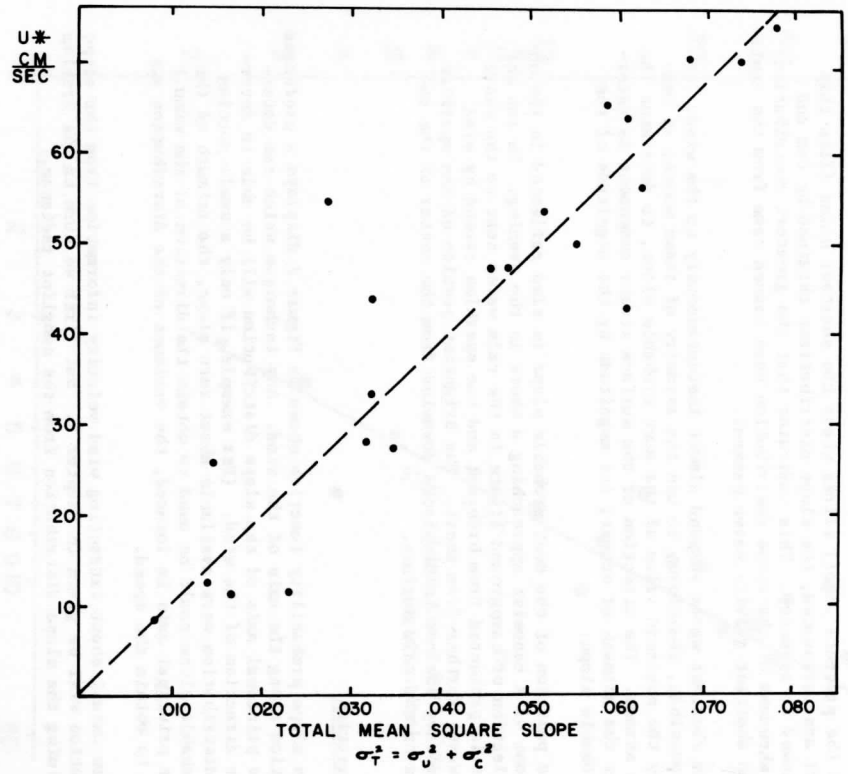

Figure 7

Observed wind shear vs. observed total mean square slope

Relationship Between Wind Stress and the Most Probable Slope

A direct relationship may exist between the most probable slope (M) along the principal axis of the distribution and the surface stress. Figure 8 shows M values obtained from the Cox and Munk slope distribution as a function of the wind speed measured at 42 feet. The points plotted are individual estimates of M. M is seen to be proportional to the square of the observed wind. If τ/d_a is proportional to the square of the observed wind, it must also vary in proportion to M.

In the presence of oil slicks where the shortest waves (less than 1 meter) are attenuated, the slope distributions obtained by Cox and Munk showed no asymetry. This indicates that the greatest contribution to the skewness of the slope distribution does indeed come from the capillary and shortest gravity waves present.

The shortest waves respond almost instantaneously to the wind. It may be possible, therefore, to use the asymetry of these waves, as measured by the non-zero value of the most probable slope, to determine the surface stress. The direction of the surface stress component is determined by the azimuth of accent; its magnitude by the magnitude of the most probable slope.

The position of the most probable slope is also reflected in the observations of a canoeist approaching a shore in the evening. He can see the reflection of campground lights in the calm water next to the shore where it is protected from breezes, and the sparkles caused by wind driven waves further from shore. The brightest portion of the sparkles from the wavy surface is displaced downwind from the center of the reflection on the calm surface.

Wind Direction

The slope probability function shown in Figure 2 displays a preferred orientation along the axis of the wind. Any technique which can determine the principal axis of the slope distribution will be able to determine the direction of the wind. (For example, if only a small portion of the distribution were available about zero slope, the aximuth of the most probable slope could be used to obtain the direction of the wind.) Once the principal axis is located, the variance of the distribution may be used to obtain the speed.

More detail about extracting wind velocity information from the slope distribution will be given in Chapter 4. But first we turn to the problem of obtaining the slope distribution from the sunglint radiance.

THE TOTAL RADIANCE: THE SUNGLINT AND BACKGROUND RADIANCES

The sunglint radiance observed from a satellite is only part of the total radiance received from the ocean atmosphere. Information on the total radiance observed from a satellite is needed to provide a means of separating the sunglint radiance from the background radiances.

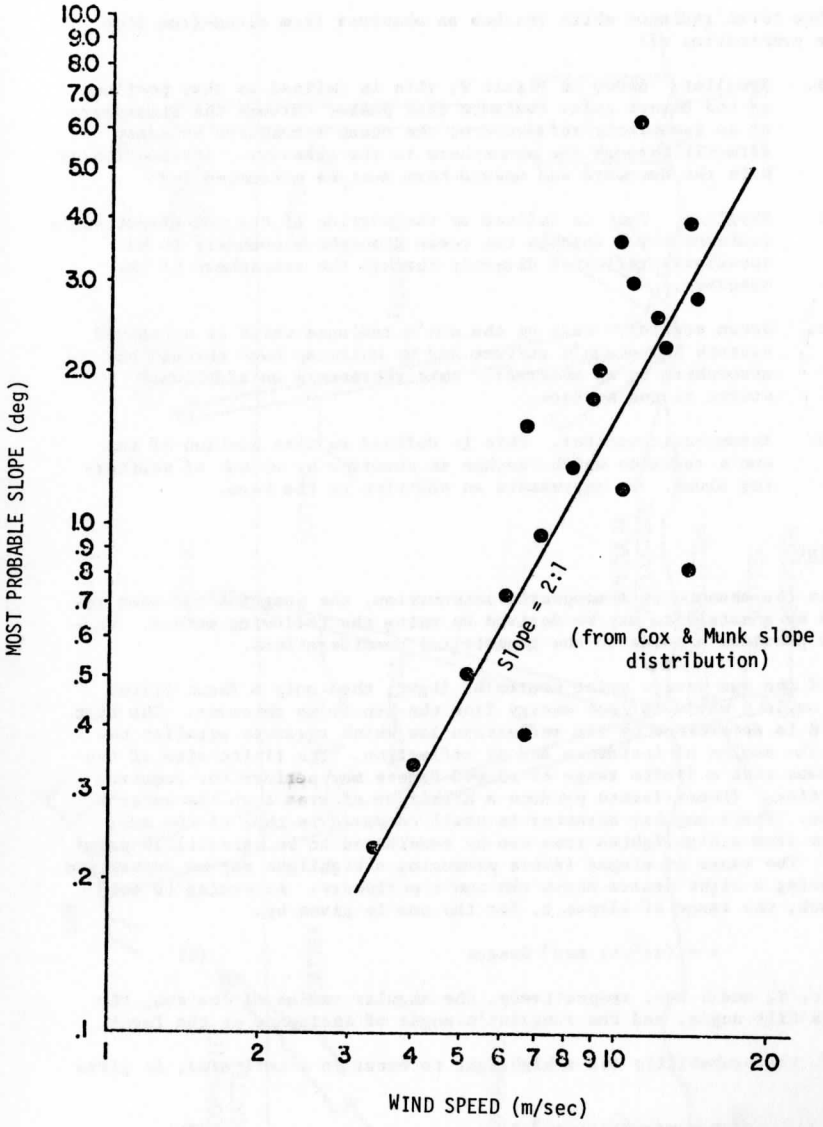

Figure 8 THE MOST PROBABLY SLOPE vs. OBSERVED WIND SPEED

The total radiance which reaches an observer from cloud-free area is the combination of:

a. Sunglint. Shown in Figure 9, this is defined as that portion of the direct solar radiance that passes through the atmosphere to be specularly reflected at the ocean atmosphere boundary directly through the atmosphere to the observer. Attenuation of both the downward and upward beam must be accounted for.

b. Skyglint. This is defined as the portion of the non-direct sun's radiance which reaches the ocean atmosphere boundary to be specularly reflected directly through the atmosphere to the observer.

c. Ocean scatter. Part of the sun's radiance which is scattered beneath the ocean's surface and by whitecap back through the atmosphere to an observer, this represents an additional source at the surface.

d. Atmospheric scatter. This is defined as that portion of the sun's radiance which reaches an observer by virtue of scattering alone. It represents an addition to the beam.

Sunglint

In the absence of atmospheric attenuation, the sunglint radiance received by a satellite may be derived by using the following method. Figure 10 provides a guide to the geometrical considerations.

If the sun were a point source of light, then only a facet tilted to an angle β would reflect energy from the sun to an observer. The tilt angle β is determined by the reflection law which requires equality between the angles of incidence and of reflection. The finite size of the sun means that a finite range of sloped facets may perform the required reflection. (These facets produce a highlight of area Δ on the water's surface. Their angular diameter is small compared to that of the sun; so rays from a highlighted area can be considered to be essentially parallel.) The range of sloped facets producing a highlight may be determined by tracing a light source about the sun's periphery. According to Cox and Munk, the range of slopes, t, for the sun is given by:

$$t = (\pi\varepsilon^2/4)\ \sec^3\beta \sec\omega \qquad (6)$$

where ε, β, and ω are, respectively, the angular radius of the sun, the facet's tilt angle, and the sunglint's angle of incidence on the facet.

P, the probability for a highlight to occur in a unit area, is given by:

$$P = p(\pi\varepsilon^2/4)\ \sec^3\beta \sec\omega \qquad (7)$$

where p is the probability per unit area that the slope β required for reflection occurs. The probability P may be interpreted as the fractional area highlighted.

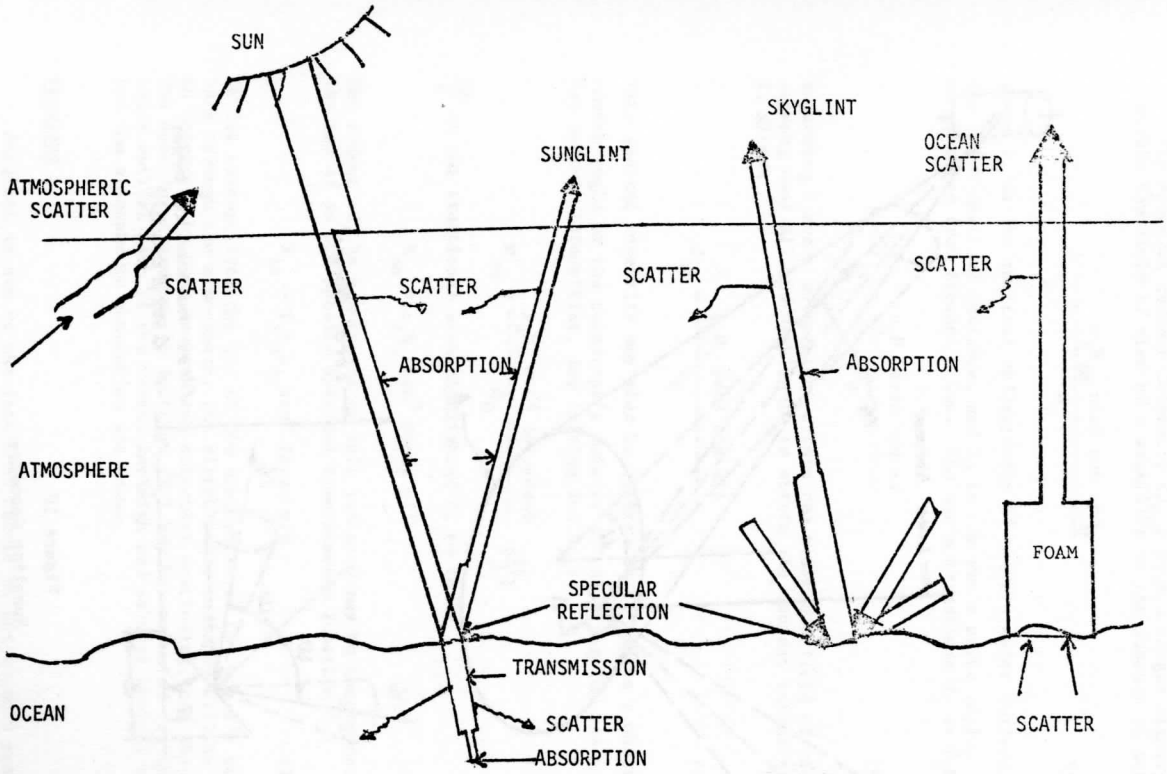

Figure 9 A SCHEMATIC REPRESENTATION OF THE SUNGLINT AND BACKGROUND RADIANCES

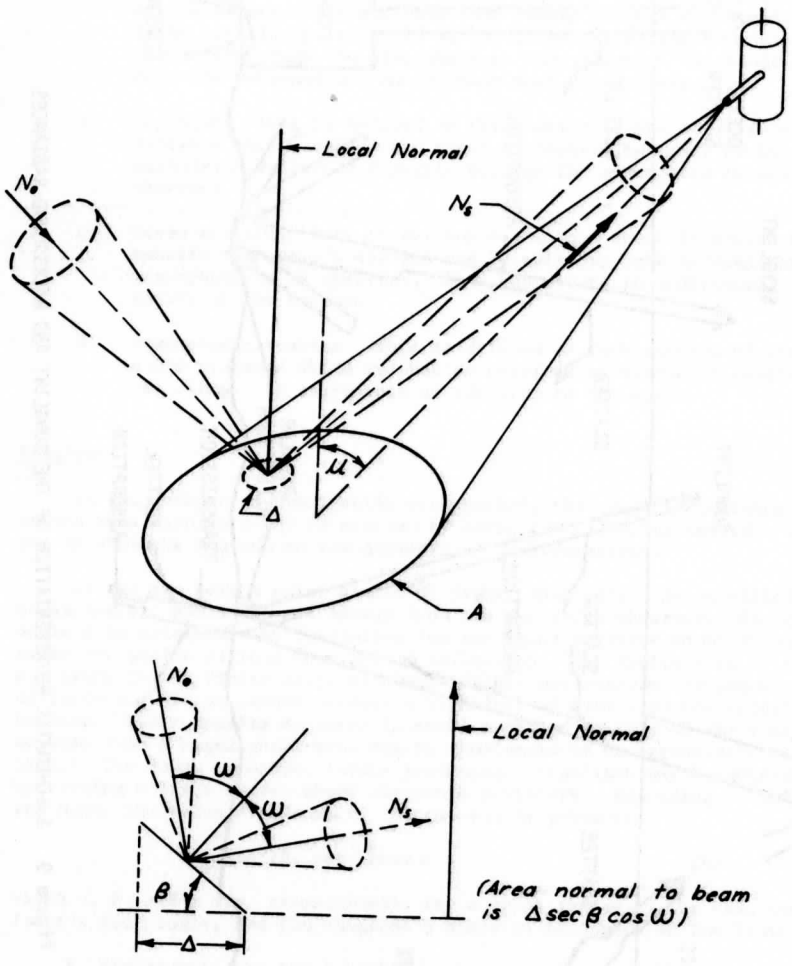

Figure 10
Sunglint Geometry

The spectral radiant intensity ($J_{\lambda s}$) from a single highlight of area Δ within the field of view of a satellite in the absence of atmosphere is:

$$J_{\lambda s_\Delta} = \frac{\rho_\lambda N_{\lambda\Theta} \sec\beta \cos\omega \Delta\Omega_\Theta}{\Omega_\Theta} \qquad (8)$$

where ρ_λ is the spectral reflectivity of the air water surface, $N_{\lambda\Theta}$ is the solar spectral radiance, and Ω_Θ is the sun's solid angle. And ω can be computed from Fresnel's Law. The sun's irradiance H_λ is $\Omega_\Theta N_\Theta$ so that:

$$J_{\lambda s} = \frac{\rho_\lambda H_\lambda \sec\beta \cos\omega\Delta}{\Omega_\Theta} \qquad (9)$$

Regarding β and ω as constant within the telescope field of view and summing over all the highlights to obtain the radiant intensity from area A, gives:

$$J_{\lambda s} = \frac{\rho_\lambda H_\lambda \sec\beta \cos\omega\Sigma\Delta}{\Omega_\Theta} \qquad (10)$$

This radiant intensity may also be written as $N_{\lambda s}$ A cos μ where μ is the zenith angle of the telescope's axis at A. Equating the two expressions for radiant intensities, and solving for $N_{\lambda s}$:

$$N_{\lambda s} = \frac{\rho_\lambda H_\lambda \sec\beta \cos\omega \sec\mu}{\Omega_\Theta} \left(\frac{\Sigma\Delta}{A}\right)$$

$\frac{\Sigma\Delta}{A}$ is the fractional area highlighted P, so that:

$$N_{\lambda s} = \rho_\lambda H_\lambda \sec^4 \beta \sec\mu \; p/4 \qquad (12)$$

The effect of the atmosphere on this radiance may be incorporated through the use of an atmospheric spectral transmission function T_λ:

$$N_{\lambda s} = T_\lambda H_\lambda \rho_\lambda \sec^4 \beta \sec\mu \; p/4 \qquad (13)$$

In its passage from the top of the atmosphere to the ocean's surface and back through the atmosphere, the direct solar radiance will be diminished in intensity by both aerosol and molecular scattering, and absorption. The spectral transmission function (T_λ) may be evaluated for this particular optical path if the normal Rayleigh and aerosol optical thickness and the atmospheric absorption are known.

Skyglint

Skyglint is due to the fact that facets on the ocean's surface will also reflect radiance from sources other than the direct solar beam. A facet, depending on its slope, may reflect the skydome, radiance from be-

low the ocean's surface, or radiance reflected from another facet. If T'_λ is taken to be the spectral transmission of the atmosphere from the surface to the satellite, then the additional radiance received by virtue of reflection from the ocean's surface (n') called skyglint, may be given by:

$$N' = \alpha \sec\mu \int_\lambda \int_{\beta,r} f_\lambda T'_\lambda Q_\lambda \rho_\lambda p \sec^3 \beta \tan\beta \cos\omega \, dr d\beta d\lambda \qquad (14)$$

Here Q_λ is the radiance incident on the facet and r is the azimuth of the slope $_\beta$. The limits of integration over slopes are such as to include all those visible.

Tacit in obtaining the expression for the sunglint radiance was the assumption that the effects of multiple reflection and wave shadowing can be ignored in its computation. Saunder's (1967) formulae show that wave shadowing can be neglected in computing the sunglint radiance for local solar and satellite zenith angles less than 60°. They also permit a conservative estimate of the sunglint produced by multiple reflection when used with the skyglint integral. For an overhead sun and nadir viewing of the sea surface, the ratio of twice reflected solar radiance to that of single reflected sunglint is less than 10^{-10}.

Ocean Scatter

Ocean scatter, back scattered radiance from below the ocean's surface and from whitecaps, is found when viewing the ocean. Back scattered radiance from below the surface finds its origin in Rayleigh and Mie scattering from particulates and air bubbles. It is strongly dependent on the absorption properties of pure water and the organic material present in a particular ocean (Jerlov, 1968). Strong and Ruff (1970) indicate that back scattered radiance from below the ocean's surface is nearly isotropic. The limited observations of oceanic whitecap surface area (Monahan, 1971) indicate a high variability with wind speed. Approximately one per cent of the total area is covered by whitecaps for an 8 m/sec wind measured at 10 meters; for lower wind speeds the maximum whitecap area coverage decreases rapidly (Figure 11).

Atmospheric Scatter

Atmospheric scatter is caused by both Rayleigh and Mie scattering in the atmosphere and contributes most significantly to the radiance observed from above the atmosphere.

Aerosols may enter into the estimate of the slope probability function through the pronounced forward scattering they produce (i.e., the aureole and its effect on the skyglint). The effect of the forward scatter may be qualitatively estimated by considering an overhead sun reflecting from a perfectly smooth surface with an aerosol layer. The reflected radiance received for vertical downlook will consist of the sun's reflected radiance and the reflected forward scatter produced by the aerosols. The total radiance observed will consist of the reflected radiance and the aerosol back scattered radiance.

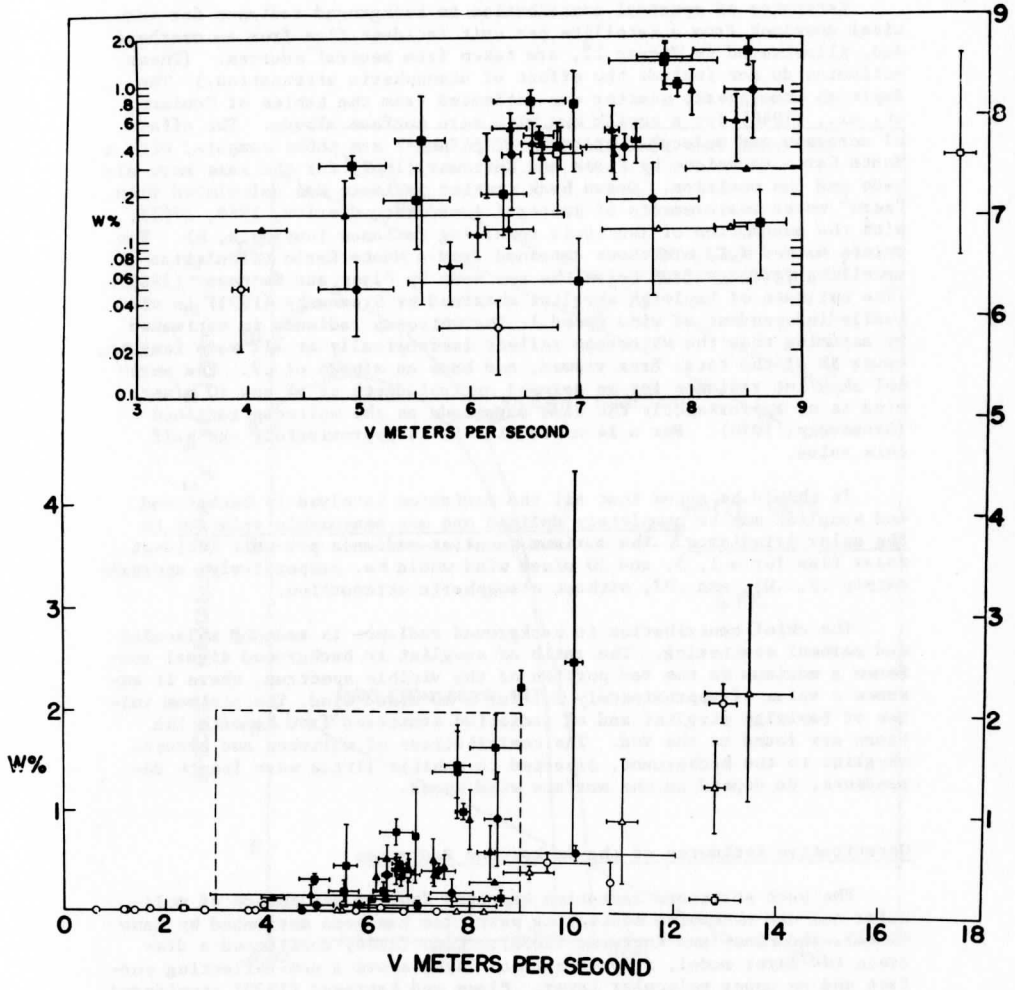

Figure 11

Present oceanic whitecap coverage (W) vs. 10 M elevation wind speed (V). Vertical bars indicate standard deviations from mean values. Horizontal bars span range of wind speeds measured during observation periods. (After E.C. Monahan)

Spectral Distribution of the Sunglint and Background Radiances

Estimates of spectral contribution to background radiance for vertical downlook from a satellite per unit incident flux from an overhead sun, illustrated in Figure 12, are taken from several sources. (These estimates do not include the effect of atmospheric attenuation.) The Rayleigh atmospheric scatter was estimated from the tables of Coulsen, et. al., (1960) for a zenith sun with zero surface albedo. The effect of aerosols and molecular scattering (points*) are those computed with a Monte Carlo technique by Plass and Kattawar (1969) for the same zero albedo and sun position. Ocean back scatter radiance was calculated from "zero" meter measurements of spectral irradiance (Jerlov, 1968, 1965), with the assumption of isotropic upwelling radiance (curves a, b). The points marked P.K. are those obtained from a Monte Carlo calculation of upwelling radiance from below the sea made by Plass and Kattawar (1969). (The estimate of Rayleigh skyglint obtained by Sromovsky (1971) is virtually independent of wind speed.) The whitecap radiance is estimated by assuming that the whitecaps reflect isotropically at all wave lengths, cover 1% of the total area viewed, and have an albedo of .7. The aerosol skyglint radiance for an aerosol optical depth of .1 and 10 m/sec wind is of approximately the same magnitude as the whitecap radiance (Sromovsky, 1970). For a 14 m/sec wind it is approximately one half this value.

It should be noted that all the radiances involved in background and sunglint may be completely defined and are measurable relative to the solar irradiance. The maximum sunglint radiance per unit incident solar flux for a 1, 5, and 10 m/sec wind would be, respectively, approximately .2, .05, and .02, without atmospheric attenuation.

The chief contribution to background radiance is made by molecular and aerosol scattering. The ratio of sunglint to background signal achieves a maximum in the red portion of the visible spectrum, where it assumes a value of approximately 2:1 for a 10 m/sec wind. The minimum values of Rayleigh skyglint and of radiation scattered from beneath the ocean are found in the red. The contributions of whitecap and aerosol skyglint to the background, expected to exhibit little wave length dependence, do depend on the surface wind speed.

Quantitative Estimates of the Background Radiances

The back scattered radiation expected from an atmosphere of molecular and non-absorbing scattering particles has been estimated by Kano (1964), and Plass and Kattawar (1970). Kano (1964) considered a discrete two layer model, a lower aerosol layer above a non-reflecting surface and an upper molecular layer. Plass and Kattawar (1970) considered an atmosphere with a continental aerosol distribution above a non-reflecting surface. It was found that the back scattered radiance from an atmosphere of molecular and aerosol scatterers had approximately the same geometrical dependence as that expected of a molecular atmosphere alone, the principal effect of aerosols in a molecular atmosphere being to change the intensity of the back scattered radiance. The atmospheric back scatter component of the background radiance is modeled as:

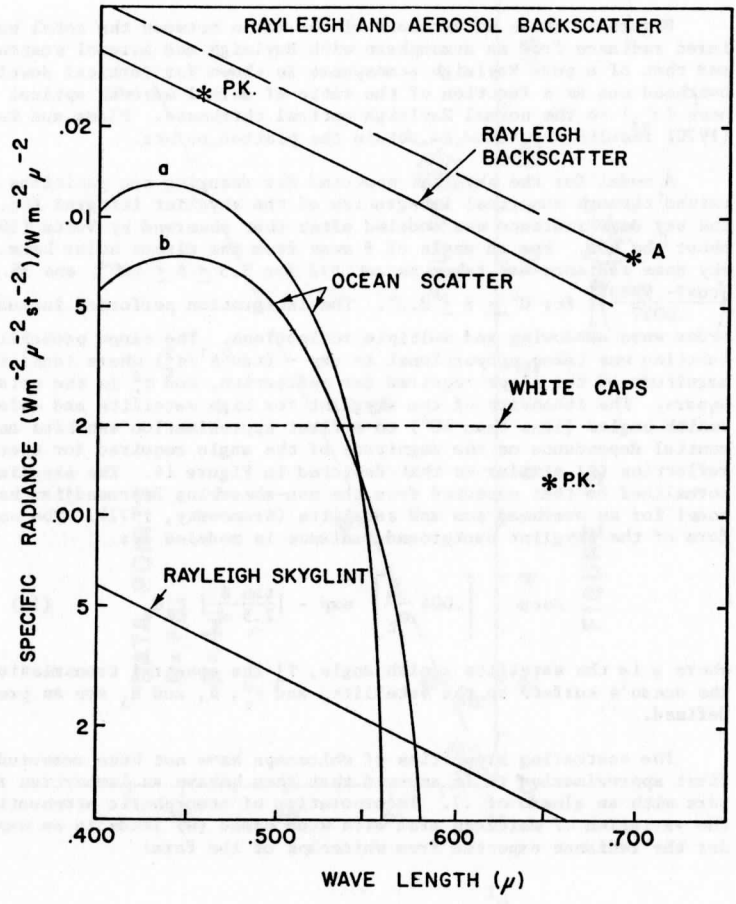

Figure 12. SPECIFIC CONTRIBUTION TO BACKGROUND RADIANCE

$$\tau_m \frac{P_r}{4\pi} H_\lambda = \frac{P_r \tau_r}{4\pi} FH_\lambda \qquad (15)$$

where τ_m is an effective optical thickness at wavelength λ, P_r is the Rayleigh phase function, and H_λ is the solar irradiance at wavelength λ above the atmosphere.

Figure 13 shows an estimate of the ratio between the total back scattered radiance from an atmosphere with Rayleigh and aerosol scatters and that of a pure Rayleigh atmosphere is shown for vertical downlook and overhead sun as a function of the ratio of normal aerosol optical thickness ($\tau_{a\lambda}$) to the normal Rayleigh optical thickness. Plass and Kattawar (1970) results were used to obtain the plotted points.

A model for the skyglint expected for changing sun positions was obtained through numerical integration of the skyglint integral (Eq. 16). The sky dome radiance was modeled after that observed by Voltz (1970) about the sun. For an angle of θ away from the direct solar beam, the sky dome radiance was taken as cot $\theta/2$ for $3.3 \leq \theta \leq 180°$, and $35.2* \left[2.* \left(\frac{\cos\theta - .9983}{.0017}\right)\right]$ for $0° \leq \theta \leq 3.3°$. The integration performed included first order wave shadowing and multiple reflections. The slope probabllity function was taken proportional to exp $- (\tan^2\beta^1/\sigma_t^2)$ where $\tan\beta^1$ is the magnitude of the slope required for reflection, and σ_t^2 is the total mean square. The intensity of the skyglint for high satellite and solar zenith angles (less than 40°) to a first approximation exhibits an exponential dependence on the magnitude of the angle required for specular reflection (β) similar to that depicted in Figure 14. The skyglint was normalized to that expected from the non-absorbing Deirmendjian haze model for an overhead sun and satellite (Sromovsky, 1971). The complete form of the skyglint background radiance is modeled as:

$$\sec\mu \left[.004 \frac{\tau_a}{\sigma_t}\right] \exp - \left|\frac{\tan\beta}{2.5\,\sigma_t}\right| T'_\lambda H_\lambda \qquad (16)$$

where μ is the satellite zenith angle, T'_λ the spectral transmission from the ocean's surface to the satellite, and σ_t^2, β, and H_λ are as previously defined.

The scattering properties of whitecaps have not been measured; to a first approximation it is assumed that they behave as lambertian reflectors with an albedo of .7. Incorporation of atmospheric attenuation and the variation of whitecap area with wind speed (W) leads to an expression for the radiance expected from whitecaps of the form:

$$.002 \frac{w^2}{64} \cos\theta_s T'_\lambda H_\lambda \qquad (17)$$

where θ_s is the zenith angle of the sun and $T'_\lambda H_\lambda$ is as previously defined.

The least known contribution to background radiance is that due to light scattered beneath the ocean. Estimates of this light's intensity,

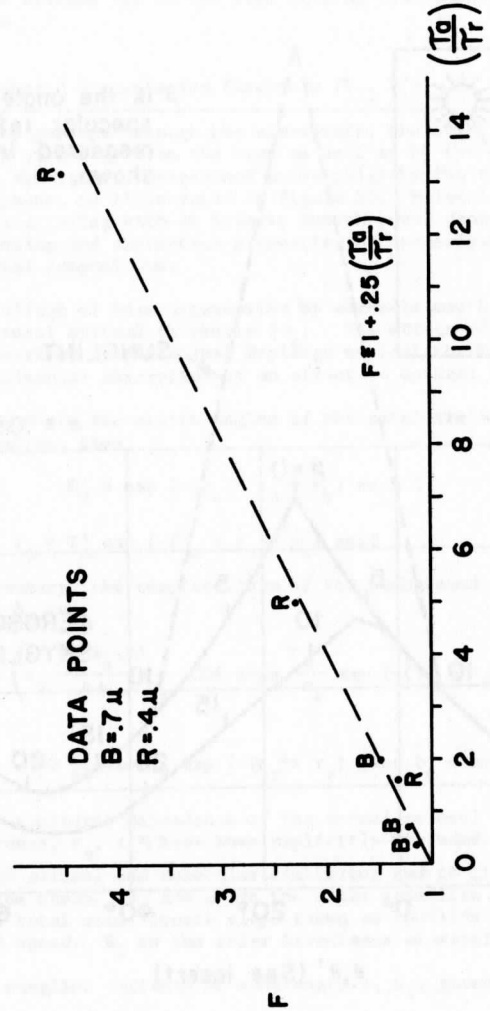

FIGURE 13 F vs. $\left(\frac{To}{Tr}\right)$

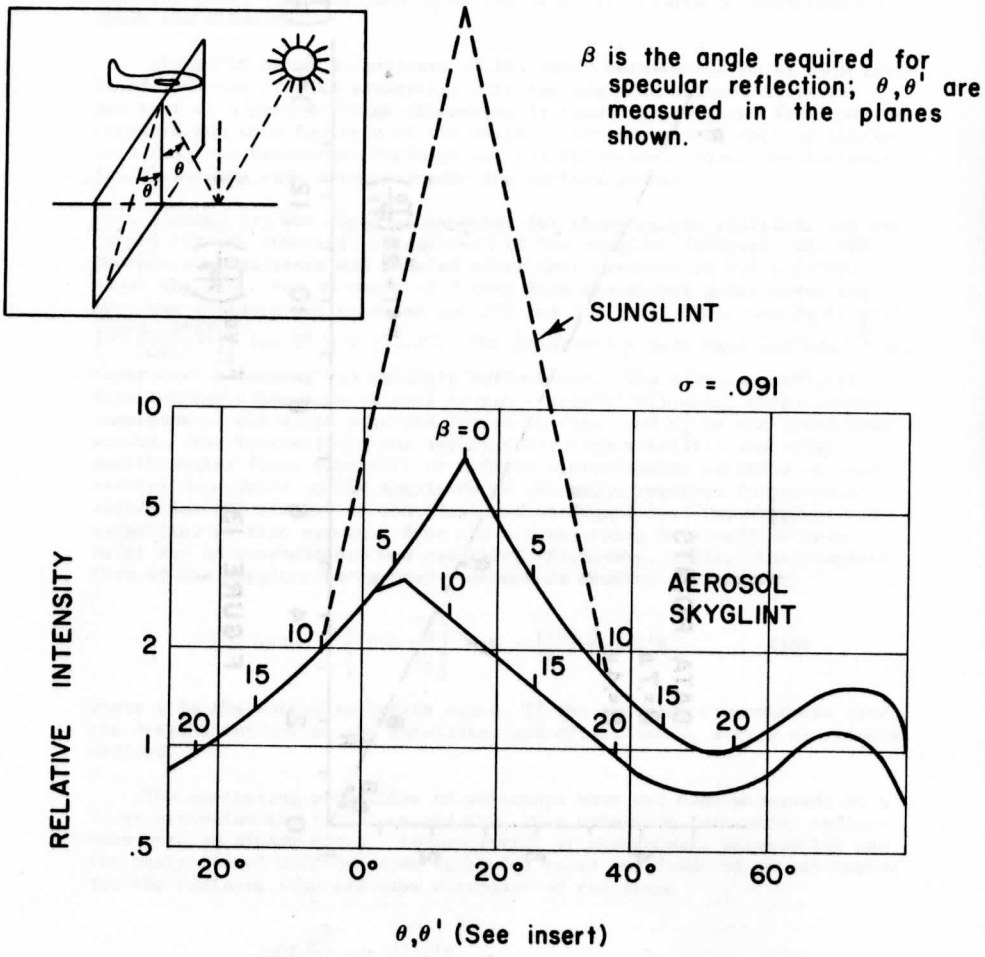
β is the angle required for specular reflection; θ,θ' are measured in the planes shown.
θ
θ'
SUNGLINT
σ = .091
β = 0
AEROSOL SKYGLINT
RELATIVE INTENSITY
10
5
2
1
.5
5
10
15
20
20°
0°
20°
40°
60°
θ,θ' (See insert)

while varying in magnitude, do show the same systematic decrease in intensity with wave length from the blue to the red portions of the spectrum. Plass and Kattawar's (1969) calculations indicate that combined ocean and atmosphere systems are of the same form as that expected from a Rayleigh atmosphere.

The Atmospheric Transmission Functions (T_λ, T'_λ)

In its passage through the atmosphere, the solar flux is depleted by scattering of energy from the beam as well as by the absorption of energy. Molecular absorption, determined principally by the tri-atomic gases of the atmosphere, is illustrated in Figure 15. Molecular scattering is Rayleigh scattering with an inverse fourth power dependance on wave length. The scattering and absorption properties of aerosols depend on their size and material composition.

The effect of beam attenuation by aerosols may be described by their normal aerosol optical thickness (τ_a). The effect of molecular scattering may be described by the normal Rayleigh optical thickness (τ_r) and the effect of molecular absorption by an effective optical thickness (τ_o).

If μ, θ are the zenith angles of the satellite and sun at the point of observation, then:

$$T'_\lambda = \exp\left[-(\tau_o + \tau_a + \tau_r)\sec\mu\right]$$

$$T_\lambda = T'_\lambda \exp\left[-(\tau_o + \tau_a + \tau_r)\sec\theta\right] \qquad (18)$$

In summary, the complete form of the background radiance at wavelength λ, B_λ is:

$$B_\lambda = \left(\tau_e \frac{P_r(\theta_s,\mu)}{4\pi} + .004 \sec\mu \frac{\tau_a^*}{\sigma_t} \exp\left[-(\tau_a + \tau_r^*)\sec\mu\right] + .002 \frac{w^2}{64} \cos\theta_s \exp\left[-(\tau_r^* + \tau_a)(\sec\theta_s + \sec\mu)\right]\right) H_\lambda \qquad (19)$$

Here the wavelength dependence of the normal aerosol and Rayleigh optical thickness, τ_a, τ_r^*, have been explicitly included. τ_e combines the effects of aerosol and molecular scattering and of light scattered from beneath the ocean. θ_s and μ are the solar satellite zenith angles. σ_t^2 is the total mean square slope taken as .00512*W where W is the surface wind speed. H_λ is the solar irradiance at wavelength λ.

The sunglint radiance at wavelength λ, G_λ, given by equation 13 is:

$$G_\lambda = \frac{p}{4}\left(\sec^4\beta \sec\mu \rho_\lambda \exp\left[-(\tau_a + \tau_r^*)(\sec\mu + \sec\theta_s)\right] H_\lambda\right) \qquad (20)$$

where p is the slope probability function and ρ_λ is the surface reflectivity. The total radiance observed from a point on the ocean's surface (o_λ), the sum of the sunglint radiance and background radiance, is taken

*Atmospheric abosrption implicitly included in Rayleigh optical thickness

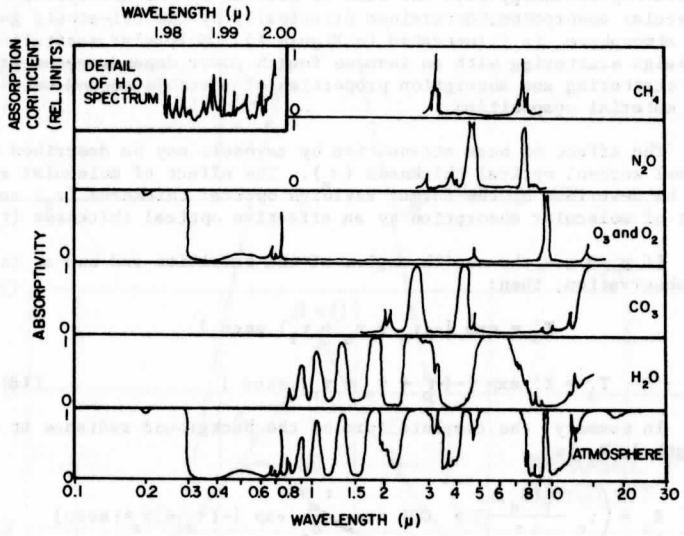
WAVELENGTH (μ)
1.98 1.99 2.00
ABSORPTION CORITICIENT (REL. UNITS)
DETAIL OF H2O SPECTRUM
CH4
N2O
O3 and O2
CO2
H2O
ATMOSPHERE
ABSORPTIVITY
0.1 0.2 0.3 0.4 0.6 0.8 1 1.5 2 3 4 5 6 8 10 20 30
WAVELENGTH (μ)

as:

$$o_\lambda = G_\lambda + B_\lambda$$

A Choice of Wavelength to View the Sunglint

The sunglint radiance is best measured when it is large compared to the background radiances and large in absolute value.

The sunglint radiance is determined by the strength of the solar flux, atmospheric attenuation, and the reflectivity of the water's surface. The effects of atmospheric attenuation on the solar flux are seen in Figure 16. The reflectivity of water decreases about 15% between .5μ and 2μ (Irvine & Pollac, 1968). The sunglint radiance between .5μ and 2μ will also show a general decrease in intensity with increasing wavelengths because of the approximately 20:1 decrease in intensity with increasing wavelength in the solar irradiance. Extreme decreases will occur in the absorption bands.

The primary contributor to the background radiance--Rayleigh back scatter--and ocean back scatter also show a decrease in intensity with increasing wavelengths (Figure 12). The decrease in Rayleigh back scatter is due to the inverse fourth power dependence of Rayleigh scattering. The decrease in ocean back scatter is due both to a decrease in Rayleigh back scatter and an increase in water absorption. The decrease of ocean back scatter with wavelengths is, therefore, expected to be greater than atmospheric Rayleigh back scatter.

The contributions to background radiance which depend on aerosols may show some decrease with increasing wavelength. However, the change is expected to be less than that due to Rayleigh scattering (Sromovsky, 1971). The back scatter from whitecaps at the surface of the ocean may not show any change with increasing wavelength.

Both the sunglint and total background radiance decrease with increasing wavelength, the latter decreasing faster than the former. The contribution to the background radiance from the aerosol skyglint, back scatter, and whitecaps at the surface of the ocean serve as a lower bound to the background signal (for the wavelengths shown in Figure 16).

For sunglint measurements, the researcher must:

1. Use longer wavelengths to minimize Rayleigh scattering in both ocean and atmosphere.

2. Use an atmospheric "window" where absorption is minimum.

3. Use a wavelength short enough so emission from the earth and its atmosphere are negligible.

4. Find wavelength where detectors of sufficient sensitivity are available.

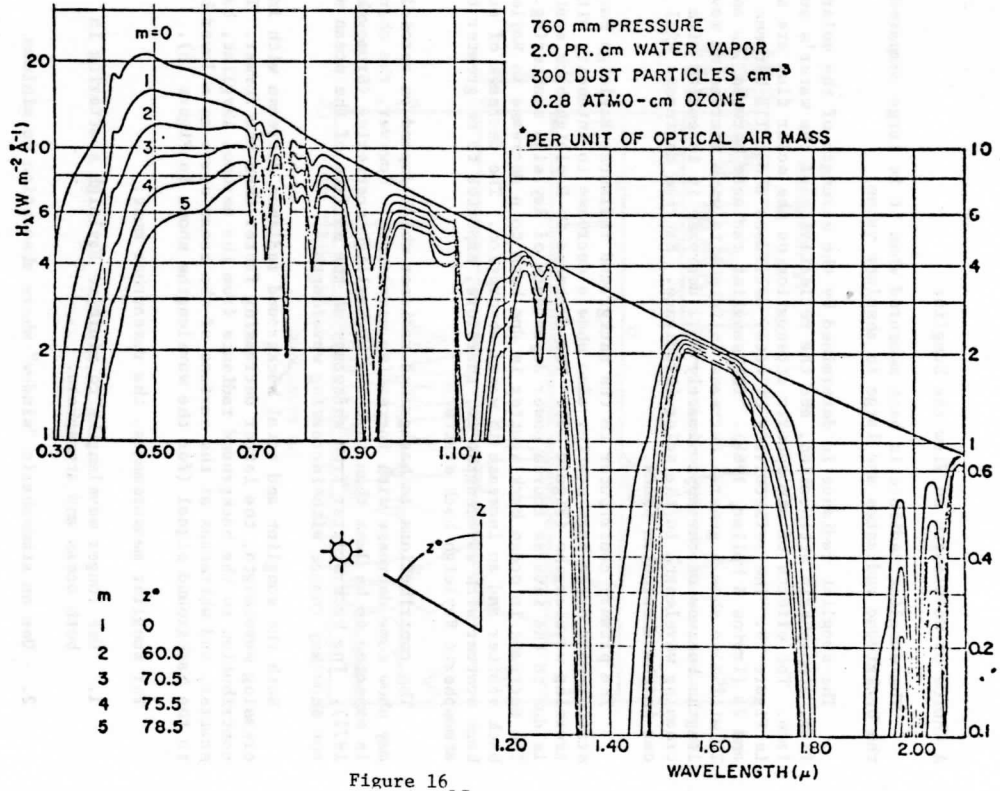

Figure 16

Solar spectral irradiance curves at sea level for various optical air masses

(after P. Moon)

SUNGLINT WIND INVERSION PRECISION ESTIMATES FOR A GEOSYNCHRONOUS SATELLITE

Introduction

In the previous chapters, it was argued that there is a relationship between the local sea surface slope distribution, responsible for the sunglitter pattern, and the surface wind or stress. A model for the total radiance, the sunglint and background radiances has also been formulated. Here, a mathematical inversion technique is used to determine the precision to which the surface wind may be obtained from geosynchronous observations of sunglint radiance.

Extraction of the surface wind from the total observed radiance from a sunglinted portion of the ocean's surface requires:

1. the separation of the sunglint radiance from the total observed radiance;

2. a relationship between the sunglint radiance and the slope probability function;

3. the extraction of the surface wind stress from the slope probability function.

The model of total radiance provides a vehicle for the first two requirements, i.e.: Total radiance = sunglint and background; Sunglint radiance = $p/4\ \sec\mu\ \sec^4\beta\ \rho_\lambda T_\lambda H_\lambda$. The empirical calibrated slope distribution obtained by Cox and Munk provides the path to the third requirement.

Previous applied wind extraction techniques are first discussed. These provide background for the more complete non-linear least square technique presented.

Techniques of Sunglint Wind Inversion

Previous approaches to the estimation of surface wind speed from sunglint have been based on approximations to the total radiance and the slope probability distribution.

If atmospheric attenuation, the $\sec^4\beta$ term, and all directional information in the slope probability function are neglected, the sunglint radiance may be taken proportional to:

$$\exp - (\tan^2\beta/\sigma_t^2) \qquad (21)$$

where β is the magnitude of angle required for specular reflection and σ_t^2 the total mean square slope. The specular reflection angles are determined by three factors: the position of the sun, the point of specular reflection, and the position of the observer. The magnitude of the angles required for specular reflection to a synchronous satellite is illustrated in Figure 17. The rapid decrease in sunglint intensity (Figure 1) is apparently due to the negative exponential dependence of the slope probability function on $\tan^2\beta$. Strong and Ruff (1970) have proposed the use of aerial extent and texture of the glitter pattern to classify three

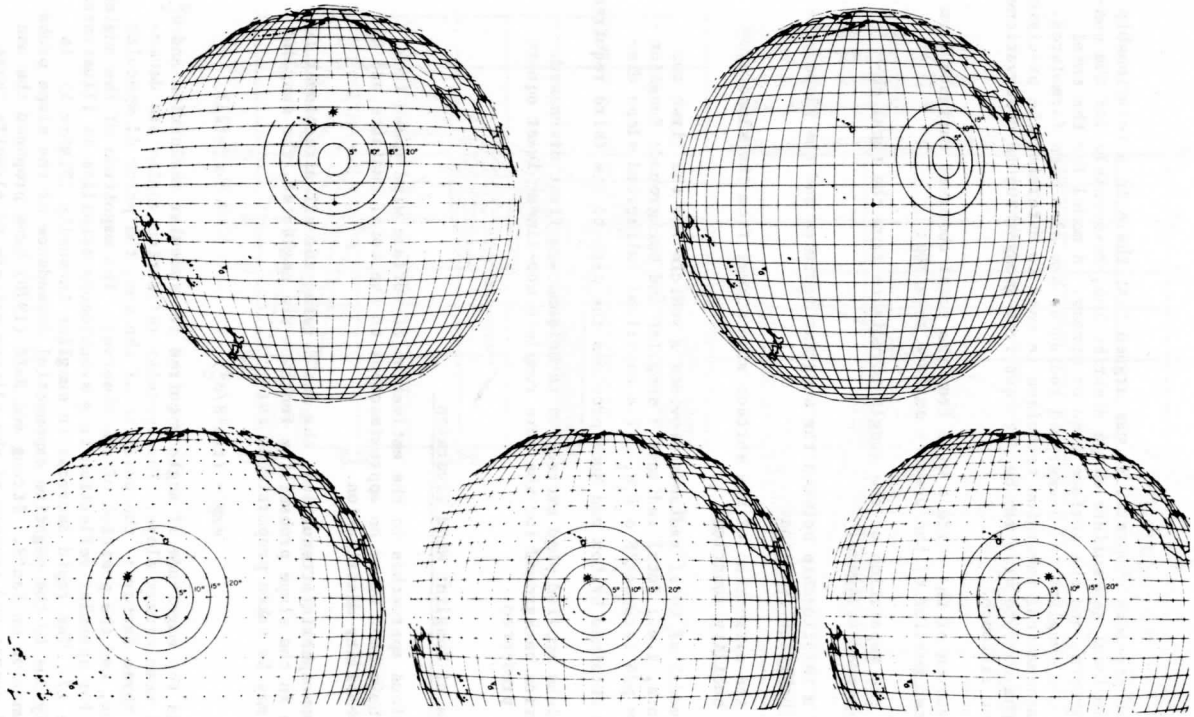

Figure 17

Angular magnitudes required for Specular reflection

"sea states" from near earth satellites. The use of this technique from synchronous altitude is handicapped by the larger aerial extent of the glitter pattern if a spatial non-homogeneity exists in the surface wind field. There is also the problem of separating sunglint from background signal.

Levanon (1969) has taken an approach more suitable for extracting information from the sunglint signal viewed from a synchronous satellite. It was assumed that over a three hour period the surface wind and its slope distribution could be considered constant over a small area of the ocean's surface. During this period, the angle required for specular reflection from the area in question will change as the position of the sun changes, sweeping a path through the slope space (Figure 18). (The sunglint intensity depends on the probability that the particular slope required for specular reflection occurs at a point on the ocean's surface. For a fixed sun position, the slope required for specular reflection changes as different portions of the surface are viewed. The slope probability function at each point, ideally determined only by the wind velocity or stress there, may or may not change. The sunglint pattern, long and narrow at sunset, is relatively circular at noon, although the water surface may remain the same. The sunglint pattern changes during the day. The wind or stress may, however, remain unchanged because the position of the specific slopes required for specular reflection changes on the water surface. The slopes required for specular reflection may be represented in a slope space.)

The relationship between the observed sunglint and the slope probability function was taken proportional to:

$$\exp - \left[\frac{\tan^2 \beta}{2} \left\{ \frac{\cos^2}{\sigma_u^2} + \frac{\sin^2 \theta}{\sigma_c^2} \right\} \right] \qquad (22)$$

Here, β is the magnitude of the angle required for specular reflection, θ is the angle between the wind velocity vector and the path in slope space in the East-West direction through the origin, and σ_u^2 and σ_c^2 are the wind and cross wind variances respectively. An arbitrary constant background signal from the radiance measured by ATS-I was subtracted from portions of the ocean's surface near the Line Islands and near Gaussian distributions resulted. Using winds available from the nearby island stations, the variances of the observed Gaussians were found to be consistent with those predicted by the empirical relationship for σ_u^2 and σ_c^2 by Cox and Munk (1956).

Since the bracketed expression in equation 22 involves both the wind speed and direction, it is impossible to use a single number (observed variance) to obtain either direction or speed uniquely. The error in wind speed expected from an uncertainty in direction may be obtained for Levanon's (1969) approximation.

Slope Space Geometry and the Slope Probability Function

As the sun moves across the sky the resultant sample in slope space is virtually a straight line in the East-West direction characterized by

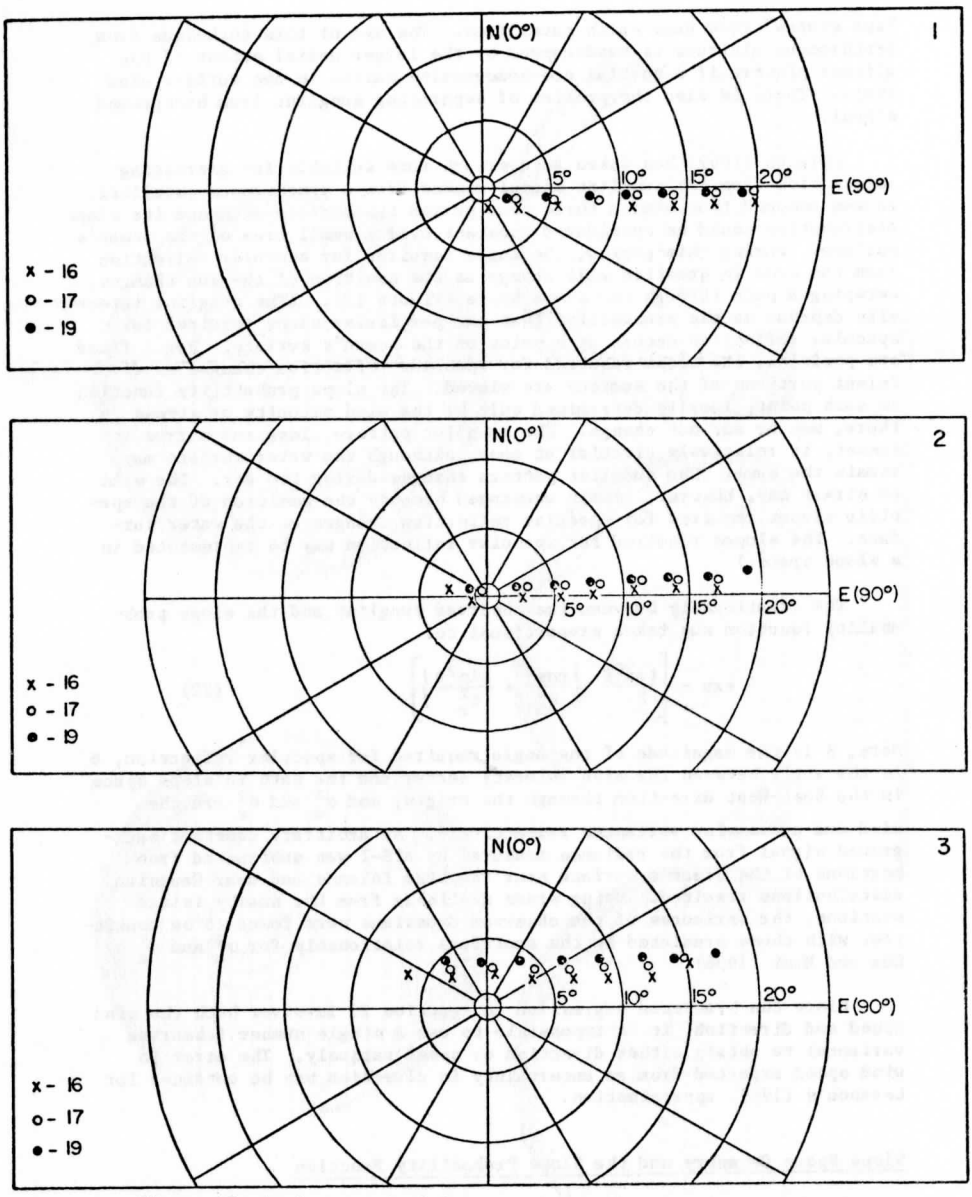

Figure 18 Angles required for specular reflection for changing sun positions at the Line Islands (1), Palmyra (2), Fanning (3) Christmas on the 16, 17, 19 of April, 1967

a fixed slope component in the North-South direction (Figure 18). In effect, a plane passes through the slope probability function (see Figure 2) at some angle relative to the true wind direction. The trace of the slope probability function in such a plane depends on the angle the plane makes with the wind velocity vector, the slope component in the North-South direction, and the wind speed. If the plane passes through the origin of the slope space ($\beta = 0$), a non-uniqueness exists. That is, if θ is the angle between the wind velocity and plane, then an identical trace will be found for this plane and the plane at $-\theta$. For a fixed slope component in the North-South direction, the trace of the slope probability function depends on the angle the plane makes with the wind velocity vector and the wind speed. The uniqueness of this angle depends on the skewness of the distribution defining the direction of the wind. If the plane passes at right angles to the wind vector, then an ambiguity exists in all cases.

Levanon's model serves as a guide in obtaining the parameters of the distribution. Consider a sample in slope space consisting of a straight line in the East-West direction characterized by a fixed slope component (say Q) in the North-South direction. Our example would also have a bivariate normal slope probability function with variances σ_u^2, σ_c^2 known functions of the surface stress or wind, with the principal axis in the direction of the wind. If the wind blows East-West or North-South, a Gaussian trace with maximum and axis symmetry at a zero East-West slope would result. For other wind directions, a Gaussian trace would also result. Its maximum and axis of symmetry, however, would be displaced. For winds not directly North-South or East-West, two equations may be obtained for the wind speed and direction θ by using shape information alone, or by using a combination of magnitude and shape information. The location of the maximum Z_M (first derivative = 0) and the inflection (second derivative = 0) depend on shape alone or the location of the maximum (Z_M) and its value there (N). Each yields two numbers from which the wind speed and direction θ may be calculated.

The application of either technique requires the separation of the sunglint radiance from the background radiance. The methods are handicapped by measurement error due to the finite number of points available for sampling the distribution.

Typical Noise Components

The magnitude of the slope distribution in its principal plane for winds of 4, 7, and 10 m/sec is depicted in Figure 19. The slope at which each trace reaches its maximum is indicated by a bar. The height of the bar is 4 times the standard deviation of the random error component expected from averaging the measurements of ATS-I, a geosynchronous satellite, over a quarter of a square degree. (The minimum achievable error component from ATS-I is about 1/3 of this value.) For observations taken 23 minutes apart, the samples in slope space are approximately 3° apart.

It was found that the random error component at this time interval was too great to permit estimation of the wind stress from shape information alone. The results of the combined approach (magnitude and shape) did yield error estimates. The assumptions involved and the technique used will now be described.

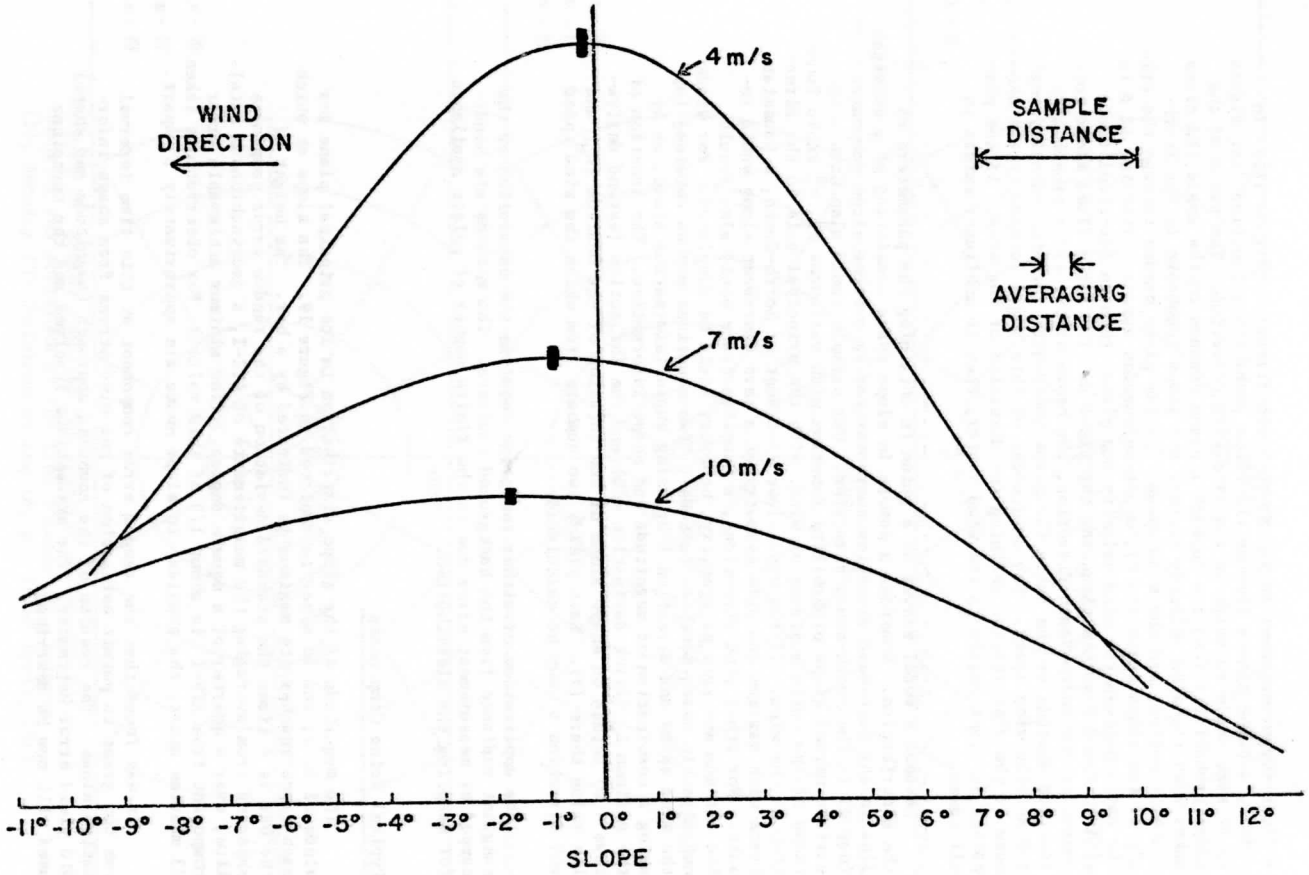

Figure 19 SECTIONS THROUGH THE PRINCIPAL PLANE OF THE SLOPE DISTRIBUTION

Basic Assumptions

To obtain an estimate of the precision to which the surface wind or stress may be obtained from the sunglint radiance measured from a geosynchronous satellite, five assumptions must first be made.

1. The distribution of slopes on the ocean's surface may be uniquely related to the surface stress averaged over a space scale of thirty miles. This stress varies slowly enough over a three hour period for the slope distribution to remain unchanged.

The similarities in the independent estimates of the slope probability function made by Schooley (1954) and by Cox (1956) indicate that it may approach a unique limit. The observed values of each investigator for the with-wind and cross-wind variances (σ_u^2, σ_c^2) are nearly the same for winds less than 10 m/sec (Figure 3). The photographic technique of Cox and Munk (1956), however, covered an area some 2500 times greater than the instantaneous flash technique used by Schooley (1954). Cox and Munk (1956) argued that the slope was affected by variability in the direction of the wind despite the presence of with-wind and cross-wind variances in their observations. It was also noted that both distributions were nearly Gaussian and were skewed in the same sense.

2. That the index of refraction of sea water may be obtained with sufficient accuracy to utilize Fresnel's formula to calculate the reflectivity of a facet on the sea surface.

The index of refraction of sea water at a particular wave length will depend on its temperature and chlorinity. Taking the observations reported in Sverdrup (1942) for the sodium wavelength as typical of visible wavelengths, it may be estimated that a 5°C error in the surface temperature will cause approximately 0.5% error in reflectivity for the slope which will be considered (angle of incidence less than 30°).

3. The primary error associated with measuring the relative radiance received by a satellite is due to random photomultiplier noise.

The parameters of the ATS-I spin scan camera were used to model the noise and obtain error estimates.

4. The forms of background radiances are as modeled.

The total observed radiance from a sunglint area of the ocean's surface o_λ is a function of several variables. Thus, o_λ = f ("Wind Stress," Rayleigh Optical Depth, Aerosol Optical Depth, Sub-surface Ocean Back Scatter; Aerosol Albedo; Geometry).

For a particular geometry (set of points in slope space) three models are considered in an attempt to determine the feasibility of using the sunglint radiance to determine the surface wind stress:

A. o_λ = f ("Wind Stress", Lumped Background, Rayleigh and

Aerosol Optical Depths Assumed Known).

B. o_λ = f ("Wind Stress", Rayleigh Optical Depth, Aerosol Optical Depth, Sub-surface Ocean Back Scatter; Aerosol Albedo = 1).

C. o_λ = f ("Wind Stress", Rayleigh Optical Depth, Aerosol Optical Depth, no Sub-surface Ocean Back Scatter; Aerosol Albedo = 1).

5. The atmosphere is cloud free.

In 1974 SMS, a geosynchronous satellite with a .5 mile resolution will be placed in orbit. The resolution of SMS will permit a separation of cloud-covered and cloud-clear areas. The estimate of the random error component used in the theoretical model (see assumptions) is expected to be the same for SMS.

Mathematical Inversion Technique and Linear Error Estimate

The non-linear least squares technique used to estimate the precision to which the wind stress may be measured is explained for simple model (A). Here, it is assumed that the only unknowns are wind stress and magnitude of the background signal. The form of the background signal is assumed to be known and to vary as the cosine of the sun angle. The technique used may be easily generalized to more variables.

The model for the total radiance received from a clean, cloud free view of the ocean's surface for a particular geometry (denoted by subscript i) is taken as:

$$R_i = G_i(\vec{V}) + c \cos A_i \qquad i = 1, 2, 3...m \qquad (23)$$

where $G_i(\vec{V})$ is the sunglint radiance for $\vec{V}$, the constant surface wind velocity, and c is a constant. From a sequence of total radiance measurements $\overline{R}_i$ (i = 1, 2, 3...m), taken within a three hour period from a fixed area on the ocean's surface, a solution for $\vec{V}$ is desired. The constant c will be a by-product of the solution.

Each measurement of the total radiance R_i has an error ε_i associated with it, primarily due to photomultiplier tube noise. In a time sequence of pictures these errors are independent. If the model is correct and the error ε_i is assumed to have a Gaussian distribution with zero mean and the same variables S_i, a method of least squares can then be used to obtain estimates of V. In other words a solution is sought which minimizes $\sum_{i=1}^{n} \varepsilon_i^2 = \Sigma(\overline{R}_i - R_i)^2$. The variance S_i^2 of each observation for a photomultiplier tube noise is proportional to the true signal, however. In terms of digital number representation of the total radiance from ATS-I,

$$S_i^2 \simeq .3\ Dn_i/g \qquad (24)$$

where Dn_i is the digital number corresponding to the radiance R_i (1 Dn

$\simeq$ .3 Watt/m/sterad) and g is introduced as a possible signal improvement factor. There are many ways in which this signal improvement factor may be realized, but these are beyond the scope of this paper.

If N independent measurements are taken over a small portion of the ocean's surface for which total radiance may be considered constant, the variance may be reduced:

$$S_i \simeq .3\ Dn_i/gN \tag{25}$$

There are typically 600 samples in a 30 mile square area near the subsatellite point. To obtain an equal set of variances a new set of variables is defined.

$$\begin{aligned} \overline{Dn}_i &\rightarrow \overline{R}_i/S_i \\ Dn_i &\rightarrow R_i/S_i \\ \varepsilon_i &\rightarrow \Sigma_i/S_i \end{aligned} \tag{26}$$

with $Dn_i - \overline{Dn}_i = \varepsilon_i$. The variance of each observation is now the same (1) with zero mean. A method of least squares which minimizes the $\sum_{i=1}^{n} \varepsilon_i^2$ may be attempted to solve for $\vec{V}$ and c.

The approach taken to obtain estimates of $\vec{V}$ and c and to estimate their errors on a linear hypothesis is handily expressed in matrix form. The magnitude of $\vec{V}$, its direction θ, and a constant c, are taken as components of a column vector Y.

$$Y = \begin{vmatrix} |\vec{V}| \\ \theta \\ c \end{vmatrix} = \begin{vmatrix} y_1 \\ y_2 \\ y_3 \end{vmatrix} \tag{27}$$

A linear expansion of Dn_i is performed as some $Y = \overline{Y}$. In matrix notation,

$$Dn(Y) = Z\Delta + Dn(\overline{Y}) \tag{28}$$

where

$$Dn = \begin{vmatrix} Dn_i(Y) \\ \cdot \\ \cdot \\ Dn_m(Y) \end{vmatrix}, \quad \Delta = (Y - \overline{Y})$$

with

$$Z = z_{j,v} = \frac{\partial Dn_v}{\partial y_j} \Bigg|_{\overline{Y}} \quad \begin{matrix} v = 1,\ldots m \\ j = 1,3 \end{matrix}$$

The difference between $Dn(\overline{Y})$ and $\overline{Dn}$ is used to obtain a new estimate of Δ. For a linear model the least squares estimate of Δ is given by:

$$\Delta = (Z^t Z)^{-1} Z\left(\overline{Dn} - Dn(\overline{Y})\right)$$

Using this new value of Δ, a new value of $\overline{Y}(\overline{Y}_{new} = \Delta + \overline{Y}_{old})$ is obtained and the process is repeated. The further the figure is from the true solution and the greater the degree of non-linearity, the greater are the chances for error in Δ. To avoid wandering from a true solution and to correct for non-linearity, a simple procedure is used. Instead of using Δ as calculated, $\Delta = \Delta/(1+X)$ is employed with an X initially set to a value greater than 0. If the new guess at $\overline{Y}$ produced a reduced sum of squares, X is reduced by a factor of S: $(S > 1)$. The process is terminated when Δ is less than a set of prescribed values. An error estimate on a linear hypothesis may be obtained from V where $V = (Z^t Z)^{-1}$. Thus 95% of the observation of y_i will fall within $y_i \pm 2\sqrt{v_{ii}}$ if the model is linear.

Non-Linear Error Estimate

The problem of solving for the parameters of y_i is a non-linear one and other estimates of the precision of y_i are desirable. These may be obtained through addition of a random error component of variances S_i^2 to each modeled of the total radiance R_i and solving for the y_i. After repeating the operation many times (20) the scatter in the y_i may be used to obtain estimates of expected range of y_i. If the scatter in the y_i is assumed normal (N.H.), χ^2 may be used to estimate the confidence of the variance calculated from the scatter in the y_i. If no particular distribution is assumed for the scatter in the y_i, a non-parametric estimate of the precision of the y_i can also be obtained (N.P.S.).

The scatter in the y_i is presented in terms of the twice the standard deviation of the y_i and the maximum, minimum value of the y_i. There is at least an 85% confidence that 95% of the scatter in y_i is within limits presented on the basis of the normal assumption (N.H.) and a 60% confidence that 80% of the y_i are within the range shown based on a non-parametric test.

Slope Space Geometry and Photomultiplier Noise Model

The geometry for the models was determined by the satellite position (at the equator), the satellite sub-point on the earth (at the equator) and two sun latitude positions, one with the sun at the equator and one with the sun at 20° North. In this manner, two planes through slope space are produced. Each plane runs in the East-West direction; one passing through the origin ($\beta = 0$) and one through $\beta = 10°$. "Normal" operation of ATS-I during a 3 hour period provides either 7 or 13 samples.

The samples chosen range between zero East-West slope to approximately 22.5° East-West slope with azimuth of accent to the West. Each sample error is estimated on the assumption that it is taken from a 30 square mile area containing some (N = 600) independent observations. The random error for each observation is taken to be that of the ATS photomultiplier tube $S^2 = .3\ Dn$. Two signal improvement factors (g = 1 and g = 10) were considered.

Estimates of precision were obtained for winds of 4 m/sec, 7 m/sec, and 10 m/sec in directions parallel and at 45° to the planes in slope space. These correspond to wind directions of 45°, 90°, and 135°. Estimates of precision based on the linear hypothesis (L.H.), normal assumption (N.A.), and non-parametric statistics (N.P.S.) are labeled as such in the tables.

Reliability of Precision Estimates

The application of the technique requires that the function Dn_i be expressible in terms of its first partial derivatives. This is not necessarily true for the slope probability function p as can be seen from the traces in the principal plane in Figure 19 at $\beta = 9°$. Such points can be found by comparing first and second partial derivatives. They can either be eliminated from the computation completely, or used through direct computation of the sums of squares to find a best guess for Δ or Δ_u. This was not done for the linear model; thus estimates of precision may be large compared to their true value. However, in the absence of an error component it was found that, using randomly selected points within 1 m/sec and 20° of the selected winds, the linear technique was capable of obtaining solutions within the termination criteria Δ_M = (.01 m/sec, .5 deg). Any choice of termination criteria does not guarantee that an absolute minimum sum of squares has been reached. Thus, the precision estimates may be overly large.

The choice of geometry permits precision estimates over the full range of eye-detectable sunglint radiance, some 10° (longitude) about the specular points. The winds chosen span the range most typically found in the tropics.

Lumped Background Model (known aerosol concentration)

The first model considered was $o_\lambda = G(|\vec{V}|, \theta) + c \cos$ (sun angle) ($\lambda \simeq .5\mu$). The only unknowns were the wind speed $|\vec{V}|$, its direction θ, and a background constant c. To compare linear hypothesis precision estimates to those obtained from the generation of a random error component (g = 1, N = 600), the initial starting points for the least squares technique (y_i) were taken to be their true values. The results of the runs are in Tables 1 and 2. The precision estimates based on the L.H. are consistently larger than those based on the random component. (The actual computed 2σ values are about 20% less, without χ^2 correction, than those shown in the tables under N.A.) The blanks indicate that the solution did not deviate from the initial true value, indicating the fact that the partial derivatives with respect to direction had gone to zero.

Table 1

Precision estimates for lumped background model (7 samples, perfect initial parameters)

$\beta = 0$		PRECISION ESTIMATES								
		NOMINAL WIND DIRECTION								
		45°			90°			135°		
STATISTICAL HYPOTHESIS	NOMINAL WIND SPEED (mps)	SPEED (mps)	DIRECTION (deg)	BACKGROUND (Digital Number)	SPEED (mps)	DIRECTION (deg)	BACKGROUND (Digital Number)	SPEED (mps)	DIRECTION (deg)	BACKGROUND (Digital Number)
L.H.	4	.07	7.9	.25	.07	205	.30	.07	7.9	.25
N.H.		.04	5.1	.12	-	-	-	.04	4.6	.14
N.P.S.		3.97	40.7	-	-	-	-	3.97	131.3	-
		4.03	48.0	-	-	-	-	4.03	-	-
L.H.	7	.16	7.6	.32	.20	214	.50	.16	7.6	.32
N.H.		.12	6.4	.27	-	-	-	.098	4.9	.20
N.P.S.		6.9	39.6	-	-	-	-	6.9	132.2	-
		7.08	48.5	-	-	-	-	7.09	139.4	-
L.H.	10	.29	9.1	.40	.64	114	.96	.29	9.1	.40
N.H.		.16	6.8	.28	-	-	-	.21	6.5	.28
N.P.S.		9.9	9.9	-	-	-	-	9.08	130.6	-
		10.07	10.07	-	-	-	-	10.1	139.2	-

Table 1--continued

Δ = (.01 mps, .1 deg, .001)

β = 10		PRECISION ESTIMATES								
		NOMINAL WIND DIRECTION								
		45°			90°			135°		
STATISTICAL HYPOTHESIS	NOMINAL WIND SPEED (mps)	SPEED (mps)	DIRECTION (deg)	BACKGROUND (Digital Number)	SPEED (mps)	DIRECTION (deg)	BACKGROUND (Digital Number)	SPEED (mps)	DIRECTION (deg)	BACKGROUND (Digital Number)
L.H.	4	.32	9.4	.28	1.17	28.3	.36	1.02	15.2	.33
N.H.		.25	9.3	.21	.79	19.6	.22	.68	12.0	.18
N.P.S.		3.8	37.2	-	3.56	74.6	-	3.45	136.9	-
		4.2	53	-	4.72	102	-	4.36	149.2	-
L.H.	7	.88	7.6	.44	1.11	10.4	.32	2.0	20	.43
N.H.		.68	5.9	.27	.75	5.0	.22	.98	12.5	.20
N.P.S.		6.7	37.8	-	6.19	86.4	-	6.4	130.8	-
		7.9	47.4	-	7.4	9.6	-	7.4	149.2	-
L.H.	10	3.6	2.8	.92	1.0	9.5	.37	29.0	288.0	1.7
N.H.		1.4	12.4	.50	.53	7.1	.22	1.4	18.1	.08
N.P.S.		9.02	39.9	-	9.62	83.78	-	8.63	118.0	-
		10.69	53.6	-	10.39	94.9	-	10.44	147.5	-

Table 2

Precision estimates for lumped background model (13 samples, perfect initial parameters)

$\beta = 0$		PRECISION ESTIMATES								
		NOMINAL WIND DIRECTION								
		45°			90°			135°		
STATISTICAL HYPOTHESIS	NOMINAL WIND SPEED (mps)	SPEED (mps)	DIRECTION (deg)	BACKGROUND (Digital Number)	SPEED (mps)	DIRECTION (deg)	BACKGROUND (Digital Number)	SPEED (mps)	DIRECTION (deg)	BACKGROUND (Digital Number)
L.H.	4	.05	5.8	.19	.05	323	.23	.05	5.8	.19
N.H.		.03	4.0	.12	-	-	-	.034	4.4	.12
N.P.S.		3.98	42.0	-	-	-	-	3.97	130.9	-
		4.03	49.0					4.03	137.7	
L.H.	7	.12	5.7	.25	.16	274	.40	.12	5.7	.25
N.H.		.085	4.0	.16	-	-	-	.094	3.6	.15
N.P.S.		6.96	40.9		-	-	-	6.92	133.1	-
		7.06	48.0					7.06	137.8	
L.H.	10	.22	7.0	.32	.53	28	.79	.22	7.0	.32
N.H.		.09	4.0	.18	-	-	-	.16	4.6	.24
N.P.S.		9.9	42.0	-	-	-	-	9.87	133.1	-
		10.05	47.5					10.1	138.4	

Table 2--continued

Δ = (.01 mps, .1 deg, .001)

β = 10

		PRECISION ESTIMATES								
		NOMINAL WIND DIRECTION								
		45°			90°			135°		
STATISTICAL HYPOTHESIS	NOMINAL WIND SPEED (mps)	SPEED (mps)	DIRECTION (deg)	BACKGROUND (Digital Number)	SPEED (mps)	DIRECTION (deg)	BACKGROUND (Digital Number)	SPEED (mps)	DIRECTION (deg)	BACKGROUND (Digital Number)
L.H.	4	.24	7.3	.21	.9	7.5	.29	.76	11.5	.25
N.H.		.18	4.2	.16	.74	15.5	.2	.72	3.5	.18
N.P.S.		3.896	42.1	-	3.62	80.8	-	3.37	129.5	-
		4.189	48.5	-	4.6	101.5	-	4.60	143.2	
L.H.	7	.67	5.8	.34	.8	7.5	.25	1.5	15.1	.25
N.H.		.43	3.1	.21	.55	4.9	.19	.89	8.7	.19
N.P.S.		6.59	42.5	-	6.53	86.3	-	6.4	129.7	-
		7.3	46.8		7.35	93.4		7.46	143.2	
L.H.	10	2.9	23.0	.76	.7	7.3	.30	22.6	338.0	1.34
N.H.		.99	7.2	.26	.4	5.1	.21	1.92	23.6	.125
N.P.S.		9.3	40.1	-	9.76	87.05		8.2	113.6	
		10.8	50.0		10.22	95.7		10.9	149.0	

All the N.H. precision estimates for the 7 sample case (Table 1) are greater than those of the 13 sample case (Table 2) save one. The exception occurs in the 10° plane for the 10 m/sec wind and 135° direction. The L.H. estimates differ in the same way, however, and are quite large, indicating strong non-linearity.

To determine if the sample wind velocities could be obtained from a non-perfect initial starting guess (Y), a random component was added to each y_i. It was assumed that the direction would be known to within ± 20°, speed to within 7%. The directional error estimate was determined by a uniform distribution, the wind speed was over-estimated with a uniform distribution, and the background error by a normal distribution. The results are shown in Table 3 for the 13 sample cases (7 other sample cases are included).

The precision estimates in Table 2 are about the same as those in Table 3. It should also be noted that, in the symmetric case through the plane $\beta = 0$, the estimates of error are also symmetric. This indicates that 20 samples give a reasonable estimate of the random error.

The effects of a bias error in aerosol content on the model were determined by incorporating nominal aerosol optical depths $\tau_a(a)$ of 0.1 and .01 into the "observed radiance" with a uniform distribution and by computing the surface wind speed, direction, and background constant. A random error component (g = 1, 600 points) was added to the "observed radiance" and the randomized initial conditions were again used. The results (Table 4) indicated little effect in the case of $\tau_a = .01$ compared to the non-biased case. All directional information was lost in the case of the $\tau_a = .1$ bias. It was concluded that an estimate of aerosol concentration was needed to obtain the surface "wind stress" direction. An attempt was made to determine this concentration directly by introducing another variable, the aerosol optical depth τ_a, into the non-linear least squares model. The attempt was not successful with g = 1 and N = 600 noise; neither τ_a nor θ could be obtained.

Complete Models (unknown aerosol optical depth)

A greater signal to noise ratio, made possible by the choice of the signal improvement factor g, was utilized in conjunction with the models of background radiance to determine the feasibility of obtaining the direction of the wind stress in the presence of an unknown aerosol optical depth. Two models were considered:

a. o_λ = f ("Wind Stress"; Rayleigh Optical Depth, Aerosol Optical Depth, Sub-surface Ocean Back Scatter); $\lambda \simeq .5\mu$ (see Figure 12).

b. o_λ = f ("Wind Stress"; Rayleigh Optical Depth, Aerosol Optical Depth, no Sub-surface Back Scatter); $\lambda = .6\mu$ (see Figure 12).

The random error component was determined by g = 10, N = 600; the initial guess at wind velocity was randomized as before. The normal aerosol optical depth, used in the "observed radiance," varied randomly

Table 3

Precision estimates for lumped background model (13 samples, non-perfect initial parameters)

$\beta = 0$		PRECISION ESTIMATES								
		NOMINAL WIND DIRECTION								
		45°			90°			135°		
STATISTICAL HYPOTHESIS	NOMINAL WIND SPEED (mps)	SPEED (mps)	DIRECTION (deg)	BACKGROUND (Digital Number)	SPEED (mps)	DIRECTION (deg)	BACKGROUND (Digital Number)	SPEED (mps)	DIRECTION (deg)	BACKGROUND (Digital Number)
N.H.	4	.174	5.1	.14	.147	15.2	.09	.16	5.2	.15
N.P.S.		4.0	41.5	-	3.9	81	-	3.98	130.6	-
		4.12	48.3		4.1	99		4.1	138.6	
N.H.	7	.16	4.1	.16	.24	15	.14	.19	4.7	.16
N.P.S.		6.94	42.3	-	6.7	83.4	-	6.9	131.4	
		7.1	48.2		7.1	98.2		7.1	137.0	
N.H.	10	.18	6.0	.24	.65	18.0	.3	.25	6.9	.22
N.P.S.		9.88	41.7	-	9.2	75.6	-	9.85	129.3	-
		10.1	50.2		10.2	102.2		10.2	139.4	

Table 3--continued

Δ = (.01 mps, .1 deg, .001)

β = 10		PRECISION ESTIMATES								
		NOMINAL WIND DIRECTION								
		45°			90°			135°		
STATISTICAL HYPOTHESIS	NOMINAL WIND SPEED (mps)	SPEED (mps)	DIRECTION (deg)	BACKGROUND (Digital Number)	SPEED (mps)	DIRECTION (deg)	BACKGROUND (Digital Number)	SPEED (mps)	DIRECTION (deg)	BACKGROUND (Digital Number)
L.H.	4	(.3	7.4	.27)	(.86	17	.25)	(.89	17.4	.28)
N.H.		0.3	5.4	.16	.67	15	.19	.53	7.5	.16
N.P.S.		3.95	40.7	-	3.8	86.6	-	3.511	130	-
		4.28	48.4		4.5	105.0		4.17	141.0	
L.H.	7	(7.6	5.9	.31)	(.88	6.2	.21)	(1.0	12.6	.27)
N.H.		.45	3.8	.16	.44	5.2	.11	.78	10.5	.19
N.P.S.		6.85	41.2	-	6.78	87.3	-	6.2	123.8	-
		7.48	47.3		7.3	93.8		7.4	140.4	
L.H.	10	(1.6	13.0	.39)						
N.H.		1.7	12.0	.43	.58	3.6	.13	1.4	21.9	.14
N.P.S.		9.2	36.7	-	9.6	87.6	-	8.86	121.4	-
		11.1	51.7		10.7	92.4		10.78	151.9	

Table 4

Precision estimates for lumped background model with aerosol bias (13 samples, non-perfect initial parameters)

β = 10		PRECISION ESTIMATES								
		NOMINAL WIND DIRECTION								
		45°			90°			135°		
STATISTICAL HYPOTHESIS	NOMINAL WIND SPEED (mps)	SPEED (mps)	DIRECTION (deg)	AEROSOL OPTICAL DEPTH	SPEED (mps)	DIRECTION (deg)	AEROSOL OPTICAL DEPTH	SPEED (mps)	DIRECTION (deg)	AEROSOL OPTICAL DEPTH
N.H.	4	.3	7.2	.15	.3	35	.13	.3	10.	.16
N.P.S.		4.04	39.3	-	4.0	71.8	-	3.9	132.2	-
		4.2	47.7		4.2	108.0		4.2	143.2	
N.H.	7	.4	7.2	.15	.37	25	.21	.36	5.0	.17
N.P.S.		6.9	40.3	-	7.0	73	-	6.9	131.9	-
		7.3	48		7.2	101		7.2	139	
N.H.	10	.38	6.3	.27	.42	21	.3	.45	7.2	.23
N.P.S.		9.9	40.2	-	9.7	73.8	-	9.9	130.2	-
		10.3	48.6		10.3	102.2		10.3	140	

Table 4--continued

Δ = (.01 mps, .1 deg, .001)

$\beta = 0$

		PRECISION ESTIMATES								
		NOMINAL WIND DIRECTION								
		45°			90°			135°		
STATISTICAL HYPOTHESIS	NOMINAL WIND SPEED (mps)	SPEED (mps)	DIRECTION (deg)	AEROSOL OPTICAL DEPTH	SPEED (mps)	DIRECTION (deg)	AEROSOL OPTICAL DEPTH	SPEED (mps)	DIRECTION (deg)	AEROSOL OPTICAL DEPTH
N.H.	4	.26	7.1	.16	.56	16.4	.19	.6	7.6	.16
N.P.S.		3.9	42.2	-	3.6	85.5	-	3.5	129	-
		4.3	51.2		4.5	103.2		4.2	140	
N.H.	7	.35	6.6	.15	.76	9.2	.16	1.1	15.6	.20
N.P.S.		6.7	42.1	-	6.8	88.0	-	6.1	122.3	-
		7.3	50.1		7.6	96.6		7.7	138.9	
N.H.	10	2.0	16.5	.54	.78	4.8	.16	1.28	19.3	.16
N.P.S.		9.1	33.7	-	9.7	73.8	-	9.9	130.2	-
		10.3	48.6		10.3	103.2		10.3	140.0	

between .0 and .5 (uniform distribution). The initial guess of normal aerosol optical depth was randomly varied between .0 and .5 (uniform distribution). Precision estimates were made with two termination criteria for model a.

The precision estimates for model a are shown in Table 5. Those for model b are shown in Table 6.

The precision estimates shown in Table 5 indicate that some directional information may be obtained in the $\beta = 10°$ plane for East-West winds. There is also an indication that greater precision is possible if the termination criteria are decreased (compare Δ_B with Δ_a).

The precision estimates shown in Table 6, for the model which simulates the case of no surface ocean back scatter, are superior to those in Table 5. Because the estimates shown in Table 6 are obtained from observations taken over 1/4 of a square degree, an increase in precision is possible if the wind is spacially averaged over a larger area. The precision may be increased by a factor of two if the sunglint wind is averaged over one degree. A further increase in precision is possible if the sunglint is sampled more often. The sunglint viewed from a synchronous satellite may be sampled as rapidly as every 5 minutes. On a linear hyopthesis, this will lead to an approximate $1/\sqrt{3}$ reduction in the estimates of Table 6. By averaging over a square degree and sampling the sunglint more frequently, say once every 5 minutes, a reduction of $\frac{1}{3.46}$ in the estimates of Table 6 may be obtained.

Systematic Error

In the previous sections, the effects of random errors in measurement of the total radiance were used to estimate the precision to which the surface wind or stress may be determined. In the presence of a bias or systeamtic error these estimates may be incorrect. Here, possible sources of bias errors are considered briefly and a method is suggested for evaluating their effect.

Systematic errors may be produced by:

1. errors in navigation of satellite images,
2. non-linearities in the amplifiers which follow the photomultiplier,
3. saturation of the photomultiplier,
4. non-uniform distribution of aerosols.

Other sources of systematic error may also be present. For example, the effects of oil slicks and debris may be sufficiently significant to affect the reflectivity of the ocean's surface. Also, the implicit assumption of the uniqueness of the slope distribution may not be valid.

An estimate of the effect of systematic error may be obtained. First,

Table 5

Precision estimates for aerosol model with ocean back scatter (13 samples, non-perfect initial parameters)

Δ = (.01 mps, .1 deg, .001, .001)

β = 10

		PRECISION ESTIMATES								
		NOMINAL WIND DIRECTION								
		45°			90°			135°		
STATISTICAL HYPOTHESIS	NOMINAL WIND SPEED (mps)	SPEED (mps)	DIRECTION (deg)	AEROSOL OPTICAL DEPTH	SPEED (mps)	DIRECTION (deg)	AEROSOL OPTICAL DEPTH	SPEED (mps)	DIRECTION (deg)	AEROSOL OPTICAL DEPTH
N.H.	4	.6	24.1	.127	.4	8.3	.095	1.0	21.1	.13
N.P.S.		3.7	30.4	-.11	3.7	81	-.128	3.0	120	-.099
		4.6	60.5	.06	4.3	97	.085	4.8	149	-.124
N.H.	7	1.05	18.9	.1	1.37	11.7	.088	2.0	22.4	.122
N.P.S.		6.4	35.0	-.044	5.6	80.0	-.1	4.89	122	-.145
		7.7	59	.096	8.4	99	.039	7.28	150	.019

Table 5--continued

Δ = (.001 mps, .1 deg, .001, .001)

β = 10		PRECISION ESTIMATES								
		NOMINAL WIND DIRECTION								
		45°			90°			135°		
STATISTICAL HYPOTHESIS	NOMINAL WIND SPEED (mps)	SPEED (mps)	DIRECTION (deg)	AEROSOL OPTICAL DEPTH	SPEED (mps)	DIRECTION (deg)	AEROSOL OPTICAL DEPTH	SPEED (mps)	DIRECTION (deg)	AEROSOL OPTICAL DEPTH
N.H.	4	.5	22.1	.06	.4	7.	.014	.96	20.3	.1
N.P.S.		3.7	30	-.048	3.7	85	-.012	3.0	120	-.098
		4.5	60	-.041	4.3	95	.007	4.4	148.0	.049
N.H.	7	1.1	17.8	.06	1.39	7.7	.03			
N.P.S.		6.6	34	-.048	5.6	80	-.025			
		7.8	59	.062	8.4	95	-.033			

Table 6

Precision estimates for aerosol model without ocean back scatter (13 samples, non-perfect initial parameters)

$\beta = 0$		PRECISION ESTIMATES								
		NOMINAL WIND DIRECTION								
		45°			90°			135°		
STATISTICAL HYPOTHESIS	NOMINAL WIND SPEED (mps)	SPEED (mps)	DIRECTION (deg)	AEROSOL OPTICAL DEPTH	SPEED (mps)	DIRECTION (deg)	AEROSOL OPTICAL DEPTH	SPEED (mps)	DIRECTION (deg)	AEROSOL OPTICAL DEPTH
N.H.	4	.07	2.5	.009	.08	16.6	.01	.056	2.7	.008
N.P.S.		3.96	43.4	-.006	3.95	80	-.007	3.96	138	-.009
		4.01	46.4	+.005	4.06	101	.008	4.05	137	.005
N.H.	7	.21	2.5	.018	.17	12.8	.015	.145	1.7	.012
N.P.S.		6.8	43.0	-.01	6.8	80.8	-.011	6.8	133.5	-.009
		7.1	47.0	.016	7.1	98.8	.011	7.1	136.1	.012
N.H.	10	.35	2.2	.022	.42	13.5	.026	.41	2.9	.025
N.P.S.		9.7	43.5	-.015	9.6	77.0	-.023	9.7	132.9	-.015
		10.2	46.4	.016	10.3	97.8	.024	10.25	136.4	.017

Table 6--continued

Δ = (.01 mps, .1 deg, .001)

β = 10

STATISTICAL HYPOTHESIS	NOMINAL WIND SPEED (mps)	PRECISION ESTIMATES								
		NOMINAL WIND DIRECTION								
		45°			90°			135°		
		SPEED (mps)	DIRECTION (deg)	AEROSOL OPTICAL DEPTH	SPEED (mps)	DIRECTION (deg)	AEROSOL OPTICAL DEPTH	SPEED (mps)	DIRECTION (deg)	AEROSOL OPTICAL DEPTH
N.H.	4	.129	3.11	.008	.347	.75	.007	.98	6.6	.0312
N.P.S.		3.8	42.0	-.006	3.8	87.0	-.006	2.7	127.8	-.048
		4.2	47.0	.004	4.3	96.8	.004	4.6	139.1	.013
N.H.	7	.25	5.6	.018	.34	2.0	.012	.7	14.3	.02
N.P.S.		6.7	39.0	-.016	6.8	88.8	-.007	6.5	129.4	-.01
		7.2	49.5	.018	7.3	91.6	.010	7.7	153.2	.022
N.H.	10	1.2	10.5	.015	.71	3.1	.03	1.28	27.4	.015
N.P.S.		9.6	34.3	-.019	9.6	87.3	-.022	9.6	128.	-.004
		11.5	52.2	.003	10.5	92.6	.016	10.9	135.0	.018

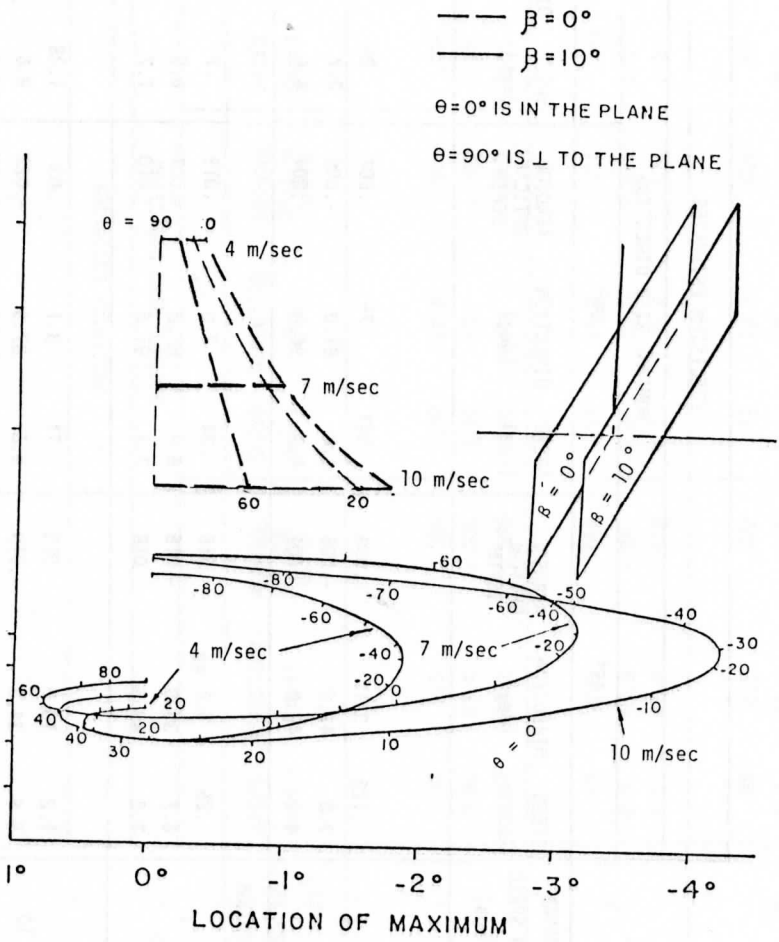

Figure 20 BIAS ERROR ESTIMATION CHART

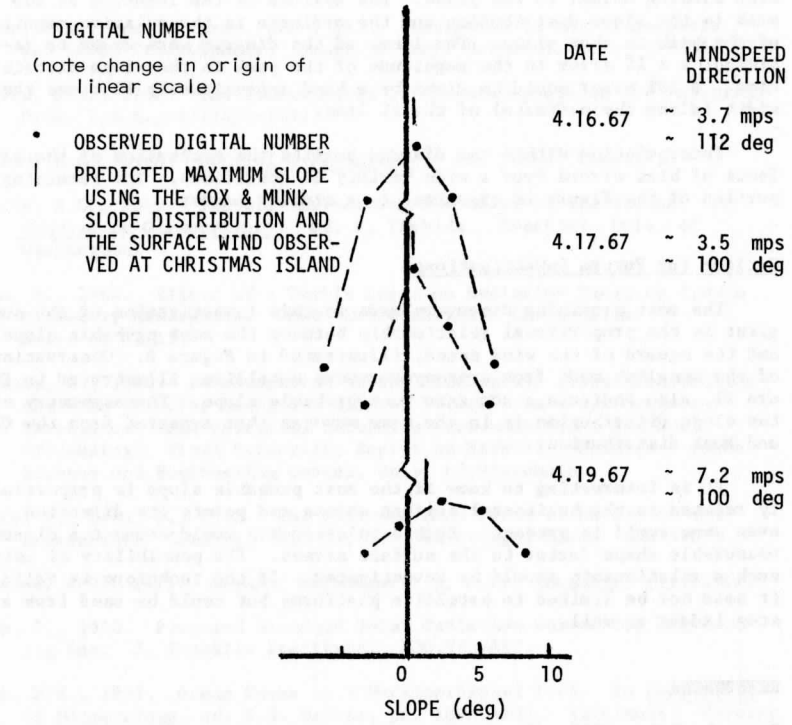

Figure 21 THE SKEWNESS OF THE 'SLOPE' DISTRIBUTION AT CHRISTMAS ISLAND OBTAINED FROM A SEQUENCE OF GEDSYNCHRONUS SATELLITE OBSERVATIONS.

the slope distribution is characterized by its maximum value and by the location of its maximum value in the plane which passes through the distribution. In a particular plane, the maximum value and its location will depend on both the wind speed and direction. In Figure 20, the maximum value and its location are shown for two planes, three wind speeds, and several directions.

The uppermost portion of the diagram shows the relationship of wind direction and speed for the plane passing through the slope $\beta = 0$. Wind speeds are shown as three lines representing 4, 7, and 10 m/sec. Wind directions relative to the plane are shown along each of the lines. Thus, $\theta = 0$ represents a wind blowing along the plane and $\theta = 90$ represents a wind blowing normal to the plane. The absicsa is the location of the peak in the slope distribution and the ordinate is the relative magnitude of the peak in that plane. The lines of the diagram were drawn to represent a $\pm$ 1% error in the magnitude of the peak in the slope distribution. A 10% error would be given by a band approximately 10 times the width (along the ordinate) of the 1% line.

Interpolation within the diagram permits the estimation of the effects of bias errors over a wide variety of conditions. The remaining portion of the figure is organized in a similar manner.

Outlook for Future Investigations.

The most promising discovery made in this investigation of the sunglint is the proportional relationship between the most probable slope and the square of the wind speed, illustrated in Figure 8. Observations of the sunglint made from a geosynchronous satellite, illustrated in Figure 21, also indicate a non-zero most probable slope. The asymmetry of the slope distribution is in the same sense as that expected from the Cox and Munk distribution.

It is interesting to know if the most probable slope is proportionally related to the horizontal surface stress and points its direction even when swell is present. Such a relationship would connect a directly measurable shape factor to the surface stress. The possibility of using such a relationship should be investigated. If the technique is valid, it need not be limited to satellite platforms but could be used from a step ladder as well.

REFERENCES

Barnett, T.P., 1968. On the Generation, Dissipation, and Prediction of Ocean Wind Waves. J. Geopnys. Res. 73:513-529.

Bascom, W., 1964. Waves and Beaches. The Dynamics of the Ocean's Surface. New York: Doubleday.

Climatological and Oceanographic Atlas for Mariners, 1960, U.S. Dept. of Commerce Weather Bureau.

Coulsen, Dave, and Sekera, 1960. Tables Related to Radiation Emerging from a Planetary Atmosphere with Rayleigh Scattering. Berkely and Los Angeles: Univ. of Calif. Press.

Cox, C.S., 1956. Ripples. In The Sea. ed. M.N. Hill, 1:720-729.

Cox, C., and Munk, W., 1959. Slopes of the Sea Surface Deduced from Photographs of the Sun Glitter. Bulletin of the Scripps Institution of Oceanography, Vol. 6, no. 9.

Duntley, S.O., 1954. Measurements of the Distirbution of Water Wave Slopes. J. Opt. Soc. Am., 44:574-575.

Goody, R.M., and Robinson, G.D., 1951. Radiation in the Troposphere and Lower Stratosphere. Quart. J. Roy. Meteorol. Soc., 77:151-187.

Howard, J.N., 1959. The Transmission of the Atmosphere in the Infrared. Proc. I.R.E., 47:1451-1457.

Jerlov, N.G., 1968. Optical Oceanography. New York: Elsevier.

Jerlov, N.G., 1965. Factors Influencing the Color of the Oceans. In Studies on Oceanography. ed. K. Yoshida. Seattle: Univ. of Washington.

Kano, M., 1964. Effect of a Turbid Layer on Radiation Emerging from a Planetary Atmosphere. Ph.D. Dissertation. Los Angeles: Univ. of Calif.

Levanon, N., 1968. Determination of the Sea Surface Slope Distribution and Wind Velocity using Sun Glitter Viewed from a Synchronous Satellite. Meteorological Satellite Instrumentation and Data Processing. Final Scientific Report on NASW-65. Madison: Space Science and Engineering Center, Univ. of Wisconsin.

Mintz, Y., Dean, G., 1952. The Observed Mean Field of Motion of the Atmosphere. Geophys. Res. P., 17. Cambridge, Mass: GRD AFCRL.

Monahan, E.D., 1971. Oceanic Whitecaps. J. Phys. Oceanogr. 1:139-144.

Moon, P., 1940. Proposed Standard Solar Radiation Curves for Engineering use. J. Franklin Institute. 230:583-617.

Munk, W.H., 1951. Ocean Waves as a Meteorological Tool. In Compendium of Meteorology. ed. T.F. Malone, pp. 1090-1102. Baltimore: Waverly Press.

Pierson, N.J., 1960. Practical Methods for Observing and Forecasting Ocean Waves by Means of Wave Spectra and Statistics. Hydrographic Office Pub. no. 603.

Phillips, O.M., 1966. The Dynamics of the Upper Ocean. Cambridge: Cambridge Univ. Press.

Plass, G.N., and Kattawar, G.W., 1970. Polarization of the Radiation Reflected and Transmitted by the Earth's Atmosphere. Applied Optics 9:1122.

Plass, G.N., and Kattawar, G.W., 1969. Radiative Transfer in an Atmosphere-Ocean System. Applied Optics 8:455.

Saunders, P.M., 1967. Shadowing on the Ocean and the Existence of the Horizon. J. Geophys. Res. 72:4643-4649.

Schooley, A.H., 1954. A Simple Optical Method for Measuring the Statistical Distribution of Water Surface Slopes. J. Opt. Soc. Am. 44:37-40.

Snodgrass, F., Groves, G.W., Kasselmann, K.F., Miller, G.R., Munk, W.H., and Powers, W.H., 1966. Propagation of Ocean Swell across the Pacific. Phil. Trans. Roy. Soc. London, A., pp. 259, 431.

Sromovsky, L.A., 1971. Sun Glint as an Atmospheric Probe. Satellite Measurement of Spectral Turbidity and Albedo, and their Rates of Change. Report no. UWI-SSEC-GAP-71-003. Madison: Space Science and Engineering Center, Univ. of Wisconsin.

Strong, A.E., and Ruff, I.S., 1970. Utilizing Satellite Observed Solar Reflections from the Sea Surface as an Indicator of Surface Wind Speed. Remote Sensing Environ. 1:181-185.

Sverdrup, H.U., Fleming, R., and Johnson, M., 1942. The Oceans. New York: Prentiss Hall.

Volz, F.E., 1970. Spectral Skylight and Solar Radiance Measurements in the Caribbean: Maritime Aerosols and Sahara Dust. J. Atmos. Sci. 27:1041.

Zaslavskiy, M.M., and Kitaygorodskiy, S.A., 1971. The Equilibrium Interval in the Spectrum of Wind Generated Surface Gravitational Waves. Akademiya Nauk S.S.S.R. Izvestiya Fizika Atmosfery i Okeana. English edition of Izvestiya, Academy of Sciences USSR Atmospheric and Oceanic Physics. 7:375-379.

CLOUD BRIGHTNESS CONTRAST AS VIEWED BY A SATELLITE

Frederick R. Mosher

ABSTRACT

The purpose of this study was to examine the requirements of a brightness normalization procedure for satellite pictures. Previous approaches to the normalization problem were reviewed and their deficiencies noted. The theoretical background of scattering from clouds was reviewed along with experimental verification of theoretical results. To see if brightness contrast is a function of scattering geometry, observations were made using the ATS III satellite. These observations showed the contrast to be a function of geometry. Thus, different parts of a cloud require different normalization corrections. The phase function of droplets and ice cylinders were also observed.

INTRODUCTION

The purpose of this study is to examine the requirements of a normalization and standardization procedure for satellite pictures. Meteorological satellites now provide pictures of the earth and its cloud cover on a routine basis. They offer the coverage and resolution needed to study and monitor mesoscale phenomena such as convection. These satellites now merely provide pretty pictures. However, they offer the possibilities of providing considerably more information, especially on mesoscale phenomena. If we are to study mesoscale phenomena from a satellite, we must first understand how light interacts with a cloud and the information about clouds garnered from light received by the instrument.

The reflected light from horizontally homogeneous clouds depends to a large extent on four variables:

a) Drop size distribution and phase state of water particles,

b) Number density of scattering particles in the cloud,

c) Cloud thickness,

d) Angular condition of the measurement system (the zenith angles of the sun and the sensor and their relative azimuth angle).

In the study of some convective process, such as cloud growth, only one variable should change at a time. If the cloud thickness changes and the sun or the satellite also moves, a method of removing the effect of change in the measurement geometry is needed. This is the normalization problem. Once the normalization problem has been satisfactorily solved, a considerable amount of information can be gathered from satellite

photographs. The volume flux through a cloud can accurately be determined along with the associated rainfall and energy release. This, combined with the extensive coverage offered by the satellite, makes it possible to explore the large scale energetics associated with convective systems. But first the normalization problem must be solved.

There have been several approaches to the normalization problem. The simplest approach has been to assume that clouds are perfect isotropic reflectors and obey Lambert's law. The intensity of the reflected light varies as the cosine of the solar zenith angle for an unchanging cloud. There has been some evidence that this is a valid assumption for very thick clouds. Martin and Suomi (1972) have shown that the tops of cumulonimbus clouds display a Lambertian behavior. Sikdar and Suomi (1972) have also shown that thick clouds behave as Lambertian reflectors for small solar zenith angles (+30° to -30°).

However, there is considerable evidence in the literature that other clouds do not behave as Lambertian reflectors. Bartman (1967) measured the scattering off stratocumulus clouds and found anisotropic reflectance. Ruff, et. al. (1968) used TIROS IV radiometer instruments to measure the angular distribution of solar radiation reflected from clouds. They found that clouds generally show an anisotropic reflectance pattern which varies with solar zenith angle. Brennan and Bandeen (1970) measured the pattern of reflectance of solar radiation from stratocumulus clouds using an aircraft-born medium resolution radiometer. They also show clouds to be anisotropic reflectors.

Since there is ample evidence that clouds are not isotropic reflectors, Sikula and Vonder Haar (1972) developed a normalization procedure based on the empirical data of Brennan and Bandeen (1970). It used empirical anisotropic factors which were tabulated for various solar zenith angles, satellite zenith angles, and the azmiuth angle between them. The procedure is an improvement over the isotropic assumption, but it still has several drawbacks. First, it needs continuous revision as more data become available. Second, it makes no allowance for variations in the types and structure of clouds. For any given sun-cloud-satellite geometry, the same normalization factor is applied to all types of clouds and to all parts of a single cloud. A cloud is a cloud is a cloud. Or is it?

The purpose of this study is to examine the requirements of a better normalization system and to provide some suggestions for improving the normalization procedures. In order to accomplish this, we must review the definition of terms and the geometry of scattering. In this review and throughout the main body of the report, we will assume that clouds are horizontally homogeneous. After defining terms, the theoretical literature will be reviewed. The dependence of the single scattering phase function of the scatter's size distribution and shape will be briefly covered. For multiple scattering, the effects of the cloud's thickness, size distribution, and phase function shape will be examined.

Experimental observations of phase functions and of real clouds will be reviewed. Observations are made to answer questions raised by the theoretical and experimental literature review, for example, the dependence of the contrast between parts of a cloud. This question is important because we must know if the same normalization factor can be applied to all parts of a single cloud, or if different factors must be

applied to different parts. Another question deals with the types of phase functions found in clouds. Included in the analysis will be a discussion of possible effects, such as data biasing and possible inhomogeneties in clouds, which could cause mininterpretations of the results.

SCATTERING

A. Geometry of Scattering and Definitions

The geometry of scattering is illustrated by Figure 1. Light coming from the sun with zenith angle θ_o and azimuth angle ϕ_o is scattered by the cloud toward a satellite with zenith angle θ and azimuth angle ϕ. The angle of scattering (α) is the angle between the sun and satellite vectors in the sun-cloud-satellite plane. The angle is related to the zenith and azimuth angles of the incident ray (θ_o, ϕ_o) and of the scattered ray (θ, ϕ) by the equation:

$$\cos \alpha = \cos \theta \cos \theta_o + \sin \theta \sin \theta_o \cos (\phi - \phi_o).$$

The "scattering angle" β is defined by

$$\beta = 180° - \alpha$$

A scattering angle β of 0° is complete forward scatter ($\alpha = 180°$), and a scattering angle of $\beta = 180°$ is complete backscatter ($\alpha = 0°$). The amount of light scattered toward the satellite is:

$$I(\alpha) = P(\alpha) \cos \theta \cos \theta_o I_o$$

where I_o is the light incident on the cloud and $P(\alpha)$ is the bidirectional reflectance. The bidirectional reflectance is the fraction of the light incident from the direction (θ_o, ϕ_o) which is reflected in the direction (θ, ϕ). If only single scattering takes place this is called the phase function.

For a perfectly diffuse (Lambertian) reflector, $P(\alpha)$ is a constant. For other reflectors, it is not. The bidirectional reflectance of a homogeneous cloud is determined by its droplet size distribution, depth, and the phase state of the cloud particles. For single scattering the dependence of the phase function upon these parameters is informative.

B. Phase Function of Various Scatterers

The phase function of a scattering body can be obtained theoretically by using Mie theory (van de Hulst, 1957). Mie theory is applicable to scattering by spheres, ellipsoids, and the infinite cylinder. Almost all research with Mie theory has used the sphere as the scattering body. The scattering off spheres is described by its phase function. In the case of a size distribution of particles, the particles are assumed to scatter independently.

The resultant phase function for the distribution is obtained by integrating over all particles in the size distribution. Hence the size distribution generally is one which approximates nature but is analytic,

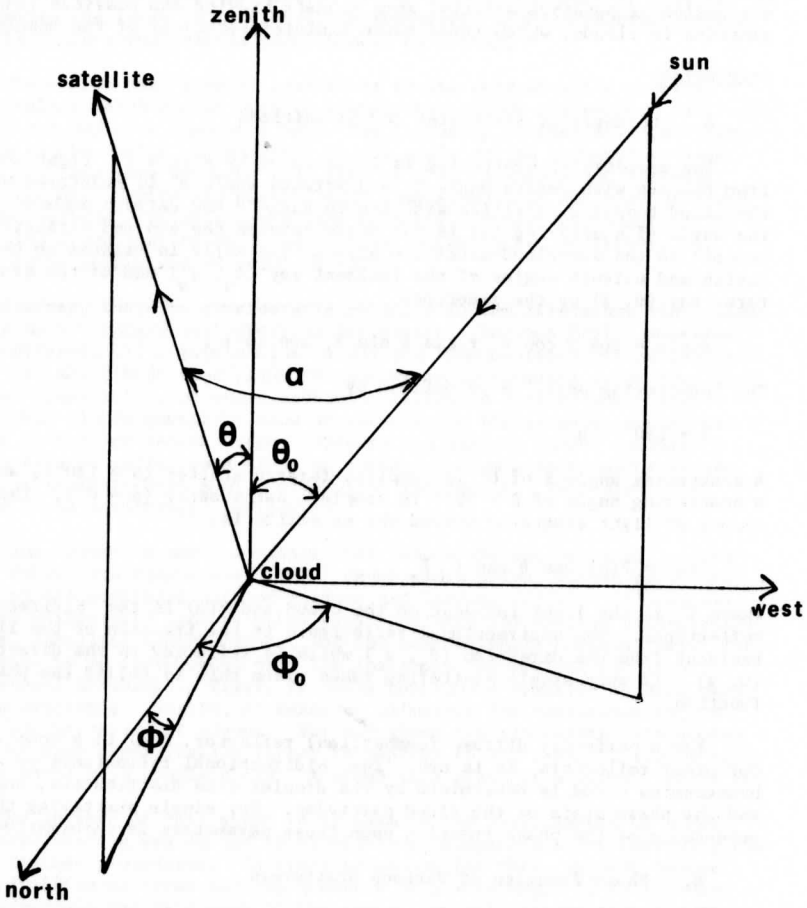

figure 1

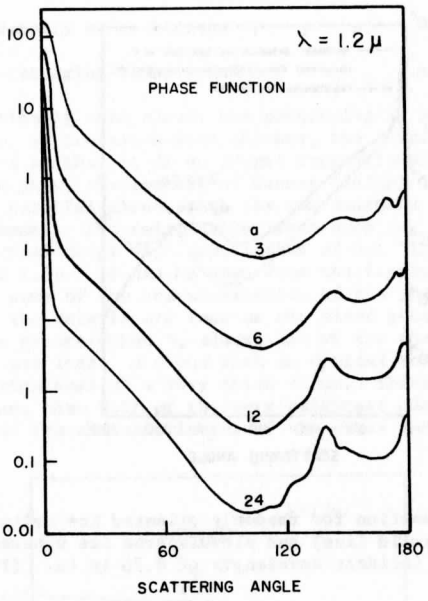

Figure 2. Phase function for single scattering by spherical particles. Results are shown for four values of a, the effective radius, in microns. The phase functions are successively displaced from one another. (From Hansen, 1971b).

such as a Gaussian or gamma distribution. The phase functions for a gamma distribution of spherical droplets of various effective radii are shown for light in the near infrared, 1.2μ in Figure 2 (from Hansen, 1971b). The size of the particle in relation to the wavelength of the light is the critical parameter which determines the phase function. Thus the phase functions in Figure 2 can be applied to other wavelengths of visible light with the size of the mean radius a being replaced by $a' = (\lambda'/1.2)a$.

The phase function for other geometries has not been studied as well as that for spheres. Ice crystals are composed of hexagonal cylinders, plates, dendrites, or a combination of these shapes. In cirrus clouds the ice crystals are generally composed of 75% cylindrical shapes. The remainder is predominately plates (Heymsfield and Knollenberg, 1972). The phase function for cylinders has been studied by Liou (1972). He used Mie theory for infinitely long cylinders having a gamma size distribution with the cylinders randomly oriented in a horizontal plane. Figure 3 shows his results. It should be noted that he shows cylinders having much less backscatter than have spheres.

C. Multiple Scattering

The phase functions presented so far have been for single scattering,

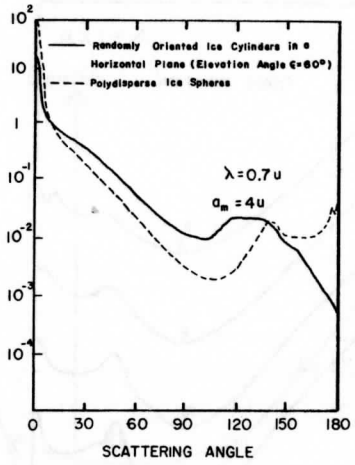

Figure 3. Phase function for randomly oriented ice cylinders in a horizontal plane (solid line) and ploydisperse ice spheres (dotted line). The mode radius at incident wavelength of 0.7μ is 4μ. (From Liou, 1972)

i.e., only one scattering event occurs for each photon scattered in the direction of the receiver. In real clouds, each photon is scattered many times from the moment it enters the cloud until it leaves. Thus simple single scattering theory cannot be used to calculate the intensity of the scattered light. Recently, several approaches to the multiple scattering problem have been developed by Dave (1964, 1970), Twomey et. al. (1966), Kattawar and Pass (1968), and Hansen (1971a). These methods can be used to determine the effects of cloud thickness, droplet distribution, and various phase functions.

1. Effect of Cloud Thickness on Scattered Light

To describe the passage of radiation through a cloud layer, one must specify the thickness of the layer. The thickness of a layer is described more concisely by using the optical, rather than the geometric, thickness, the optical thickness (τ) of a layer is such that unit radiation normally incident upon the layer is reduced in passing through the layer to $e^{-\tau}$. For visible wavelengths the absorption of the radiation by cloud droplets is negligible. Thus the reduction in intensity is due to scattering. If we assume a homogeneous cloud with fixed drop-size distribution and density of scatterers, the optical thickness may be readily converted to geometric thickness by means of the relationship:

$\tau = kd$

with d = geometric thickness

k = extinction coefficient = $\sigma\rho$

ρ = density of scatterers

σ = scattering cross section

For an optically thin cloud, the scattering is proportional to the phase function. As the cloud gets thicker, the bidirectional reflectivity is modified so that it is no longer proportional to the phase function. Figure 4 shows the results of Hansen (1971b) for sunlight reflected by a plane parallel cloud, with the sun overhead ($\theta_o = 0°$), for various optical thicknesses. The calculations were done for a gamma size distribution of spherical drops with mean radius of 6μ. The scattered light has a wavelength of 1.2μ. As can be seen from the figure, the thin clouds still maintain some of the characteristics of the single scatter phase function. But the details are lost as the cloud gets thicker. For optical thickness greater than 8, almost all of the characteristics of the phase function are lost. A cloud with an optical thickness of 8 has about one-half the brightness of a very thick cloud. Therefore a cloud with a brightness less than half of the very brightest cloud should still maintain some of the characteristics of the phase function.

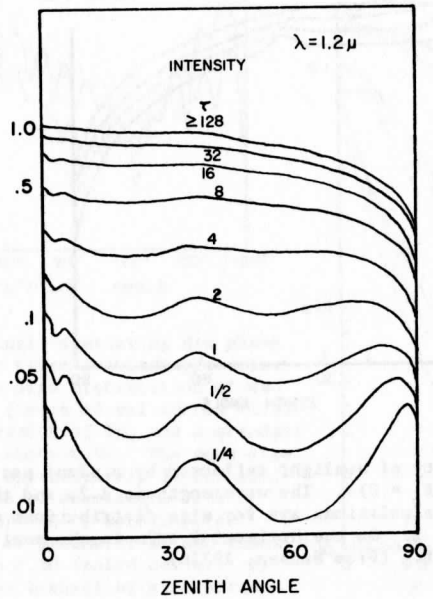

Figure 4. Intensity of sunlight reflected by a plane parallel cloud with the sun overhead ($\theta_o = 0°$). The wavelength is 1.2μ and results are shown for several optical thicknesses. On the horizontal axis is the zenith angle of the reflected light . The calculations are for a gamma size distribution with an effective radius a = 6μ. (From Hansen, 1971b)

2. Effect of Droplet Distribution

The size distribution of water droplets in the cloud has some effect on the intensity of the scattered light. Figure 5 shows the results of Hansen (1971b) for size distributions between 3μ and 24μ mean radius scattering 1.2μ light in a cloud with optical thickness of 32. The phase functions for these size distributions are shown in Figure 2. Figure 5 shows the smaller particles scattering slightly more light than the larger ones. This is due to the small amount of light absorbed by the larger particles in addition to scattering the 1.2μ light. The shapes of the curves do not vary much with size distribution. The intensity of the scattered light varies on the order of 15%. Therefore an uncertainty of approximately 15% can be introduced into results where the size distribution is unknown.

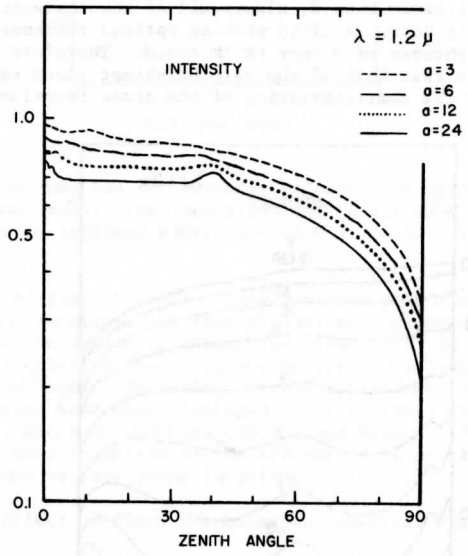

Figure 5. Intensity of sunlight reflected by a plane parallel cloud with the sun overhead ($\theta_o = 0$)). The wavelength is 1.2μ and the cloud thickness is 32. The calculations are for size distributions with various effective radii a in μ. On the horizontal axis is the zenith angle θ of the reflected light. (From Hansen, 1971b)

3. Effect of Phase Function Shape

There is a variation in phase function shape caused by the size distribution (Figure 2) and by possible geometry effects (Figure 3). The preceding section showed that the dropled distribution has an effect, but that the role played by changes in phase function, as opposed to the role played by changes in the small abosrption, in the droplets is unclear.

Howell (1968) examined the problem of the sensitivity of multiple-scattering calculations to the single scatter phase function. He set the single scattering albedo to unity so that there was no absorption allowed in his calculations. Figure 6 shows the phase functions he used and Figure 7 shows the reflected intensity for various optical thicknesses and source-observer geometries. In his notation, $\mu_o = \cos \theta_o$ is the cosine of the zenith angle of the source, and $\mu = \cos \theta$ is the cosine of the zenith angle of the observer. As can be seen from Figure 7, the variation in phase function has some effect on the scattering from clouds with thin and moderate optical thicknesses, but has very little effect on scattering from very thick clouds.

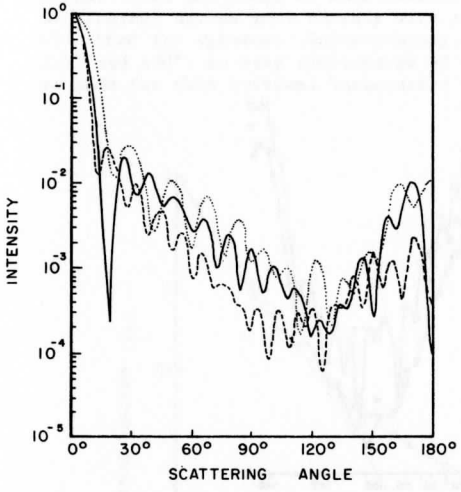

Figure 6. Single-scattering Mie phase functions for three scattering models: 1) A Gaussian size distribution of water droplets (index of refraction =1.33) with a mean radius of 2μ, and a standard deviation of about 0.5μ. The mean size parameter is approximately 17 for incident radiation of wavelength 0.76 μ (dashed curve). 2) A monodisperse aerosol of size parameter 16 and index of refraction 1.50 (solid curve). 3) A monodisperse aerosol of size parameter 11 and index of refraction 1.50 (dotted curve).

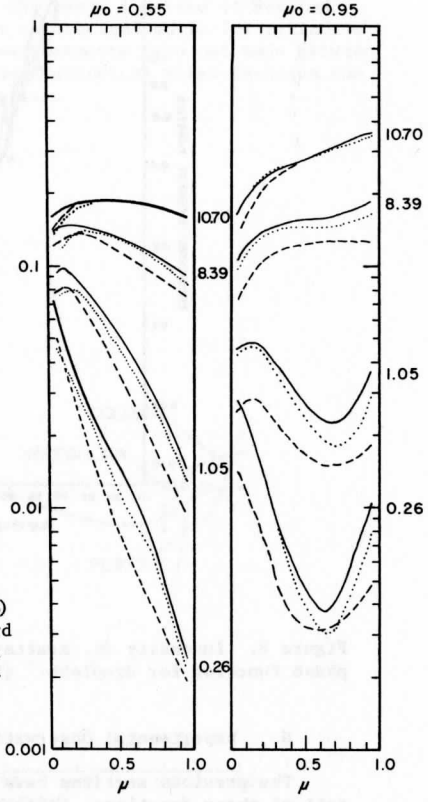

Figure 7. Intensity of reflected light by a plane parallel cloud for the three scattering models described in Figure 6. Optical thickness in indicated beside each set of curves. The cosine of the zenith angle of the source ($\mu_o = \cos \theta_o$) is indicated above each graph. The horizontal axis is the cosine of the zenith angle of the reflected light ($\mu = \cos \theta$). (From Howell, 1968)

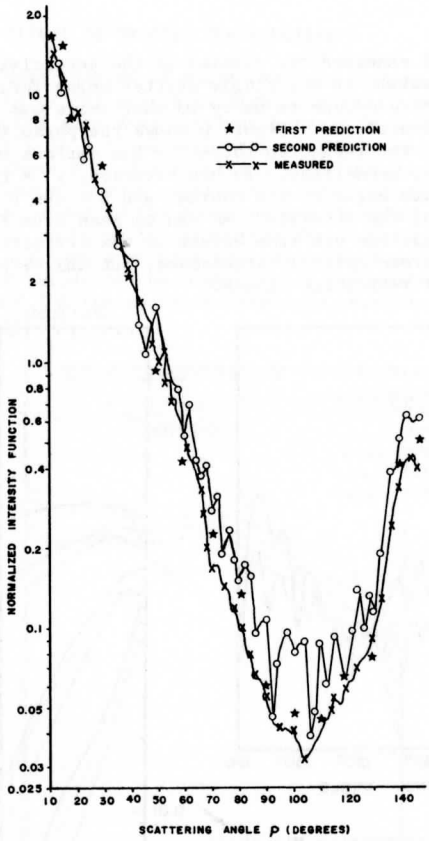

Figure 8. Intensity vs. scattering angle for measured and theoretical phase function for droplets. (From Setzer, 1969)

D. Experimental Observations

The previous sections have presented theoretical results using theoretical phase functions. This section will present experimental observations of phase functions and of real clouds.

1. Experimental Observations of Phase Function

Laboratory experiments by Setzer (1969) comparing theoretical and measured droplet scattering phase functions show very good agreement be-

tween the two. Figure 8 visualizes the results of his work. These results are supportive of theoretical calculations using spheres.

Scattering off ice crystals has been studied experimentally by Huffman and Thursby (1969). They generated ice crystals in a laboratory cold chamber and measured the scattering off a thin cloud of these crystals. The type of crystal was controlled by the temperature of the cold chamber. Figure 9 shows the phase function measured for ice crystals and the phase function for spheres with a similar size distribution. As can be seen from the figure, the phase function of ice crystals is not the same as that of spheres. Figure 10 shows Liou's (1972) phase function of random cylinders compared with Huffman and Thursby's (1969) results. Over the range of measurements, the phase function of Huffman and Thursby agrees more closely with the theoretical curve for cylinders than that for spheres. Unfortunately, measurements were not made between 150° and 180°, so only conjectures of the theoretical phase function can be made for this critical backscatter region.

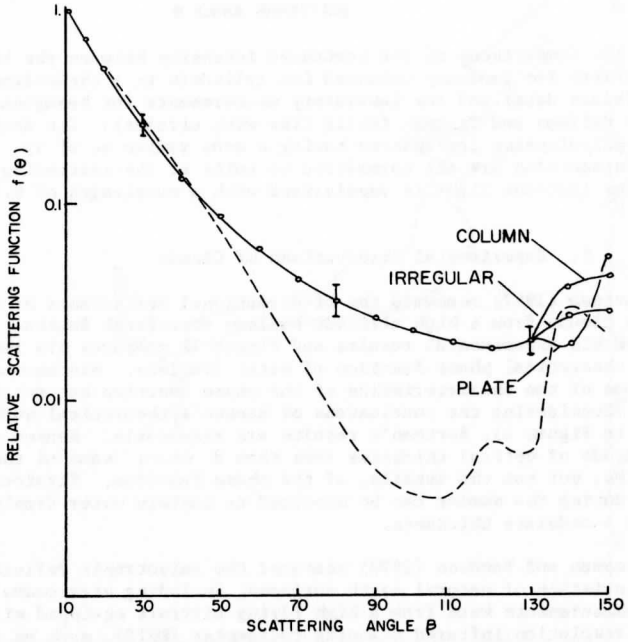

Figure 9. Measured values of the relative scattering phase function for ice crystals grown at three temperatures (solid curve) and computed values for water droplets (dashed curve). (From Huffman and Thursby, 1969)

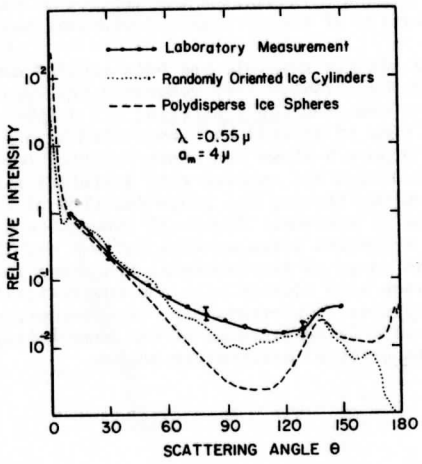

Figure 10. Comparisons of the scattered intensity between the theoretical calculations for randomly oriented ice cylinders in a three-dimensional space (black dots) and the laboratory measurements for hexagonal columns made by Huffman and Thursby (solid line with circles). The dotted line is for polydisperse ice spheres having a mode radius α_η of 4μ. The scattered intensities are all normalized to unity at the scattering angle of 10°. The incident light is unpolarized with a wavelength of 0.55μ.

2. Experimental Observations of Clouds

Bartman (1967) measured the bi-directional reflectance of stratocumulus clouds from a high altitude balloon over South Dakota. Figure 11 shows his experimental results and Figure 12 compares his results with a theoretical phase function of water droplets. His measurements show some of the characteristics of the phase function but not the details. Considering the conclusions of Hansen's theoretical works (shown in Figure 4), Bartman's results are reasonable. Hansen concluded that clouds of optical thickness less than 8 show some of the characteristics, but not the details, of the phase function. Stratocumulus clouds during the summer can be expected to contain water droplets and to have a moderate thickness.

Brennan and Bandeen (1970) measured the anisotropic reflectance characteristics of natural earth surfaces, including stratocumulus clouds. Their measurements were from a high flying aircraft equipped with a medium resolution infrared scanning radiometer (MRIR), such as those on the Nimbus satellite. The aircraft flew a rosette pattern over the target area. The results of strato cumulus clouds show a strong forward scattering peak and a weaker backward scattering peak. This again would indicate a moderate to thin cloud with anisotropic scattering.

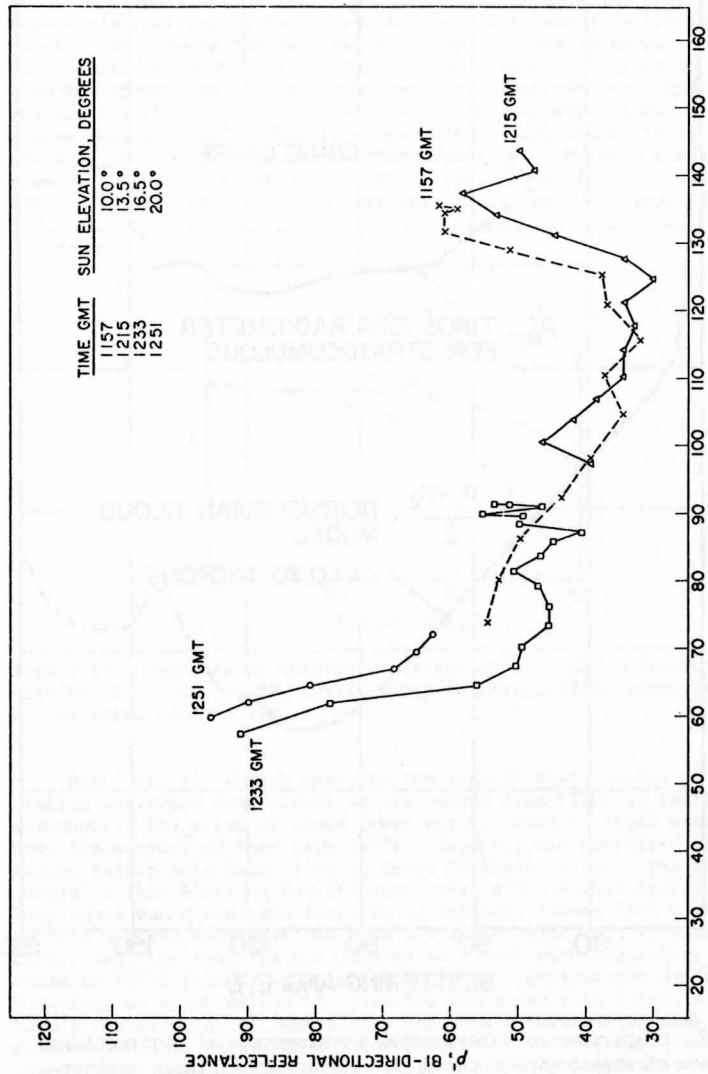

Figure 11. Bidirectional reflectance of stratocumulus clouds, ρ' for 0.55-0.75-micron channel of TIROS #103A radiometer, 2 June, 1962 balloon flight. (from Bartman,67)

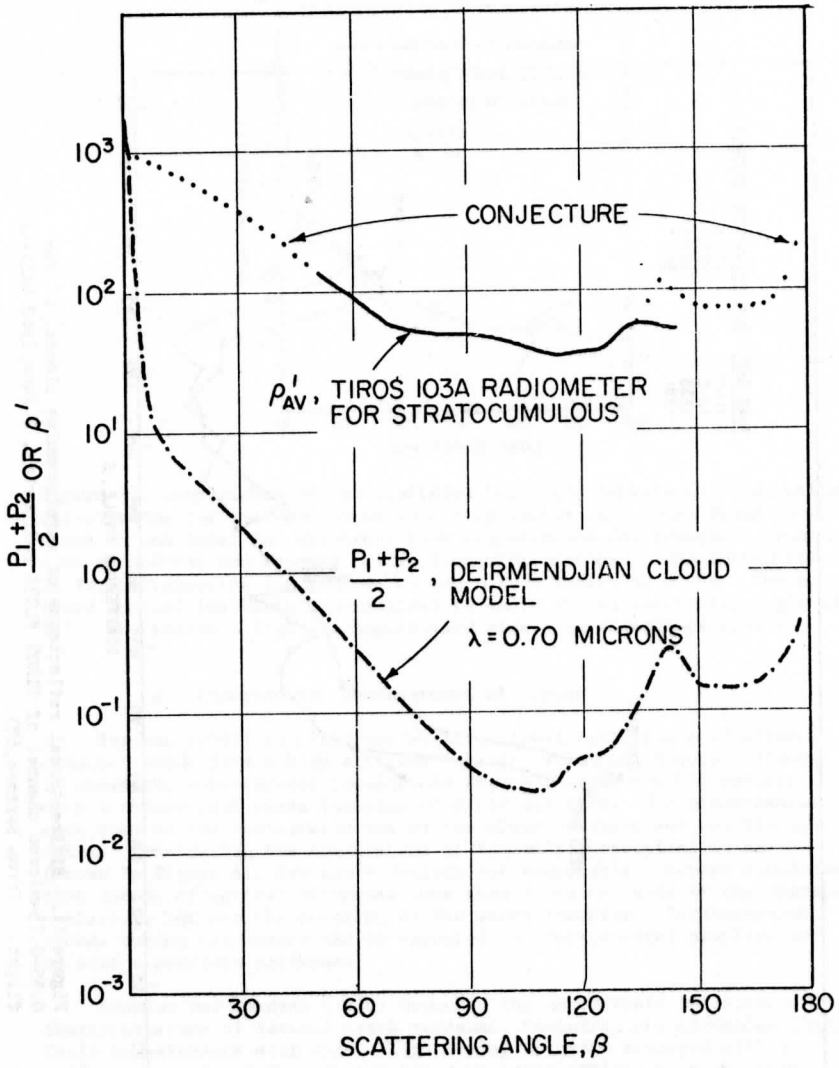

Figure 12. Comparison of experimental measurements of bidirectional reflectance of stratocumulus cloud with theoretical single scattering pattern of water cloud model. (from Bartman,67)

Martin and Suomi (1972) and Sikdar and Suomi (1972) have shown, for deep convective clouds in the tropics, that the intensity of the brightest parts displays a cosine function for solar zenith angles less than 30°. This would indicate isotropic scattering. The result is consistent with theoretical results for very thick clouds. Figure 13 shows the theoretical results of Hansen (1971b) for a cloud of optical thickness of greater than 128 (from Figure 4) and a cosine curve plotted on the same log scale. The theoretical curve follows an approximate cosine curve for angles less than 30°. This is reasonable because the multiple scattering averages out the details of the phase function. The more scattering events, the more the averaging. Hence the resultant bidirectional reflectivity will tend toward a constant, i.e., isotropic scattering.

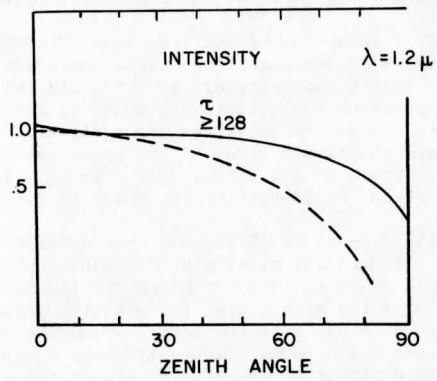

Figure 13. Theoretical results of intensity of light reflected from a very thick cloud, $\tau \geq 128$, (solid line) (Hansen, 1971b) compared to a cosine curve (dashed line).

Ruff, et. al. (1968) measured the angular distribution of solar radiation reflected from clouds as determined from TIROS IV radiometer instruments. The areas of cloud cover were limited to those with a black body temperature of less than 255°K. Analysis was performed only on the median values calculated from at least 50 observations. The results generally show a strong forward scattering and a weaker back scattering. This again would indicate that, on an average, clouds have a moderate to thin optical thickness and show a water droplet type of phase function. Yet, the analysis was limited to clouds with black body temperatures of 255°K (-18°C) or less. Since these temperatures are below freezing, we might expect ice crystals and a phase function, such as Liou's (Section II, B), which does not have a backscatter peak. If the clouds were thin enough that their emissivity was not one, their actual temperature could be higher than their black body temperature and the clouds could be water clouds. Or the phase function for a spherical geometry could more adequately describe the scattering in clouds than could a cylindrical geometry, even though the tops of the clouds examined by the satellite are below freezing.

OBSERVATIONS

A. Nature of the Data

In order to measure the angular characteristics of scattering off a natural unchanging cloud, there are two basic approaches:

1. Provide a rapid movement of the instrument over the cloud by means of a satellite or an aircraft. The solar zenith angle will remain constant while the observer's zenith and azimuth angles change.

2. Provide a relatively long elapsed time interval between the beginning and the end of the sequence with the observation angles remaining constant and the solar angles changing.

In this study I chose the second approach. The observation platform is the ATS III geostationary satellite. This satellite provides a picture of the entire earth approximately every 23 minutes and has a resolution at the subpoint of approximately 2 nautical miles. The data produced by the satellite can be digitized and navigated. The digitization produces 256 linear brightness levels. The spin-scan camera in the satellite does not contain a calibration unit. Thus, all brightness levels are relative and cannot be converted into absolute levels of solar energy.

Day 258 of 1969 (Sept. 15, 1969) was chosen for this study because good quality ATS III data was available throughout the day and the data had been previously digitized and navigated. Three tropical cloud clusters, three smaller areas with convective activity persisting throughout the day, and six individual convective cells, lasting only part of the day, were chosen for this study. Figure 14 shows the area of study. Figure 15 is an enlargmment of the area and shows the clouds studied. The cloud clusters were labeled A, B, and C; the smaller areas which had convection throughout the day were labeled 1, 2, and 3; the remaining individual clouds were labeled 5 through 10.

B. Processing of the Data

The digitized brightness values of the cloud were obtained using SSEC's McIDAS system. Since the spin-scan camera has good resolution, it generates an enormous amount of data. Each digitized picture of the earth occupies an entire reel of computer tape. The system displays the general area of interest on a TV monitor and selection of the cloud is made by means of a cursor. The coordinates of the cursor can then be used to obtain the position of the desired data on the computer tape.

Using the McIDAS system and the associated retrieval programs, a rectangular grid of brightness centered on the cloud, was obtained. The grid dimensions were chosen so that the cloud of interest was just covered. Adjacent clouds were excluded. The grid was limited to no more than 25 x 25. When the cloud had more than 25 lines and elements, the data array was reduced so that there were no more than 625 members. For example, if the data array contained 67 lines and 183 pixels in each line the data volume (12,261 data points) was reduced by using every third

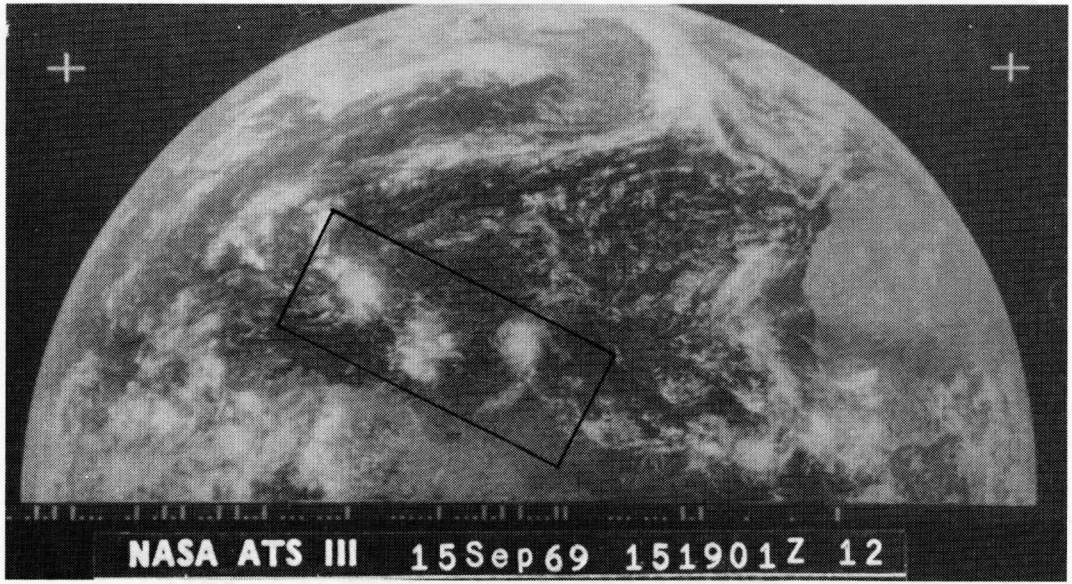

Figure 14

Area of Study

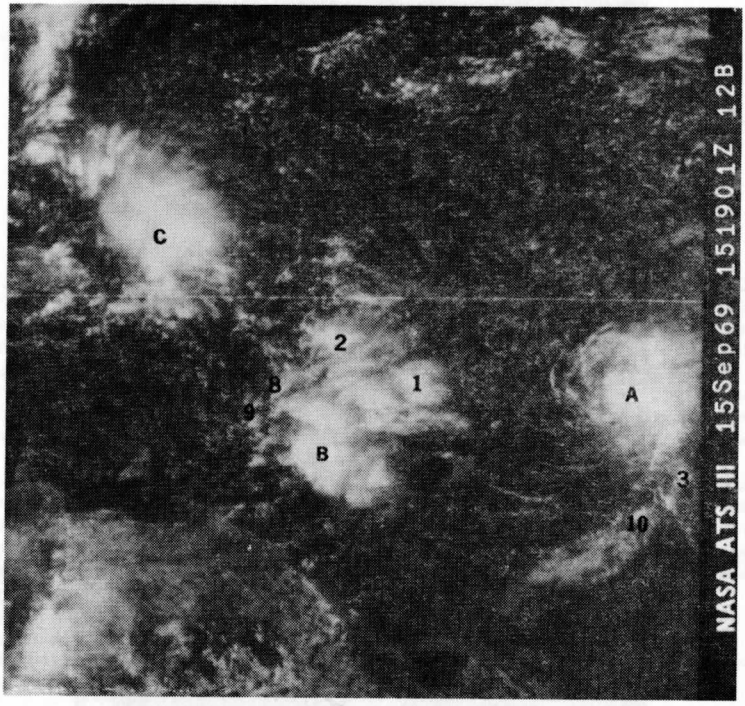

Figure 15

Area of study showing some of the clouds studied. Clouds #5 (9.1N,46.3W), #6 (6.8N,50W), and #7 (11.3N,61.4W) are not shown.

line and averaging every group of 9 pixels in the lines used. These values were then printed in a grid and checked for noise, possible saturation of the camera, and misalignment of the coordinates.

The problem of defining a cloud arose. Generally, there is not a clear dividing line between cloud and sea. As the size of the cloud becomes smaller than the resolution of the camera, the resultant brightness value obtained is a combination of cloud and sea. Hence the relative fraction of small clouds or holes in clouds can produce varying brightness values and a blending of cloud and sea. The problem was solved by making an arbitrary decision and defining items brighter than 40 digital counts as being a horizontally homogeneous cloud. Everything else was disregarded. This decision caused some problem in the analysis of the data which will subsequently be discussed.

Once the brightness values less than 40 digital counts were disregarded, the remaining data was ordered according to brightness, placed in 10 or 20 groups, and then averaged. If, for example, there were 356 members of the array left, they would be ordered according to brightness values and then placed in groups of 36 or 18. These groups would be averaged and their average and standard deviation would be printed. The groups were labeled according to their relative brightness ranking. Group 90-100% was the brightest 10% of the array. Group 45-50% was the group which had 10 groups brighter than it and 9 groups dimmer.

The grouping was done in this manner because the effects of changing sun-cloud-satellite geometry were desired, rather than the effects of the changing thickness. The lifetime of an individual cumulus cell is approximately 30 minutes. If the system under study lasts longer than 30 minutes, it is because new cells are forming as older ones die. The forming and decay of the cells causes the thickness at these points of the cell to change. By looking at one point, it would be difficult to separate the change in intensity due to sun-cloud-satellite geometry effects from the change in intensity due to thickness changes. However, one can assume that, since the convective area lasts for a long time in a relatively steady state fashion, the areas covered by the different thicknesses of cloud should remain approximately constant. Hence the thickness in each group remains constant and each group is horizontally homogeneous.

The scattering angles were obtained by using a subroutine written by Dennis Phillips. This determined the position on the earth of the cloud from the orbit characteristics of the satellite and from the line and element numbers of the cloud's center. The position of the cloud, in turn, allows us to find the vectors to the satellite, the cloud and the sun from the earth's center. The zenith angles of the sun and satellite are determined by use of the vector dot product.

$$|\vec{A} \cdot \vec{B}| = |\vec{A}| \cdot |\vec{B}| \cos \theta$$

The dot produce was obtained by evaluating the vector components definition of the dot product. The scattering angle α was obtained by determining the vector from the cloud to the satellite and using the dot product with the sun's vector to evaluate the angle. The "scattering angle" β, used in all the previous sections, is $\beta = 180° - \alpha$. The

range of solar zenith angles and the back-scattering angles was determined by the position of the cloud on the earth. The minimum solar zenith angle and the minimum scattering angle were also computed.

The data processing outlined above was performed on the clouds of interest nine times during the day.

C. Analysis of Data

Analysis of the data was performed primarily to answer two questions:
(1) Is the contrast in a cloud a function of scattering geometry? and
(2) What type of phase function is acting in real clouds?

1. Cloud Contrast

The normalization procedure of Sikula and Vonder Haar (1972) applies the same correction factor to all parts of a cloud. This assumes that the relative contrast between the brighter and the dimmer parts of a cloud remains constant for various sun-cloud-satellite geometries. A review of the theoretical literature (Section II. C) suggests that this is not a good assumption.

Figure 16 shows cloud area 2 for several times during the day. Isopleths of equal digital brightness have been drawn in. As the day progresses, the level of brightness first increases and then decreases. Along with the changes in brightness, there is first an increase in contrast and then a decrease. This corresponds to the changes in the brightness levels. There are two probable causes for this relationship: 1) the changes in contrast are due to scattering geometry changes, or 2) Changes in the thickness of the area are producing this effect. The short-lived convective clouds 5 - 10 also showed this change in brightness and in contrast. Complete separation of the two effects is very difficult.

One possible answer to separation is symmetry. Changes in contrast due to changes in the sun's position should be symmetric with regard to the scattering angle. However, the changes in thickness, due to the growth and decay of the cloud, would not necessarily be symmetric about the scattering angle. Figure 17 shows the ratio of the average intensities of the brightest group to various other groups of cloud 1. In the preceding section, it was explained that the data from each cloud was divided into twenty groups and each group was averaged. The brightest group was labeled 95-100%, the next brightest group 90-95%, etc. This grouping procedure allows individual areas of the cloud to change thickness, but assumes that the relative areas covered by any particular thickness remains constant. The ratio of the intensity of one brightness group to the other groups of the cloud is a very useful method of analysis for several reasons. During 1969 there were several instances of unrecorded gain changes in the satellite receiving center. A ratio will not be affected by these possible gain changes. A ratio also has the advantage of eliminating the effect of the sun's zenith angle on brightness since both parts of the cloud have the same sun-cloud-satellite geometry. The ratio of intensities is, therefore, a ratio of the bidirectional reflectance. If the two parts of the cloud have the same bidirectional reflectance function, their ratio will be a straight line.

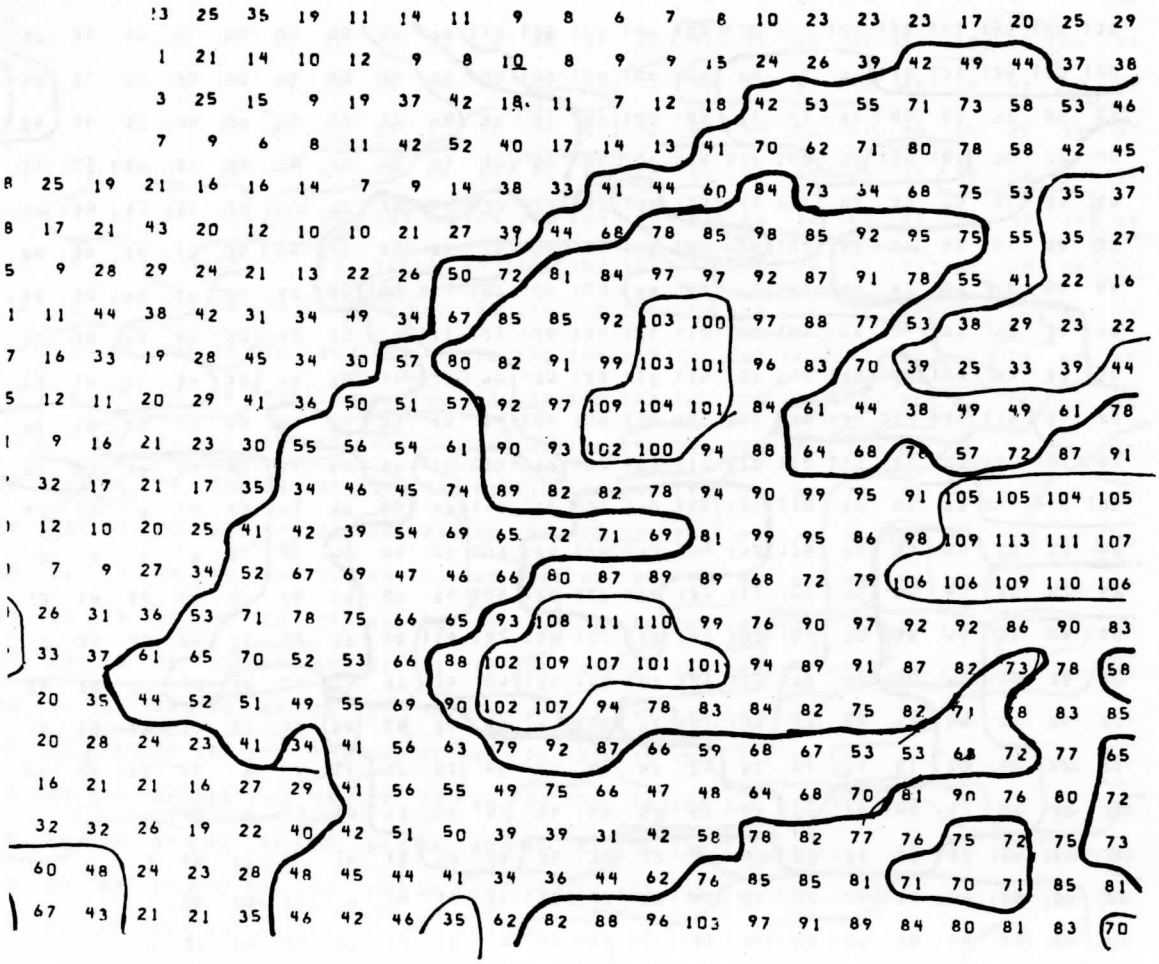

Figure 16,a. Cloud area #2 digitized brightness values for time= 1250Z, scattering angle = 149°, local time=0858

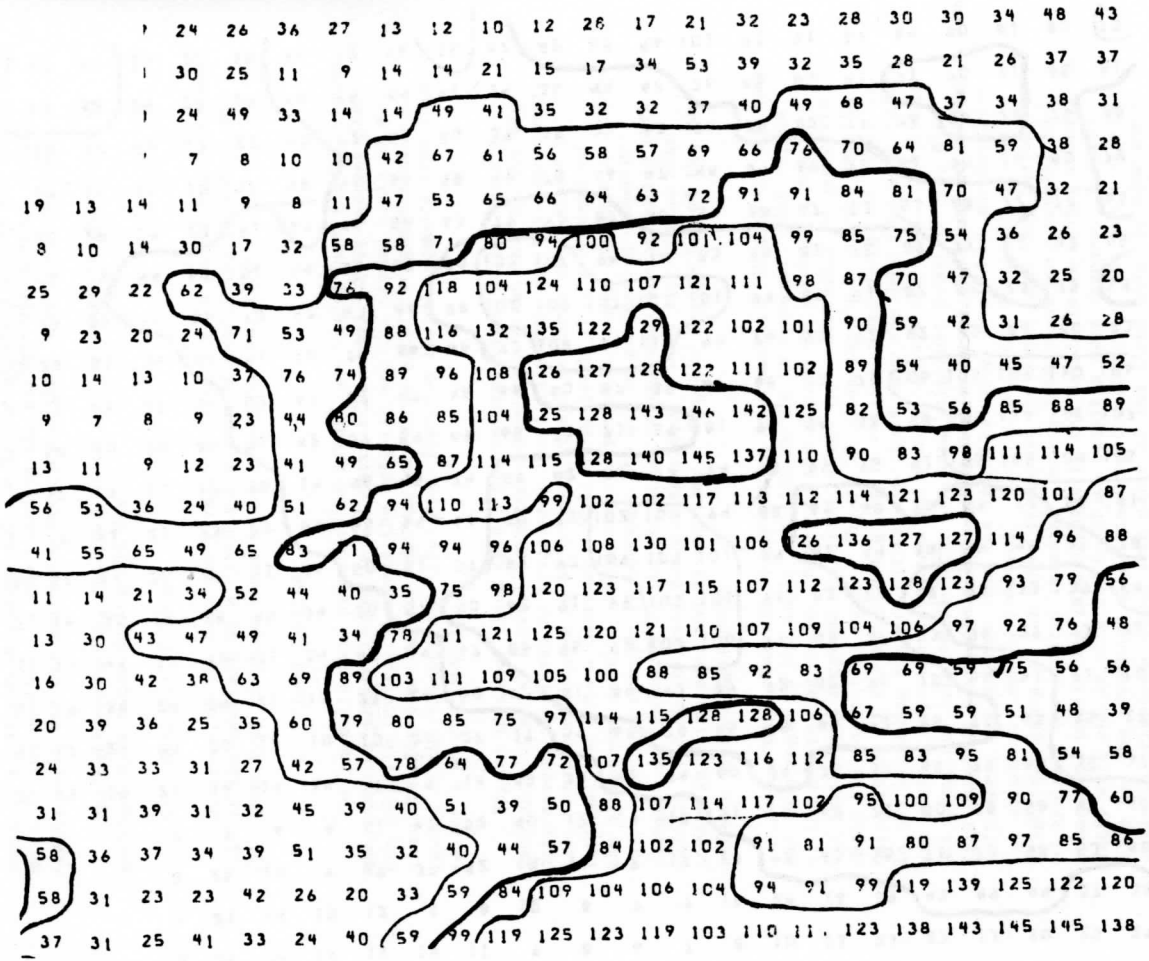

Figure 16,b. Cloud area #2 digitized brightness values for time = 1358Z, scattering angle = 166°, local time=1009

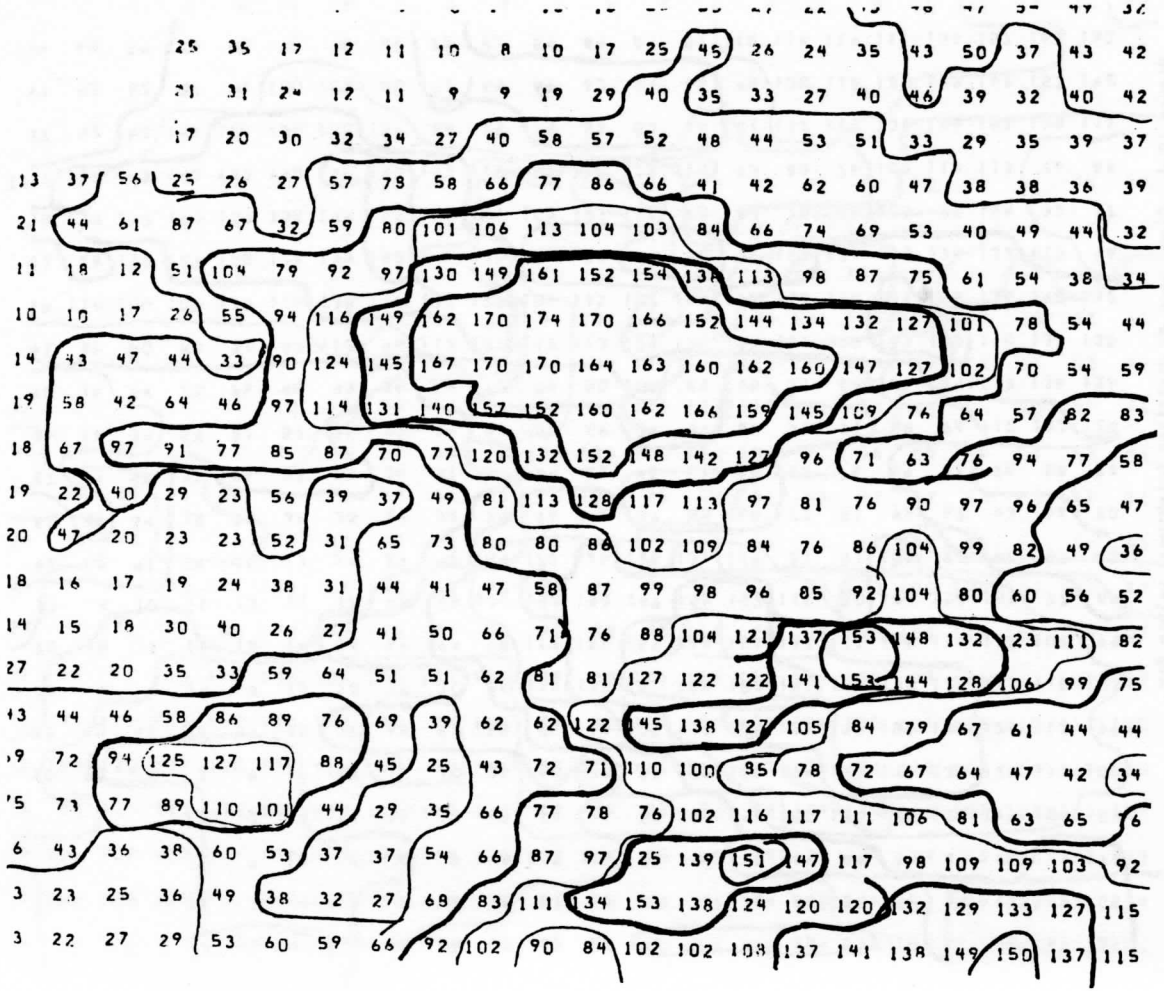

Figure 16,c. Cloud area #2 digitized brightness values for time = 1520Z, scattering angle = 170°, local time = 1129

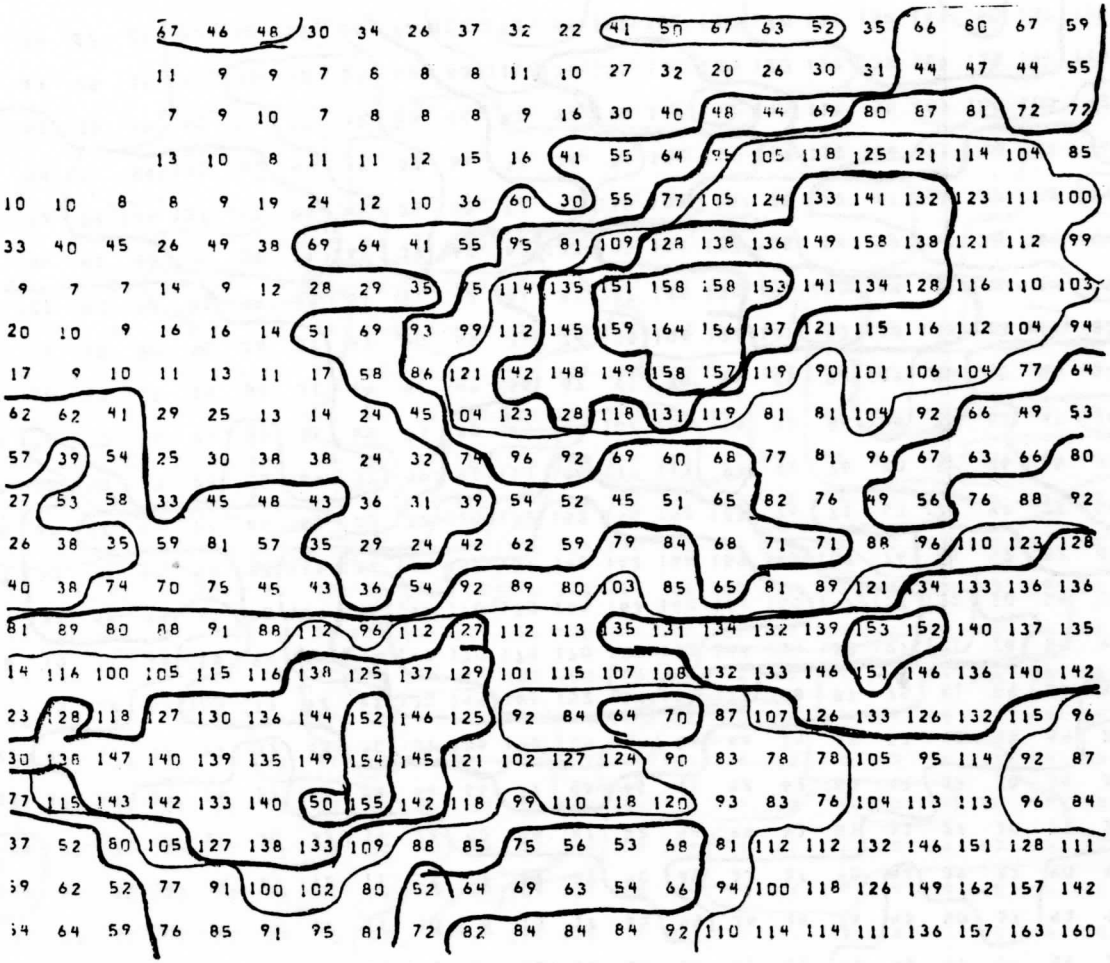

Figure 16,d. Cloud area #2 digitized brightness values for time = 1700Z, scattering angle = 147°, local time = 1308

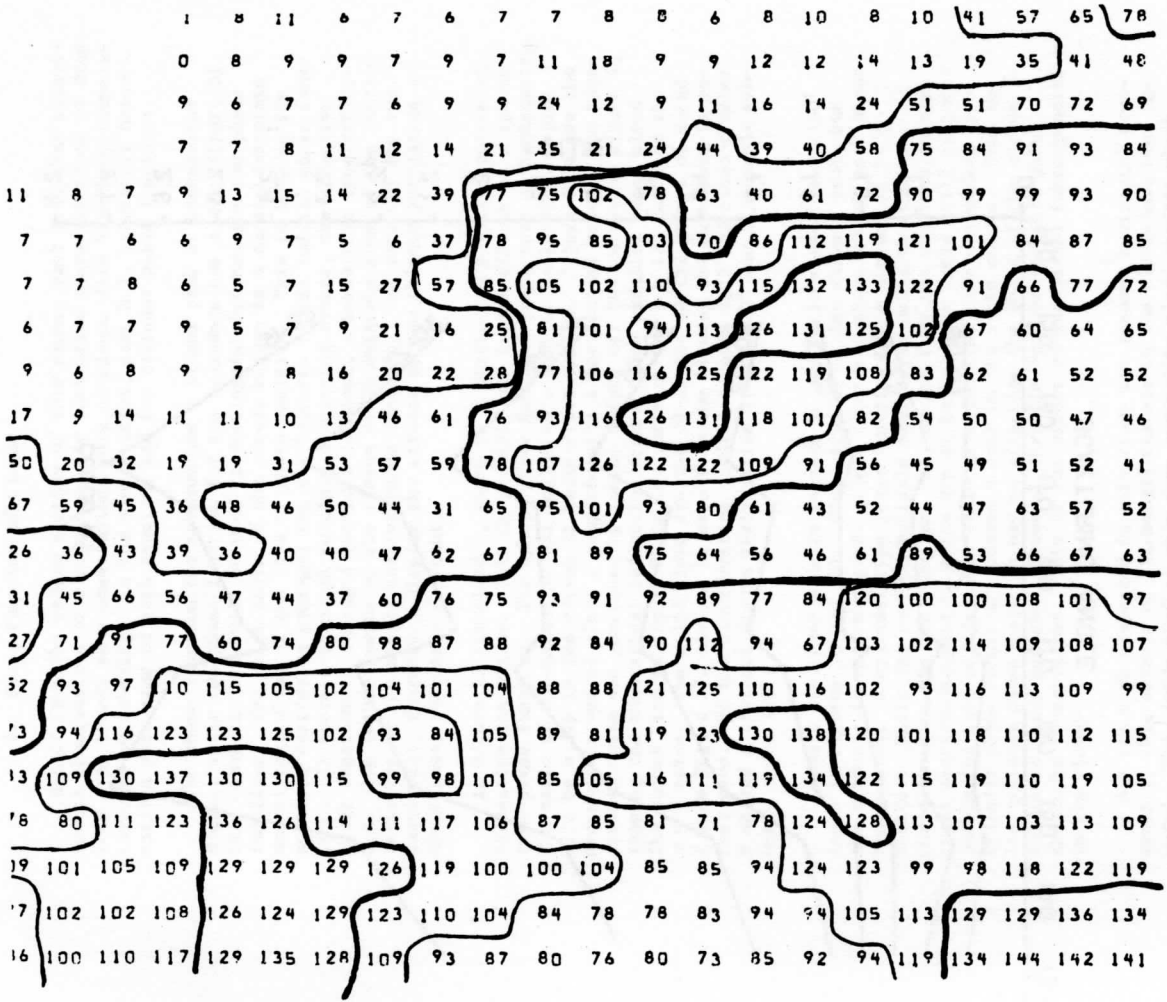

Figure 16,e. Cloud area #2 digitized brightness values for time = 1756Z, scattering angle = 133°, local time = 1405

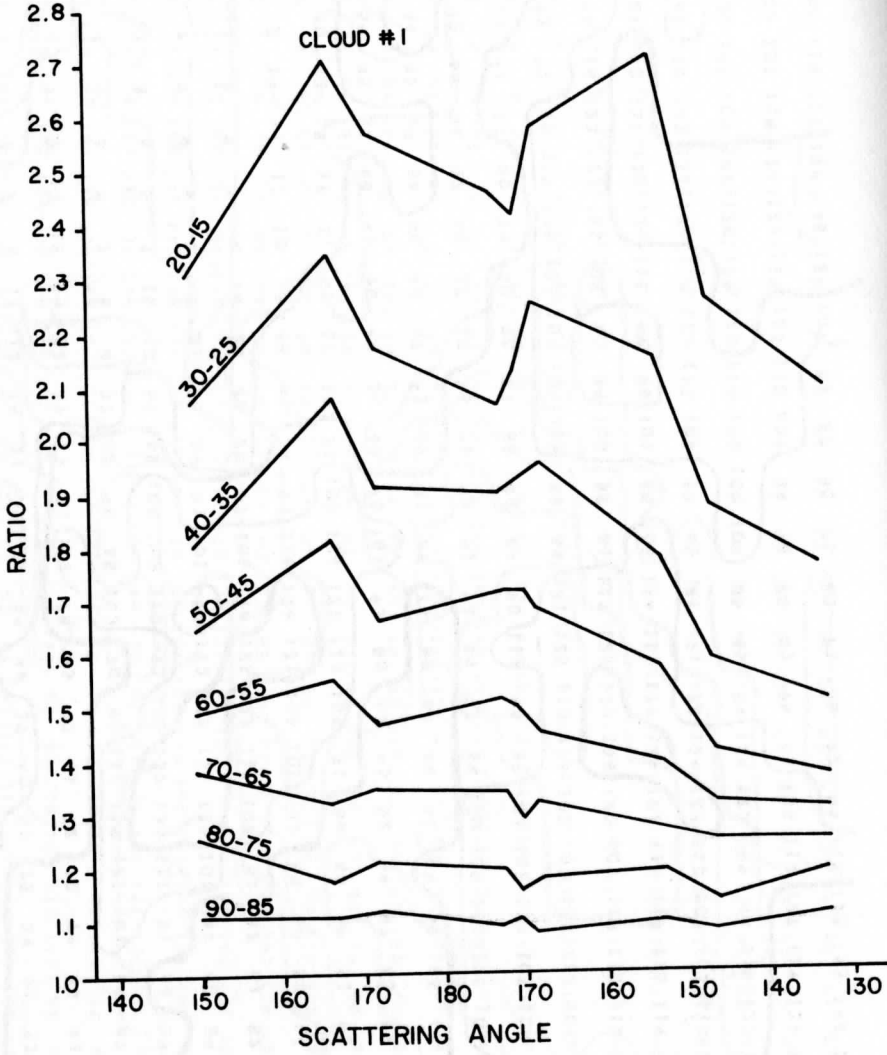

Figure 17

Ratio of the brightess group to the other groups in Cloud #1. The group labels are shown by each line of the graph.

2. Phase Function of Clouds

Recall from the second section of this paper, part D.2, that experimental observations of clouds had only identified phase functions of droplets even though some ovservations were of clouds with blackbody temperatures below freezing. In the same section, part D.1, laboratory observations were made of both droplets and ice cylinder phase functions.

The phase function for spheres has a slight peak at backscatter angles, while the phase function for ice cylinders has a dip (Figure 3). This characteristic will be used to distinguish between the two phase functions. The thick parts of the clouds behave in a quasi-Lambertain manner regardless of the type of phase function. This is because the multiple scattering averages out the features of the initial phase function. If there are enough multiple scattering events, the effective phase function is averaged out to a constant, a Lambertian type reflector. The thinner parts of the clouds still maintain some of the characteristics of the single scatter phase function. The ratio of the two parts will, therefore, display the effects of the thinner part since the thicker part is a constant.

In Figure 17 for cloud 1, there is a distinct dip in the curves at backscattering angles. This is probably due to the effects of a sphere type phase function. The sphere phase function has a peak at backscatter. The ratio of a constant at all angles to a peak at backscatter angles will be a dip in the curves at backscatter angles. Figure 20 shows the measured curves of cloud 1 compared with a theoretical curve. The theoretical curve was generated by taking points off the curves of Figure 4, showing the theoretical reflection from a plane parallel water cloud. The dashed line in Figure 20 is the ratio of the $\tau \geq 128$ curve to the $\tau = 8$ curve. The solid lines are the 30-25 and 20-15% groups of cloud 1 from Figure 17. As can be seen from the figure, the agreement is rather good. Of the cloud systems studied, clouds 1, 3 and cloud cluster B showed a distinct dip in their ratios around 180° and reasonable symmetry about 180°.

Cloud 2 evidences a definite peak in the ratio curves about 180° (seen in Figures 18 and 19). Cloud cluster C also shows a peak, but the symmetry is not very good. Cloud cluster A shows a weak peak about backscatter. A cylinder type phase function has a minimum at backscatter. While the case of multiple scattering using the cylinder phase function has not been run, the results from the previous theoretical sections suggest that the dip at backscatter would still be noticeable for thin clouds. The ratio of a constant to a dip caused by a cylinder phase function produces a peak in the ratio curves. Thus the ice cylinder phase function may be affecting the shape of the curves for these cloud systems. However, there is another variable which should be investigated. This is the effect of horizontal inhomogeneities in the clouds.

All the work presented in this study has assumed horizontal homogeneity. The effects of breaks and texture in the clouds have been ignored. The clouds studied were deep convecting cloud systems which appeared to be reasonably "solid." Breaks in the clouds larger than the resolution of the camera were ignored by the method of grouping (see part B in the third section). The brightness level of the sea surface

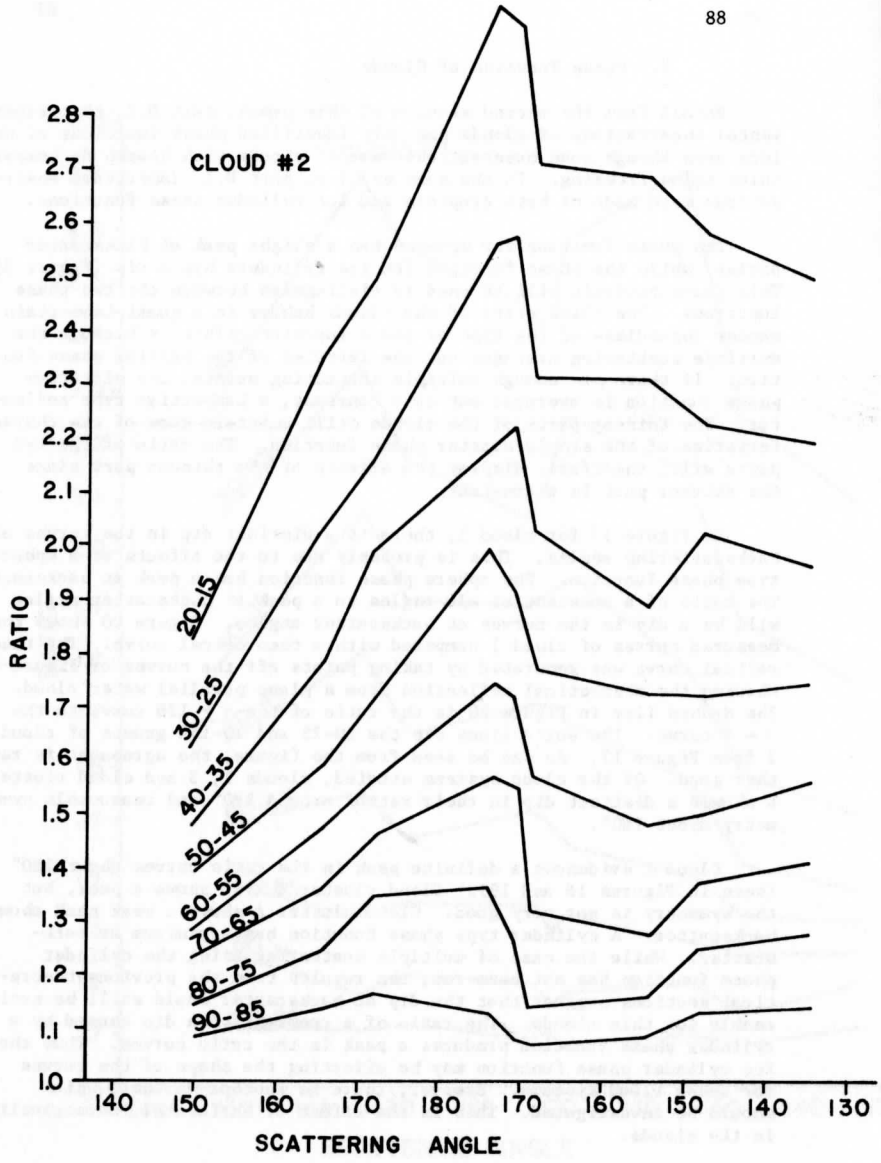

Figure 18

Ratio of the brightest group to the other groups in Cloud #2. The group labels are shown by each line of the graph.

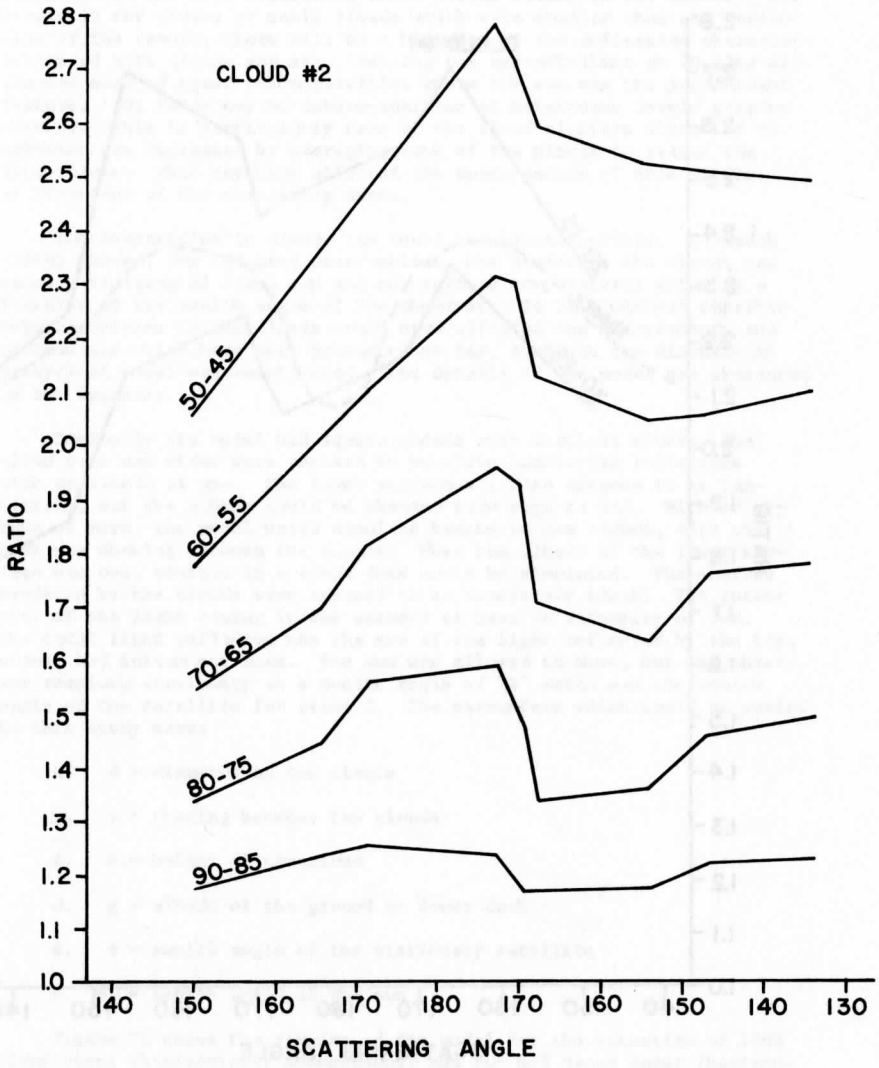

Figure 19

Ratio of the brightest group of the modified bidirectional reflectivity to the dimmer groups of Cloud #2. The group labels are shown by each line of the graph.

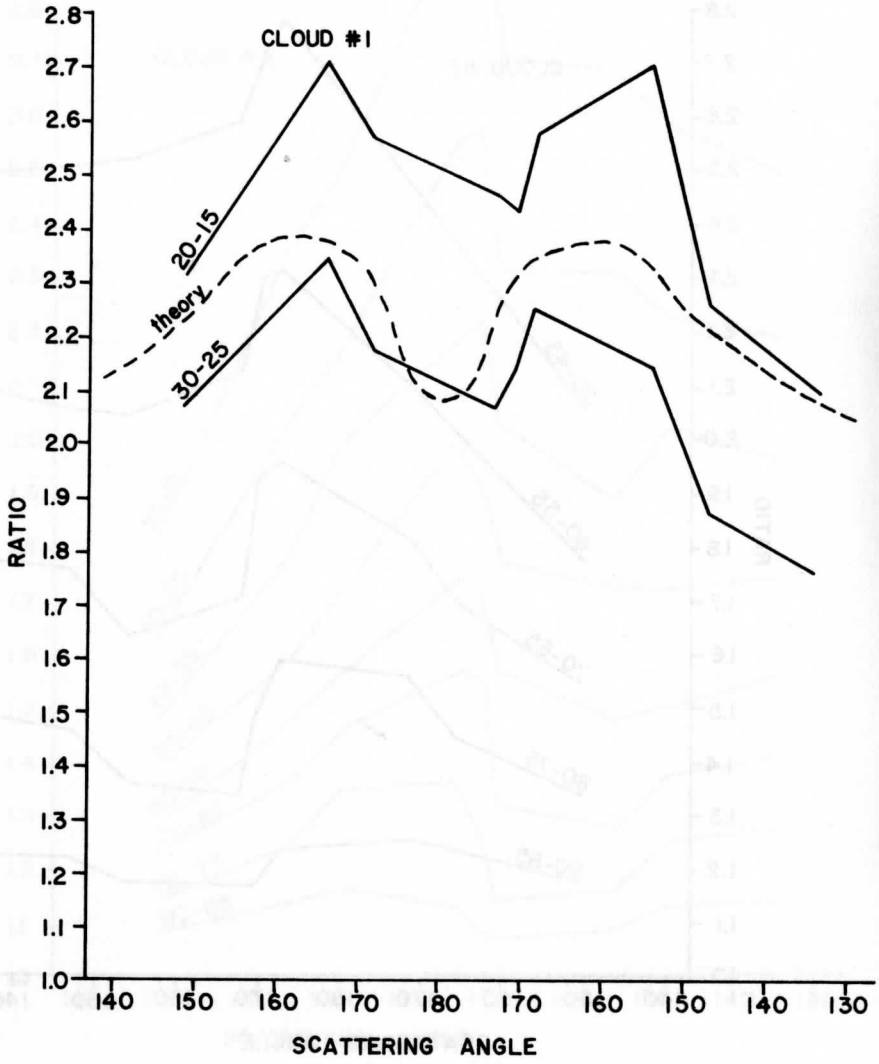

Figure 20. Measured curves for cloud #1 (solid lines) compared with theory (dashed line). Theoretical curve is the ratio of $\tau > 128/\tau = 8$ with points taken from figure 4 for a plane parallel water cloud.

was less than 15 digital counts. Ignoring all the data with brightness levels of 40 and less eliminated these larger breaks in the clouds. For breaks in the clouds or small clouds which were smaller than the resolution of the camera, there will be a blending of the reflective characteristics of both clouds and sea. Setting the cut-off limit at 40 also eliminated some of these inhomogeneities where the sea was the predominant feature. But there may be inhomogeneities at brightness levels greater than 40. This is particularly true of the cloud clusters where the resolution was decreased by averaging some of the pixels to reduce the data volume. This may have affected the measurements of intensities as functions of the scattering angle.

Inhomogeneities in clouds can cause measurement errors. U. Radok (1966) showed, for infrared observations, how breaks in the clouds can cause a blending of cloud top and sea surface temperatures which is a function of the zenith angle of the observer. To test whether possible inhomogeneities in the clouds could have affected the measurements and conclusions which have been presented so far, a simple two dimensional analytical model was constructed. The details of the model are presented in the appendix.

Basically the model had square clouds with vertical sides. The cloud tops and sides were assumed to be white Lambertian reflectors with an albedo of one. The lower surface was also assumed to be Lambertian, but the albedo could be changed from zero to one. With an albedo of zero, the model would simulate breaks in the clouds, with the dark sea showing between the clouds. When the albedo of the lower surface was one, texture in a cloud deck could be simulated. The shadows produced by the clouds were assumed to be completely black. The intensity of the light coming in was assumed to have an intensity of one. The total light reflected was the sum of the light reflected by the top, sides, and bottom surfaces. The sun was allowed to move, but the observer remained stationary at a zenith angle of 24° which was the zenith angle of the satellite for cloud 2. The parameters which could be varied in this study were:

a. d = diameter of the clouds

b. s = spacing between the clouds

c. h = height of the cloud

d. g = albedo of the ground or lower deck

e. θ = zenith angle of the stationary satellite

f. θ_o = zenith angle of the sun

Figure 21 shows the results of the model for the situation of 100% cloud cover (horizontally homogeneous) and for 66% cloud cover (horizontally inhomogeneous). For the 66% cloud cover case the value of the diameter was 2 and the spacing was 1. The height was varied from 1 to 2. The albedo of the lower surface was varied from 0 to 1. The solid lines in the figure are for the albedo of the lower surface as 1, and the dashed

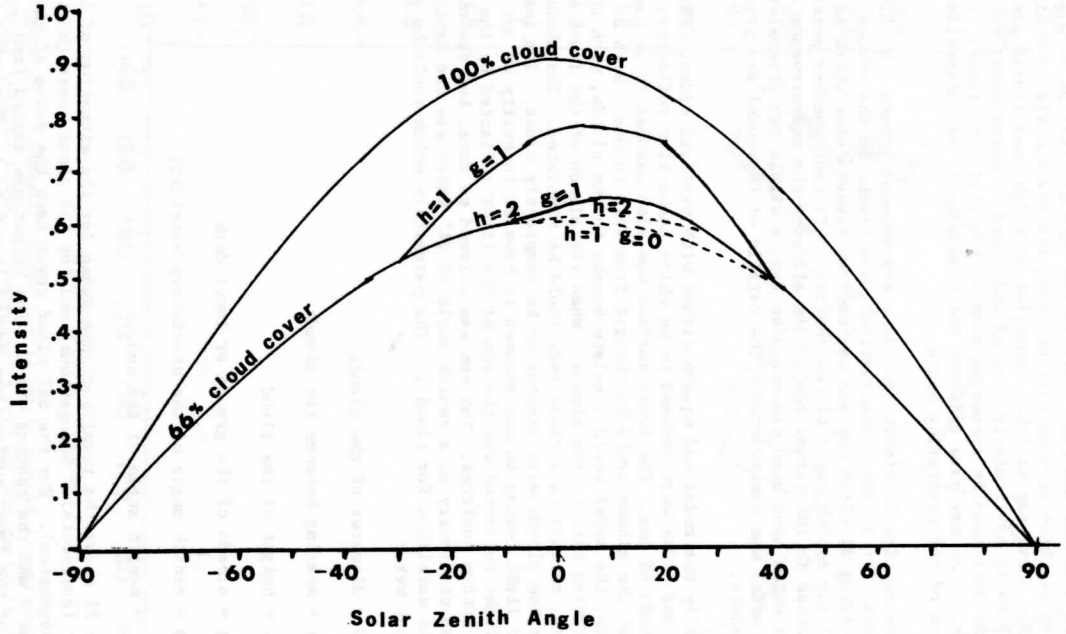

Figure 21

Effects of inhomogeneities in a Lambertian reflecting surface for a stationarv observer at 24° zenith angle. The albedo of the lower surface was varied from zero (dashed lines) to one (solid lines). The 66% cloud cover has a cloud diameter of 2 and a spacing between the clouds of 1. The height was varied from 1 to 2.

lines are for the lower surface albedo as 0. As can be seen from Figure 21, one effect that the inhomogeneities cause is a decrease in the overall brightness of the cloud. Also the cloud is brightest just before the local noon.

In order to see how the inhomogeneities might have affected the analysis presented in the previous sections, the ratio of the 100% cloud cover curve to the 66% cloud cover curve was computed and plotted with the scattering angle (Figure 22). The curves from the 30-25% group from cloud 1 (Figure 17) and cloud 2 (Figure 18) are also shown on Figure 22 for comparison. For the case in which the albedo of the lower surface was zero, the ratio of the unbroken to broken cloud cover produces an asymmetric curve which rises from a constant toward another constant. The asymmetry is caused by the observed vertical wall first being illuminated and then being in shadow. The degree of asymmetry is controlled by the amount of cloud cover with all the other variables remaining constant, and with the degree of asymmetry increasing with decreasing cloud cover. For the case in which the lower boundry has an albedo of 1, the curves are still asymmetric, but a dip is produced around backscatter angles. This dip is caused by the bottom surface coming out of the shadows and increasing the amount of reflected light. The dip in the curves becomes deeper and broader when the spacing between the clouds is increased, or when the height of the cloud is decreased.

This model admittedly oversimplifies the real world. Clouds are not square and they have three dimensions. Clouds are not really Lambertian reflectors either. In order to treat the problem of horizontal inhomogeneities properly, actual three dimensional cloud geometries should be used. The effects of scattering inside the cloud and transmission of light through the cloud should be included. Perhaps this could be properly treated using a Monte Carlo simulation technique. While the results would be extremely interesting, the effort required for this is, unfortunately, beyond the scope of the present work.

What conclusions can reasonably be drawn from this simple study? In the model presented, the primary mechanism causing an alteration of the reflected properties of the surface was shadow. Shadows decreased the amount of light reflected. The asymmetries of the reflected light pattern were caused by the off-center position of the observer. The observer could see one wall, but not the other. Since the dimensions of the model were relative, the texture which was simulated could be either clouds above a cloud deck, or convective bumps within a single horizontal cloud. If the side walls had not been straight, but bumpy like a staircase, the reflected patterns would be changed slightly. As the sun came up, the horizontal surfaces would be illuminated more quickly because they would not have to wait until the sun reached the bottom. As the sun begins to go down, the shadows on the steps would be in the same ratio of light to dark as the straight wall case. Thus, for negative solar zenith angles the result would not change. This simple model has, therefore, shown that horizontal inhomogeneities producing shadows can cause a localized maximum in the reflected light when the shadows are at a minimum within the field of view.

How then does all this apply to the measured data? It will be recalled that the measurements of cloud 1 were explained by using the re-

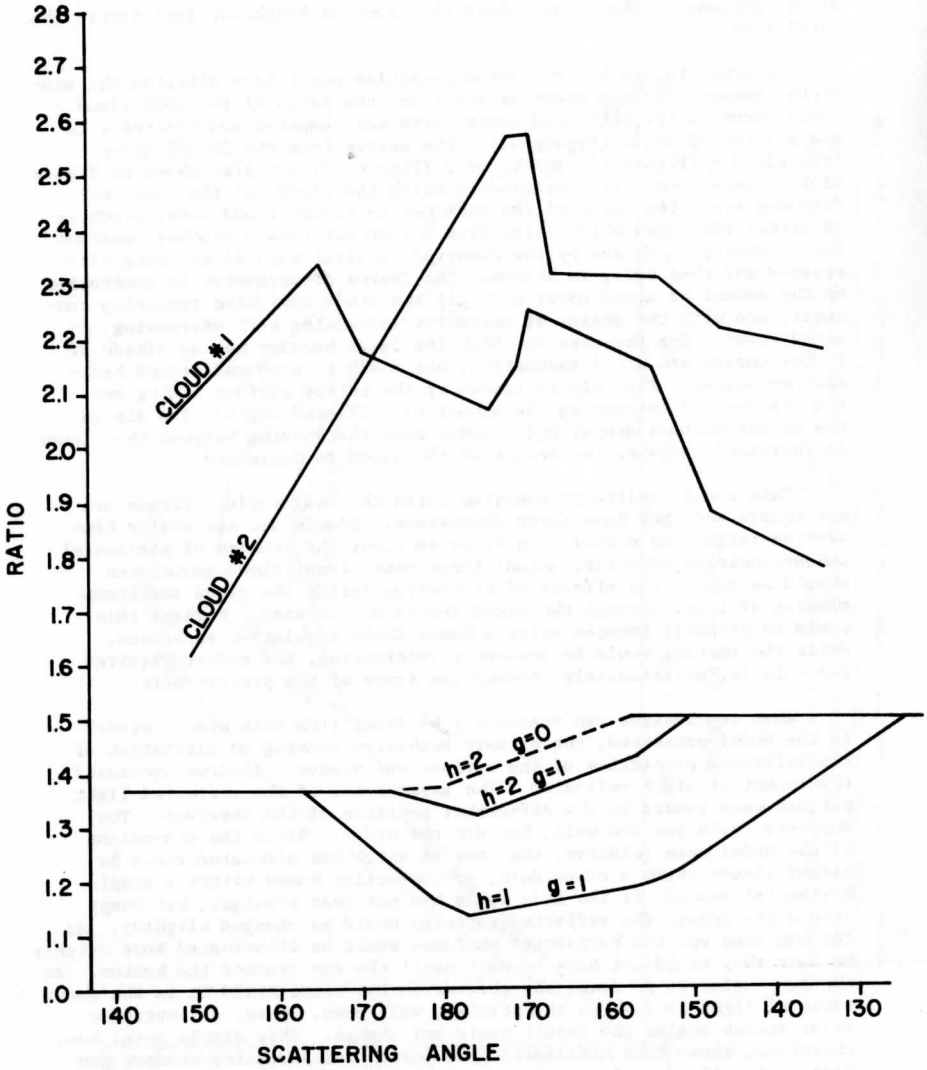

Figure 22

Ratio of the intensities of a homogeneous cloud cover to that of the inhomogeneous 66% cloud cover. The solid lines are for the cases in which the lower surface had an albedo of 1, and the dashed lines for when it was zero. The measured ratios of clouds #1 and #2 for the 30-25% groups are shown for comparison.

sults of multiple scattering from horizontally homogeneous water clouds (see Figure 20). Cloud 2 was the problem. A possible explanation had been offered using the phase function for ice cylinders. However, this phase function is a recent theoretical result and has not had extensive experimental verification. Horizontal inhomogeneities were studied to determine if other physical mechanisms could cause the same observational patterns. It has been shown that shadows can produce a local mixiumum of the reflected intensity. If we assume that the dimmer parts of the cloud have the inhomogeneities then we obtain the opposite effect needed to explain cloud 2's behavior. A local minimum for the dimmer parts of the cloud is needed. If, however, the brightest parts of the clouds have the inhomogeneities and the shadows, the behavior of cloud 2 is explained. Unfortunately, it is impossible to determine the local maxima of the brightest parts of cloud 2 because of possible gain changes at the satellite receiving center (the reason for doing the analysis using ratios). The raw data of the intensity of the brightest part of cloud 2 did increase, while the dimmer parts decreased. But it is very difficult to draw conclusions from this. Consequently, it is impossible to definitely assign a cause to cloud 2's behavior. Further study with better data will be required to determine if the phase function for ice cylinders can be found in nature.

CONCLUSIONS

The following conclusions can be drawn from this study.

1. Very thick horizontally homogeneous clouds behave as quasi-Lambertian reflectors because of multiple scatterings.

2. Thin horizontally homogeneous clouds show anisotropic reflectance because of the shape of the single-scatter phase function.

3. Evidence of phase functions for spheres and possibly for cylinders can be found in thin horizontally homogeneous clouds.

4. Different thicknesses of clouds will require different normalization corrections.

5. Droplet size distributions play a minor role in normalization requirements as compared to thickness requirements.

6. Horizontal inhomogeneities in clouds causing shadows can modify the reflected characteristics of clouds by producing a local maximum of intensity when the shadows in the field of view are a minimum. Asymmetries in the reflected light patterns can be caused by off-center observation.

The following recommendations are made concerning future attempts at developing a better normalization procedure.

1. The normalization procedure requires data on reflectance characteristics of various cloud thicknesses for various sun-cloud-satellite geometries.

2. In addition to empirical data, a theoretical multiple scattering model, using the horizontally homogeneous assumption, should be considered in the development of a data base for normalization.

3. The effects of both sphere and cylinder type phase functions should be studied using a theoretical multiple scattering model to test for significant differences in the reflected light intensity for various cloud thicknesses.

4. Further theoretical and experimental research is required to better understand the effects of inhomogeneities in clouds on the brightness of clouds.

5. Further research is required to determine the degree to which the texture of clouds produces shadows on these clouds.

6. Further experiments are required to determine if an ice cylinder phase function can be found in nature.

Bibliography

Bartman, Fred, L.: The Reflectance and Scattering of Solar Radiation by the Earth. NASA Report NAS-54(03), 1967

Brennan, B. and Bandeen, W. R.: Anisotropic Reflectance Characteristics of Natural Earth Surfaces. Applied Optics, Vol. 9, No. 2, 405-412, February 1970

Dave, J. V.: Meaning of Sucessive Iteration of the Auxiliary Equation in the Theory of Radiative Transfer. Astrophysics Journal, Vol. 140, 1292-1303, 1964

Dave, J. V.: Intensity and Polarization of the Radiation Emerging from a Plane-Parallel Atmosphere Containing Monodispersed Aerosols. Applied Optics, Vol. 9, 2673-2684, 1970

Hansen, J. E.: Multiple Scattering of Polarized Light in Plantary Atmospheres. Part I. The Doubling Method. Journal of the Atmospheric Sciences, Vol. 28, 120-125, 1971

Hansen, J. E.: Multiple Scattering of Polarized Light in Planetry Atmospheres. Part II. Sunlight Reflected by Terrestial Water Clouds. Journal of the Atmospheric Sciences, Vol. 28, 1400-1426, November 1971

Heymsfield, A. J. and Knollenberg, R. G.: Properties of Cirrus Generating Cells. Journal of the Atmospheric Sciences, Vol. 29, 1358-1366, Oct. 1972

Howell, H. B.: On the Sensitivity of Multiple-Scattering Calculations to the Single-Scattering Phase Function. Journal of the Atmospheric Sciences, Vol. 25, 1090-1094, November 1968

Huffman, Paul J. and Thursby, William R.,Captain, USAF: Light Scattering by Ice Crystals. Journal of the Atmospheric Sciences, Vol. 26, 1073-1077, September 1969

Kattawar, G. W. and Plass, G. N. : Radiance and Polarization of Multiple Scattered Light from Haze and Clouds. Applied Optics, Vol. 7, 1519-1527, 1968

Liou, Kuo-Nan: Light Scattering by Ice Clouds in the Visible and Infrared: A Theoretical Study: Journal of the Atmospheric Sciences, Vol. 29, 524-536, April 1972

Martin, David W. and Suomi, Verner E.: A Satellite Study of Cloud Clusters over the Tropical North Atlantic Ocean, Bulletin of the American Meteorological Society, Vol. 53, No. 2, 135-156 February 1972

Radok, U.: An Appraisal of Tiros III Radiation Data From Southeast Asia. Colorado State Univ. Atmospheric Science Paper No. 102, Enviromental Science Services Administration Grant WBG-61, August 1966

Ruff, I., Koffler, R., Fritz, S., Winston, J.S., and Rao, P. K.: Angular Distribution of Solar Radiation Reflected from Clouds as Determined from TIROS IV Radiometer Measurements. Journal of the Atmospheric Sciences, Vol. 25, 323-332, March 1968

Setzer, David E.: Comparison of Measured and Predicted Aerosol Scattering Functions. Applied Optics, Vol. 8, 905-911, May 1969

Sikdar, D. N. and Suomi, V. E.: On the Remote Sensing of Mesoscale Tropical Convection Intensity from a Geostationary Satellite. Journal of Applied Meteorology, Vol. 11, 37-43, February 1972

Sikula, Gerald J. and Vonder Haar, Thomas H.: Very Short Range Local Area Weather Forcasting Using Measurements from Geosynchronous Meteorological Satellites. Colorado State Univ. Atmospheric Science Paper No. 185, Air Force Contract No. F19628-71-C-0073, 1972

Van de Hulst, H. C.: Light Scattering by Small Particles. New York, Wiley, 470pp. 1957

APPENDIX

Practically all studies on the reflective characteristics of clouds have assumed that the clouds are horizontally homogeneous. The clouds are assumed to be flat and without texture. Real clouds are not necessarily like this. To determine if breaks and texture in the clouds, smaller than the camera's resolution, influence the observations made by the satellite, a simple two dimensional study was done. This appendix will outline the construction of the model used.

The clouds were assumed to be square with vertical straight walls as is shown in Figure 1. The satellite was assumed to be stationary at a 24° zenith angle (θ) and the sun (θ_o) was allowed to change. The satellite zenith angle of 24° was the zenith angle of observation for cloud 2 and was approximately the angle for cloud 1. The cloud tops and sides were assumed to be white Lambertian reflectors with an albedo of one. The lower surface was also assumed to be Lambertian, but the albedo could be changed from zero. This simulated breaks in the clouds and the dark sea showing between the breaks. An albedo of one simulated texture in a cloud deck. The shadows were assumed to be completely black. The parameters which could be varied in this study were:

a. d = the diameter of the cloud

b. s = the spacing between the clouds

c. h = the height of the cloud

d. g = albedo of the ground or lower deck

e. θ = zenith angle of the stationary satellite

f. θ_o = zenith angle of the sun

The light coming in was assumed to have an intensity of one. The light reflected from the various surfaces was:

1. top of clouds $I_1 = \cos \theta_o \cos \theta$

2. side of clouds $I_2 = \sin \theta_o \sin \theta$

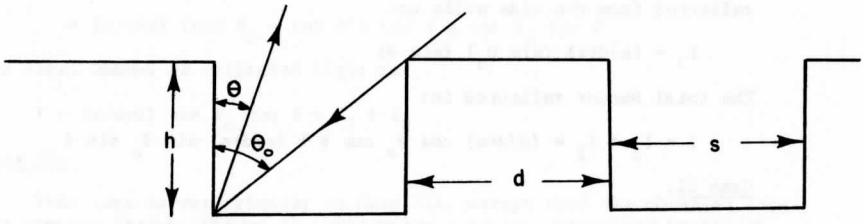

Figure 1. Geometry of Study

3. bottom surface $I_3 = g \cos \theta_o \cos \theta$

The angle θ' is the zenith angle where the observer first can see the lower boundary surface. θ_o' is the same zenith angle and is the angle where the sun first strikes the sea (shown by Figure 2).

$$\theta' = \theta_o' = \tan^{-1} s/h$$

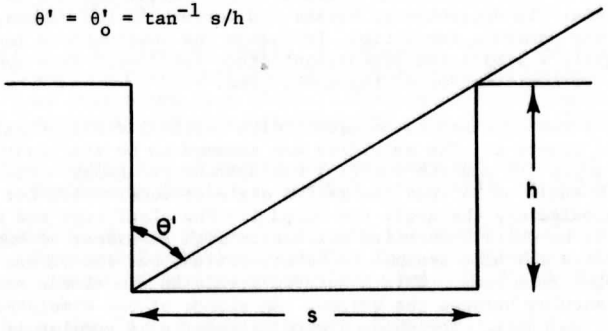

Figure 2. Definition of zenith angle θ'

In this model the satellite remained stationary and the sun was allowed to move, producing shadows on the walls and bottom surfaces. Depending upon the position of the observer and the sun, the following cases would determine the reflected intensity:

Case I.

The observer can see no shadows and cannot see the bottom surface.

$(\theta > \theta_o, \theta > \theta')$

The light reflected from the top surfaces is proportional to the area covered by the top surfaces:

$$I_1 = (d/d+s) (\cos \theta_o) (\cos \theta)$$

Since the observer cannot see the sea and can see no shadows, the light reflected from the side walls is:

$$I_2 = (s/d+s) (\sin \theta_o) (\sin \theta)$$

The total amount reflected is:

$$I = I_1 + I_2 = (d/d+s) \cos \theta_o \cos \theta + (s/d+s) \sin \theta_o \sin \theta$$

Case II.

The observer can see shadows on the vertical wall, but still cannot see the sea (shown by Figure 3).

$(\theta < \theta_o,\ \theta_o > \theta_o')$

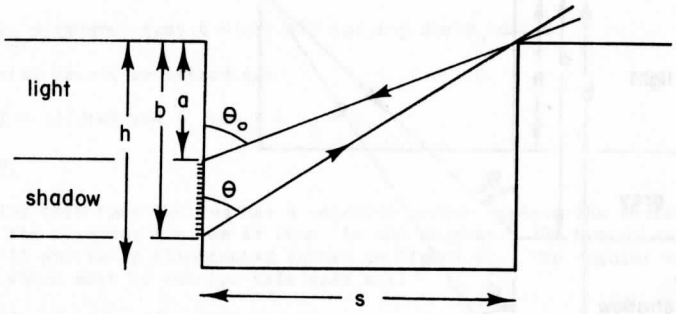

Figure 3. Geometry for Case II

The observer can see part of the wall in sunlight and part of the wall in shadow. The amount of light reflected from the wall is:

$$I_2 = (a/b)\ (s/d+s)\ \sin\theta_o\ \sin\theta = \cot\theta_o\ \tan\theta\ (s/d+s)\ \sin\theta_o\ \sin\theta$$

The total amount of light reflected in this case is:

$$I = (d/d+s)\ \cos\theta_o\ \cos\theta + (s/d+s)\ \cot\theta_o\ \tan\theta\ \sin\theta_o\ \sin\theta$$

Case III.

In this case the observer can see the lower surface and can still see the shadow produced by the sun (shown in Figure 4).

$$(\theta < \theta',\ \theta_o < \theta_o',\ \theta < \theta_o)$$

The fraction of the total reflected light which is contributed by the wall is:

$$I_2 = (h/b)(s/d+s)\ \sin\theta_o\ \sin\theta = (s/d+s)\ \cot\theta'\ \tan\theta\ \sin\theta_o\ \sin\theta$$

The fraction contributed by the bottom surface is:

$$I_3 = (a-h/b)\ (s/d+s)\ g\ \cos\theta_o\ \cos\theta$$

$$= (s/d+s)\ (\cot\theta_o - \cot\theta')\ \tan\theta\ g\ \cos\theta_o\ \cos\theta$$

The total amount of reflected light is:

$$I = (d/d+s)\ \cos\theta_o\ \cos\theta + I_2 + I_3$$

Case IV.

This case is very similar to Case III, except that the observer cannot see any shadow (Figure 5). Parameter a is now determined by the observer (θ), while in Case III it was determined by the sun (θ_o). In this

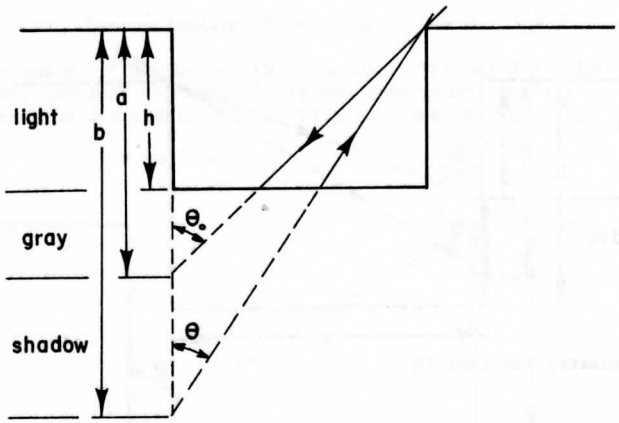

Figure 4. Geometry of Case III

case the angle limits are:

$(\theta < \theta',\ \theta_o < \theta_o',\ \theta > \theta_o)$

The intensity (I_2) is the same as in Case III:

$$I_2 = (s/d+s) \cot \theta' \tan \theta \sin \theta_o \sin \theta$$

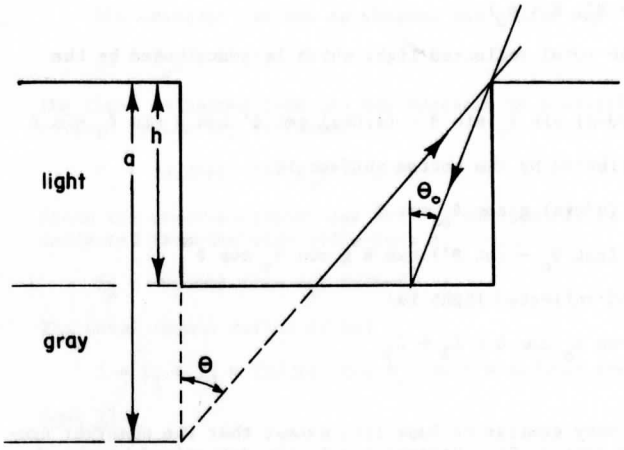

Figure 5. Geometry for Case IV

I_3 is changed slightly and becomes:

$$I_3 = (s/d+s)\ (\cot\theta - \cot\theta')\ \tan\theta\ g\ \cos\theta_o\ \cos\theta$$

The total amount reflected is:

$$I = (d/d+s)\ \cos\theta_o\ \cos\theta + I_2 + I_3$$

Case V.

For this case the sun has a negative zenith angle. The vertical wall which the observer can see is thus in the shadows. The bottom surface is still partially illuminated (shown in Figure 6). The angular conditions which must be met for this case are:

$$(\theta_o < 0,\ \theta < \theta',\ y + z < s)$$

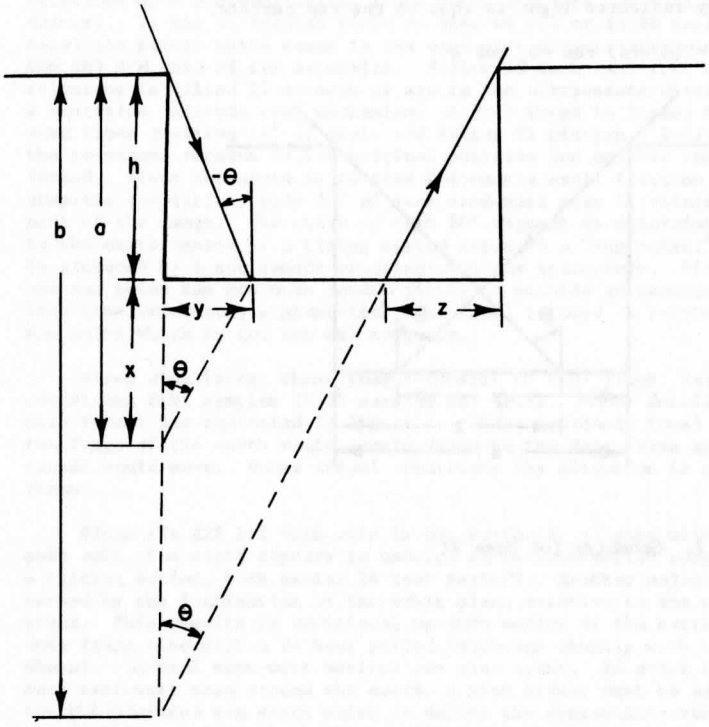

Figure 6. Geometry for Case V

The light reflected from the bottom surface is:

$$I_3 = (b-a/b)\ (s/d+s)\ g \cos \theta_o \cos \theta$$

$$= (s/d+s)\ \frac{\cot \theta - \cot \theta' [\tan(-\theta_o) \cot \theta + 1]}{\cot \theta}\ g \cos \theta_o \cos \theta$$

The total reflected light is:

$$I = (d/d+s) \cos (-\theta_o) \cos \theta + I_3$$

Case VI.

The final case is when the visible parts of the wall and of the bottom surface are completely in shadow (Figure 7). The conditions for this case are:

$$(\theta_o < 0,\ y + z > s)$$

The only reflected light is that of the top surface.

$$I = (d/d+s) \cos -\theta_o \cos \theta$$

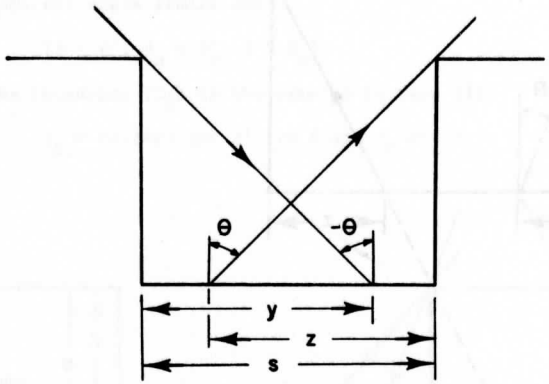

Figure 7. Geometry for Case VI

TECHNIQUES FOR IMPROVING WIND FIELDS DERIVED FROM ATS III IMAGES

Lawrence Sromovsky

INTRODUCTION

A time series of geometrically precise images of the earth from a geosynchronous platform, produced by the Multi-color Spin Scan Cloud Camera (MSSCC) on ATS III, makes it possible to determine wind vectors by measuring the displacement of clouds between images. That this simple concept is quite difficult to implement can best be understood by considering some details of the image data produced by the spin scan camera. The camera is actually a small (5 in. primary) high resolution telescope with photomultiplier light detectors (one for each of three colors). It has an angular field of view of 0.1 mr (3.58 km at the subsatellite point) which scans in the east-west direction as a result of the 100 RPM spin of the satellite. Following each east-west scan, the telescope is tilted 27 seconds of arc in the north-south direction by a precision latitude step mechanism. A full image is formed by 2407 scan lines covering 18° of angle and taking 24 minutes. In 2.4 minutes the telescope returns to its original position and another image is formed. Since the earth is in view for only a small fraction of each complete revolution, only 20° of each east-west scan is retained as part of the image. The start of each 20° segment is determined relative to the earth center by a timing system keyed to a "sun pulse." This is produced by a sun sensor rotating with the spacecraft. Since the raw sun pulse has too much random jitter to provide an accurate line-by-line time reference, a phase-lock loop (PLL) is used to provide a smoothed sun pulse which is (or can be) adequate.

After digitizing, these images consist of 2407 lines, each image containing 8192 samples (2.35 samples per IFOV). Other details of the data format are indicated in Figure 1. Under extremely ideal conditions the image of the earth would remain fixed in the data frame and only the clouds would move. Under actual conditions the situation is quite different.

Since the ATS III spin axis is not perfectly aligned with the earth's spin axis, the earth appears to undergo an up-down motion coupled with a tilting motion, both having 24 hour periods. Another major effect is caused by the inclination of the orbit plane relative to the equatorial plane. This results in additional up-down motion of the earth in the data frame also with a 24 hour period (although usually with a different phase). General east-west motions can also occur. In order to center each east-west scan around the earth, a time offset must be added to the PLL-produced sun synch pulse to define the appropriate start time for each line. Since both the satellite and the earth rotate relative to the sun, this offset must be different for each line in order to compensate correctly. This is normally handled by a constant offset and a

derivative value. If the constant component is in error, the earth will not appear in the center of the frame; if the derivative component is in error, the earth will be skewed and drift in the E-W direction from one frame to the next.

Remarkably enough, all of the effects so far described can be modelled by a fairly small set of parameters. These parameters can be determined by fitting the model to measured positions of a landmark on a time sequence of images. Once the parameters are determined the images are "navigated." In other words, it is now possible to transform satellite coordinates of line and element into earth coordinates of latitude and longitude. The details of this procedure can be found in the literature (Smith and Phillips, 1972). Given the navigation transform, the raw cloud displacements, which are combinations of cloud motions relative to the earth and earth motions in the data frame, can be reduced to relative displacements with respect to the earth and, thus, to wind vectors.

With ATS III data of relatively high quality, it is possible to derive wind vectors with a consistency of 1.5 m/sec (Smith and Phillips, 1972). This is a remarkable accomplishment considering that a combined navigation and displacement error of only 1 line between successive full frames (26 minutes apart) produces a 3 m/sec error in the N-S wind component at the subsatellite point. Larger errors are produced elsewhere. Even a 1 element error can yield a 1 m/sec error in the E-W component. When deriving winds from half-frame images (13 min apart), these errors are twice as large.

It is unfortunate that much of the significant ATS III data which has substantial supporting surface measurements, much as that provided during the BOMEX period, are not of high quality. In many cases application of standard, even though sophisticated, techniques do not yield reliable wind vectors because of data vagaries which cannot be modelled. Yet, the value of this data to research is great enough to warrant a special effort to develop new techniques to deal with it. The remainder of this paper discusses two specific problems: 1) line numbering errors and line start timing errors, and 2) techniques which have proven to be at least partially successful in ameliorating them.

CORRECTION OF LINE NUMBERING ERRORS

The line number encoded on each scan line of an MSSCC ATS III image is not equal to the actual line number. The line encoded as 1 is that initiated by the ground station operator upon hearing a telemetered tone indicating the approximate time of the first scan line. Due to a variety of circumstances, the line number can be in error by 5 lines or more. If this error were constant from frame to frame it would present no problems. However, it varies randomly and cannot be modelled. Since even a one line error leads to wind errors of at least 3 m/s, this is a significant problem.

In order to explain how it can be dealt with, it is necessary to consider the navigation process first. The navigation technique developed at the University of Wisconsin (Smith and Phillips, 1972) requires the

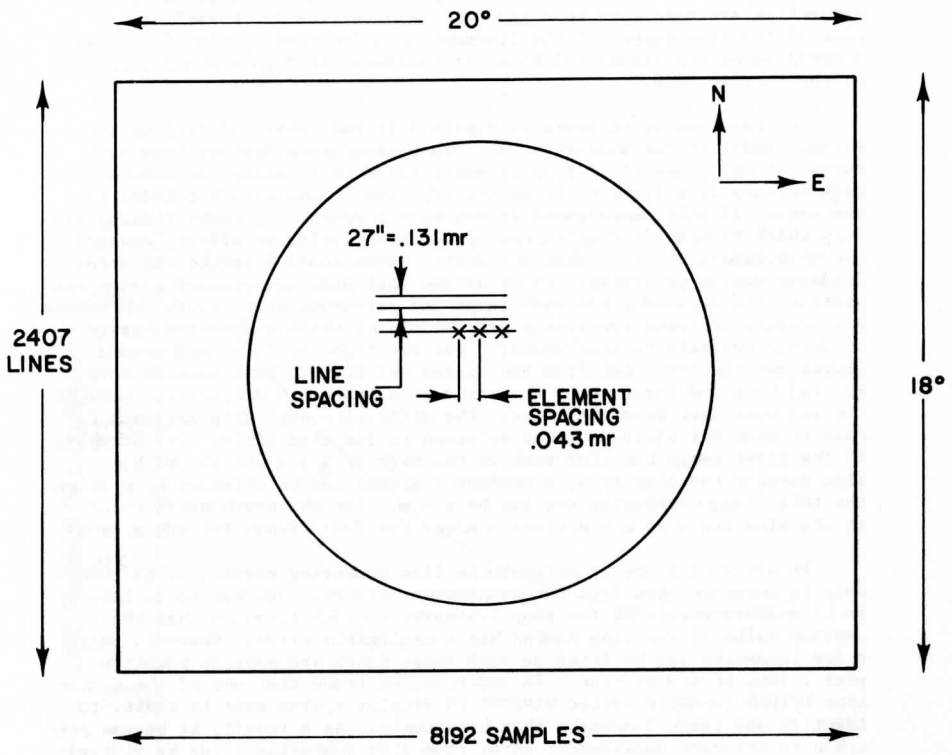

FIGURE I. ATS III MSSCC DATA FORMAT

measurement of the position of a single landmark in a sequence of images. The sequence of line numbers alone is used to determine the attitude of the spin axis. The sequence of element positions determines constant and derivative errors in frame centering (in angular terms these are referred to as β and $\dot{\beta}$). Fixed camera parameters and NASA-provided orbit parameters are also used to derive the final navigation transform. A plot of the line number of the landmark as a function of time (or frame number) shows the sinusoidal behavior indicated in Figure 2 and explained in the introduction.

The smoothed curve shown in Figure 2 is the result of fitting the dynamic model to the measurements. The measurements deviate from the curve for two reasons: (1) measurement error in tracking the same landmark feature from frame to frame and (2) line number errors encoded in the data. If only measurement errors were present, the curve fitting process which is heavily constrained by dynamics would, in effect, average the measurement errors. Thus the fitted curve would describe the actual landmark motion precisely. If we assume that only measurement errors are present, the derived winds show large and erroneous north-south components. A procedure followed previously was the use of three successive images to obtain two sets of wind vectors, one set from the first and second images and the other set from the second and third. Line numbers were shifted back and forth until the residual north-south differences between the two wind sets were minimized. The difficulty with this approach is that it does not yield a unique solution to the wind field. For example, if the first image has line numbers too high by n and the second has line numbers too high by m, a minimum residual can be obtained by placing the third image numbering too low by n - m. Yet the north-south error in the wind field is n - m times 3 m/sec for full frames for any m or n.

In order to properly correct the line numbering errors, it is necessary to separate them from the measurement errors. One way to do this is to measure positions for many landmarks on each frame so that the average value of the line number has a negligible error. However, only a few landmarks can be found on each image which are easy to identify over a long period of time. In addition, we found that use of the prototype McIDAS (usually called WINDCO) TV display system made it easier to identify and track landmarks than previously. As a result, it became possible to separate measurement error from line numbering error by virtually eliminating the former. By using carefully chosen landmarks, pattern overlays, and TV loops between enlarged landmark images, a trained operator could track landmarks to within 0.5 lines almost routinely. (It should be noted that this accuracy does not apply to the absolute position of the landmark, only to its relative position.) Once these accurate landmark measurements became available the navigation model was used to average the line numbering noise, just as before when it was used to smooth both line numbering and measurement noise. Now it became possible to redefine the line numbering so that the landmark fell exactly on the smooth curve, eliminating the line numbering error. The only requirement, in addition to accurate measurements, is that the time sequence of images be long enough so that the line numbering noise is effectively averaged by the curve fitting procedure. Tests, based on the absence of bias effects in the N-S wind residuals between successive vector fields, indicate that a two to three hour period is adequate.

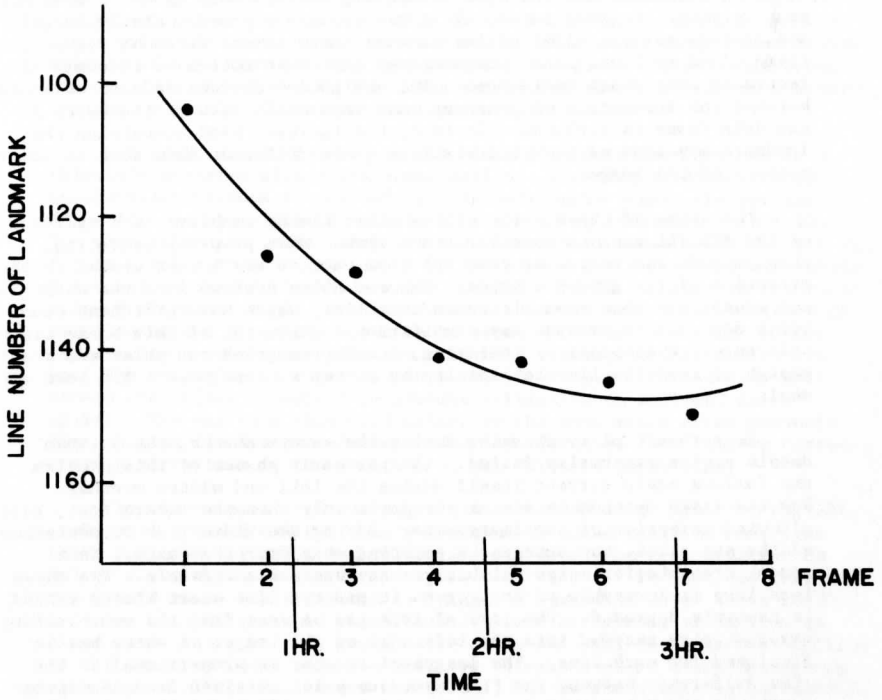

FIGURE 2. LINE POSITION OF A LANDMARK AS A FUNCTION TIME (FRAME NO.). THE SOLID LINE REPRESENTS THE MOTION PREDICTED BY THE NAVIGATION TRANSFORM. THE SOLID CIRCLES INDICATE MEASURED POSITIONS.

LINE START TIMING ERRORS

1. The Problem:

Precision display hard copy ATS images frequently show obvious line start timing errors. These appear as irregular deviations of the earth edge from a smooth curve. The characteristics of this jitter are quite variable. Visual inspection of the imaged earth edges shows small amplitude line-to-line jitter, (not a serious problem because of the averaging done in both navigation and cloud displacement calculations), pseudo/regular deviations of varying amplitude, and discrete large amplitude shifts. Quantitative analysis of the digital image data for day 204, 1969 (by techniques to be discussed later) show that the line-to-line jitter has an amplitude of four to six elements, the sudden shifts up to 10 to 15 elements, and the slow meandering oscillations up to 20 elements peak to peak. In some cases, all three forms are present simultaneously and provide serious difficulties to wind computations based on frame-to-frame cloud motions, since the observed east-west motion is strongly affected by line start deviations. The navigation process is also affected because the assumption of constant east-west drift rate of the earth in the data frame is violated. In fact, the latitude band containing the landmark may show east-west deviations quite different from that of other regions of the image.

The cause of these serious line start timing problems is a malfunction of the ATS III antenna used for video link. When properly operating, this antenna was despun so that its beam pattern was always peaked in the direction of the ground station. The sun pulse derived from the on-board sun sensor was also transmitted on this link, which had sufficient bandwidth and gain to prevent any significant degradation of this basic timing reference. When properly operating, the PLL-smoothed sun pulse was stable enough to keep the line-to-line timing jitter to less than 1 ATS scan element.

As a result of overheating during the summer months, the antenna despin system eventually failed. (In the early phases of this problem the failure would correct itself during the fall and winter months). Now the video antenna points at the earth only when the camera does, thus allowing reception of the image data. During the video link transmission of the sun pulse, the antenna is pointing away from the earth. This causes transmission noise which makes the sun pulse unusable. The phase lock loop is incapable of locking on it and the line start timing system is severely degraded. The loss of lock can be seen from the synchronizer error display encoded into the left edge of the image. A white bar is displayed for each line. The length of the bar is proportional to the time difference between the PLL input sun pulse received from the spacecraft and the PLL output sun pulse used to establish the line start timing. In problem cases, the difference exceeds the range of display (64 elements), indicating virtual loss of the received sun pulse. An attempt to correct this problem was to transmit the sun pulse on the VHF link which did not have a despun (failed) antenna and thus suffered from less transmission noise. Although this has resulted in substantial improvement of gross errors, timing errors sufficiently large to interfere with wind field determinations are still present. This is due to the low quality of the received sun pulse. Especially bad errors occur during passes of NOAA 2, which requires use of the same antenna used to receive the ATS III sun pulse, and as a result of ignition noise produced by heavy equipment used

in construction work at the ground station.

2. Detecting the Earth Edge

Since the original timing reference based on the sun pulse provided low quality research data, it was necessary to establish a new timing reference. The obvious choice was the earth itself, specifically the fairly sharp boundary between the earth and space, i.e., the earth's limb. The only question was whether the variations of cloud cover and atmospheric scattering would allow a sufficiently accurate specification of this boundary for use as a timing reference. An examination of line plots of ATS III data for day 204, 1969, (Figure 3), indicated that accurate detection of the earth's edge was not a trivial matter. Large signal variations were present in the earth portion of the plot (due to cloud variations and noise) and in the space portion of the plot (due to unknown and variable noise sources). Both variable space offsets and large noise spikes interfered with thresholding on low radiance values. These would otherwise be desirable to avoid the large variations caused by clouds. Nevertheless, a fairly successful program was initiated.

The basic algorithm used in the earth edge detection program is a threshold detector with noise compensation. Starting at element N (a substantial distance to the left of the left earth edge), the average noise for the space view is obtained by averaging samples N to N + 50. The algorithm next looks along the scan line 14 elements ahead (to N + 64). If the samples from N + 64 to N + 68 all exceed the sum of the mean space noise and a pre-set threshold value, then N + 64 is returned as the position of the earth edge. If this condition is not met, N is increased by one element and the entire process is repeated. The 14 element buffer between space noise averaging and threshold testing is required to prevent the averaging of signal with noise. Five successive samples must exceed the offset threshold to prevent triggering on isolated noise spikes. The use of a threshold offset by the mean space noise prevents line-to-line (or frame-to-frame) variations in noise from causing corresponding variations in the position of the detected earth edge.

The first tests with the algorithm were made with data from day 204, 1969, which showed considerable variations in noise amplitude and line start position. In addition to testing the algorithm's sensitivity to noise, a search was made for the optimum threshold. The optimum threshold should cause the algorithm to trigger at an altidude of 20 km to 30 km above the surface. At significantly lower attitudes, variations in cloud cover near the limb would cause erroneous variations in the position of the detected earth edge. A very low threshold would cause triggering at a high altitude well above the clouds, but it would also be susceptible to noise in the signal.

Thresholds of 5, 10, 20, and 40 digital counts were tested. (The ATS signal data ranges from 0 to 255 digital counts, the maximum signal roughly corresponding to the radiance of the brightest cloud.) The 5 threshold displayed a significant correlation with noise variations and a large scatter as well. The 10 and 20 thresholds produced edges that were not noise correlated. The 40 threshold was also not noise correlated, but it did show large variations in edge position. These were incon-

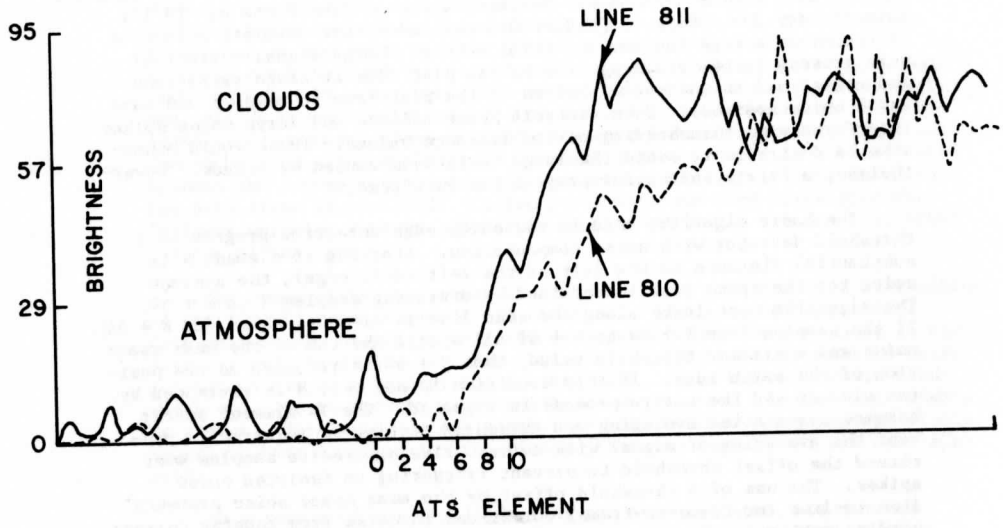

FIGURE 3. SAMPLE PLOTS OF ATS III RADIANCE ALONG A SCAN LINE NEAR THE EARTH'S LIMB. SPACE IS TO THE LEFT AND THE EARTH TO THE RIGHT. NOTE THE SIGNIFICANT NOISE PRESENT IN THE SPACE REGION.

sistent with both expected jitter behavior and with the results of 10 and 20 thresholds. The 40 threshold thus appears to cause triggering on clouds. As a result of this preliminary testing, the 10 and 20 thresholds were chosen for standard usage.

In normal operation, the detection program finds edges for both 10 and 20 thresholds. The mean of the two edges is used for the final detected earth edge and the difference is used to check the quality of the detection. The difference is typically about three samples ±2 RMS.

3. Comparison of Edge Detection and Landmark Measurements

Landmark measurements made for navigation of ATS III images for day 204, 1969 are uniquely suited for testing the consistency of the earth edge detection algorithm. The landmark used was a small island off the coast of South America. The island occupied approximately one ATS field of view and could be isolated to one line and within one or two samples (most landmark measurements are based on patterns extending over many lines and elements). Neglecting earth rotation within the ATS data frame (this is justifiable because the spin axis inclination is small), the landmark element position and the earth edge element position, for the same line on which the landmark falls, should differ by a constant. The measured element positions of the landmark are shown in Figure 4. The linear dependence assumed by the navigation model is obviously violated because the deviations are too large to be caused by measurement errors. However, Figure 5 demonstrates that the combined measurement error in the landmark position and the detection error in the earth edge position are within 2 elements. The RMS error difference in positions is 1.35 elements. The anomalous behavior of the measured landmark motion thus can be expalined by line start timing errors. In addition, the earth edge detection program is shown to be sufficiently consistent to warrant its use in correcting these errors.

4. Frame to Frame Comparison of Earth Edges

Comparison of the detected earth edge position, as a function of line number, with a smooth earth edge reveals moderate amplitude (4-8 elements) line-to-line jitter and sudden large shifts (10-15 elements) taking place within a few lines and lasting for many lines. Perhaps most disturbing are the large amplitude (up to 20 elements peak-to-peak) meandering oscillations with a varying period of several hundred lines. The last effect is not readily observable in hard copy images, but is extremely important in the computation of frame-to-frame cloud motions. An example of the timing error differences is shown in Figure 6.

The earth edge irregularities and the inferred line start irregularities are not the same in each frame. Thus, part of the observed cloud motion in the data frame is due to differences in line start timing errors. For many of the day 204, 1969 images, this large motion is readily observable on the SSEC McIDAS prototype TV display system when viewed as a movie loop. The general characteristics of this motion were found to be in agreement with that predicted from the earth edge behavior. In other words, the latitude regions and sign of the erroneous motions appeared to be consistent with the relative motion of the detected earth edge. Certain regions of latitude which had the same line start timing error should appear as nulls in the anomolous motion. The position of

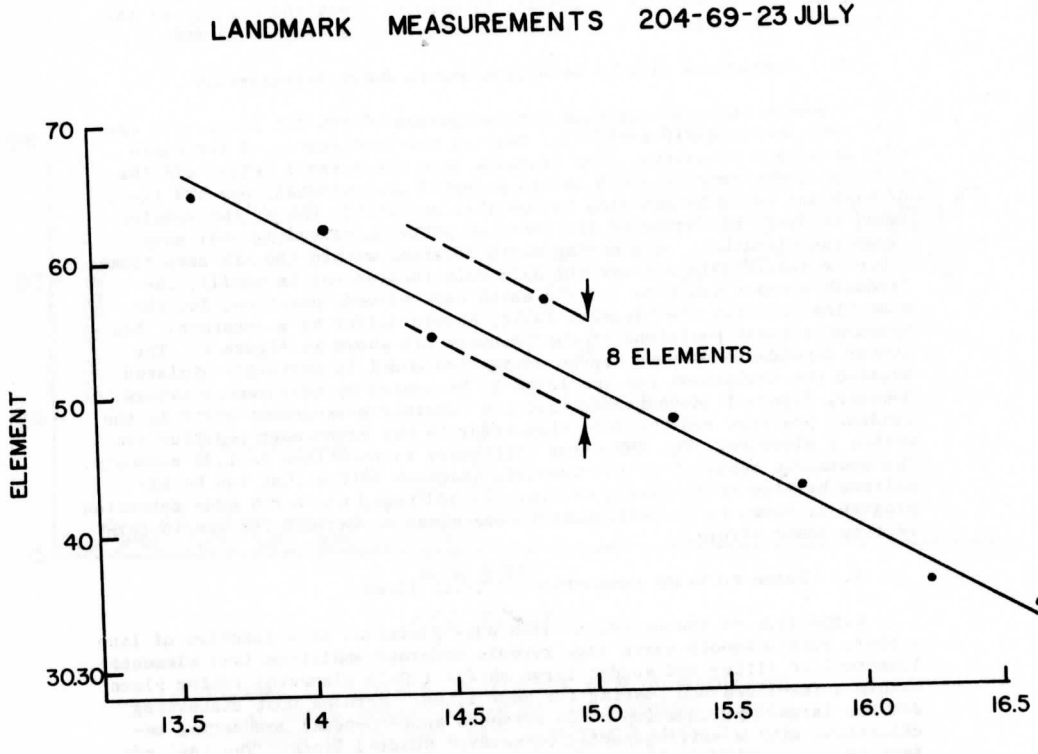

FIGURE 4. ELEMENT POSITION OF THE 204,69 LANDMARK AS A FUNCTION OF TIME. NORMAL BEHAVIOUR SHOULD BE A LINEAR FUNCTION.

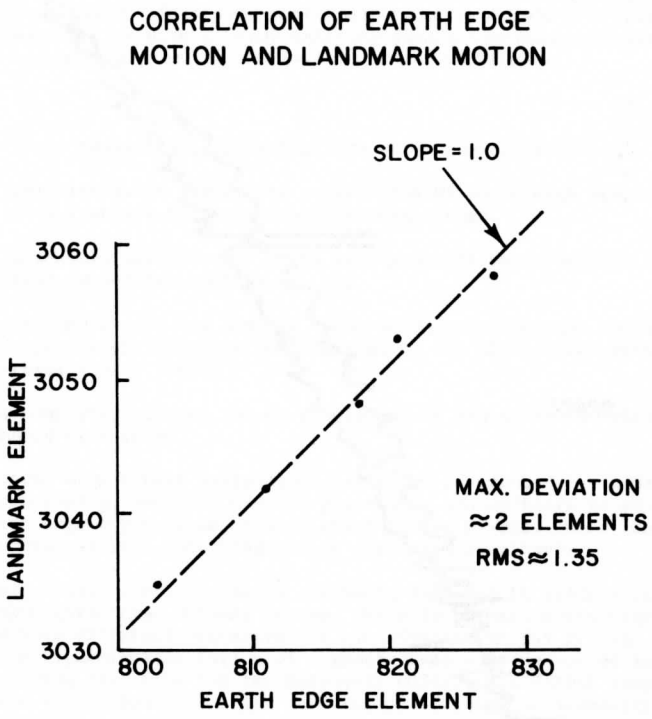

FIGURE 5. CORRELATION OF EARTH EDGE MOTION AND LANDMARK MOTION IS INDICATED BY THE NEAR UNIT SLOPE OF THE PLOTTED POINTS.

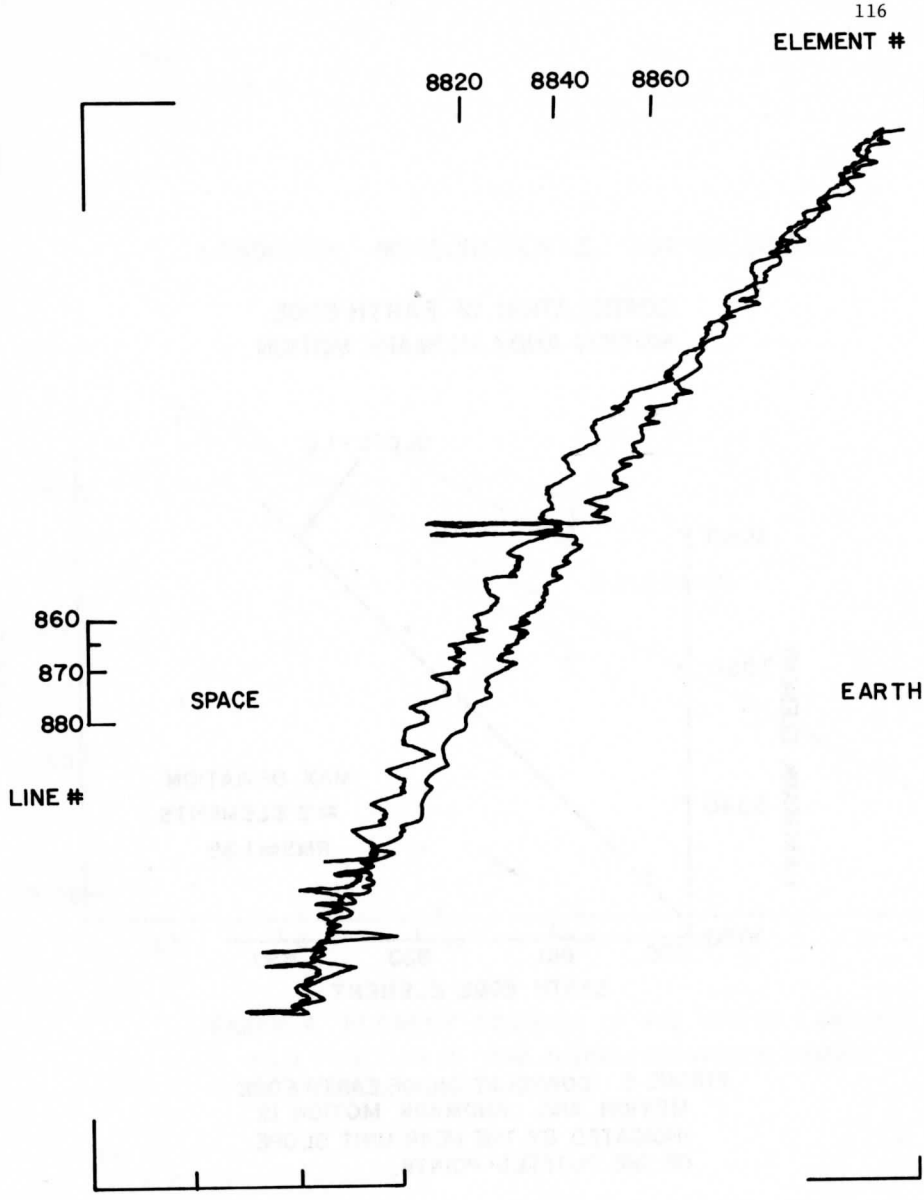

FIGURE 6. EARTH EDGE POSITIONS DETECTED ON TWO SUCCESSIVE FRAMES FROM DAY 204, 1969 ATS III IMAGES.

these nulls also appeared to agree with predictions. All these approximate visual checks indicated that an accurate numerical check with analysis of digital data was warranted.

DEVELOPMENT OF A DATA PROCESSING TECHNIQUE TO CORRECT TIMING ERRORS

Given a measured position of the earth edge for each line of each ATS image in a sequence, there are a number of ways in which that information can be used to improve the accuracy of cloud motion vectors. The method we have chosen after some experimentation is one which maintains maximum compatibility with already existing data processing software. The basic operations involved can be summarized as follows:

a. image navigation, including line numbering corrections,

b. calculation of navigation predictions of earth edge position as a function of line number for each image,

c. threshold detection of earth edge position as a function of line number for each image, and

d. preparation of new digital tapes which are identical to raw tapes except for line shifts equal to the differences between results of b and c.

After d is completed, images can be displayed and processed for wind sets using standard techniques.

The first step (image navigation), although a standard procedure in ATS data processing, required special procedures and software to allow use of earth edge corrections of line start timing errors. Most important was the removal of line numbering errors discussed previously.

The procedures described above are being employed in processing data on the WINDCO (prototype McIDAS) system. We plan to employ somewhat different and more efficient procedures on the advanced McIDAS system. We have already begun implementation of a generalized edge detection and line start correction algorithm for the Datacraft 6024/5, the McIDAS computer. This program allows for line start corrections without the necessity of rewriting data tapes. In the execution of this program the Datacraft reads one line of image data from the raw data tape (actually a 9-track copy), detects the position of the earth edge on this line, and compares the detected position to the position predicted by the navigation program. Using the difference between positions to define a line shift, the Datacraft loads the line of image data on the McIDAS digital disk (and, eventually, on the analog disk as well) with appropriate line start corrections included. Thus, the display and digital data are simultaneously corrected while the raw data is being read in a line at a time. Tests of this software are now in progress.

Although obvious data timing improvements in the corrected tapes can

be seen by comparing time sequence TV displays of raw and corrected data, we need to make the comparison on a quantitative basis. We used wind sets derived from corrected and raw data to make this comparison. Three images at times t_1, t_2, and t_3 are used for each data type. Cloud tracers are selected separately from each data type, although overlays are used to keep the distribution of tracers approximately the same. Winds are derived from cloud motions between t_1 and t_2 and between t_2 and t_3. The differences (residuals) between these two wind sets are measures of the quality of the derived winds. Many factors can influence these residuals, including cloud tracer characteristics, navigation accuracy, noise, and line start timing stability. The last factor has significant effects only on the U-component (east-west component) of the residuals. Tests should reveal a sharpening of the distribution of east-west residuals in the winds derived from corrected data as compared to those for the uncorrected data. In addition, the corrected data winds should not display any latitude bands of east-west accelerations.

In response to specific research needs of scientists at the Space Science and Engineering Center, corrected digital tapes have been written for ATS III data from days 202, 203, 204, 1969. The corrected images are 800 line swaths encompassing the target area of the BOMEX experiment. We now have 16 such corrected images for day 204. Ten are based on left hand limb detection and six based on right hand limb detection. In addition, seven corrected images have been written for day 203 based on left hand limb detection and eight for 202 data. All of the latter are based on right hand limb detection. The difference between the left hand and right hand edges of some ATS pictures is the amount of communication noise present. This noise on the right hand side is so large for days 202 and 204 that a new algorithm was required. For day 203 the noise was so bad that the algorithm failed completely.

Six images were chosen from those on day 204/69. The data from that day showed the largest line start timing errors of the three processed and had corrected images available based on both left and right hand edge detection. It also had already been partially processed at the time the test was started. The times chosen are tabulated below.

Table 1. Images used for verification tests of line start timing corrections (204/69)

Left Hand Correction	Right Hand Correction
T1 = 1426 11	T1 = 1308 42
T2 = 1451 44	T2 = 1335 02
T3 = 1518 33	T3 = 1400 47

In all, twelve images were processed for winds. This resulted in four distinct sets of wind fields. Two were based on raw digital data (termed "raw" winds) and two on corrected digital data (termed "corrected" winds). Each set was processed as follows:

1) three successive images were loaded on the analog disc of the TV display system and displayed in sequence.

2) cloud tracers were flagged by a joystick cursor on each of the three images.

3) the triplet of coordinate pairs (line and element) of each tracer region were automatically punched on tape and later decoded and punched on cards. These coordinates gave approximate cloud motion.

4) the coordinates were submitted to the WINDCO program which selected digital data boxes centered at these coordinates from the appropriate digital tapes. Cross correlation of these data arrays was used to measure the precise line and element displacement of each cloud tracer identified. Displacements were calculated between T1 and T2 and between T2 and T3.

5) the navigation transform was used to convert the line and element displacement pairs to wind vector pairs. The wind vectors of each pair were differenced to produce residual vectors. Thus three vector fields resulted from each wind set: (A) the wind field derived from T1 and T2, (B) the wind field derived from T2 and T3, and (C) the residual (or acceleration field) which is the difference between (A) and (B).

The results of the comparison are displayed in Figures 7 through 14. Figure 7 displays the raw wind field for T1 - T2 from the later time set of Table 1. Note the change of wind direction between 10°N and 15°N relative to the general flow out of the east above 13°N. An examination of Figure 8, displaying the raw wind field for T2 - T3 shows an opposite effect, i.e., an increase of easterly speed. The residual field for this pair of wind fields, shown in Figure 9, reveals this anomalous behavior quite clearly. A similar anomaly of smaller magnitude can be seen at about 18°N. The corrected winds for the same time intervals, shown in Figures 10 and 11, do not display such anomalous behavior. The residual field for the corrected winds (Figure 12) verified a dramatic improvement compared to the raw residual field of Figure 9. Residuals are much smaller and show no correlation with latitude. The improvement in the U component (east-west component) wind consistency can be seen in a plot of frequency distribution of residuals for both raw and corrected data (Figure 13). Note the sharpening of the distribution in the corrected wind field.

The results for the earlier time period do not show such dramatic improvement for several reasons: (1) the timing errors of the raw data are not so large, (2) the right hand edge detection (which must be used for this time period) is not as accurate as left hand detection because of transmission noise, and (3) fewer tracers were selected. The simplest way to display the limited improvement is to compare the U component residuals of the raw and corrected winds for this earlier time period. This is done in Figure 14. A definite improvement is indicated there, although it is not so easy to see in the vector field plots.

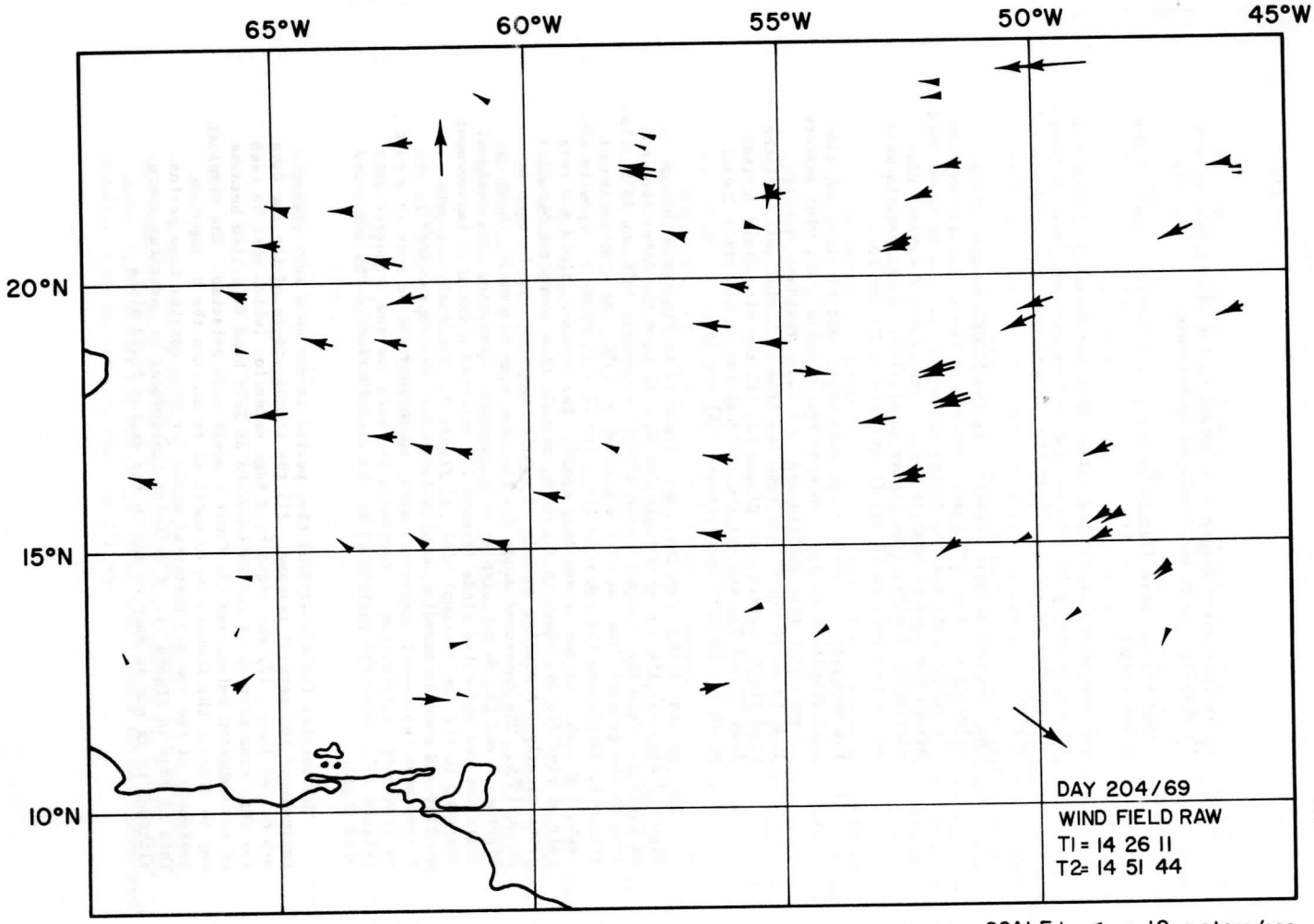

FIGURE 7

SCALE : ← = 10 meters/sec

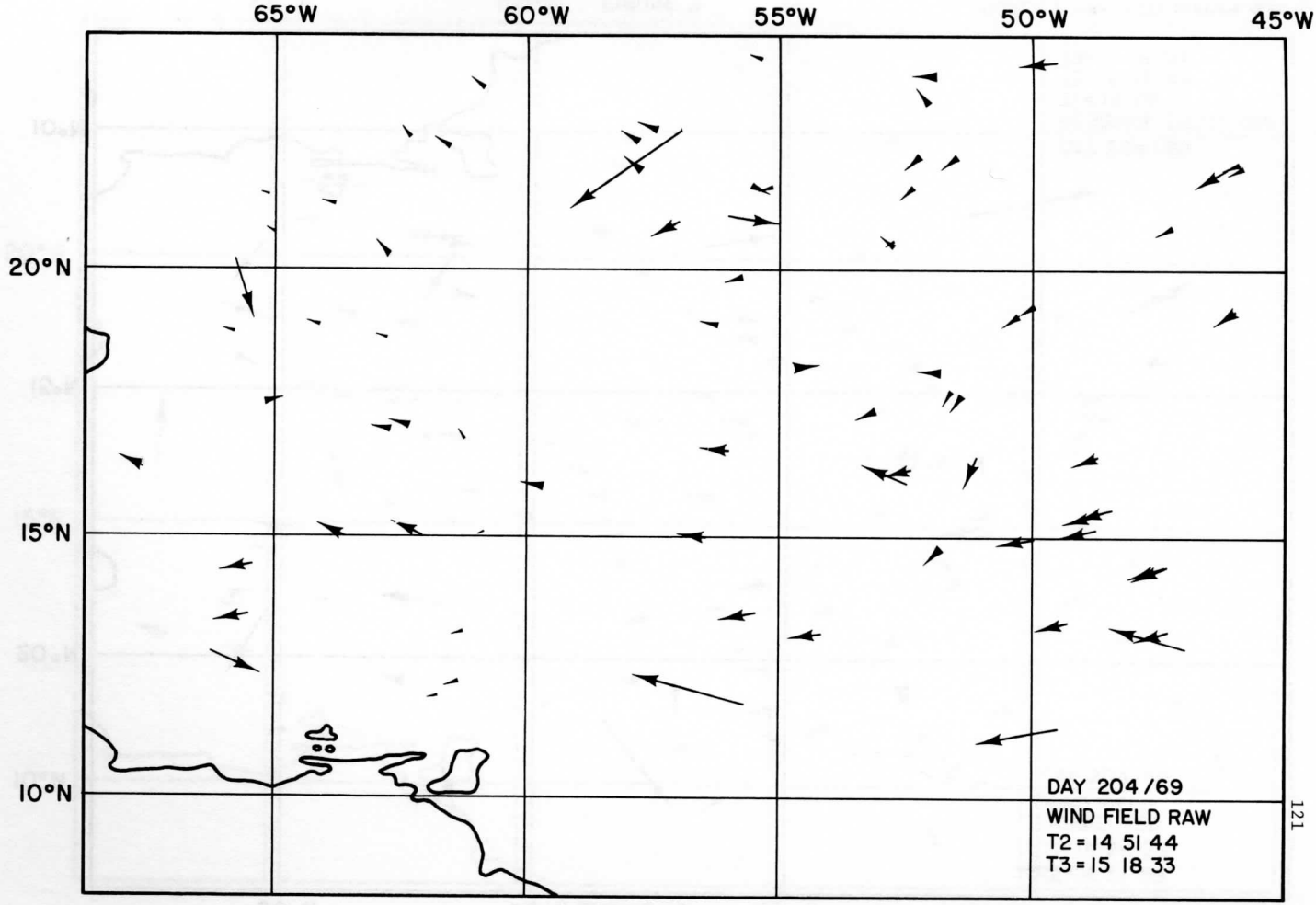

FIGURE 8

SCALE : ← = 10 meters/sec

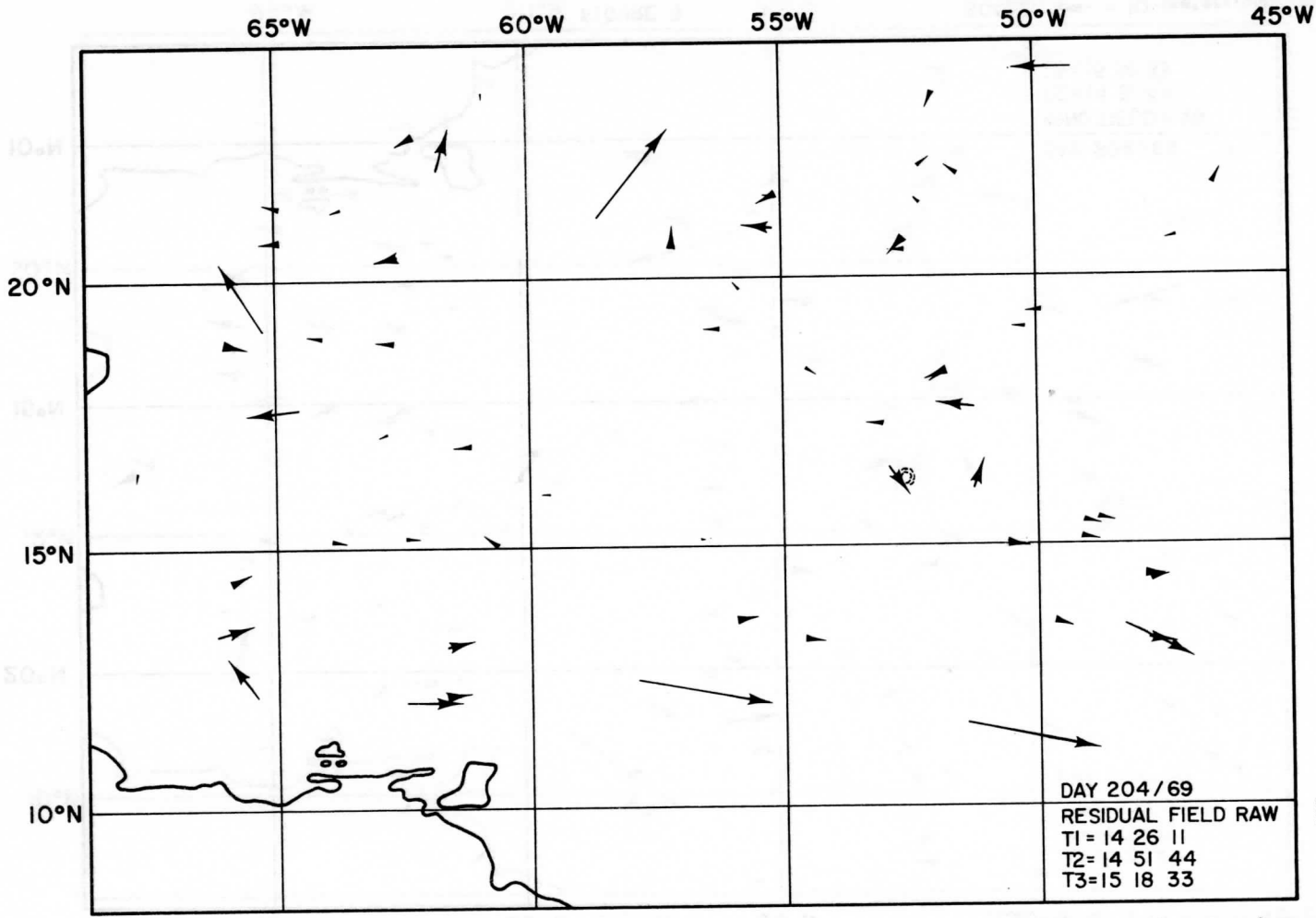
65°W
60°W
55°W
50°W
45°W
20°N
15°N
10°N
DAY 204/69
RESIDUAL FIELD RAW
T1 = 14 26 11
T2= 14 51 44
T3=15 18 33
SCALE : ← = 10 meters/sec

FIGURE 9

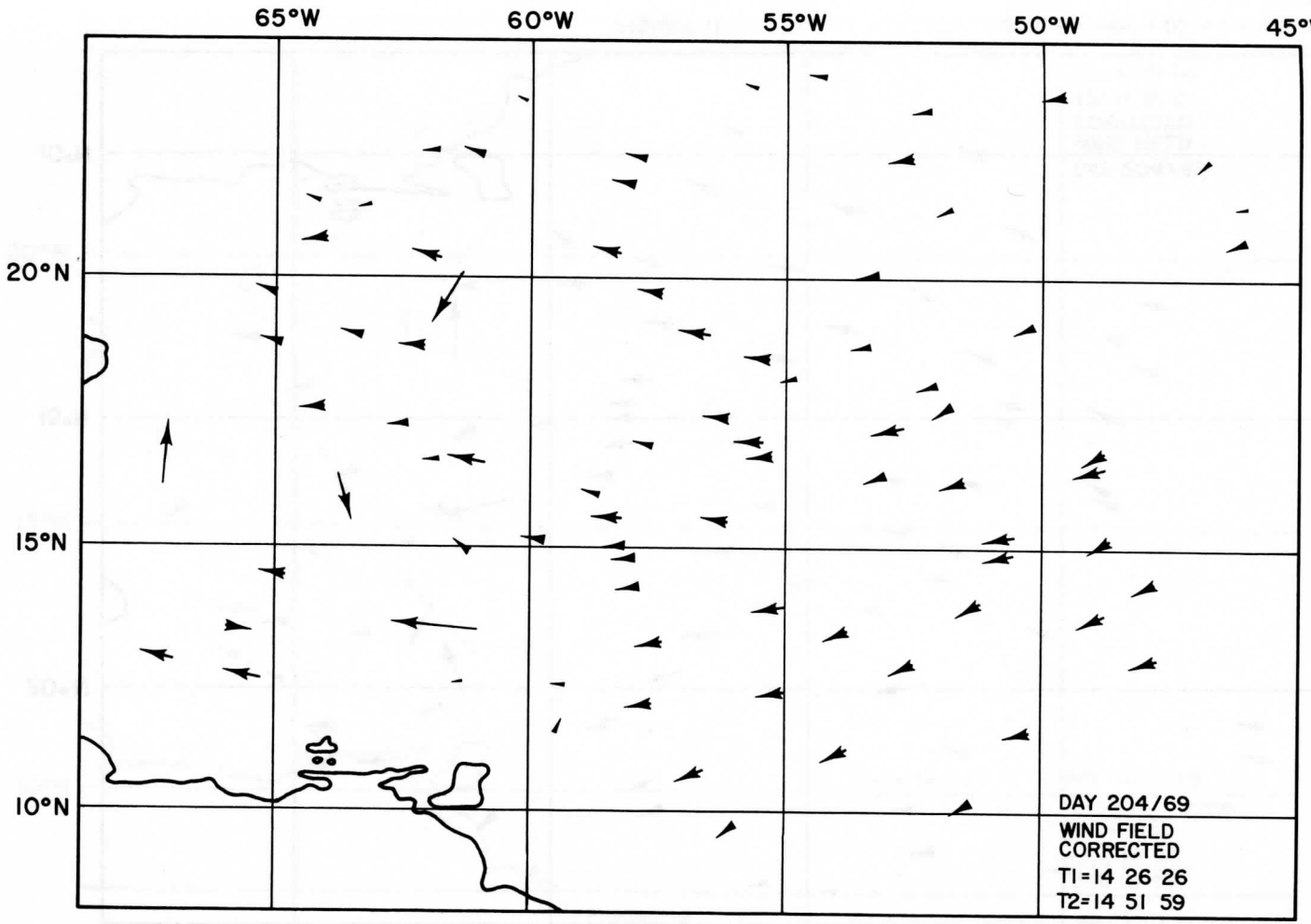

FIGURE 10

SCALE : ← = 10 meters/sec

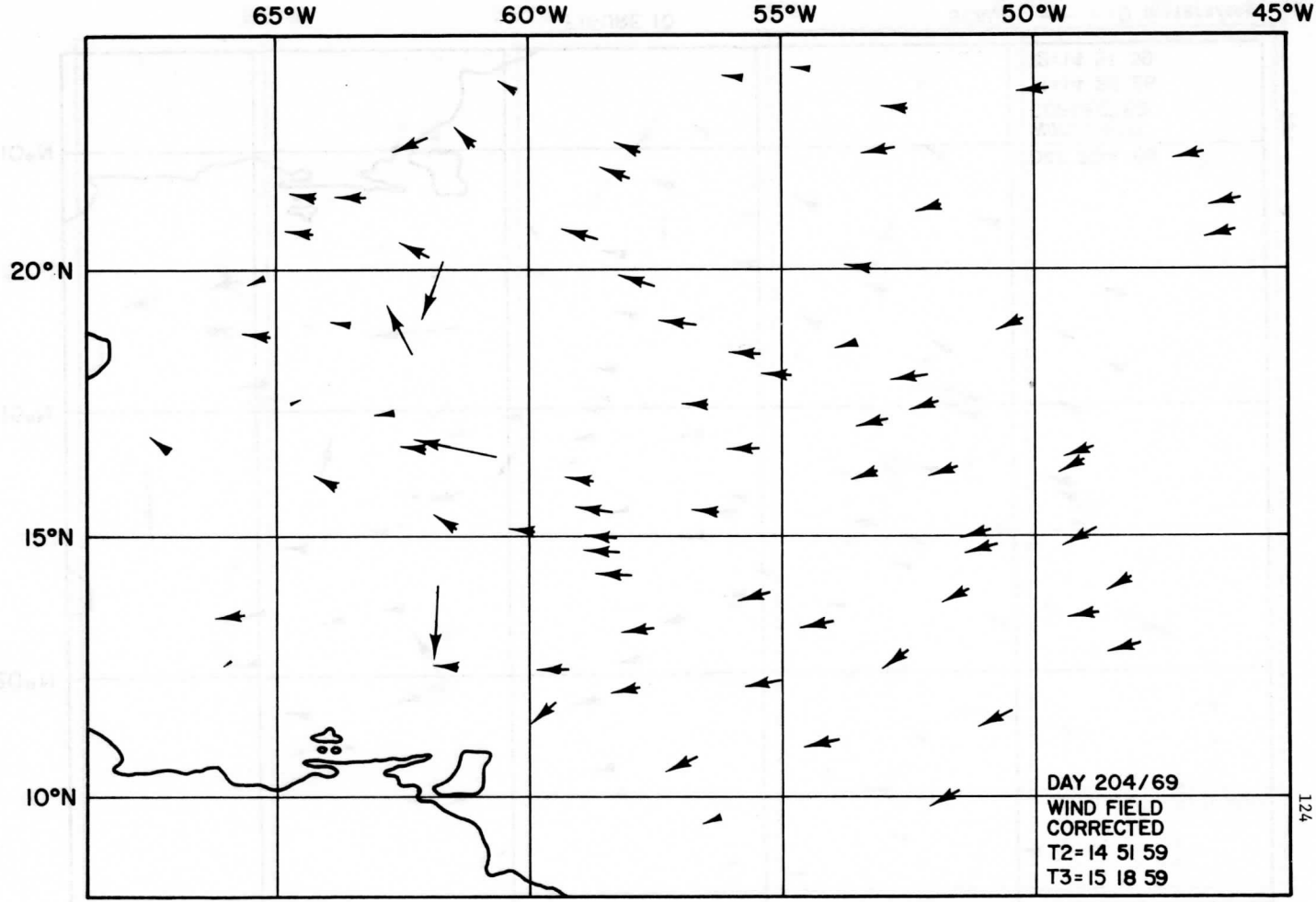

FIGURE 11

SCALE: ← = 10 meters/sec

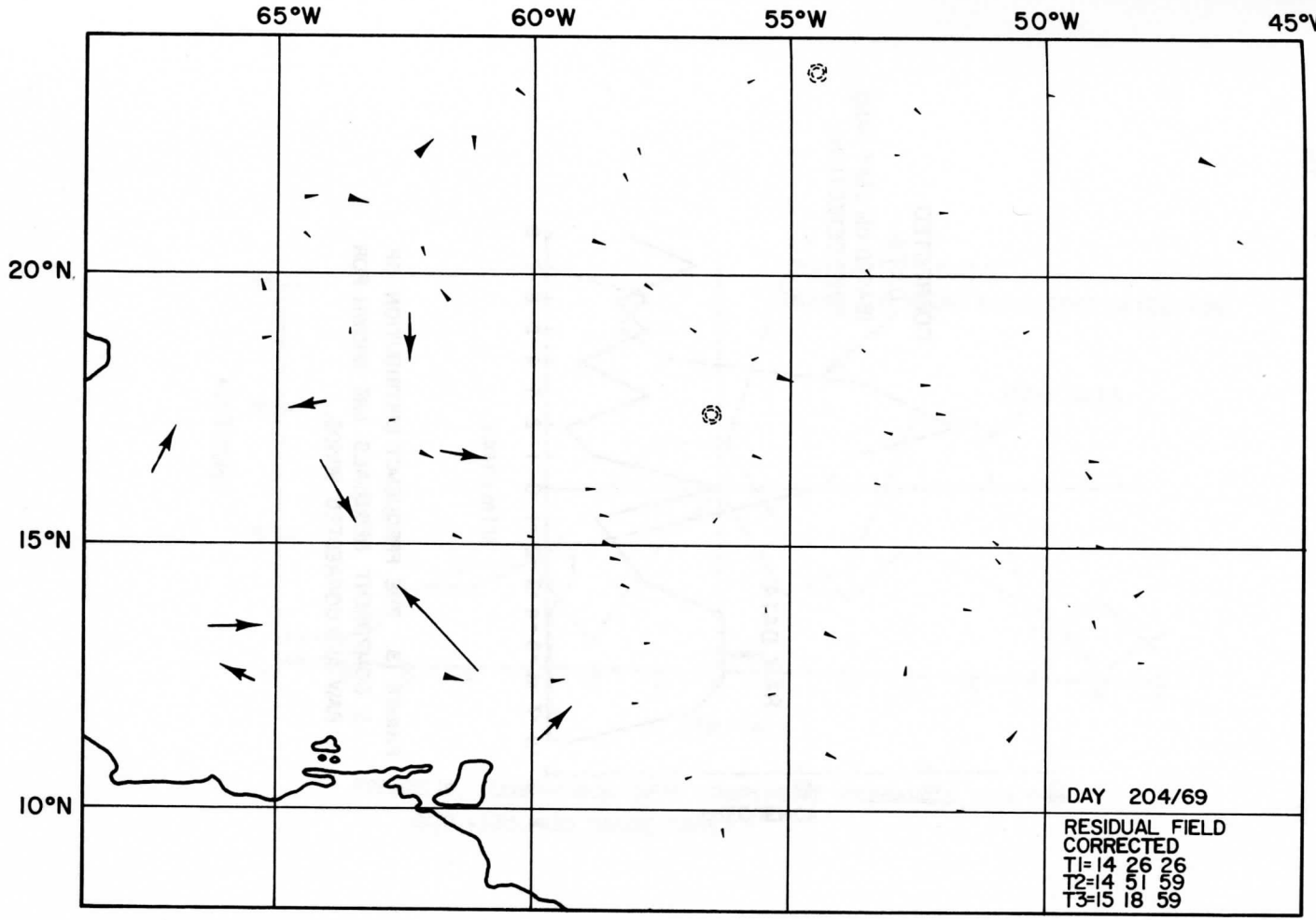

FIGURE 12

SCALE : ← = 10 meters/sec

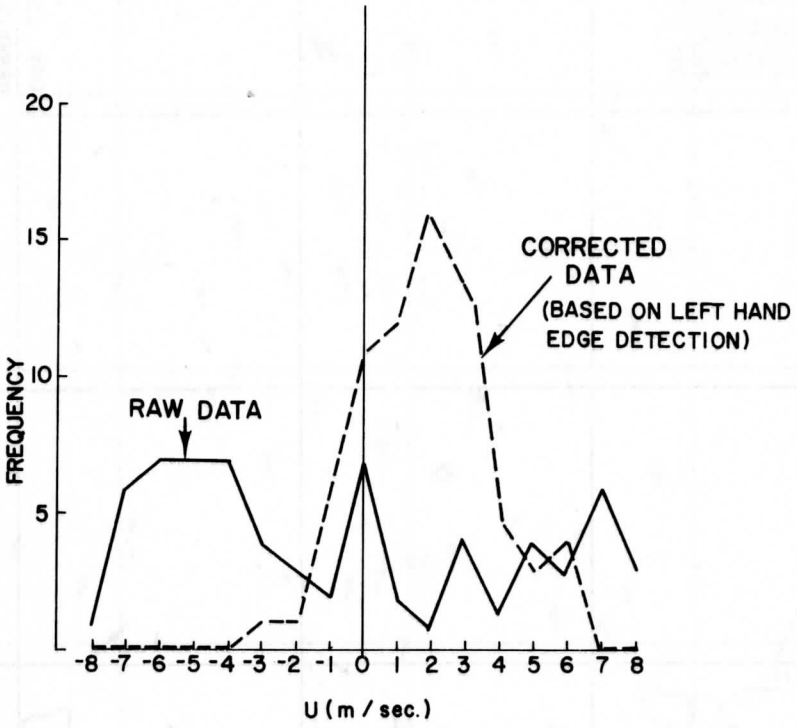

FIGURE 13. THE FREQUENCY DISTRIBUTION OF U COMPONENT RESIDUALS ARE SHOWN FOR RAW AND CORRECTED WINDS.

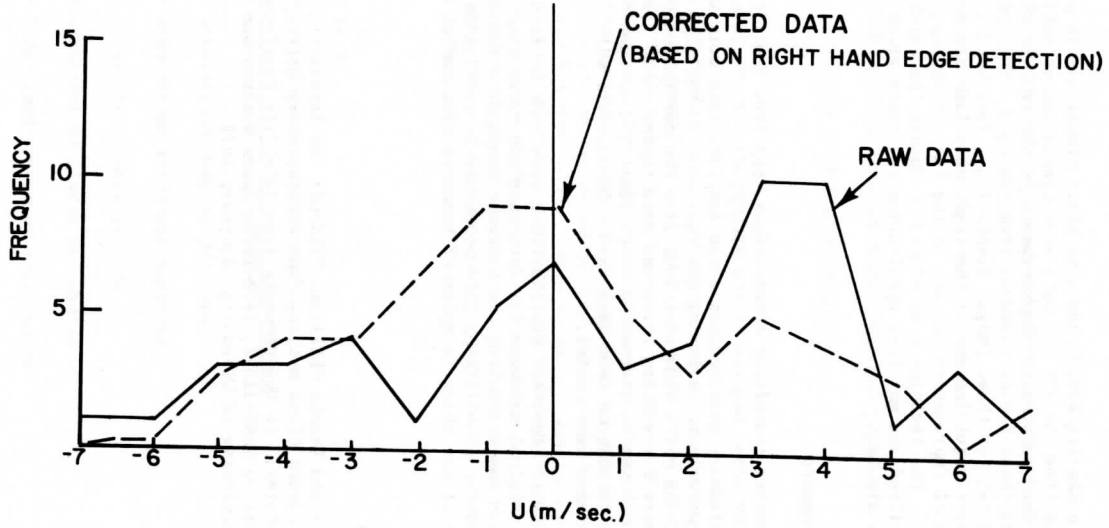

FIGURE 14. COMPARISON OF U COMPONENT RESIDUALS FOR THE 1308, 1335, 1400 IMAGE TRIPLET.

CONCLUSION

Line numbering errors and line start timing errors present in much of the data from the ATS III spin scan camera can be sufficiently corrected to produce substantial improvements in the derived wind fields as compared to those fields produced from raw data. The improvement is especially great for those images displaying a left hand limb in illumination. Images requiring use of the right hand limb are more limited in the degree of improvement because of the large transmission noise frequently present. The techniques developed to detect the earth limb can be further refined and may find application in other areas of image processing and analysis.

ACKNOWLEDGEMENTS

The author gratefully acknowledges important contributions to this work made by other members of the SSEC staff. J. T. Young provided the accurate landmark measurements which inspired this work in the first place and aided greatly in verifying its results. D. Phillips provided software for predicting earth edge positions from the navigation parameters; this was necessary for writing corrected data tapes. Both Young and Phillips provided much useful discussion which clarified navigation and data processing techniques that were used. Discussions with J. Benson and E. Smith were also very useful.

Especially important contributions were made by R. A. DeDecker who wrote the original software for detecting the earth edge. His major contribution was assembling the software components for the entire correction procedure and verifying this procedure by critically following through every step of the chain in spite of numerous problems with data tapes and hardware.

REFERENCES

Smith, Eric and Dennis Phillips, "WINDCO: An Interactive System for Obtaining Accurate Cloud Motions from Geostationary Satellite Spin Scan Camera Pictures," in Measurements from Satellite Platforms, Annual Scientific Report on NAS5-11542, 1970-1971, Space Science and Engineering Center, University of Wisconsin, February 1972.

POINTING ERROR ANALYSIS OF GEOSYNCHRONOUS SATELLITES

Aniruddha Das and T. C. Huang

THERMOELASTIC FLUTTER MODELS FOR ELEMENTS OF FLEXIBLE SATELLITES

ABSTRACT

Models of thermally induced flutter of the flexible elements of a satellite, such as beams, circular plates, and cylindrical shells, have been obtained. These models form the necessary blocks for analyzing the motion of satellites. The heat input is considered to be caused by solar radiations. The partial differential equations for all the elements of the satellite are linear in the space dependent variables and non-linear in the time-dependent variables. These equations are coupled through the motion of the center of the satellite's mass. Galerkin's method has been used to remove the space-dependence of these equations. In this paper, a further reduction of the equations is made into singular perturbation equations. These are amenable to solution for complex problems of extremely large number of degrees of freedom.

NOMENCLATURE

A	= Area.
dA	= Infinitesimal area element.
A_1^*	= Generalized mass matrices.
A_2^*	= Generalized damping matrices.
A_3^*	= Generalized stiffness matrices.
$\underline{A}_4^*$	= Generalized force vectors.
a	= Diameters of plates and shells.
B	= Body fixed system of coordinates.
$\underline{C}$	= Reversed displacement vector of the center of mass of the satellite in the B-based coordinates.
D	= Stiffness of plates or shells.

E = Young's modulii.

F = Force.

G = Displacement matrix, Eq. (35).

G_1, G_2, G_3 = Acceleration matrices, Eq. (38).

h = Thicknesses of plates and shells.

I = Identity matrix, also area moments of inertia of the beam cross-sections.

$[I_j]$ = Operator which selects the jth row of an array.

J_n = Bessel functions of the first kind:

k = Thermal constants for beams, plates and shells.

L = Linear differential operator, also local system of coordinates.

L_1 = Error in linear differential operator, L.

ℓ = Lengths of beams and shells.

M = Total mass of the satellite.

m = Discrete masses.

dm = Infinitesimal mass element.

N = Inertially fixed system of coordinates.

p = Beam function exponent.

p_2, p_3 = Shell function exponents.

$\underline{q}, \underline{q}^*$ = Generalized position coordinates.

$\underline{R}$ = Position vector of the reference points of the structural elements in the B-based coordinates.

r = Radial distance measure of plates.

s = Length along the beam axes.

T = Temperature function for shells.

$\underline{u}$ = Arbitrary vector, also generalized solution vector.

$\underline{v}$ = Arbitrary vector, also error in $\underline{u}$.

w = Mapping function, Eq. (A1) of Appendix A.

$\underline{X}$ = Position vector of the center of mass of the satellite in the N-based coordinates.

y = Displacements of the flexible elements of the satellite in the B-based coordinates.

z = Axial length measure of shells, also equal to $r[\exp(i\theta)]$.

α = Angle between the plane of the heat wave-front and the beam, plate or shell axes.

α^* = Thermal coefficient of expansion.

Θ = Matrix for transforming N-based vectors to B-based vectors.

θ = Deformation gradient for beams, plates and shells; also angular measure for plates.

κ = Curvature for beams, plates and shells.

Λ_1 = Generalized coupled mass matrices.

Λ_2 = Generalized coupled damping matrices.

Λ_3 = Generalized coupled stiffness matrices.

μ = Poisson's ratio.

μ^* = Matrix for transforming L-based vectors to B-based vectors.

ρ = Linear density of beams; area densities of plates and shells.

τ = Thermal constant.

ϕ, Ψ, Ψ^* = Shape functions.

$\underline{\omega}$ = Angular velocity vector of the satellite.

ω^*, ω^{**} = Transformed angular velocities, Eqs. (7) and (23).

SUBSCRIPTS

b = Beams.

E = Elastic.

I = Inertial.

P = Plates.

s = Shells.

T = Thermal.

SUPERSCRIPT

L = Local coordinates.

INTRODUCTION

The theory presented in this paper forms a part of a comprehensive study [1], conducted by the authors, on the comparative pointing accuracies of different classes of flexible satellites. One of these is a dual-spin satellite. Its assumed configuration is shown in Figure 1. The configuration consists of two composite bodies, each with a cylindrical shell, two circular plates, four beams with four tip-masses, two rigid bodies, and four spring-mass-damper systems.

A successful continuous model of thermally induced flutter of a flexible beam attached to a spacecraft was introduced by Etkin and Hughes [2]. It was considerably refined by Yu [3] and modified by Das [4]. The present study extends the results for beams to plates and shells. Velman [5] and Likins and his associates [6-11] displayed discrete dynamic modeling of flexible satellites with a large number of degrees of freedom. The equations of motion were obtained directly from Newton's laws and Euler's equations.

Grote, et. al. [12] obtained the equations for a similar large system from an energy principle and Lagrange's equations. In these investigations [6-12], the flexible elements were modeled as discrete spring-mass-damper systems. This necessitates the introduction of a larger number of degrees of freedom than that required for continuously distributed mass modeling. Another advantage of continuous mass models is that the effects of heat inputs on the structure of the satellite can be easily taken into consideration.

Recently, Meirovitch and Calico [13] compared the stability bounds of satellites with flexible beams by different methods. It was found that the estimates of the continuous model produced the widest bounds. Continuous modeling can be justified on these bases even though a long period of computing time is required for integrating the continuous functions.

In the present study, the partial differential equations for beams, plates, and shells have been obtained by extending the methods used by Likins [6] for discrete masses and Yu [3] for non-rotating beams. The space-dependence of these equations is linear, although the time-dependence is kept non-linear. The derivation of these equations is presented in the following sections.

INERTIA FORCES

Let dm_i be the mass of an infinitesimal structural element of the flexible satellite, shown in Figure 2. Let $(\underline{R}_i+\underline{s}_i)$ and s_i be the nominal position vectors of dm_i at P with respect to the body coordinate system (B) fixed on the satellite, and a local coordinate system (L) fixed on the element. The origin of B is at the nominal center of mass (O) of the satellite. Let X be the position vector locating the center of mass (C.M.) with respect to an inertially fixed coordinate system (N) with its origin at O'. Define the vectors $\underline{y}_i$, $-\underline{C}$ and $\underline{\omega}$ to be the displacements of dm_i, the displacement of O, and the angular velocity of the satellite, respectively. Thus, the inertia force $\underline{F}_{iI}$ on dm_i is given [10] by:

$$\underline{F}_{iI} = -dm_i \left[\Theta\ddot{\underline{X}} + \ddot{\underline{C}} + \ddot{\underline{y}}_i + 2\tilde{\omega}(\dot{\underline{C}}+\dot{\underline{y}}_i)\right.$$

$$\left. + (\dot{\tilde{\omega}}+\tilde{\omega}\tilde{\omega})(\underline{C}+\underline{R}_i+\underline{s}_i+\underline{y}_i)\right] \qquad (1)$$

In the above equation, Θ is the matrix for transforming vectors based on the coordinate system (N) to those in the system (B). The vectors $\underline{F}_{iI}$, $\underline{C}$, $\underline{R}_i$ and $\underline{y}_i$ are based in the system (B). The operation ($\sim$) defines the cross product of two vectors $\underline{u}$ and $\underline{v}$, as follows:

$$\underline{u} \times \underline{v} = \tilde{u}\underline{v} = -\tilde{v}\underline{u} \qquad (2)$$

For a system of discrete masses (dm_i) the vector ($\underline{C}$) can be expressed as

$$\underline{C} = -\frac{1}{M}\sum_i \underline{y}_i \, dm_i \qquad (3)$$

where M is the total mass of the satellite. For a continuous mass distribution, the summation in Eq. (3) is to be replaced by appropriate integrations.

BEAM EQUATIONS

The equations for beams are considered first. The force-equilibrium equation for a small element of the ith beam is given by:

$$(\underline{F}^L_{ibE} - \underline{F}^L_{ibT}) = \underline{F}^L_{ibI} \qquad (4)$$

The equation is expressed in a local coordinate frame (L) fixed to the particular beam being considered. The origin of the local frame of coordinates is always taken at the junction of the beam and the main satellite body. The coordinate axis No. 1 is always taken along the axis of the beam. The distance along this axis is 's'. Figure 3 shows the general configuration of a beam.

Let $\underline{y}^L_{ib}$ be the beam displacements in the local frame, and $\underline{y}_{ib}$ be those in the coordinate system B. Let the transformation matrix $[\mu^*_{ib}]$, which relates the body-fixed coordinate frame B and the local coordinate frame L_i fixed on the ith beam, be defined by:

$$\underline{y}_{ib} = [\mu^*_{ib}]\underline{y}^L_{ib} \qquad (5)$$

Then, using Eq. (5), $\underline{F}^L_{ibI}$ is obtained from Eq. (1) as:

$$\underline{F}^L_{ibI} = -\rho_{ib}\cdot ds\cdot \left\{[\mu^*_{ib}]^T[\Theta\ddot{\underline{X}}+\ddot{\underline{C}}+2\dot{\omega}\dot{\underline{C}}+(\dot{\tilde{\omega}}+\tilde{\omega}\tilde{\omega})\underline{C}]\right.$$

$$\left. + \ddot{\underline{y}}^L_{ib} + 2\omega^*\dot{\underline{y}}^L_{ib} + (\dot{\omega}^*+\omega^{**})\left[\underline{R}^L_{ib}+\begin{Bmatrix} s \\ 0 \end{Bmatrix}+\underline{y}^L_{ib}\right]\right\} \qquad (6)$$

in which the symbols ω^* and ω^{**} are defined as:

$$\omega^* = [\mu^*_{ib}]^T \tilde{\omega} [\mu^*_{ib}]$$

and

$$\omega^{**} = [\mu^{*}_{ib}]^{T} \tilde{\tilde{\omega}}\tilde{\omega} [\mu^{*}_{ib}] \tag{7}$$

and $\underline{R}^{L}_{ib}$ is the position vector of the origin of the local frame with respect to the body coordinate frame. It is expressed, however, in the local coordinate frame.

Considering axially rigid, prismatic, Euler beams, $\underline{F}^{L}_{ibE}$ is given by:

$$\underline{F}^{L}_{ibE} = \begin{Bmatrix} 0 \\ E_{ib} \cdot I_{ib,3} \cdot \dfrac{\partial^4 y^{L}_{ib,2}}{\partial s^4} \\ E_{ib} \cdot I_{ib,2} \cdot \dfrac{\partial^4 y^{L}_{ib,3}}{\partial s^4} \end{Bmatrix} \cdot ds \tag{8}$$

Expressions for the thermal curvatures (κ^{L}_{ibT}) of the beams are taken from Refs. [3,4]. These expressions are:

$$\kappa^{L}_{ibT,j} = k_{ibT,j} \cdot \tau_{ibT,j} \cdot [\cos\alpha_{ib,j} - (\theta_{ib,j} - \tau_{ibT,j} \cdot \dot{\theta}_{ib,j} + \tau^{2}_{ibt,j} \cdot \ddot{\theta}_{ib,j} - \ldots)\sin\alpha_{ib,j}] \text{ for } j = 2,3, \tag{9}$$

where α are the angles between the plane of the incident heat wave-front and the nominal beam axes [3] and

$$\theta_{ib,j} = \frac{\partial y^{L}_{ib,j}}{\partial s} \quad ; \quad j = 2,3. \tag{10}$$

The thermal force ($F^{L}_{ibT,j}$) is related to $\kappa_{ibT,j}$ by:

$$\begin{Bmatrix} F^{L}_{ibT,1} \\ F^{L}_{ibT,2} \\ F^{L}_{ibT,3} \end{Bmatrix} = \begin{Bmatrix} 0 \\ E_{ib} \cdot I_{ib,3} \cdot \dfrac{\partial^2}{\partial s^2} \kappa^{L}_{ibT,2} \\ E_{ib} \cdot I_{ib,2} \cdot \dfrac{\partial^2}{\partial s^2} \kappa^{L}_{ibT,3} \end{Bmatrix} \tag{11}$$

Hence, the governing equations of the beams' motion are obtained by substituting Eqs. (6,8,11) into Eq. (4) as:

$$\left\{\begin{array}{c} 0 \\ E_{ib}\cdot I_{ib,3}\cdot\left[\frac{\partial^4}{\partial s^4} + \tau_{ibT,2}\cdot k_{ibT,2}\cdot\sin\alpha_{ib,2}\cdot\frac{\partial^3}{\partial s^3}\left(1-\tau_{ibT,2}\cdot\frac{\partial}{\partial t}\right)\right] y^L_{ib,2} \\ E_{ib}\cdot I_{ib,2}\cdot\left[\frac{\partial^4}{\partial s^4} + \tau_{ibT,3}\cdot k_{ibT,3}\cdot\sin\alpha_{ib,3}\cdot\frac{\partial^3}{\partial s^3}\left(1-\tau_{ibT,3}\cdot\frac{\partial}{\partial t}\right)\right] y^L_{ib,3} \end{array}\right\}$$

$$+ \rho_{ib}\left[\frac{\partial^2}{\partial t^2} + 2\omega^*\frac{\partial}{\partial t} + \dot{\omega}^* + \omega^{**}\right]\underline{y}^L_{ib} + (\dot{\omega}^*+\omega^{**})\begin{bmatrix}\underline{R}^L_{ib}+\{0\}^s\\ 0\end{bmatrix}$$

$$+ [\mu^*_{ib}]^T[\ddot{\theta}\underline{X} + \ddot{\underline{C}} + 2\tilde{\omega}\dot{\underline{C}} + (\dot{\tilde{\omega}}+\tilde{\omega}\tilde{\omega})\underline{C}] = \underline{0} \qquad (12)$$

Cubic and higher powers of $\underline{\tau}_{ibT}$ have been neglected in obtaining the above equation.

PLATE EQUATIONS

The local coordinate system (L) fixed to a circular plate is shown in Figure 4. The origin of L is at the center of the plate and d_{ip} is the angle between the plate-normal and the direction of the sun.

In the derivation of the equations for plates, it is assumed that the thermal twisting moments and in-plane forces on the plates are negligible. Hence, the lateral force equations for the plates are given by [14]:

$$D_{ip}\left[\nabla^4 y_{ip,3} - (1+\mu_{ip})\nabla^2(\kappa_{ipT,1}+\kappa_{ipT,2})\right]dA = -F_{ipI,3} \qquad (13)$$

In deriving Eq. (13), the thermal curvature term is obtained with the following approximations:

$$\kappa_{ipT,1} + \mu_{ip}\,\kappa_{ipT,2} = (1+\mu_{ip})\kappa_{ipT,1}$$

and

$$\kappa_{ipT,2} + \mu_{ip}\,\kappa_{ipT,1} = (1+\mu_{ip})\kappa_{ipT,2}$$

This assumption leads to a very simple form of Eq. (13). It is partially justified by uniformity of the temperature distribution over the plate. The plate thermal curvatures are considered to have a form similar to that of the beams, given in Eq. (9). Thus $\kappa_{ipT,j}$ are given by:

$$\kappa_{ipT,j} = k_{ipT}\cdot\tau_{ipT}[\cos\alpha_{ip}-(\theta_{ip,j}-\tau_{ipT}\cdot\dot{\theta}_{ip,j})\cdot\sin\alpha_{ip}] \qquad (14)$$

for j = 1 and 2, where

$$\theta_{ip,1} = \frac{\partial y_{ip,3}}{\partial n_1} = (\cos\theta \cdot \frac{\partial}{\partial r} - \frac{\sin\theta}{r} \frac{\partial}{\partial \theta}) \, y_{ip,3} \tag{15}$$

and

$$\theta_{ip,2} = \frac{\partial y_{ip,3}}{\partial n_2} = (\sin\theta \frac{\partial}{\partial r} - \frac{\cos\theta}{r} \frac{\partial}{\partial d}) y_{ip,3} \tag{16}$$

are the slopes of the plate surface. Then, using Eqs. (1 and 14), the plate equations of motion can be deduced from Eq. (13) in the following form:

$$\begin{aligned} D_{ip} \cdot \Bigg[& \frac{1}{4}_{a_{ip}} \nabla^4 y_{ip,3} + \frac{1}{3}_{a_{ip}} (1+\mu_{ip}) \cdot k_{ipT} \cdot \sin\alpha_{ip} \cdot \Big[\cos\theta \cdot (\frac{\partial}{\partial r} + \frac{1}{r} \frac{\partial}{\partial \theta}) \\ & + \sin\theta \cdot (\frac{\partial}{\partial r} - \frac{1}{r} \frac{\partial}{\partial \theta}) \Big] \cdot (1 - \tau_{ipT} \frac{\partial}{\partial t}) \nabla^2 y_{ip,3} \Bigg] \\ & + \rho_{ip} \Big[\ddot{y}_{ip,3} - (\omega_1^2 + \omega_2^2) \cdot y_{ip,3} + (\omega_1 \omega_3 - \dot{\omega}_2) a_{ip} \cdot r \cdot \cos\theta \\ & + (\omega_2 \omega_3 + \dot{\omega}_1) a_{ip} \cdot r \cdot \sin\theta - (\omega_1^2 + \omega_2^2) \cdot R_{ip,3} \Big] \\ & + \rho_{ip} \cdot [I_3] \cdot [\ddot{\Theta}\underline{X} + \ddot{\underline{C}} + 2\tilde{\omega}\dot{\underline{C}} + (\dot{\tilde{\omega}} + \tilde{\omega}\tilde{\omega})\underline{C}] = 0 \end{aligned} \tag{17}$$

where

$$[I_3] = \begin{bmatrix} 0 & 0 & 0 \\ 0 & 0 & 0 \\ 0 & 0 & 1 \end{bmatrix}$$

Equation (17) has r and θ as the independent space variables, such that the circular plate boundaries are given by

$$r = 1$$

and

$$\nabla^2 = (\frac{\partial^2}{\partial r^2} + \frac{1}{r} \frac{\partial}{\partial r} + \frac{1}{r^2} \frac{\partial^2}{\partial \theta^2}) \, .$$

SHELL EQUATIONS

The local frame of coordinates for the shells are taken in the radial, tangential, and axial directions. Thus, the body frame to the local frame coordinate transformation matrices ($[\mu^*_{is}]$) for the shells are of the form

$$[\mu^*_{is}]^T = \begin{bmatrix} \cos\theta & \sin\theta & 0 \\ -\sin\theta & \cos\theta & 0 \\ 0 & 0 & 1 \end{bmatrix}$$

Following Vlasov [15] and Kraus [16], the equations for the radial displacements of the shells are given by:

$$dA\cdot\left[\frac{h_{is}^2}{12a_{is}^2}(\nabla^4+2\nabla^2+1)\nabla^4 - \frac{h_{is}^2}{6a_{is}^2}(1-\mu_{is})\left(\frac{\partial^4}{\partial z^4} - \frac{\partial^4}{\partial z^2\partial\theta^2}\right)\nabla^2 + (1-\mu_{is}^2)\frac{\partial^4}{\partial z^4}\right] y^L_{is,1} = -\frac{a_{is}^2(1-\mu_{is}^2)}{E_{is}\cdot h_{is}}\cdot\nabla^4 F^L_{isI,1} - \frac{\alpha^*_{isT}}{12}\cdot(1+\mu_{is})\cdot T_{is} \tag{18}$$

in which the function T_{is} is defined [16] as:

$$T_{is} = h_{is}^2\,\nabla^6\left[\frac{1}{\alpha^*_{isT}}(\kappa^L_{ist,2} + \kappa^L_{ist,3})\right] \tag{19}$$

In Eq. (18) the independent axial coordinate (z) has been scaled down by a factor a_{is}. Thus, the true measure of axial distance is $a_{is}z$. The thermal curvatures of the shells are also considered to have the same form as those of the beams given by Eq. (9). However, $\theta_{ib,j}$ and the beam thermal constants are to be replaced by $\theta_{is,j}$ and the shell thermal constants, respectively. The shell displacement gradients ($\theta_{is,j}$) are given by:

$$\theta_{is,2} = \frac{1}{a_{is}}\frac{\partial}{\partial\theta}\,y^L_{is,1}$$

and

$$\theta_{is,3} = \frac{1}{a_{is}}\frac{\partial}{\partial z}\,y^L_{is,1} \tag{20}$$

The angle of incidence of the radiant heat wave-front varies over the surface of the spinning shell. Thus, the form of $\kappa^L_{isT,j}$ is finally given by:

$$\kappa^L_{isT,j} = k_{isT,j}\cdot\tau_{isT,j}\cdot\sin\alpha_{is,j}\cdot[\cos(\omega_3 t+\theta) - (\theta_{is,j} - \tau_{isT,j}\cdot\dot{\theta}_{is,j}+\ldots)\cdot\sin(\omega_3 t+\theta)] \tag{21}$$

Following Eq. (6), $\underline{F}^L_{isI}$ is given by:

$$\underline{F}^{L}_{isI} = -\rho_{is} \cdot dA\{[\mu^{*}_{is}][\ddot{\theta}\underline{X} + \ddot{\underline{C}} + 2\tilde{\omega}\dot{\underline{C}} + (\dot{\tilde{\omega}}+\tilde{\omega}\tilde{\omega})(\underline{C}+\underline{R}_{is}) + \ddot{\underline{y}}^{L}_{is}$$

$$+ 2\omega^{*}\cdot\ddot{\underline{y}}^{L}_{is} + (\dot{\omega}^{*}+\omega^{**})\underline{y}^{L}_{is}]\} \qquad (22)$$

in which it is defined that

$$\omega^{*} = [\mu^{*}_{is}]^{T}\,\tilde{\omega}\,[\mu^{*}_{is}]$$

and

$$\omega^{**} = [\mu^{*}_{is}]^{T}\,\tilde{\omega}\,\tilde{\omega}\,[\mu^{*}_{is}]. \qquad (23)$$

It is now assumed that the axial and tangential deformations of the shells are negligible. Hence, using Eqs. (19-23), Eq. (18) is reduced to the following form:

$$\left\{ \frac{h^{2}_{is}}{12a^{2}_{is}}(\nabla^{4}+2\nabla^{2}+1)\nabla^{4} - \frac{h^{2}_{is}}{6a^{2}_{is}}(1-\mu_{is})\left(\frac{\partial^{4}}{\partial z^{4}} - \frac{\partial^{4}}{\partial z^{2}\partial\theta^{2}}\right)\nabla^{2} \right.$$

$$+ (1-\mu^{2}_{is})\frac{\partial^{4}}{\partial z^{4}} + \frac{a^{2}_{is}(1-\mu^{2}_{is})}{E_{is}\cdot h_{is}}\rho_{is}\left\{\nabla^{4}\left[\frac{\partial^{2}}{\partial t^{2}} - [\omega^{2}_{3} + \frac{1}{2}(\omega^{2}_{1}+\,^{2}_{2})]\nabla^{4}\right.\right.$$

$$+ \frac{1}{2}[(\omega^{2}_{1}-\omega^{2}_{2})\cos 2\theta + 2\omega_{1}\omega_{2}\sin 2\theta][\nabla^{4}-8\nabla^{2}-16(\frac{\partial^{2}}{\partial\theta^{2}}+1)]$$

$$- 4[(\omega^{2}_{1}-\omega^{2}_{2})\sin 2\theta - 2\omega_{1}\omega_{2}\cos 2\theta][\frac{\partial}{\partial\theta}\nabla^{2} - 4\frac{\partial}{\partial\theta}]$$

$$+ \frac{1}{12}k_{isT}(1+\mu_{is})h^{2}_{is}\cdot\sin\alpha_{is,3}\cdot[\cos(\omega_{3}t+\theta)$$

$$\left.\left. + \frac{1}{2a_{is}}\sin(\omega_{3}t+\theta)(1-\tau_{isT}\cdot\frac{\partial}{\partial t})(\frac{\partial}{\partial z}+\frac{\partial}{\partial\theta})\nabla^{6}\right]\right\} y^{L}_{is,1}$$

$$+ \frac{a^{2}_{is}\cdot(1-\mu^{2}_{is})\cdot\rho_{is}}{E_{is}\cdot h_{is}}\left\{8a_{is}[(\omega^{2}_{2}-\omega^{2}_{1})\cos 2\theta + 2\omega_{1}\omega_{2}\sin 2\theta]\right.$$

$$\left. + [I_{1}][\mu^{*}_{is}][\ddot{\theta}\underline{X} + \ddot{\underline{C}} + 2\tilde{\omega}\dot{\underline{C}} + (\dot{\tilde{\omega}}+\tilde{\omega}\tilde{\omega})\underline{C}]\right\} = 0 \qquad (24)$$

in which

$$[I_{1}] = \begin{bmatrix} 1 & 0 & 0 \\ 0 & 0 & 0 \\ 0 & 0 & 0 \end{bmatrix} \qquad (24a)$$

In this section, ∇^2 is defined by:

$$\nabla^2 = \frac{\partial^2}{\partial z^2} + \frac{\partial^2}{\partial \theta^2} \quad .$$

GALERKIN'S METHOD

The governing Eqs. (12, 17 and 24) for the beams, plates, and shells are reduced to ordinary second order differential equations by using Galerkin's method [17]. It is applied by taking the variables y^L_{ib} , $y_{ip,3}$ and $y^L_{is,1}$ in the following form:

$$y^L_{ib} = \Psi_{ib}(s) \cdot q_{ib}(t)$$

$$y_{ip,3} = \Psi_{ip}(r,\theta) \cdot q_{ip}(t)$$

$$y^L_{is,1} = \Psi_{is}(\theta,z) q_{is}(t) \qquad (25)$$

Each of the variables (q) are unknown time-dependent vector functions. The space dependent functions (Ψ) are assumed to correspond to the free vibration modes of the beams, plates, and shells. The beam functions, ($\Psi_{ib}(s)$) form a (3 x n) functional matrix for each beam, when $q_{ib}(t)$ is a (n x 1) column vector for each beam. For each plate and shell, Ψ_{ip} and Ψ_{is} are (1 x m) and (1 x ℓ) row vectors, when $q_{ip}(t)$ and $q_{is}(t)$ are taken as (m x 1) and (ℓ x 1) column vectors respectively. The functions Ψ must be chosen to simulate the load systems on the beam, plate, and shell elements, and to satisfy, at least, the geometric boundary conditions. The convergence of the solutions depends greatly on the choice of these functions.

In the following sections, the three sets of functions Ψ, for beams, plates, and shells, are given.

BEAM FUNCTIONS

The beam functions, selected for the assumed configuration of the satellite (Figure 1) are modelled for rigid translations, rigid rotations, and free flexural vibrations. Only cantilever modes are assumed for the beams, but the functional matrix can easily be augmented to include other modal shapes.

The vector, q_{ib}, for each beam, is taken as:

$$q_{ib} = \{q_{ib,j}\} \quad \text{for } j = 1\text{-}7. \qquad (26)$$

These seven elements accommodate three translations and two each of rigid rotations and transverse flexural vibrations. The shape function matrix

is assumed to be:

$$[\Psi_{ib}] = \begin{bmatrix} 1 & 0 & 0 & 0 & 0 & 0 & 0 \\ 0 & [\exp(p_{ib}\cdot s)-1] & s & 1 & 0 & 0 & 0 \\ 0 & 0 & 0 & 0 & [\exp(p_{ib}\cdot s)-1] & s & 1 \end{bmatrix} \quad (27)$$

By varying the beam exponent (p_{ib}), which is a function of the natural frequency, the vibration modes can be modified to have point masses and rigid bodies at the ends of the beams.

In Eq. (27) the exponent p_{ib} satisfies the following equation [18]:

$$\frac{1}{\rho_{ib}} [\rho_{ib}^2 - m_{ib}^2 r_{ib}^2 p_{ib}^4][1-\cos(p_{ib}\cdot \ell_{ib})\cdot\cosh(p_{ib}\cdot \ell_{ib})]$$

$$- m_{ib} p_{ib}\cdot(1+r_{ib}^2 p_{ib}^2)\cdot\cos(p_{ib}\cdot \ell_{ib})\cdot\cosh(p_{ib}\cdot \ell_{ib})$$

$$+ m_{ib} p_{ib}\cdot(1-r_{ib}^2 p_{ib}^2)\cdot\sin(p_{ib}\cdot \ell_{ib})\cdot\cosh(p_{ib}\cdot \ell_{ib}) = 0 \quad (28)$$

In the above, m_{ib} is the mass at the end of the beam and r_{ib} is the radius of gyration of the end-mass about the junction point. For point masses, r_{ib} is equal to zero.

PLATE FUNCTIONS

The choice of shape functions (Ψ_{ip}) for the circular plates is governed by the assumption that the flexural displacements of the plate are zero at the boundary r=1. The functions considered allow rigid translation of the plates and have flexural modes up to the second harmonic. Thus, $y_{ip,3}(r,\theta)$ for each plate is taken to be:

$$y_{ip,3} = q_{ip,1}(t) + q_{ip,2}(t)\, J_0(\lambda_0 r)$$

$$+ q_{ip,3}(t)\cdot(r-1)\cdot r^2 + q_{ip,4}(t)\cdot(r-1)\cdot r^3$$

$$+ [q_{ip,5}(t)\cdot J_1(\lambda_1 r) + q_{ip,6}(t)\cdot(r-1)\cdot r$$

$$+ q_{ip,7}(t)\cdot(r-1)\cdot r^2]\cdot\cos\theta + [q_{ip,8}(t)\cdot J_1(\lambda_1 r)$$

$$+ q_{ip,9}(t)\cdot(r-1)\cdot r + q_{ip,10}(t)\cdot(r-1)\cdot r^2]\cdot\sin\theta$$

$$+ [q_{ip,11}(t)\cdot J_2(\lambda_2 r) + q_{ip,12}(t)\cdot(r-1)\cdot r^2 + q_{ip,13}(t)\cdot(r-1)\cdot r^3]\cos 2\theta$$

$$+ [q_{ip,14}(t)\cdot J_2(\lambda_2 r) + q_{ip,15}(t)\cdot(r-1)\cdot r^2 + q_{ip,16}(t)\cdot(r-1)\cdot r^3]\sin 2\theta$$

$$+ \sum_{j=1}^{n_i} q_{ip,16+j}(t)\cdot\psi^*_{ip,j}(r,\theta) \quad (29)$$

In the above equation, J_0, J_1, and J_2 are Bessel functions of the first kind. The constants λ_0, λ_1, and λ_2 are the first root of

$$J_0(\lambda) = 0$$

and the second roots of:

$$J_1(\lambda) = 0$$

and

$$J_2(\lambda) = 0,$$

respectively. It is assumed that there are n_i point loads on the ith plate. The functions $\psi^*_{ip,j}(r,\theta)$ are used to model the plate deflections due to the spring-mass-damper systems, rigid bodies, and any other sub-systems attached to the plates. The points at which an external system is attached to a plate are considered those at which a concentrated force is applied on the plate. At least one of the functions $\psi^*_{ip,j}(r,\theta)$ must correspond to one load point. Thus, each spring-mass-damper system generally requires one such shape function. If a rigid body is connected to the plate at four points, then four shape functions have to be taken for that rigid body.

The functions $\psi^*_{ip,j}$ are taken to be the dynamic deflection functions as warranted by the Rayleigh-Ritz and Galerkin's methods. Thus for a centrally connected load,

$$\psi^*_{ip,j}(r,\theta) = J_0(\lambda_0 r). \tag{30}$$

There are no closed form solutions for the deflections of a plate. This is due to concentrated forces acting at an arbitrary point on the plate for specified boundary conditions. For this reason, the shape function to model a point load, acting at an arbitrary point (r_0,θ_0) on the plate, is taken as:

$$\psi^*_{ip,j}(r,\theta;r_0,\theta_0) = J_0(\lambda_0 r^*) \tag{31}$$

where

$$r^* = \left\{ \frac{r^2 - 2rr_0\cos(\theta-\theta_0)+r_0^2}{1-2rr_0\cos(\theta-\theta_0)+r^2r_0^2} \right\} 1/2 \tag{31a}$$

The choice of this form is explained in Appendix A.

SHELL FUNCTIONS

The flexural displacements of the shells are assumed to be zero at the boundaries $z = -\zeta'_{is}$ and $z = \zeta''_{is}$ of the shells (Figure 5). For the

configuration shown in Figure 1, the load system on the shells consists of: a) the moments applied at the plate-shell junctions, and b) the concentrated forces and moments at the beam-shell junctions. The shell shape functions must be compatible with these load systems and boundary conditions.

Concentrated forces and moments at a point (z_0,θ_0) can be modeled by Dirac's delta functions, $\delta(z-z_0)\cdot\delta(\theta-\theta_0)$. In view of the Laplacian operator form defined in Eq. (24a) and used in the equations for the shells, the delta functions are given [19] by:

$$\delta(z-z_0) = \frac{1}{\ell_{is}} + \sum_{n=1}^{\infty} \frac{2}{\ell_{is}} \cdot \cos \frac{n\pi z}{\ell_{is}} \cdot \cos \frac{n\pi z_0}{\ell_{is}}$$

$$= \sum_{n=1}^{\infty} \frac{2}{\ell_{is}} \sin \frac{n\pi z}{\ell_{is}} \cdot \sin \frac{n\pi z_0}{\ell_{is}} \qquad (32)$$

The function $\delta(\theta-\theta_0)$ is expressed similarly. Thus, from Eqs. (5.17b) and (5.17c) of Kraus [16] and from the requirements just mentioned, the shape functions of the shell for the four symmetrically placed beams are taken as:

$$y^L_{is,1} = q_{is,1}(t) + (z+\zeta'_{is})(z-\zeta''_{is})\,[q_{is,2}(t)\cdot\exp(p_2 z)$$

$$+ q_{is,3}(t)\cdot\exp(p_3 z)] + q_{is,4}(t)\cdot\sin z^*\cdot\cos\theta$$

$$+ q_{is,5}(t)\cdot\sin 2z^*\cdot\cos\theta + q_{is,6}(t)\cdot\sin z^*\cdot\sin\theta$$

$$+ q_{is,7}(t)\cdot\sin 2z^*\cdot\sin\theta + q_{is,8}(t)\cdot\sin z^*\cdot\cos 2\theta$$

$$+ q_{is,9}(t)\cdot\sin 2z^*\cdot\cos 2\theta + q_{is,10}(t)\cdot\sin z^*\cdot\sin 2\theta$$

$$+ q_{is,11}(t)\cdot\sin 2z^*\cdot\sin 2\theta \qquad (33)$$

In Eq. (33),

$$z^* = \frac{\pi(z+\zeta'_{is})}{\ell_{is}} \qquad (33a)$$

The shape functions, shown in Eq. (33) which are associated with $q_{is,2}$ and $q_{is,3}$ appear due to the moment loadings of the shells. There should be at least two such functions for each shell to account for the moments at the two edges of the shells. The indices p_2 and p_3 are taken from Ref. [16] as equal to $\pm(a_{is}\cdot h_{is})^{1/2}\cdot(3-3\mu_{is}^2)^{1/4}$. The displacement series, due to the concentrated loads, is taken up to the second harmonic only. More terms can be included to increase the modeling accuracy. This series can also be easily modified to simulate the loading of any other configuration of attached sub-systems.

ELIMINATION OF SPACE VARIABLES

Having chosen the shape functions, the space dependent variables are eliminated in the following manner:

Let the (3r x 1) vector ($q_{id}(t)$) model the displacements of all other discrete mass elements of the satellite. Let the vector $\underline{q}^*$ be defined a:

$$\underline{q}^* = [\, q_{id}, q_{jb}, q_{kp}, q_{ms} \,]^T \tag{34}$$

where i = 1,2,3, ... r. The ranges of j, k, and m are the numbers of beams, plates, and shells respectively.

The displacement vector ($\underline{C}$) of the center of the whole satellite's mass can be expressed as:

$$\underline{C} = -\frac{1}{M}\left\{ \sum_i m_i \, q_{id} + \sum_j \rho_{jb} [\mu^*_{jb}] \int_0^{\ell_{jb}} [\Psi_{jb}] q_{jb} \, ds \right.$$

$$+ \sum_k \rho_{kp} \int_0^1 \int_0^{2\pi} [\Psi_{kp}] q_{kp} \cdot \begin{Bmatrix} 0 \\ 0 \\ 1 \end{Bmatrix} dA$$

$$\left. + \sum_m \rho_{ms} \int_0^{\ell_{ms}} \int_0^{2\pi} [\Psi_{ms}] \cdot q_{ms} \cdot \begin{Bmatrix} \cos\theta \\ \sin\theta \\ 0 \end{Bmatrix} dA \right\}$$

This equation is equivalent to the linear equation

$$\underline{C} = [G]\underline{q}^* \tag{35}$$

where [G] is a (3 x n) matrix of constants and $\underline{q}^*$ is a (n x 1) column vector.

The acceleration vector, $\ddot{\underline{X}}$ of the whole satellite is expressed as

$$\ddot{\underline{X}} = \frac{1}{M} \underline{F}_s(t) \tag{36}$$

where $\underline{F}_s(t)$ is the external force. Frequently a satellite consists of several composite bodies. For example, there are two composite bodies in a dual-spin satellite. In that case, each composite body can be analyzed in a similar manner. The acceleration vector ($\ddot{\underline{X}}$) of each composite body of mass M and modeled by $\underline{q}^*$, is then expressed as:

$$\ddot{\underline{X}} = \frac{1}{M} [\underline{F}_s + \underline{F}_R] \tag{37}$$

In this equation, $\underline{F}_s$ is the external force on the composite body being considered and $\underline{F}_R$ is the reaction force exerted on that composite body by the remaining parts of the satellite. For a dual-spin geosynchronous satellite, $\underline{F}_s = 0$ and $\underline{F}_R$ can be expressed as:

$$\underline{F}_R = G_1 q^* + G_2 \dot{\underline{q}}^* + G_3 \underline{\theta}^* + G_4 \dot{\underline{\theta}}^* \tag{38}$$

where $\underline{\theta}^*$ is the relative angular displacement between the two composite bodies.

Following the discrete mass analyses of Likins and his associates [7,8,9 and 10], the equations of motion of the discrete mass elements of the satellite can be expressed as:

$$[A^*_{1id}]\ddot{\underline{q}}_{id} + [A^*_{2id}(\underline{\omega},\dot{\underline{\omega}},t)]\dot{\underline{q}}_{id} + [A^*_{3id}(\underline{\omega},\dot{\underline{\omega}},t)]\underline{q}_{id}$$
$$+ [\Lambda_{1id}]\ddot{\underline{q}}^* + [\Lambda_{2id}(\underline{\omega},\dot{\underline{\omega}},t)]\dot{\underline{q}}^* + [\Lambda_{3id}(\underline{\omega},\dot{\underline{\omega}},t)]\underline{q}^*$$
$$= \{A^*_{4id}(\underline{\omega},\dot{\underline{\omega}},\underline{F}_s,\underline{\theta}^*,\dot{\underline{\theta}}^*,t)\} \tag{39}$$

by substituting Eq. (35) and Eqs. (36) or (37) into Eq. (1) and by introducing appropriate damping and stiffness matrices.

Expressions for $\underline{y}^L_{ib}$ from Eqs. (25), (26) and (27) and the expressions for $\underline{C}$ and $\Theta\ddot{\underline{X}}$ from Eqs. (35), and (36), or (37) are now substituted in Eq. (12). The resulting equations then become free of the partial differential operators. These equations are successively multiplied by 1, $\exp(p_{ib}\cdot s)$ and s and integrated with respect to s between $(0,\ell_{is})$. Thus, the purely time-dependent equations for the beams are obtained. These equations then have the form:

$$[A^*_{1ib}]\ddot{\underline{q}}_{ib} + [A^*_{2ib}(\underline{\omega},\dot{\underline{\omega}},t)]\dot{\underline{q}}_{ib} + [A^*_{3ib}(\underline{\omega},\dot{\underline{\omega}},t)]\underline{q}_{ib}$$
$$+ [\Lambda_{1ib}]\ddot{\underline{q}}^* + [\Lambda_{2ib}(\underline{\omega},\dot{\underline{\omega}},t)]\dot{\underline{q}}^* + [\Lambda_{3ib}(\underline{\omega},\dot{\underline{\omega}},t)]\underline{q}^*$$
$$= \{A^*_{4ib}(\underline{\omega},\dot{\underline{\omega}},\underline{F}_s,\underline{\theta}^*,\dot{\underline{\theta}}^*,t)\} \tag{40}$$

Equations (17) and (24) are similarly rendered free of the partial differential operators. Purely time-dependent equations for the plates and shells are obtained by integrating these equations over the surfaces of the plates and shells. The shape functions Ψ_{ip} and Ψ_{is} are used as the weighting functions for the integrals. This procedure leads to two more sets of equations of a form similar to that of Eq. (40), except that the subscripts b are replaced by p or s. All these purely time-dependent equations, together with their detailed derivations and solutions, will be reported in Ref. [20].

ASSEMBLED EQUATIONS

When the Eqs. (39), (40), and the similar plate and shell equations are combined, the resulting equations take the form:

$$[A_1^*]\ddot{q}^* + [A_2^*(\omega,\dot{\omega},t)]\dot{q}^* + [A_3^*(\omega,\dot{\omega},t)]q^*$$

$$= \{A_4^*(\omega,\dot{\omega},F_s,\theta^*,\dot{\theta}^*,t)\} \qquad (41)$$

The generalized mass matrix, $[A_1^*]$ is an (n x n) matrix of constants when q^* is an (n x 1) column vector. These equations are non-linear, because the angular velocity vector ω is also a dependent variable. The system response can be obtained when the three angular momentum equations of the whole satellite is adjoined to the system of equations presented in Eq. (41). Usually n is a very large number. This is the reason that previous investigators [6,7,8,9,10,11] of such large systems usually linearized their equations to obtain the response characteristics. In a following paper [21], a general method of reducing the order of q^* and finally eliminating q^*, to obtain equations in ω only, will be discussed.

ERROR BOUNDS OF THE SOLUTIONS

The analysis presented here is based primarily on the assumed solutions of the partial differential equations for the beams, plates, and shells. These solutions are obviously not exact. The Galerkin's method only minimizes the error corresponding to the assumed form of the solution. A scheme to estimate this error, based on the assumed solution, is now explained.

For beams, plates, and shells, the solution 'u' is sought for an equation of the form

$$Lu = \mu u + f \qquad (42)$$

where L is a linear differential operator, μ and f are functions independent of u. Let v be the error in the assumed solution, given by $(u+v)$. Now, let $(u+v)$ actually satisfy an equation

$$L(u+v) = \mu(u+v) + f - L_1(u+v) \qquad (43)$$

where L_1 also is a linear operator. Then from Eqs. (42) and (43)

$$Lv = \mu v - L_1(u+v)$$

or

$$(\mu - L)v = L_1(u+v)$$

or

$$v = (I-\mu^{-1}L)^{-1}\cdot\mu^{-1}\cdot L_1(u+v)$$

It is assumed that $\mu^{-1}L$ is a contraction operator. Then

$$v \approx (I+\mu^{-1}L)\mu^{-1}L_1(u+v)$$

or

$$\|\underline{v}\| = \| (I+\mu^{-1}L)\mu^{-1}L_1(\underline{u}+\underline{v}) \| \qquad (44)$$

In Eq. (44), $L_1(\underline{u}+\underline{v})$ is the quantity obtained by substituting the assumed solution in the governing differential equation. Also, L and μ^{-1} are known operators. Then the maximum values of the error $\underline{v}$ are obtained by taking suitable norms in Eq. (44) over the complete time and spatial domain of the operators L and μ. An easily calculated norm is in the space L_∞ and this will be used. Hence, the following operations are required:

a) Carry out the complete analysis and obtain the coefficients of the Galerkin functions,

b) evaluate the norms in Eq. (44),

c) if $\|\underline{v}\|$ is too high, increase the number of Galerkin's functions and repeat the procedure,

d) if $\|\underline{v}\|$ is small, then the assumed solution is satisfactory.

CONCLUSIONS

Equations of motion for thermally induced flutter of beam, plate, and shell elements of a satellite were obtained. The use of Galerkin's method to reduce complex partial differential equations of these elements to ordinary differential equations is found to have many advantages. Numerical or perturbation methods can be easily applied on the reduced equations of finite number of degrees of freedom. A useful shape function has been presented for modeling point loads on the plates. The equations of all the satellite elements are coupled. Singular perturbation equations and a perturbation scheme will be presented in Ref. [20].

ACKNOWLEDGEMENTS

This work was supported in part by the National Aeronautics and Space Administration under Contract No. NAS5-21798 through the Space Science and Engineering Center, University of Wisconsin, Madison, Wisconsin.

REFERENCES

1. Das, A., and Huang, T. C., "Pointing Error Analysis of Geosynchronous Satellites, Parts I, II and III," Annual Scientific Report on NAS5-11542, Space Science and Engineering Centre, Madison, Wisconsin, December 1972, pp. 99-228.

2. Etkin, B., and Hughes, P. C., "Exploration of the Anomalous Spin Behaviour of Satellites with Long Flexible Antennae," J. of Spacecraft and Rockets, Vol. 4, No. 9, September 1967, pp. 1139-1145.

3. Yu, Y. Y., "Thermally Induced Vibration and Flutter of a Flexible Boom," J. of Spacecraft and Rockets, Vol. 6, No. 8, August 1969, pp. 902-910.

4. Das, A., "Comments on 'Thermally Induced Vibration and Flutter of a Flexible Boom'," J. of Spacecraft and Rockets, Vol. 10, No. 3, April 1973.

5. Velman, J. R., "Attitude Dynamics of Dual-Spin Satellites," Space Systems Division Research Report, Hughes Aircraft Co., SSD60419R, September 1966.

6. Likins, P. W., "Attitude Stability of Dual-Spin Systems," Space Systems Research Report, Hughes Aircraft Co., SSD60377R, September 1966.

7. Likins, P. W., and Mingori, D. L., "Liapunov Stability Analysis of Freely Spinning Systems," Proc. 18th International Astronautical Congress, Belgrade, September 1967, pp. 89-102.

8. Likins, P. W., and Wirsching, P. H., "Use of Synthetic Modes in Hybrid Coordinate Dynamic Analysis," AIAA Jnl., Vol. 6, October 1968, pp. 1867-1872.

9. Likins, P. W., and Gale, A. H., "A Study of the Dynamics of Spacecraft with Flexible Appendages with Special Attention to a Gyrostat with a Flexible Despun Section," Aerospace Technology Research Report, Hughes Aircraft Co., Space Systems Division, SSD90003R, 1969.

10. Likins, P. W., and Gale, A. H., "The Analysis of Interactions Between Attitude Control Systems and Flexible Appendages," Paper IAF AD29, 19th International Aeronautical Congress, New York, October 1968.

11. Likins, P. W., and Fleischer, G. E., "Results of Flexible Spacecraft Attitude Control Studies Utilizing Hybrid Coordinates," J. of Spacecraft and Rockets, Vol. 8, No. 3, March 1971, pp. 264-272.

12. Grote, P. B., McMunn, J. C., and Gluck, R., "Equations of Motion of Flexible Spacecraft," J. of Spacecraft and Rockets, Vol. 8, No. 6, June 1971, pp. 561-567.

13. Meirovitch, L., and Calico, R. A., "A Comparative Study of Stability Methods for Flexible Satellites," AIAA Journal, Vol. 11, No. 1, January 1973, pp. 91-98.

14. Timoshenko, S. P., and Woinowsky-Krieger, S., Theory of Plates and Shells, McGraw-Hill, 1959, pp. 49-50.

15. Vlasov, N. Z., General Theory of Shells and its Application in Engineering, National Technical Information Service Translation No. N64-19883, Eq. (13.2), Part 2.

16. Kraus, H., Thin Elastic Shells, Wiley, New York, 1967, pp. 202-203, pp. 131-133.

17. Fung, Y. C., Foundations of Solid Mechanics, Prentice-Hall, 1965, pp. 338-339.

18. Meirovivitch, L., Analytical Methods in Vibration, MacMillan Co., 1967, pp. 161-164.

19. Stakgold, I., Boundary Value Problems of Mathematical Physics, Vol. I, MacMillan Co., 1967, pp. 263-267.

20. Das, A., and Huang, T. C., "Pointing Error Analysis of Geosynchronous Satellites, Parts IV, V and VI," Annual Scientific Report on NAS5-11542, Space Science and Engineering Centre, Madison, Wisconsin, December 1973.

21. Huang, T. C., and Das, A., "Singular Perturbation Equations for Flexible Satellites," 24th International Astronautical Congress, Baku, U.S.S.R., October 1973.

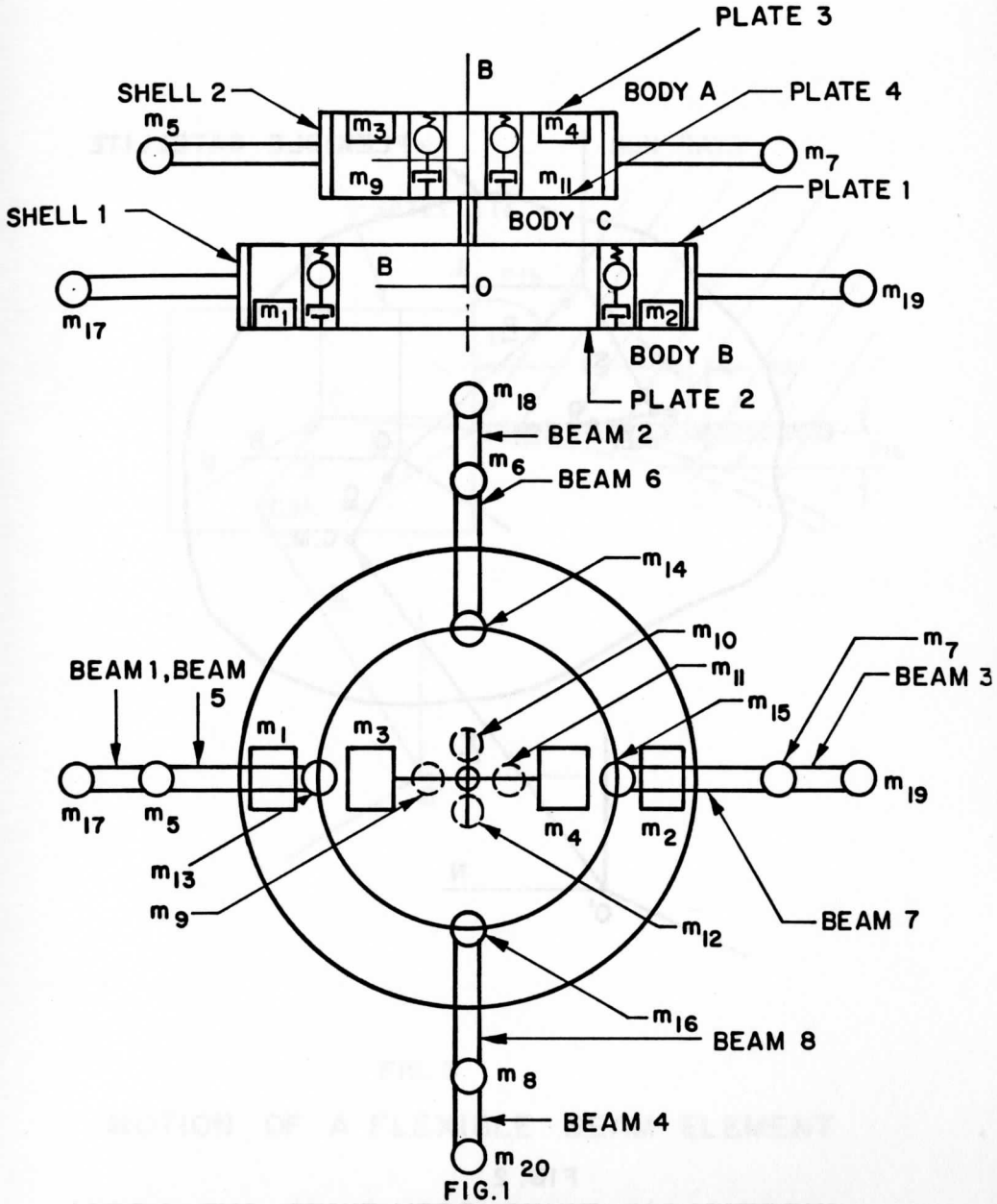

FIG.1

ASSUMED CONFIGURATION OF THE FLEXIBLE SATELLITE

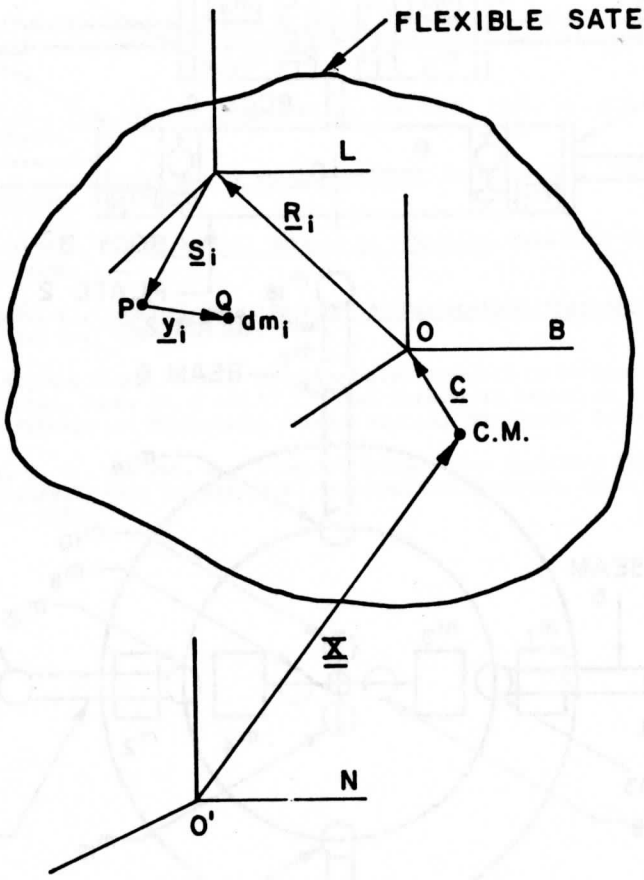

FIG. 2
INERTIALLY FIXED, BODY FIXED AND LOCAL SYSTEMS OF COORDINATES.

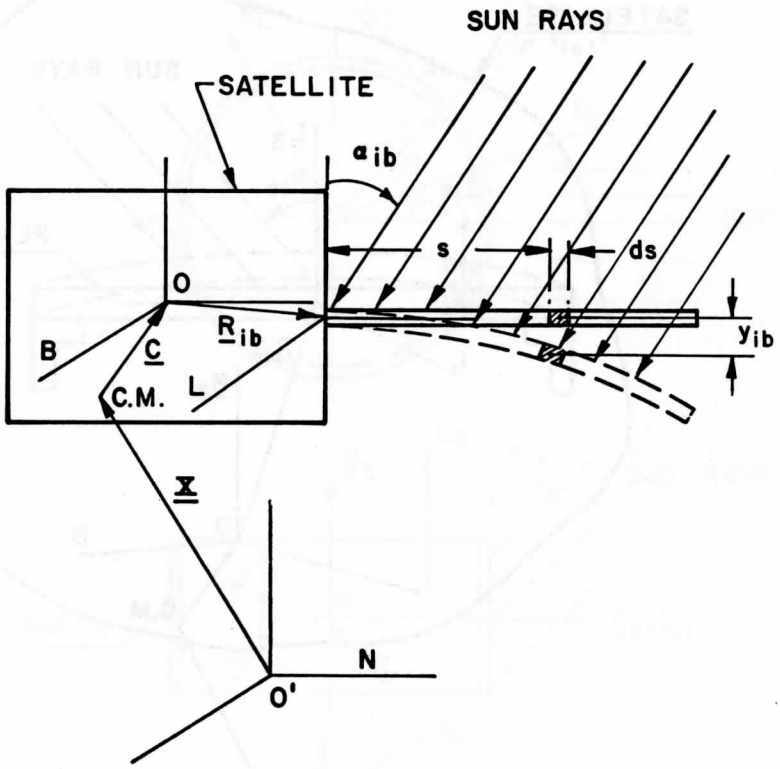

FIG. 3

MOTION OF A FLEXIBLE BEAM ELEMENT

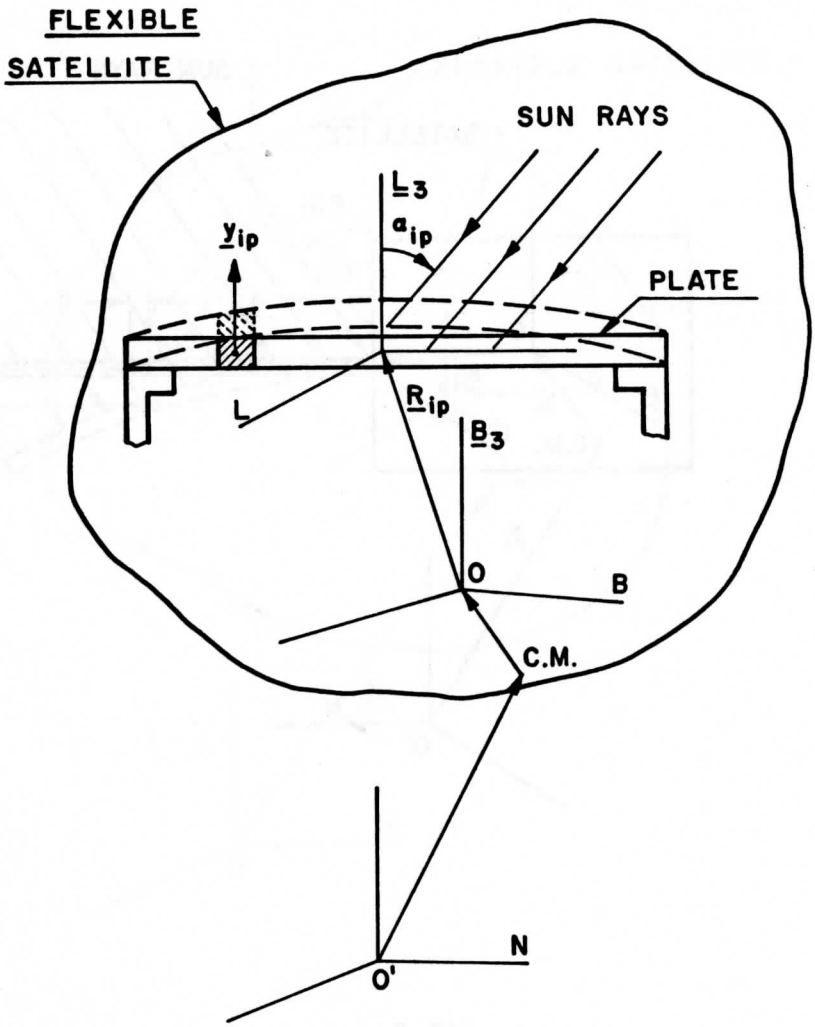

FIG. 4

MOTION OF A FLEXIBLE PLATE ELEMENT

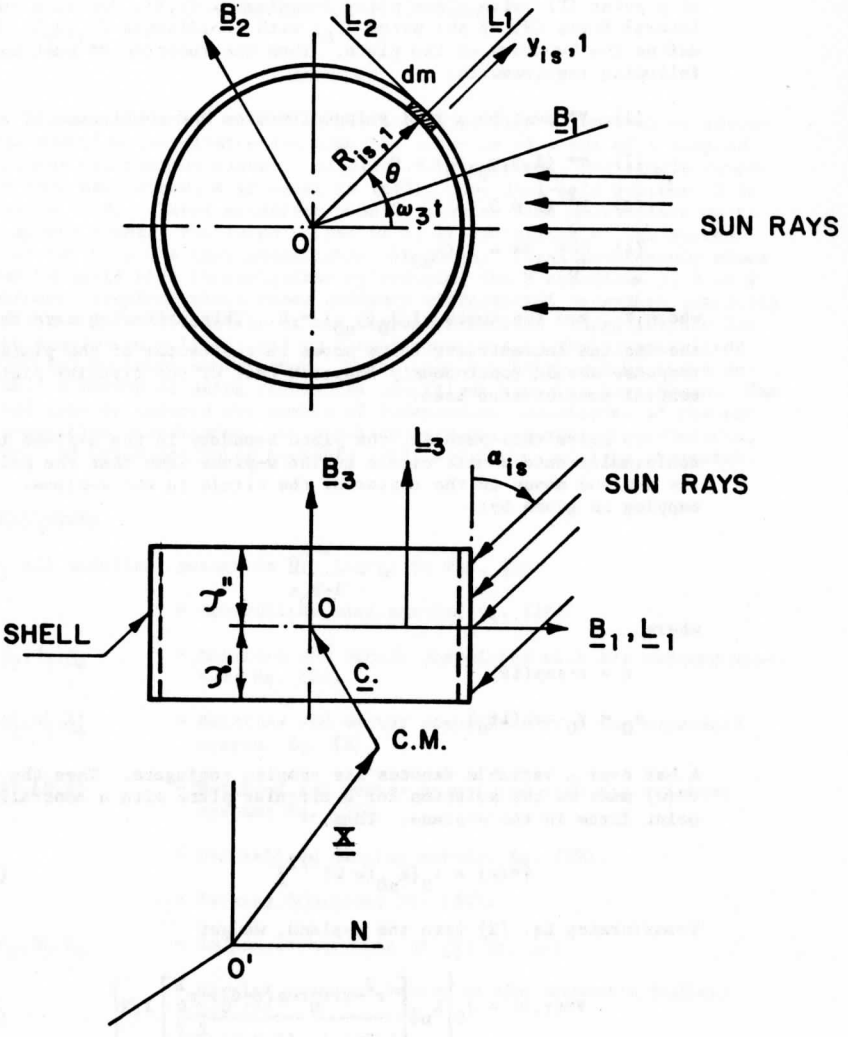

FIG. 5

MOTION OF A FLEXIBLE SHELL ELEMENT

APPENDIX A

Let $\Psi^*(r,\theta;r_0,\theta_0)$ be the dynamic displacement of a circular plate at a point (P) with plane polar coordinates (r,θ), due to a concentrated lateral force (F) at the point (P_0) with coordinates (r_0,θ_0). Let $r = 1$ define the boundary of the plate. Then the function Ψ^* must satisfy the following requirements:

(1) Ψ^* must be a real valued function and continuous at all points.

(2) $\Psi^*(1,\theta;r_0,\theta_0) = 0$

(3) $\nabla^2 \Psi^* \neq 0$

(4) $\lim_{r_0 \to 0} \Psi^* = J_0(k_{n0} r)$

where k_{n0} are the roots of $J_0(k_{n0}) = 0$. This criterion says that, as the applied concentrated force moves to the center of the plate, the response should continuously approach that of the circular plate with central concentrated load.

To solve this problem, the plate boundary in the z-plane is mapped conformally onto a unit circle in the w-plane such that the point P_0 in the z-plane moves to the center of the circle in the w-plane. This mapping is given by:

$$w = \frac{z - z_0}{1 - \bar{z}_0 z} \tag{A1}$$

where

$$z = r \cdot \exp(i\theta)$$

$$z_0 = r_0 \cdot \exp(i\theta_0)$$

A bar over a variable denotes its complex conjugate. Then the function $\Psi^*(w)$ must be the solution for a circular plate with a centrally acting point force in the w-plane. Thus,

$$\Psi^*(w) = J_0[k_{n0}(w\,\bar{w})^{1/2}] \tag{A2}$$

Transforming Eq. (2) into the z-plane, we get

$$\Psi^*(r,\theta) = J_0\left\{k_{n0}\left[\frac{r^2 - 2rr_0\cos(\theta-\theta_0) + r_0^2}{1 - 2rr_0\cos(\theta-\theta_0) + r^2 r_0^2}\right]^{1/2}\right\} \tag{A3}$$

This function $\Psi^*(r,\theta)$ has previously been used in Eqs. (31) and (31a).

SINGULAR PERTURBATION EQUATIONS FOR FLEXIBLE SATELLITES

Aniruddha Das and T. C. Huang

ABSTRACT

The dynamic model of a flexible satellite with n generalized structural position coordinates requires the solution of a set of N coupled nonlinear ordinary or partial differential equations. For single composite body satellites, N is equal to (n+3). For dual-spin systems, N is equal to (n+9). These equations usually involve time derivatives up to the second order. For large values of n, linearization of the system has so far been the only practicable operation. The present study shows a way to avoid this linearization by reducing the N equations to 3 or 9 nonlinear, coupled, first order ordinary differential equations involving only the angular velocities of the composite bodies. The solutions for these angular velocities lead to linear equations in the n generalized structural position coordinates. These then can be solved by known methods. A method of using continuity conditions has also been shown. The method greatly reduced the number of independent coordinates of the set of n-position coordinates. In a following paper, asymptotic solutions, as well as inner and outer boundary layer solutions, will be presented.

NOMENCLATURE

All undefined notations are listed in Ref. [2].

A	= Generalized mass matrix; Eq. (39).
$A_1, A_2, A_3, \underline{A}_4$	= Matrices and vector associated with the reduced system; Eq. (23).
$A_1', A_2', A_3', \underline{A}_4'$	= Matrices and vector associated with the separated system; Eq. (8).
$A_1^*, A_2^*, A_3^*, \underline{A}_4^*$	= Matrices and vector associated with the original system; Eq. (5).
B	= Generalized damping matrix; Eq. (39).
$\underline{d}$	= Forcing function; Eq. (39).
G_5, G_6, G_7, G_8	= Component matrices of $\underline{T}_R^*$; Eq. (1).
$\underline{H}$	= Angular momentum vector of the composite bodies; Eq. (2).
$\underline{h}$	= Component of $\underline{v}$; Eq. (45).
$\underline{h}^*$	= Angular momentum vector of moving parts or reaction wheels; Eq. (2).

I = Moment of inertia matrix of the composite bodies; Eq. (2).

k = Number of stiff and linear structural coordinates; also number of plates.

$L, L_{db}, L_{bs}, L_{sp}, L_{dp}$ = Continuity matrices; Eqs. (21), (10), (14), (19), (20).

ℓ = Number of nonlinear structural coordinates; also lengths of beams and shells.

$M_1, M_2, \underline{M}_3, M_4, \underline{M}_5$ = Matrices and vectors obtained in the elimination process; Eqs. (27), (30).

m = Number of soft and linear structural coordinates; number of shells; discrete masses.

N = Total number of degrees of freedom of a flexible satellite.

n = Total number of degrees of freedom of the satellite structure.

$P_1, P_2, P_3, \underline{P}_4$ = Matrices and vector associated with the final generalized Euler's equations; Eq. (22).

$P'_1, P'_2, P'_3, \underline{P}'_4$ = Matrices and vector associated with the augmented Euler's equations after separation of the non-linearities; Eq. (7).

$P^*_1, P^*_2, P^*_3, \underline{P}^*_4$ = Matrices and vector associated with the original Euler's equations; Eq. (4).

p = Nominal nutation frequency.

$\underline{q}$ = Reduced independent structural coordinates; Eqs. (21), (22), (23).

$\underline{q}^*$ = Unreduced set of structural coordinates; Eq. (5).

$\underline{q}'; \underline{q}^m, \underline{q}^\ell$ = Soft or nonlinear component of $\underline{q}^*$; Eq. (6).

$q''; q^k$ = Stiff and linear component of $\underline{q}^*$; Eq. (6).

$\underline{q}_{id}, \underline{q}_{ib}, \underline{q}_{ip}, \underline{q}_{is}$ = Position coordinates of discrete masses, beams, plates and shells, respectively.

r = N-n; also radial measure for plates.

$\underline{T}^*_E$ = Environmental and control torques on the composite bodies; Eq. (3).

$\underline{T}^*_R$ = Reaction torques between composite bodies; Eqs. (1), (3).

$\underline{v}, \underline{v}_1$ = State vectors; Eqs. (43), (44).

$\underline{y}$ = $\underline{M}_3$, the generalized force; Eq. (39).

$\underline{y}_{id}$ = Discrete mass coordinates.

$\underline{y}_{ib}, \underline{y}_{ip}, \underline{y}_{is}$ = Beam, plate and shell coordinates, respectively.

ε = Largest eigenvalue of $[A_1 A_3^{-1}]$.

θ = Angular measure for plates and shells.

$\underline{\theta}^*$ = Relative angular displacement vector.

$\underline{\omega}$ = Angular velocity vector of the composite bodies.

INTRODUCTION

This investigation is the second part of a study [1] of pointing accuracies of flexible satellites. In the preceding section [2], the equations of motion of beam, plate, and shell elements of a flexible satellite were obtained. The continuous mass distributions of these elements were modeled by a finite set of generalized position coordinates in Ref. [2] through a Galerkin's procedure. In this part, the equations for the angular velocities of the composite bodies of a satellite, with similar distributed mass elements, will first be obtained in terms of the generalized coordinates introduced in Ref. [2]. Equations of motion of the individual elements, given by Eq. (41) of Ref. [2], and the equations of motion of the composite bodies developed here form the basic system for any dynamic model of flexible satellites. Similar equations with discrete mass systems have been studied extensively [3-12]. The present investigation initiates a new approach to these equations through the formulation of a set of singularly perturbed equations.

Earlier studies [3-12] can be broadly divided into two groups. The first group of papers [3-8] attempts to model a flexible satellite structure with a large number of degrees of freedom. The dominant method of solution adopted by this group is linearization and consequent determination of the normal modes. The second group of papers [9-12] considers only a small number of degress of freedom of the satellite structure, but undertakes much more involved nonlinear analyses. The reason for this difference is that it is impracticable to analyze a large nonlinear coupled system. A method of resolving this dualism is presented here for nonlinear analysis of a flexible satellite with large number of degrees of freedom.

OUTLINE OF THE METHOD

Let 'n' be the number of degrees of freedom of a satellite structure. Let 'r' be the number of angular velocities of the satellite. Thus, r can either be three for a single-body satellite or nine for a

dual-spin satellite when the three components of the relative angular velocity vector between the two bodies are independent. In general, 'n' is a large number. Let 'p' be the nominal nutation frequency of the satellite when all the flexible elements are assumed rigid. Let n = ℓ+m+k, where 'ℓ' is the number of flexible element position coordinates of the satellite which have significant nonlinearities requiring detailed analysis. And 'm' is the number of coordinates which are linear and have uncoupled natural frequencies close to or much lower than 'p'. Thus 'k' is the number of generalized position coordinates of the satellite which are relatively stiff and appear linearly with respect to themselves in the (n+r) equations of motion of the system. If n is large and k is small, then obviously no simple approach can be made. But in usual designs, both n and k are large. In this case the method presented will be very useful.

Let $\{q^{\ell}\}$, $\{q^{m}\}$ and $\{q^{k}\}$ be the three sets of position coordinates, with, respectively, ℓ, m and k elements. In the numerical design data used, the numbers 'ℓ' and 'm' are taken equal to zero, since the space dependencies were taken linearly and the uncoupled natural frequencies of the elements were much greater than 'p'. Because $\{q^{k}\}$ appears linearly, it can be eliminated from the set of governing equations of motion. This elimination leads to a reduced set of (ℓ+m+r) equations. This is then approached by a perturbation technique. The small parameter used in such a scheme is the inverse of the square of the smallest nominal natural frequency of the system of k equations for the $\{q^{k}\}$. For a linearly coupled satellite, such analytic condensation of a large system into a small system sharply extends the value and the scope of the previously mentioned second group of studies [9-12]. This analysis of the 'r' equations is presented in greater detail corresponding to the dual spin configuration (r=9) shown in Figure 1 of Ref. [2].

EQUATIONS FOR THE COMPOSITE BODIES

Let the environmental and control torques on one of the composite bodies of the satellite be denoted by $\underline{T}^{*}_{E}$. Let the reaction torques exerted on this composite body by the other connected composite body be given by $\underline{T}^{*}_{R}$. Let the (nx1) column vector of the generalized position coordinates of the composite body under consideration be {q*}. Then $\underline{T}^{*}_{R}$ can be obtained as:

$$\underline{T}^{*}_{R} = [G_5]\dot{\underline{q}}^{*} + [G_6]\underline{q}^{*} + [G_7]\dot{\underline{\theta}}^{*} + [G_8]\underline{\theta}^{*} \qquad (1)$$

where $\underline{\theta}^{*}$ is the relative angular displacement vector of the composite bodies forming a dual-spin satellite. Following the analysis of Refs. [4,6], the linearized form of the inertial time derivative of the angular momentum vector ($\underline{H}$) of the composite body is obtained as:

$$\dot{\underline{H}} = I\dot{\underline{\omega}} + \tilde{\omega}I\underline{\omega} + \dot{\underline{h}}^* + \tilde{\omega}\underline{h}^* + \sum_i m_i[\tilde{R}_{id}\ddot{\underline{q}}_{id} + \tilde{\omega}\tilde{R}_{id}\dot{\underline{q}}_{id}] + \sum_j \rho_{jb}\int_0^{\ell_{jb}}\{[\mu^*_{ib}][R^L_{ib} + \begin{matrix}s\\0\end{matrix}\}]\ddot{y}_{ib} + \tilde{\omega}[\mu^*_{ib}][R^L_{ib} + \begin{matrix}s\\0\end{matrix}\}]\dot{y}_{ib}\}\,ds + \sum_k \rho_{kp}\iint\{\tilde{R}_{kp}\ddot{y}_{kp} + \tilde{\omega}\tilde{R}_{kp}\dot{y}_{kp}\}\,dA + \sum_m \rho_{ms}\iint\{\tilde{R}_{ms}\ddot{y}_{ms} + \tilde{\omega}\tilde{R}_{ms}\dot{y}_{ms}\}\,dA \qquad (2)$$

In Eq. (2) above, the subscripts d, b, p and s denote the discrete mass and the beam, plate, and shell elements of the flexible composite body. The nominal moment of inertia matrix of the composite body is denoted by 'I'. And $\underline{h}^*$ is the momentum vector of moving parts or reaction wheels inside the composite body. The summations are taken over the numbers of the different structural elements present in the composite body.

The three equations for the rotational motion of each composite body are given by the vector equation:

$$\dot{\underline{H}} = \underline{T}^*_E + T^*_R \qquad (3)$$

Then from Eqs. (1) and (2), Eq. (3) is expressed as

$$[P^*_1]\ddot{\underline{q}}^* + [P^*_2(\underline{\omega},\dot{\underline{\omega}})]\dot{\underline{q}}^* + [P^*_3(\underline{\omega},\dot{\underline{\omega}})]\underline{q}^* = \{\underline{P}^*_4(\underline{\omega},\dot{\underline{\omega}},\underline{\theta}^*,\dot{\underline{\theta}}^*,\underline{T}^*_E,t)\} \qquad (4)$$

In obtaining Eq. (4), the integrals of Eq. (2) on the structural displacement coordinates ($\underline{y}$) were carried out by using the shape functions introduced in Eq. (25) of Ref. [2]. The matrices P^*_1, P^*_2 and P^*_3 have (3xn) elements, while $\underline{P}^*_4$ is a (3x1) vector. The elements of $[P^*_1]$ are constants. For a dual spin satellite, there are two sets of equations in the form of Eq. (4) and another set of three scalar equations of the relative angular velocities of the two composite bodies, thus forming a total of nine equations.

SEPARATION OF NON-LINEARITIES

The equations of motion of the individual structural elements of a composite body were obtained in Eq. (41) of Ref. [2]. These are given as:

$$A^*_1\ddot{\underline{q}}^* + [A^*_2(\underline{\omega},\dot{\underline{\omega}},\underline{\theta}^*,\dot{\underline{\theta}}^*,t)]\dot{\underline{q}}^* + [A^*_3(\underline{\omega},\dot{\underline{\omega}},\underline{\theta}^*,\dot{\underline{\theta}}^*,t)]\underline{q}^* = \underline{A}^*_4(\underline{\omega},\dot{\underline{\omega}},\underline{\theta}^*,\dot{\underline{\theta}}^*,t) \qquad (5)$$

Let $\underline{q}^*$ be composed of $\underline{q}'$ and $\underline{q}''$ in the form

$$q^* = [q'', q']^T \tag{6}$$

where the elements of q' are those generalized position coordinates which are either significantly nonlinear, or have uncoupled natural frequencies comparable to, or less than, 'p'. The set of equations involving $\ddot{q}'$ are now removed from Eq. (5) and added to the set of equations given by Eq. (4). After this transfer, the augmented set is expressed as:

$$[P_1']\ddot{q}'' + [P_2'(\omega, \dot{\omega})]\dot{q}'' + [P_3'(\omega, \dot{\omega})]q''$$

$$= P_4'(\omega, \omega, \theta^*, \dot{\theta}^*, q', \dot{q}', \ddot{q}', T_E^*, t) \tag{7}$$

The depleted set of equations is expressed as:

$$[A_1']q'' + [A_2'(\omega, \dot{\omega}, \theta^*, \dot{\theta}^*, t)]\dot{q}'' + [A_3'(\omega, \dot{\omega}, \theta^*, \dot{\theta}^*, t)]q''$$

$$= A_4'(\omega, \dot{\omega}, \theta^*, \dot{\theta}^*, q', \dot{q}', t) \tag{8}$$

In Eq. (7), P_1', P_2' and P_3' are still rectangular matrices with $(3+\ell+m)$ rows and k columns. The matrices A_1', A_2' and A_3' remain (kxk) square matrices.

CONTINUITY CONDITIONS

By using the continuity conditions applicable to the structure, an initial condensation of the vector q'' is performed. The conditions must remain independent of time. These continuity conditions are given below. They correspond to the configuration shown in Figure 1 of Ref. [2]. The details of derivation of these conditions can be found in Ref. [1].

a. End Mass-Beam Continuity Conditions:

The displacement of the beams at the ends must equal the displacement of the point mass at the respective beam ends. Thus,

$$y_d = [\mu_b^*][\Psi_b(\ell_b)]q_b \tag{9}$$

for a particular end-mass and beam junction. Equations similar to Eq. (9) can be obtained for all such end mass and beam junctions. These equations are expressed together as:

$$q_{id} = [L_{db}]q_{ib} \tag{10}$$

The matrix $[\Psi_b(s)]$ is that of the shape functions for the beams introduced in Ref. [2].

b. Beam-Shell Continuity Conditions:

The in-plane rotations of the shells and, therefore, the inplane moments have been assumed to be zero. The force continuity in the radial direction was previously considered in deriving the equations for the

beam-end masses. The continuity conditions for the shear forces in the transverse directions of the beams are neglected, as the shell displacements in those directions are taken to be zero. The remaining continuity conditions for each beam-shell junction are for the radial displacement: two rotations and two moments.

Referring to Eq. (25) of Ref. [2], the displacement relations are given by:

$$[\Psi_{ib}]q_{ib} = [\Psi_{is}]q_{is} \tag{11}$$

where Ψ_{ib} and Ψ_{is} are evaluated at the beam-shell junctions.

The conditions under which the slopes of the beams at the joints are equal to the slopes of the shells at the junctions are:

$$[\underline{\nabla}\,\Psi_{ib}]q_{ib} = [\underline{\nabla}\,\Psi_{is}]q_{is} \tag{12}$$

where $\underline{\nabla}$ is the appropriate gradient operator and the equation corresponding to the first row is to be neglected.

The moment continuity conditions are obtained by equating the bending moments of the beams to the bending moments of the shells at the junctions. They are thus given by:

$$\frac{\partial^2}{\partial s^2} E_{ib} \begin{bmatrix} 0 & 0 & 0 \\ 0 & I_{ib,3} & 0 \\ 0 & 0 & I_{ib,2} \end{bmatrix} [\Psi_{ib}(s)]q_{ib}$$

$$= \frac{E_{is} \cdot h_{is}^3}{12a_{is}^2(1-\mu_{is}^2)} \begin{Bmatrix} 0 \\ \left(\frac{\partial^2}{\partial \theta 2} + \mu_{is}\frac{\partial^2}{\partial z^2}\right) \\ \left(\frac{\partial^2}{\partial z^2} + \mu_{is}\frac{\partial^2}{\partial \theta^2}\right) \end{Bmatrix} [\Psi_{is}(\theta,z)]q_{is} \tag{13}$$

where all functions are to be evaluated at the junctions.

Combining Eqs. (11), (12), and (13) for all junctions, the beam-shell junction continuity conditions are obtained in the form:

$$q_{ib} = [L_{bs}]q_{is} \tag{14}$$

c. Plate-Shell Continuity Conditions:

The condition for the continuity of the edge-moments is that the bending moments on the shell at an edge must be equal and opposite to the bending moment on the plate connected to the shell at the circular junction.

Thus, the conditions become:

$$\frac{1}{a^2} D_p \left[\frac{\partial^2 y_{ip,3}}{\partial r^2} + \mu_p \left(\frac{1}{r} \frac{\partial y_{ip,3}}{\partial r} + \frac{1}{r^2} \frac{\partial^2 y_{ip,3}}{\partial \theta^2} \right) \right] r = 1$$

$$+ \frac{1}{a^2} D_s \left[\frac{\partial^2 y_{is}}{\partial z^2} + \mu_s \frac{\partial^2 y_{is}}{\partial \theta^2} \right] z = z_1 = 0 \qquad (15)$$

for all θ.

The force continuity conditions at the plate-shell junctions are neglected because the plate and shell displacements at these junctions are assumed to be zero.

Equating the displacements at the junctions:

$$q_{ip,1}(t) = 0 \qquad (16)$$

and

$$q_{is,1}(t) = 0 \qquad (17)$$

The rotational continuity conditions are obtained from the assumption that the plates and the connected shells rotate by equal amounts at the junctions. Thus the slope continuity conditions are obtained as:

$$\left\{ \frac{\partial}{\partial r} [\Psi_{ip}(r,\theta)] \right\}_{r=1} q_{ip} + \frac{\partial}{\partial z} [\Psi_{is}(\theta,z)]_{z=z_1} q_{is} = 0 \qquad (18)$$

The positive sign means that the plate positive deflection is in the direction opposite to the positive shell axis.

Eqs. (15) and (18), $r = 1$, and $z = z_1$ define the appropriate junction of the plate and shell under consideration. Note that the previous continuity conditions given by Eqs. (10-14), which are prescribed at a single point only, can be easily obtained. In contrast, the conditions given by Eqs. (15) and (18) are continuous over the complete range of θ. Previous investigators [13, 14] have solved similar problems by evaluating similar conditions at several discrete points on the range $0 \leq \theta \leq 2\pi$. Instead of such discrete point evaluation, each harmonic component of Eqs. (15) and (18) should be equal to zero as done in Ref. [1]. This means that a finite number of continuity conditions are obtained from Eqs. (15) and (18) by multiplying these successively by 1, $\cos(n\theta)$ and $\sin(n\theta)$, $(n = 1,2,3, \ldots)$, and then integrating with respect to θ between the limits $(0,2\pi)$. These integrations are performed by using the shape functions of the corresponding plates and shells. The technique yields a relation between the plate and shell generalized displacement coordinates in the form:

$$q_{is} = [L_{sp}] q_{ip} \qquad (19)$$

d. Rigid Body-Plate Continuity Conditions

The force and moment continuity conditions between a plate and a rigid body, mounted on the plate, form the equations of motion of the rigid body. Hence, these conditions are included in Eq. (8).

The remaining conditions to be satisfied are obtained by equating the displacements and rotations of the rigid bodies to appropriate linear combinations of the plate displacements at the junction points. These conditions, which depend on the geometry and orientations of the rigid bodies, are discussed in detail in Ref. [1]. It is sufficient to note here that these conditions, too, have a linear form, given by:

$$\underline{q}_{id} = [L_{dp}]\underline{q}_{ip} \tag{20}$$

REDUCED EQUATIONS

The continuity conditions for all structural joints can be expressed together as:

$$\underline{q}'' = [L]\underline{q} \tag{21}$$

where [L] is a (kxk') matrix of constants. And $\underline{q}$ is a reduced (k'x1) vector, because k' is necessarily much less than k. In the modelling [1] of the configuration of Figure 1, Ref. [2], the (110x1) vector was reduced to a (41x1) vector, leading to a considerable saving of computer memory space.

Equation (21) shows that not all the elements of $\underline{q}''$ are independent. The matrix [L] specifies the geometric and structural constraints of a particular satellite configuration. The constraint matrices are normally used, after the formal solution of a vibrating system, to obtain the frequency equations. In the following analysis, [L] is used before the formal solution of the system to eliminate dependent space variables. Note that the coordinates of those structural elements, which are joined to other elements through springs or dampers, always remain independent. Thus, the displacement coordinates of the point mass of a spring-mass-damper system cannot be expressed in terms of the coordinates of other structural elements by equations similar to Eqs. (10) - (21).

Using Eq. (21), Eq. (7) can be expressed as:

$$P_1' L \ddot{\underline{q}} + P_2' L \dot{\underline{q}} + P_3' L \underline{q} = \underline{P}_4$$

This equation is redefined as:

$$[P_1]\ddot{\underline{q}} + [P_2(\underline{\omega},\dot{\underline{\omega}})]\dot{\underline{q}} + [P_3(\underline{\omega},\dot{\underline{\omega}})]\underline{q} = \underline{P}_4 \tag{22}$$

Similarly, from Eq. (21), Eq. (8) becomes:

$$(L^T A_1' L)\ddot{\underline{q}} + (L^T A_2' L)\dot{\underline{q}} + (L^T A_3' L)\underline{q} = L^T A_4'$$

This equation is redefined as:

$$[A_1]\ddot{\underline{q}} + [A_2(\underline{\omega},\dot{\underline{\omega}},\underline{\theta}^*,\dot{\underline{\theta}}^*,t)]\dot{\underline{q}} + [A_3(\underline{\omega},\dot{\underline{\omega}},\underline{\theta}^*,\dot{\underline{\theta}}^*,t)]\underline{q}$$
$$= A_4\ (\underline{\omega},\dot{\underline{\omega}},\underline{\theta}^*,\dot{\underline{\theta}}^*,\underline{q}',\dot{\underline{q}}',t) \qquad (23)$$

Here A_1, A_2 and A_3 remain non-singular square matrices.

SINGULARLY PERTURBED FORMULATION

The singularly perturbed equations are obtained from equations (22) and (23) by eliminating $\underline{q}(t)$. To do this, Eq. (22) is added to Eq. (23) by adding the elements of P_i to the elements of the first $(3+m+\ell)$ rows of the corresponding A_i. This operation yields:

$$[A_1+P_1]\ddot{\underline{q}} + [A_2+P_2]\dot{\underline{q}} + [A_3+P_3]\underline{q} = (\underline{A}_4+\underline{P}_4)$$

The matrix (A_1+P_1) is square and non-singular. Hence:

$$\ddot{\underline{q}} = [A_1+P_1]^{-1}[(\underline{A}_4+\underline{P}_4) - (A_2+P_2)\dot{\underline{q}} - (A_3+P_3)\underline{q}]. \qquad (24)$$

Also, from Eq. (23), $\underline{q}$ is given by:

$$\ddot{\underline{q}} = A_1^{-1}[\underline{A}_4 - A_2\dot{\underline{q}} - A_3\underline{q}] \qquad (25)$$

Subtracting Eq. (24) from Eq. (25), $\ddot{\underline{q}}$ is eliminated to give:

$$[A_2 - A_1(A_1+P_1)^{-1}(A_2+P_2)]\dot{\underline{q}} + [A_3 - A_1(A_1+P_1)^{-1}(A_3+P_3)]\underline{q}$$
$$= [A_4 - A_1(A_1+P_1)^{-1}(A_4+P_4)]. \qquad (26)$$

With appropriate definitions, this equation is rewritten as:

$$M_1\dot{\underline{q}} + M_2\underline{q} = \underline{M}_3. \qquad (27)$$

Equation (27) is now differentiated with respect to time. The expression for $\ddot{\underline{q}}$ is substituted from Eq. (25) to form

$$(\dot{M}_1 + M_2 - M_1A_1^{-1}A_2)\dot{\underline{q}} + (\dot{M}_2 - M_1A_1^{-1}A_3)\underline{q}$$
$$= (\dot{\underline{M}}_3 - M_1A_1^{-1}\underline{A}_4) \qquad (28)$$

Eliminating $\dot{\underline{q}}$ from Eqs. (27) and (28), the equation for $\underline{q}$ is obtained as

$$[\dot{M}_2 - M_1A_1^{-1}A_3 - (\dot{M}_1 + M_2 - M_1A_1^{-1}A_2)M_1^{-1}M_2]\underline{q}$$
$$= [\dot{\underline{M}}_3 - M_1A_1^{-1}\underline{A}_4 - (\dot{M}_1 + M_2 - M_1A_1^{-1}A_2)M_1^{-1}\underline{M}_3] \qquad (29)$$

This equation is of the form

$$M_4 q = \underline{M}_5 \tag{30}$$

or

$$q = M_4^{-1} \underline{M}_5 \tag{31}$$

Equation (23) is now differentiated once and Eq. (27) is differentiated twice to obtain:

$$\dddot{q} + A_1^{-1}A_2\ddot{q} + A_1^{-1}(\dot{A}_2+A_3)\dot{q} + A_1^{-1}A_3 q = A_1^{-1}\dot{\underline{A}}_4 \tag{32}$$

and

$$M_1\dddot{q} + (2\dot{M}_1+M_2)\ddot{q} + (\ddot{M}_1+2\dot{M}_2)\dot{q} + \ddot{M}_2 q = \ddot{\underline{M}}_3 \tag{33}$$

From these equations, $\dddot{q}$ is eliminated. This results in:

$$(2\dot{M}_1+M_2-M_1A_1^{-1}A_2)\ddot{q} + (\ddot{M}_1+2\dot{M}_2-M_1A_1^{-1}\dot{A}_2-M_1A_1^{-1}A_3)\dot{q}$$
$$+ (\ddot{M}_2-M_1A_1^{-1}\dot{A}_3)q = (\ddot{\underline{M}}_3-M_1A_1^{-1}\dot{\underline{A}}_4) \tag{34}$$

Successive substitution of the expressions for $\ddot{q}$ from Eq. (23), for q from Eq. (27), and for q from Eq. (31) into Eq. (34) yields:

$$[A_1M_2^{-1}]\ddot{\underline{M}}_3 + [(A_2-A_3M_2^{-1}M_1+A_1M_2^{-1}M_1A_1^{-1}A_3)M_2^{-1}]\dot{\underline{M}}_3$$
$$+ [A_3M_2^{-1}]\underline{M}_3 = \underline{A}_4 \tag{35}$$

In obtaining Eq. (35) it has been assumed that A_2 is small compared to A_1 and A_3. Thus, only the terms linear in $A_1^{-1}A_2$ and $A_3^{-1}A_2$ were retained. On further simplification, Eq. (35) reduces to:

$$[(P_1A_1^{-1}-P_3A_3^{-1})A_1M_2^{-1}]\ddot{\underline{M}}_3 + [(P_2A_2^{-1}-P_3A_3^{-1})A_2M_2^{-1}]\dot{\underline{M}}_3$$
$$+ \underline{M}_3 = (P_1A_1^{-1}-P_3A_3^{-1})\underline{A}_4 \tag{36}$$

The vector $(\underline{M}_3)$ appearing here, is given by Eqs. (26) and (27) as:

$$\underline{M}_3(\omega,\dot{\omega},\underline{\theta}^*,\dot{\underline{\theta}}^*,q',\dot{q}',\ddot{q}',\underline{T}_E^*,t)$$
$$= [\underline{A}_4-A_1(A_1+P_1)^{-1}(\underline{A}_4+\underline{P}_4)]. \tag{37}$$

The simplifications made to obtain Eq. (36) are not essential for the further development of the theory. It should be noted that the vector $\underline{M}_3$ can be considered as a generalized force. The Eq. (36) involves only the angular velocities and the critical position coordinates $q'(t)$. Solving for $\underline{M}_3$ from Eq. (36) and using that solution as a forcing function for the differential expression on the right hand side of Eq. (37), yields the

condensed equations applicable for the structure of the flexible satellite. The non-critical position coordinates ($\underline{q}''$) are obtained from Eqs. (21) and (31) as:

$$\underline{q}'' = L\, M_4^{-1}\, \underline{M}_5 \tag{38}$$

The quantities M_4 and $\underline{M}_5$ are defined by Eqs. (29) and (30).

The eigenvalues of $[A_1 A_3^{-1}]$ are the reciprocals of the squares of the natural frequencies of $\underline{q}''(t)$. Since $\underline{q}''(t)$ is assumed to represent comparatively rigid elements of the flexible satellite, these eigenvalues can be considered small. Let ε be the largest eigenvalue of $A_1 A_3^{-1}$. Then the terms of the Eq. (35) can be expressed as:

$$\varepsilon A\ddot{\underline{y}} + \varepsilon B\dot{\underline{y}} + \underline{y} = \varepsilon \underline{d} \tag{39}$$

with appropriate definitions of A, B and $\underline{d}$, and where

$$\underline{y}(t) = \underline{M}_3. \tag{40}$$

Equation (39) proves to be very useful. As the elements represented by $\underline{q}''(t)$ become increasingly rigid, $\underline{q}''(t)$, $\underline{A}_4$ and ε approach zero. The equation (39) then also approaches

$$\underline{y} = \underline{0} \tag{41}$$

and consequently

$$\underline{P}_4 = \underline{0} \tag{42}$$

The Eq. (42) can easily be identified as one of the special classes of equations studied in Refs. [9, 10, 11 and 12]. In fact, the assumption $\underline{q}'(t) = \underline{0}$ leads Eq. (42) to the rigid body Euler's equation. Thus a continuous dependence of the vector $\underline{M}_3$ on the flexible elements of the satellite has been established through the parameter ε and Eq. (39). Appearance of the small parameter ε as coefficient of the highest order derivatives of $\underline{y}$ in Eq. (39) classifies this equation as the singularly perturbed equation mentioned earlier.

PERTURBED SOLUTION SCHEME

Let $\underline{v}(t)$ be the vector defined by:

$$\underline{v} = [\underline{\omega}, \dot{\underline{\omega}}, \underline{q}', \dot{\underline{q}}']^T \tag{43}$$

The process of solution of Eq. (39) is based on the perturbation series given by:

$$\underline{v} = \underline{v}_0 + \varepsilon \underline{v}_1 + \varepsilon^2 \underline{v}_2 + \varepsilon^3 \underline{v}_3 + \ldots \tag{44}$$

Let $\underline{h}$ be defined by:

$$\underline{v} = \underline{v}_0 + \underline{h} \tag{45}$$

Then $\underline{y}(v,t)$ can be expanded in a Taylor's series about the point $(\underline{v}_0,t)$ as:

$$y_i(\underline{v},t) = y_i(\underline{v}_0,t) + \varepsilon y_{i,j}(\underline{v}_0,t)v_{1j}$$
$$+ \varepsilon^2[y_{i,j}(\underline{v}_0,t)v_{2j} + \frac{1}{2}\, y_{i,jk}(\underline{v}_0,t)v_{1j}v_{1k}] + \ldots \qquad (46)$$

where

$$y_{i,j} = \frac{\partial y_i}{\partial v_j}$$

and

$$y_{i,jk} = \frac{\partial^2 y_i}{\partial v_j \partial v_k} \quad \text{etc.}$$

Differentiation of Eq. (46) results in

$$\dot{y}_i(\underline{v},t) = \dot{y}_i(\underline{v}_0,t) + \varepsilon[\dot{y}_{i,j}(\underline{v}_0,t)v_{1j}$$
$$+ y_{i,j}(\underline{v}_0,t)\dot{v}_{1j}] + \varepsilon^2[\dot{y}_{1,j}(\underline{v}_0,t)v_{2j} + y_{i,j}(\underline{v}_0,t)\dot{v}_{2j}$$
$$+ \frac{1}{2}\,\dot{y}_{i,jk}(\underline{v}_0,t)v_{1j}v_{1k} + y_{i,jk}(\underline{v}_0,t)\dot{v}_{1j}v_{1k}] + \ldots$$

Expansions for $\ddot{\underline{y}}(v,t)$, $A(v,t)$, $B(v,t)$, and $\underline{d}(v,t)$ are similarly obtained. Each of these expansion series approaches the nominal values as the satellite becomes increasingly rigid. Substituting these series into Eq. (39), and subsequently separating the coefficients of ε^0, ε, ε^2, etc., the perturbation equations are obtained as:

$$y_i(\underline{v}_0,t) = \underline{0} \qquad (47)$$

$$[y_{i,j}(\underline{v}_0,t)]\underline{v}_{1j} = d_i(\underline{v}_0,t) \qquad (48)$$

$$[(d_{i,j}-y_{i,j})(\underline{v}_0,t)]v_{2j} + \frac{1}{2}\,[(d_{i,jk}-y_{i,jk})(\underline{v}_0,t)]v_{1j}v_{1k}$$
$$= [A_{ij}(\underline{v}_0,t)]\ddot{d}_j(\underline{v}_0,t) + [B_{ij}(\underline{v}_0,t)]\dot{d}_j(\underline{v}_0,t) \qquad (49)$$

Equations (47), (48), and (49) are generated by ε^0, ε, and ε^2 respectively. Equations corresponding to higher powers of ε are similarly obtained. The Eq. (49) can be further simplified:

The gradient of Eq. (48) with respect to $\underline{v}$ yields:

$$d_{i,j} = y_{i,kj}v_{1k} + y_{i,j} \qquad (50)$$

and hence:

$$d_{i,jk} - y_{i,jk} = y_{i,jk\ell}v_{1\ell} + y_{i,jk} \qquad (51)$$

Substituting Eqs. (50) and (51) and neglecting $\ddot{d}_j(\underline{v}_0,t)$ and $\dot{d}_j(\underline{v}_0,t)$ in Eq. (49) gives:

$$[y_{i,jk}(\underline{v}_0,t)]v_{1k}v_{2j} + \frac{1}{2}[y_{i,jk\ell}(\underline{v}_0,t)]v_{1j}v_{1k}v_{1\ell}$$
$$+ \frac{1}{2}[y_{i,jk}(\underline{v}_0,t)]v_{1j}v_{1k} = 0$$

Neglecting the cubic term of this equation, v_{2j} is given as:

$$v_{2j} = -\frac{1}{2}v_{1j} \tag{52}$$

Thus collecting terms containing ε^0, ε and ε^2, $\underline{v}(t)$ is given by:

$$v_i = v_{0i} + \varepsilon(1-\frac{\varepsilon}{2})[y_{i,j}(\underline{v}_0,t)]^{-1}d_j(\underline{v}_0,t) \tag{53}$$

where $\underline{v}_0$ is to be solved from Eq. (47).

CONCLUSIONS

Beginning with the zeroth order solution ($\underline{v}_0$) of Eq. (39), a standard procedure for obtaining the higher order terms of the series given in Eq. (44) has been set up. All higher order terms satisfy purely algebraic equations. This means that every term of the series for $\underline{v}$ is determined solely from the preceding terms which are already determined. This is caused by the singular nature of Eq. (39). Although the method appears similar to the Energy Sink technique, it is not. The reason is the appearance of the vector $\underline{A}_4$ in the expression for $\underline{y}$ or $\underline{M}_3$, given by Eq. (37). Another feature of Eq. (39) is that it has only $(3+m+\ell)$ rows of equations which are not identities when $\underline{q}'(t)$ is a $(m+\ell)$ vector. Thus, $\underline{y}(t)$ is essentially a $(3+m+\ell)$ vector. The singular nature of Eq. (39) also indicates the existence of two boundary layer solutions of $\underline{y}(t)$. These are valid near the origin of the time scale, forming two transient zones. Special cases of Eq. (36), such as the boundary layer solutions and the convergence of the series given in Eq. (44), will be considered in a forthcoming paper.

ACKNOWLEDGEMENT

This work was supported in part by the National Aeronautics and Space Administration under Contract No. NAS5-21798 through the Space Science and Engineering Center, University of Wisconsin, Madison, Wisconsin.

REFERENCES

1. Das, A., and Huang, T. C., "Pointing Error Analysis of Geosynchronous Satellites, Parts I-III," Technical Report, Space Science and Engineering Center, Madison, Wisconsin, December 1973; NASA Contract Report No. NAS5-11542.

2. Huang, T. C., and Das, A., "Thermoelastic Flutter Models for Beam, Plate and Shell Elements of Flexible Satellites," Paper presented at the 24th International Astronautical Congress, Baku, U.S.S.R., October 1973.

3. Velman, J. R., "Attitude Dynamics of Dual-Spin Satellites," Space Systems Division Research Report, Hughes Aircraft Co., SSD 60419R, September 1966.

4. Likins, P. W., "Attitude Stability of Dual-Spin Systems," Space Systems Research Report, Hughes Aircraft Co., SSD 60377R, September 1966.

5. Likins, P. W., and Wirsching, P. H., "Use of Synthetic Modes in Hybrid Coordinate Dynamic Analysis," AIAA Jnl., Vol. 6, October 1968, pp. 1867-1872.

6. Likins, P. W., and Gale, A. H., "The Analysis of Interactions Between Attitude Control Systems and Flexible Appendages," Paper IAF AD29, 19th International Aeronautical Congress, New York, October 1968.

7. Likins, P. W., and Fleischer, G. E., "Results of Flexible Spacecraft Attitude Control Studies Utilizing Hybrid Coordinates," Jnl. of Spacecraft and Rockets, Vol. 8, No. 3, March 1971, pp. 264-272.

8. Grote, P. B., McMunn, J. C., and Gluck, R., "Equations of Motion of Flexible Spacecraft," Jnl. of Spacecraft and Rockets, Vol. 8, No. 6, June 1971, pp. 561-567.

9. Likins, P. W., Tseng, G., and Mingori, D. L., "Stable Limit Cycles Due to Nonlinear Damping in Dual-Spin Spacecraft," Jnl. of Spacecraft and Rockets, Vol. 8, No. 6, June 1971, pp. 568-574.

10. Cretcher, C. K., and Mingori, D. L., "Nutation Damping and Vibration Isolation in a Flexibly Coupled Dual-Spin Spacecraft," Jnl. of Spacecraft and Rockets, Vol. 8, No. 8, August 1971, pp. 817-823.

11. Bainum, P. M., Fuechsel, P. G., and Fedor, J. V., "Stability of a Dual-Spin Spacecraft with a Flexible Momentum Wheel," Jnl. of Spacecraft and Rockets, Vol. 9, No. 9, September 1972, pp. 640-646.

12. Mingori, D. L., Tseng, G. T., and Likins, P. W., "Constant and Variable Amplitude Limit Cycles in Dual-Spin Spacecraft," Jnl. of Spacecraft and Rockets, Vol. 9, No. 11, November 1972, pp. 825-830.

13. Trubert, M. R., "A Practical Approach to Spacecraft Structural Dynamics Problems," Jnl. of Spacecraft and Rockets, Vol. 9, No. 11, November 1972, pp. 818-824.

14. Huang, T. C., and Saczalsky, K. J., "Coupled Response of Spatial Vibratory Structures Mounted on Isotropic Plate Elements," Jnl. of Engineering for Industry, February 1972, pp. 15-22.

ANALYSIS OF GENERALIZED FORCES IN THE EQUATIONS OF MOTION OF FLEXIBLE SATELLITES

Aniruddha Das and T. C. Huang

ABSTRACT

The formulation and existence of a generalized force is presented. The generalized force appears in the singularly perturbed formulation of flexible satellites. The concept of this force sharply reduces the number of degrees of freedom and the equations of motion of satellites with large number of flexible elements. This paper presents an analysis of this force showing its existence and convergence criteria. The complete solution was obtained in three time zones, the inner boundary layer, the outer boundary layer, and the large time extending beyond these boundary layers. A stability criterion is proposed for this generalized force.

NOMENCLATURE

A, A_1 = Generalized mass matrices; Eqs. (17), (1).

A_2, A_3 = Generalized damping and stiffness matrices, respectively; Eq. (1).

$\underline{A}_4$ = Force vector associated with Eq. (1).

$\underline{a}$ = Constant vector; Eq. (56).

B = Generalized damping matrix; Eq. (17).

B_1, B_2 = Inertia matrices; Eq. (2).

$\underline{B}_3$ = Force vector; Eq. (2).

$\underline{b}$ = Constant vector; Eq. (56).

D = Matrix defined by Eq. (29).

$\underline{d}$ = Generalized force; Eq. (17).

F = Operator; Eq. (25).

$\underline{f}$, $\underline{g}$ = Functions; Eq. (41).

I = Identity matrix.

k = Lifschitz constant, Eq. (27).

M = Maximum response magnitude; Eq. (30).

M_1, M_2, M_4 = Matrices defined by Eqs. (6), (7), (12).

$\underline{M}_5$ = Generalized force; Eq. (12).

P = Matrix defined by Eq. (22).

P_1, P_2, P_3, $\underline{P}_4$ = Matrices and vector associated with the generalized Euler's equation; Eq. (2).

Q = Matrix defined by Eq. (23).

$\underline{q}$ = Position vector of the structure of the satellite; Eq. (1).

T = Time interval; Eq. (26).

t = Real time.

U = Set of allowable responses; Eq. (26).

$\underline{u}$, $\underline{u}_1$, $\underline{u}_2$, $\underline{v}$, $\underline{x}$ = State variables; Eqs. (20), (27).

$\underline{y}$ = Generalized force; Eq. (8).

$\underline{\nabla}$ = Gradient operator

δ = Arbitrary constant; Eq. (26).

ε = Small parameter; Eq. (17).

τ = Fast time; Eqs. (49), (60).

$\underline{\omega}$, $\underline{\omega}_o$, $\underline{\omega}_n$, $\underline{\omega}_n^*$; = Angular velocity and its component vectors; Eqs. (36), (37).

n = 1,2, ...

INTRODUCTION

This investigation is a part of a comprehensive study [1,2,3,4] on the pointing accuracies of various types of flexible satellites. It was shown [in 2,4] that a singularly perturbed formulation of the response of a flexible satellite is a viable method of analysis. This formulation leads to a generalized force which should be zero for an ideally rigid satellite. For flexible satellites, this force is not zero. The values of this force can be obtained by perturbation techniques. The response of the satellite can then be solved from these values.

SINGULARLY PERTURBED EQUATIONS

The formulation of singularly perturbed equations and the generalized force will be described. References [1,2,4] can be consulted for a more detailed discussion.

Let it be assumed that, by any of the existing methods such as lumped mass, Galerkin's, the finite element, etc., the equations of motion of a flexible satellite have been obtained in the following forms:

$$[A_1]\ddot{\underline{q}} + [A_2(\underline{\omega},t)]\dot{\underline{q}} + [A_3(\underline{\omega},t)]\underline{q} = \underline{A}_4(\underline{\omega},t) \tag{1}$$

and

$$[B_1]\dot{\underline{\omega}} + [B_2(\underline{\omega},t)]\underline{\omega} + [P_1]\ddot{\underline{q}} + [P_2(\underline{\omega},t)]\dot{\underline{q}} + [P_3(\underline{\omega},t)]\underline{q} = \underline{B}_3(\underline{\omega},t) \tag{2}$$

In Eqs. (1) and (2), $\underline{q}$ is the $(n\times 1)$ generalized position vector of the flexible structural elements of the satellite. The vector $\underline{\omega}$ is usually the angular velocity vector of the satellite. In most cases, equation (2) is the generalized Euler's equation, while Eq. (1) is the force equations of motion of the structural elements. The matrices A_1, A_2, A_3, B_1, and B_2 are all square matrices. The matrices P_1, P_2, and P_3 are $(3\times n)$ rectangular matrices. Thus, Eq. (1) has n structural equations and Eq. (2) has three angular momentum equations. The conditions when Eq. (2) contains more than three equations are discussed in [4]. Let Eq. (2) be rearranged in the form:

$$[P_1]\ddot{\underline{q}} + [P_2(\underline{\omega},t)]\dot{\underline{q}} + [P_3(\underline{\omega},t)]\underline{q} = \underline{P}_4(\underline{\omega},t) \tag{3}$$

where $\underline{P}_4(\underline{\omega},t)$ is a (3×1) vector. It can be verified [1,3,5,6] that the elements of the matrices A_1 and P_1 are all constants. Adding the Eq. (3) to Eq. (1), we get:

$$[A_1+P_1]\ddot{\underline{q}} + [A_2+P_2]\dot{\underline{q}} + [A_3+P_3]\underline{q} = (\underline{A}_4+\underline{P}_4) \tag{4}$$

Eliminating $\ddot{\underline{q}}$ from Eqs. (1) and (4), we obtain

$$[A_2-A_1(A_1+P_1)^{-1}(A_2+P_2)]\dot{\underline{q}} + [A_3-A_1(A_1+P_1)^{-1}(A_3+P_3)]\underline{q}$$

$$= [\underline{A}_4-A_1(A_1+P_1)^{-1}(\underline{A}_4+\underline{P}_4)] \tag{5}$$

Let it be defined that

$$M_1 = [A_2-A_1(A_1+P_1)^{-1}(A_2+P_2)] \tag{6}$$

$$M_2 = [A_3-A_1(A_1+P_1)^{-1}(A_3+P_3)] \tag{7}$$

and

$$\underline{y} = [A_4-A_1(A_1+P_1)^{-1}(\underline{A}_4+\underline{P}_4)] \tag{8}$$

Hence, Eq. (5) becomes

$$M_1\,\dot{\underline{q}} + M_2\,\underline{q} = \underline{y} \tag{9}$$

Differentiating Eq. (9) once with respect to time and using the value of $\ddot{\underline{q}}$ from Eq. (1), we get

$$(\dot{M}_1+M_2-M_1A_1^{-1}A_2)\dot{q} + (\dot{M}_2-M_1A_1^{-1}A_3)q = \dot{y} - M_1A_1^{-1}A_4 \tag{10}$$

Then, from Eqs. (9) and (10), we have:

$$[\dot{M}_2-M_1A_1^{-1}A_3-(\dot{M}_1+M_2-M_1A_1^{-1}A_2)M_1^{-1}M_2]q$$

$$= [\dot{y}-M_1A_1^{-1}A_4 - (\dot{M}_1+M_2-M_1A_1^{-1}A_2)M_1^{-1}y] \tag{11}$$

Equation (11) is of the form

$$M_4q = M_5 \tag{12}$$

or

$$q = M_4^{-1}M_5 \tag{13}$$

where M_4 and M_5 are appropriately defined from Eq. (11). Now, differentiating Eq. (1) once and Eq. (9) twice, and eliminating $\ddot{q}$ from those, the following equation can be obtained:

$$(2\dot{M}_1+M_2-M_1A_1^{-1}A_2)\ddot{q} + (\ddot{M}_1+2\dot{M}_2-M_1A_1^{-1}\dot{A}_2-M_1A_1^{-1}A_3)\dot{q}$$

$$+ (\ddot{M}_2-M_1A_1^{-1}\dot{A}_3)q = (\ddot{y}-M_1A_1^{-1}\dot{A}_4) \tag{14}$$

Successive substitution of the expressions for $\ddot{q}$ from Eq. (1) for $\dot{q}$ from Eq. (9), and for q from Eq. (13) into Eq. (14) yields:

$$[A_1M_2^{-1}]\ddot{y} + [(A_2-A_3M_2^{-1}M_1+A_1M_2^{-1}M_1A_1^{-1}A_3)M_2^{-1}]\dot{y}$$

$$+ [A_3M_2^{-1}]y = A_4 \tag{15}$$

In obtaining Eq. (15), it was assumed that A_2 is small compared to A_1 and A_3 and thus, only the terms linear in $A_1^{-1}A_2$ and $A_3^{-1}A_2$ were retained. On further simplification, Eq. (15) reduces to:

$$[(P_1A_1^{-1}-P_3A_3^{-1})A_1M_2^{-1}]\ddot{y} + [(P_2A_2^{-1}-P_3A_3^{-1})A_2M_2^{-1}]\dot{y}$$

$$+ y = (P_1A_1^{-1}-P_3A_3^{-1})A_4 \tag{16}$$

Since M_2^{-1} is proportional to A_3^{-1} and the stiffness matrix A_3 is assumed to be larger than either A_1 or A_2, Eq. (16) can be expressed as:

$$\varepsilon A\ddot{y} + \varepsilon B\dot{y} + y = \varepsilon d \tag{17}$$

In Eq. (17) ε is the largest eigenvalue of $[A_1A_3^{-1}]$ and can be considered a small parameter. The matrices A and B and the vector d are defined by Eqs. (16) and (17). The vector $y(\omega,t)$ is the generalized force and is defined by Eq. (8). Equation (17) is the singularly perturbed equation mentioned earlier. Note that the simplifications made in deriving Eq. (16) relate mainly to the definitions of the matrices A and B. Since

the coefficients of $\ddot{\underline{y}}$ and $\dot{\underline{y}}$ in Eq. (17) are small, those simplifications are not essential for the further development of this theory.

STRUCTURE OF THE EQUATIONS

The Eq. (17) will now be explained in more detail. Since

ε = maximum eigenvalue of $[A_1 A_3^{-1}]$,

ε approaches zero as the satellite becomes increasingly rigid. From Eq. (1) we see that $\underline{A}_4$ also approaches zero as $\varepsilon \to 0$. Thus, the limiting form of Eq. (17) is given by:

$$\underline{y} = 0 \tag{18}$$

and consequently, from Eq. (8),

$$\underline{P}_4(\underline{\omega},t) = 0 \tag{19}$$

Comparison of Eqs. (2) and (3) shows that Eq. (19) is simply the Euler's equation for the satellite when the effects of the flexibilities are neglected. Equation (17) can now be identified as a more general equation in which the effects of the flexibilities are included. A perturbation scheme for solving Eq. (17) is given in Refs. [2] and [4].

A primary advantage of this formulation is that Eq. (17) generally contains only three equations. The conditions in which it can have more than three equations are discussed in Ref. [4]. This can be seen from the following:

$$\begin{aligned}\underline{y} &= \underline{A}_4 - A_1(A_1+P_1)^{-1}(\underline{A}_4+P_4) \\ &= \underline{A}_4 - (I+P_1A_1^{-1})^{-1}(\underline{A}_4+\underline{P}_4) \\ &= \underline{A}_4 - [I-P_1A_1^{-1} + P_1A_1^{-1}P_1A_1 \quad ---](\underline{A}_4+\underline{P}_4)\end{aligned}$$

or

$$\underline{y} \cong P_1A_1^{-1}\underline{A}_4 - \underline{P}_4$$

Thus $\underline{y}$ has three rows, the same number as in Eq. (2). This fact is very useful in designing control system parameters, or a Kalman filter for satellite response.

CONVERGENCE CRITERIA

Systems of equations with small parameters have been studied widely [7,8]. The method of asympototic expansion is usually adopted for solving such systems. This method has been followed in [4]. But asymptotic expansions can be worked successfully only if certain convergence criteria are satisfied. The three most important criteria are:

(1) the time domain of the analysis must be such that the operators involved remain contractions;

(2) the remainder of the truncated solution series stays smaller than the error limits; and

(3) jump conditions should be absent in the original governing Eq. (17).

SELECTION OF THE TIME DOMAIN

The determination of a time domain in which a valid analysis of Eq. (17) can be made can use the method shown by Holtzman [9].

Let

$$\dot{\underline{y}} = \underline{x}$$

$$\underline{u} = [\underline{x},\underline{y}]^T$$

$$\underline{v} = [\underline{d},\underline{0}]^T \tag{20}$$

Then Eq. (17) is given by:

$$\dot{\underline{u}} = P\underline{u} + Q\underline{v} = \underline{f}(\underline{u}(t),t) \tag{21}$$

where

$$P = \begin{bmatrix} -A^{-1}B & -\frac{1}{\varepsilon}A^{-1} \\ I & 0 \end{bmatrix} \tag{22}$$

and

$$Q = \begin{bmatrix} A^{-1} & 0 \\ 0 & 0 \end{bmatrix} \tag{23}$$

The formal solution of Eq. (21) is:

$$\underline{u}(t) = \underline{u}(0) + \int_0^t \underline{f}(\underline{u}(t),t)dt \tag{24}$$

or

$$\underline{u}(t) = F[\underline{u}(t)] \tag{25}$$

where the operator F is defined by Eqs. (24) and (25).

Now, let $\underline{u}_1(t)$ be the exact solution of Eq. (17) and $\underline{u}_2(t)$ be an approximate solution obtained by an asymptotic expansion. Let both the solutions have the same initial values, i.e.:

$$\underline{u}(0) = \underline{u}_1(0) = \underline{u}_2(0)$$

The problem, then, is to find a time interval [0,T] which will ensure that $(\underline{u}_1-\underline{u}_2)(t)$ is small for $0 \leq t \leq T$ when $[F(\underline{u}_1)-(F(\underline{u}_2)]$ is small. In other words, the interval [0,T] must be such that F is a contraction operator.

Let R be the 2m-dimensional Cartesian space containing the m-dimensional vectors $\underline{x}$ and $\underline{y}$. Let $\underline{u}$ belong to a set U such that

$$\underline{u} \in U = \{\underline{u}:\underline{u}\in R, |\underline{u}(t) - \underline{u}(0)| \leq \delta\}$$

$$\text{for } 0 \leq t \leq T > 0 \tag{26}$$

where δ is an arbitrary positive constant. Let there exist a constant k, such that

$$|f(\underline{u}_1,t) - f(\underline{u}_2,t)| \leq k|\underline{u}_1 - \underline{u}_2| \tag{27}$$

where

$$\underline{u}_1,\underline{u}_2 \in U \text{ and } t\in[0,T]$$

Let it also be assumed that there exists a positive number M, such that

$$|f(\underline{u},t)| \leq M \text{ for } \underline{u} \in U;\ t\in [0,T].$$

Now from Eqs. (21), (22) and (23), we have

$$|f(\underline{u}_1,t) - f(\underline{u}_2,t)| = |P\underline{u}_1-P\underline{u}_2+Q\underline{v}(\underline{u}_1,t)-Q\underline{v}(\underline{u}_2,t)$$

$$\tilde{=} |P(\underline{u}_1-\underline{u}_2) + [Q\nabla\underline{v}]\cdot(\underline{u}_1-\underline{u}_2)|$$

$$\leq |P + Q\nabla\underline{v}|\cdot|\underline{u}_1-\underline{u}_2|$$

$$= \left|\begin{bmatrix} -A^{-1}B & A^{-1}(\frac{\partial d}{\partial \underline{y}} - \frac{1}{\varepsilon} I) \\ I & 0 \end{bmatrix}\right| \cdot |\underline{u}_1-\underline{u}_2| \tag{28}$$

Comparing Eqs. (27) and (28), it can be seen that the constant k is given by

k = the largest eigenvalue of the matrix [D]

where [D] is the matrix, given by

$$[D] = \begin{bmatrix} -A^{-1}B & A^{-1}(\nabla_{\underline{y}} d - \frac{1}{\varepsilon} I) \\ I & 0 \end{bmatrix} \tag{29}$$

The variables $\underline{u}(t)$, $\underline{u}(0)$, M and T must satisfy

$$|u(t) - u(0)| \leq \int_0^t |f(\underline{u},t)|dt \leq MT \tag{30}$$

Hence:

$$\|F(\underline{u}_1)-F(\underline{u}_2)\| = \max_{t\in[0,T]} \left| \int_0^t [f(\underline{u}_1,t)-f(\underline{u}_2,t)]dt \right|$$

$$\leq \max_{t\in[0,T]} \int_0^t k|\underline{u}_1(t)-\underline{u}_2(t)|dt$$

$$\leq k\,T\,\|\underline{u}_1-\underline{u}_2\| . \qquad (31)$$

From Eqs. (30) and (31) it can be seen that F will be a contraction if

$$MT < \delta$$

and

$$kT < 1.$$

Hence the required time interval is given by:

$$T < \min. \{\frac{\delta}{M}, \frac{1}{k}\} \qquad (32)$$

Since δ is arbitrary, it is evident that the effective constraint on T is given by:

$$T < \frac{1}{k} \qquad (33)$$

In view of Eq. (33), the interval [0,T] can be very large if k approaches zero. This can happen if

$$A^{-1}B = I \qquad (34)$$

or if

$$\underline{y} = \varepsilon\, \underline{d} \qquad (35a)$$

that is, if

$$A\ddot{\underline{y}} + B\dot{\underline{y}} = 0 \qquad (35b)$$

This analysis thus shows that

$$\underline{y} = 0 \qquad (35c)$$

is a stable singular point of Eq. (17). Hence, it is proved that an asymptotic expansion of Eq. (17) about the point $\underline{y} = 0$ will converge. From the discussion in Section 3, it is seen that this point is the solution to the generalized Euler's equations.

TRUNCATION OF THE SOLUTION SERIES

Let it be assumed that the solution $\underline{y}(\underline{\omega},t)$ of Eq. (17) is approached

through the asymptotic expansion of $\underline{\omega}$ in the form

$$\underline{\omega} = \underline{\omega}_0 + \varepsilon\underline{\omega}_1 + \varepsilon^2\underline{\omega}_2 + \ldots \tag{36}$$

The solution scheme for $\underline{\omega}$ for such a series is given in Ref. [4]. An important requirement in this analysis is the number of terms of this series that are necessary for the solution to be arbitrarily close to the exact one in the interval $0 < t \leq T$. There is an algorithm for estimating

$$\underline{y}^*_{n+1} = \underline{y}\left(\sum_{m=0}^{n+1} \varepsilon^m \underline{\omega}_m\right) \tag{37}$$

from the value of $\underline{y}^*_n$. Let the partial sums of the series given by Eq. (36) be defined by:

$$\underline{\omega}^*_n = \sum_{m=0}^{n} \varepsilon^m \underline{\omega}_m(t) \tag{38}$$

Then Eq. (17) can be approximately expressed as:

$$\underline{y}^*_{n+1} = \varepsilon[\underline{d}(\omega^*_{n+1},t) - A(\omega^*_n,t)\ddot{\underline{y}}^*_n - B(\omega^*_n,t)\dot{\underline{y}}^*_n].$$

Therefore,

$$\underline{y}^*_{n+1} \cong \varepsilon[\underline{d}(\underline{\omega}^*_n,t) + \nabla\underline{d}(\underline{\omega}^*_n,t)\cdot(\underline{y}^*_{n+1}-\underline{y}^*_n) - A(\underline{\omega}^*_n,t)\ddot{\underline{y}}^*_n - B(\underline{\omega}^*_n,t)\dot{\underline{y}}^*_n] \tag{39}$$

Assuming that the valid time domain of the analysis is very large, the condition given by Eq. (35b) is almost satisfied. Thus, from Eq. (39), we get

$$[I-\varepsilon\nabla\underline{d}(\underline{\omega}^*_n,t)]\underline{y}^*_{n+1} = \varepsilon[\underline{d}(\underline{\omega}^*_n,t) - \nabla\underline{d}(\underline{\omega}^*_n,t)\cdot\underline{y}^*_n]$$

or

$$\underline{y}^*_{n+1} \cong \varepsilon[I+\varepsilon\nabla\underline{d}(\underline{\omega}^*_n,t)][\underline{d}(\underline{\omega}^*_n,t) - \nabla\underline{d}(\underline{\omega}^*_n,t)\cdot\underline{y}^*_n]$$

$$\cong \varepsilon[\underline{d}(\underline{\omega}^*_n,t) - \nabla\underline{d}(\underline{\omega}^*_n,t)\cdot\underline{y}^*_n]$$

Therefore,

$$(\underline{y}^*_{n+1}-\underline{y}^*_n) = -\varepsilon[\nabla\underline{d}(\underline{\omega}_n,t)\cdot\underline{y}^*_n] \tag{40}$$

Equation (40) gives an approximate estimate for $\underline{y}^*_{n+1}$. It also bears out the fact that

$$\underline{y}_o = 0$$

is a stable singular point, because the right hand side of Eq. (40) is negative.

JUMP CONDITIONS

Note that the present formulation leads to the governing equation of the system given by Eq. (17), a singular perturbation equation. Several investigators [10-14] have studied singular perturbation equations with a small parameter appearing with the highest derivative of the dependent variable. They have shown that the general symptotic expansions are not valid in the presence of jump conditions.

The existence of jump conditions can be explained as follows. Let

$$\underline{x} = \dot{\underline{y}} \; ; \; \ddot{\underline{x}} = \dot{\underline{y}}$$

Then the phase velocity vector ($\underline{v}$) is defined by:

$$\underline{v} = [\dot{\underline{x}}, \dot{\underline{y}}]^T$$

Therefore a general singularly perturbed system will have the form:

$$\underline{v} = [\dot{\underline{x}}, \dot{\underline{y}}]^T = [\frac{1}{\epsilon} \underline{f}(\underline{x},\underline{y}), \; \underline{g}(\underline{x},\underline{y})]^T \tag{41}$$

where $\underline{f}$ and $\underline{g}$ are regular functions.

Or,

$$\underline{v} = [\frac{1}{\epsilon} \underline{f}(\underline{x},\underline{y}), 0]^T + [0, \underline{g}(\underline{x},\underline{y})]^T \tag{42}$$

The second vector on the right hand side of Eq. (42) is always regular, while the first vector becomes infinite as ϵ approaches zero. This means that, when the phase point $P(\underline{x},\underline{y})$ is not on the surface $\underline{f}(\underline{x},\underline{y}) = 0$, the component $\dot{\underline{x}}$ of the phase velocity away from the surface is very large. However, the component $\dot{\underline{y}}$ is limited. Such motion is maintained until $P(\underline{x},\underline{y})$ comes close to the surface $\underline{f}(\underline{x},\underline{y}) = 0$. Following that, the variables change with finite velocities. For some $\underline{y}$, the point $P(\underline{x},\underline{y})$ may again move away from this surface and the system lose equilibrium. A system which behaves in this unstable manner is said to give a jump. Asymptotic expansions are not valid for such systems. Thus, a stable system of the form given by Eq. (41) must satisfy the degenerate state given by:

$$\underline{f}(\underline{x},\underline{y}) = 0 \tag{43a}$$

$$\underline{g}(\underline{x},\underline{y}) = \dot{\underline{y}} = \underline{x} \tag{43b}$$

If a singular system satisfies Eq. (43a), then $\underline{x}$ can be solved from Eq. (43a) as:

$$\underline{x} = \underline{x}(\underline{y}) \tag{44}$$

and then Eq. (44) can be substituted into Eq. (43b) to yield an explicit

solution for $\underline{y}$. But for a jumping system, $\dot{\underline{x}}$ is unbounded and it is impossible to obtain Eq. (44) from Eq. (43a). The jump condition, that is, the condition for unbounded $\dot{\underline{x}}(t)$, is:

$$\lim_{\varepsilon \to 0} [\text{Det.}[\frac{\partial \underline{f}}{\partial \underline{x}}]] = 0 \tag{45}$$

Hence, asymptotic expansions are not valid for a system for which Eq. (45) is satisfied.

Due to the presence of ε in Eq. (17) with the terms containing $\dot{\underline{y}}(t)$, $\underline{d}(t)$ and $\ddot{\underline{y}}(t)$, the values of $\dot{\underline{x}}(t) = \underline{y}(t)$ remain finite. In other words, there is no jump when $\varepsilon \to 0$, although Eq. (17) is singularly perturbed. This becomes evident by allowing $\varepsilon \to 0$, so that Eq. (17) becomes

$$\underline{y}(\underline{\omega}, t) = 0. \tag{46}$$

Hence, subtracting this equation from Eq. (17),

$$\lim_{\varepsilon \to 0} \ddot{\underline{y}}(\underline{\omega}, t) = \lim_{\varepsilon \to 0} \dot{\underline{x}} = A^{-1}(\underline{d} - B\underline{x}) < \infty \tag{47}$$

By comparing Eqs. (17) and (41),

$$\underline{f}(\underline{x}, \underline{y}) = \varepsilon A^{-1}[\underline{d} - B\underline{x}] - A^{-1}\underline{y}.$$

Hence,

$$\lim_{\varepsilon \to 0} [\frac{\partial \underline{f}}{\partial \underline{x}}] = \lim_{\varepsilon \to 0} [-\varepsilon A^{-1}B) = 0 \tag{48}$$

It should be noted that Eq. (17) has a peculiar property of satisfying Eq. (45) although $\underline{x}$ remains finite as $\varepsilon \to 0$. The property of satisfied jump conditions in a system in equilibrium is exhibited by singularly perturbed equations where the small parameter appears with all the derivatives of the dependent variable.

Equation (46) provides the only stable singular point of the system. An asymptotic expansion about this point is valid. Such a scheme for solving Eq. (17) is given in Ref. [4].

BOUNDARY LAYERS

It has thus far been proved that Eq. (17) is amenable for solution by an asymptotic series. One advantage is that such solution procedures lead to purely algebraic instead of differential equations. This can be verified from Ref. [4]. With this procedure, the asymptotic solutions for $\underline{y}(t)$ are independent of the initial conditions, $\underline{y}(0)$. Thus, for purely long term responses of a satellite, the asymptotic solutions are satisfactory. For determining the transient response of the satellite near the time t=0, a different approach must be taken. It is a physical reality that, immediately after a controlling or a disturbing torque pulse, the behavior of a satellite is markedly different than it is in a

quiescent period. This observation leads to the premise that there may exist two or more response periods, such that the nature of the satellite response varies from period to period. And it is likely that the effect of the initial conditions ($\underline{y}(0)$) on the satellite will be dominant in the periods close to t=0.

This physical concept is mathematically verified by the introduction of boundary layers in the time domain. Such boundary layers have been studied in Refs. [8,11,15,16 and 17] and are shown to exist in all singularly perturbed systems. The essential feature is that this procedure divides the total response period into several parts and the solution is obtained separately. The thicknesses of the layers are of the order of ε, the small parameter. In the present formulation, both $\ddot{\underline{y}}$ and $\dot{\underline{y}}$ are associated with ε. Hence, there are two boundary layers to be investigated.

THE INNER BOUNDARY LAYER SOLUTION

The inner boundary layer solution for $\underline{y}(\underline{\omega}, \tau)$ is obtained by considering the fast time ('τ') as the independent variable, where τ is related to real time (t) by

$$t = \varepsilon\tau \quad \text{for } 0 \leq t \leq \varepsilon \tag{49}$$

The angular velocity vector ($\underline{\omega}$) was given previously by Eq. (36). Let $\underline{y}(\underline{\omega}, \tau)$ be expanded in a Taylor's series about $\underline{\omega}_o$. Then, expanding the matrix $A_{ij}(\underline{\omega},\tau)$ around $\tau = 0$ and $\underline{\omega} = \underline{\omega}_o$ in a Taylor's series, we get,

$$A_{ij}(\underline{\omega},\tau) = A_{ij}(\underline{\omega},0) + \varepsilon\dot{A}_{ij}(\underline{\omega},0)\,\tau + \frac{\varepsilon^2}{2}\ddot{A}_{ij}(\omega,0)\,\tau^2 + \ldots \tag{50}$$

$$A_{ij}(\underline{\omega},0) = A_{ij}(\underline{\omega}_o,0) + \varepsilon A_{ij,k}(\underline{\omega}_o,0)\omega_{1k} + \varepsilon^2\left[A_{ij,k}(\underline{\omega}_o,0)\omega_{2k} + \frac{1}{2}A_{ij,k\ell}(\underline{\omega}_o,0)\omega_{1k}\omega_{1\ell}\right] + \ldots \tag{51}$$

$$\dot{A}_{ij}(\underline{\omega},0) = \dot{A}_{ij}(\underline{\omega}_o,0) + \varepsilon\dot{A}_{ij,k}(\underline{\omega}_o,0)\omega_{1k} + \ldots \tag{52}$$

Similarly, $B(\underline{\omega},t)$ and $\underline{d}(\underline{\omega},t)$ are expanded in Taylor's series around $\tau = 0$ and $\underline{\omega} = \underline{\omega}_o$. Substituting these expansions in Eq. (17) and using the relations

$$\frac{dy}{dt} = \frac{1}{\varepsilon}\frac{dy}{d\tau}, \qquad \frac{d^2y}{dt^2} = \frac{1}{\varepsilon^2}\frac{d^2y}{d\tau^2} \tag{53}$$

the coefficients of ε^{-1} and ε^0 generate the following equations:

$$\frac{d^2}{d\tau^2}\underline{y}(\omega_o,\tau) = 0 \tag{54}$$

$$[A(\underline{\omega}_o,0)][\nabla \underline{y}(\underline{\omega}_o,\tau)]\frac{d^2}{d\tau^2}\underline{\omega}_1 + B(\underline{\omega}_o,0)\frac{d}{d\tau}\underline{y}(\underline{\omega}_o,\tau) + \underline{y}(\underline{\omega}_o,\tau) = 0 \qquad (55)$$

Equations for $\underline{\omega}_2$, $\underline{\omega}_3$, and other higher order terms of the series given by Eq. (36) can be obtained by substituting Eqs. (51), (52), (53), etc. into Eq. (17) and separating the coefficients of ε, ε^2, ε^3, and higher powers of ε.

Note that the original governing equation (17) does not degenerate into algebraic equations, but leads to a set of differential equations. Of these, the first two are Eqs. (54) and (55). The interval in which these equations is valid is given by $0 \leq t \leq \varepsilon$ or $0 \leq \tau \leq 1$. Thus, the effects of the initial values of the generalized force $(\underline{y})$ are not lost. This is in sharp contrast to the asymptotic solutions in which the independent variable was unscaled real time (t).

The solution of Eq. (54) is:

$$\underline{y}(\underline{\omega}_o,\tau) = \underline{a}\tau + \underline{b} \qquad (56)$$

where '$\underline{a}$' and '$\underline{b}$' are constants. Using Eq. (56) and the boundary conditions

$$\dot{\underline{\omega}}_1(0) = \underline{\omega}_1(0) = 0 \qquad (57)$$

the solution of Eq. (55) is obtained by integrating twice

$$\ddot{\underline{\omega}}_1(\tau) = -\{[\nabla \underline{y}(\underline{\omega}_o,0)]^{-1}[A(\underline{\omega}_o,0)]^{-1}\}[B(\underline{\omega}_o,0)\underline{a} + \underline{a}\tau + \underline{b}] \qquad (58)$$

Thus, considering the first two terms only, the vector $\underline{\omega}$ is given by:

$$\underline{\omega}(\tau) = \underline{\omega}_o(\tau) + \varepsilon\underline{\omega}_1(\underline{\omega}_o,\tau) \qquad (59)$$

The constants $\underline{a}$ and $\underline{b}$ are obtained by matching the solution given by Eq. (59) with the asymptotic solution for $\underline{\omega}$ at $\tau = 1$. Keep in mind that $\underline{w}_o(\tau)$ is to be solved first from Eq. (56), the solution of the first of a set of generalized Euler's equations obtained from the perturbation scheme.

THE OUTER BOUNDARY LAYER SOLUTION

The scaling procedure does lead to a different family of solutions for the generalized force $\underline{y}(\underline{\omega},t)$ near $t = 0$. This is corroborated by experience. But the linear nature of $\underline{y}(\underline{\omega}_o,\tau)$, as seen from Eq. (56), means that $\underline{y}$ becomes infinite as τ becomes large. Thus Eq. (56) does not satisfy the requirement of a boundary layer solution having the same form as the asymptotic solution when τ becomes infinite. For this reason, a different solution for $\underline{y}$ is obtained in an outer boundary layer which extends beyond the inner boundary layer.

The thickness of the outer boundary layer is taken to be $\sqrt{\varepsilon}$. The fast time (τ) in this case is given by:

$$t = \sqrt{\varepsilon}\ \tau \qquad \text{for } 0 \le t \le \sqrt{\varepsilon} \text{ or } 0 \le \tau \le 1.$$

With this scale, we have

$$\frac{dy}{dt} = \frac{1}{\sqrt{\varepsilon}} \frac{dy}{d\tau}$$

and

$$\frac{d^2y}{dt^2} = \frac{1}{\varepsilon} \frac{d^2y}{d\tau^2} \tag{60}$$

Using the series of Eq. (36), the functions $A(\underline{\omega},t)$, $B(\underline{\omega},t)$, and $d(\underline{\omega},t)$ are expanded in Taylor's series about $\underline{\omega} = \underline{\omega}_o$ and $t = 0$ as shown in Section 9. These series and the relations given in Eq. (60) are substituted in Eq. (17). Then, separating the terms containing ε^0 and $\sqrt{\varepsilon}$, and equating that to zero, we get:

$$A_{ij}(\underline{\omega}_o,0)\ddot{y}_j(\underline{\omega}_o,\tau) + \sqrt{\varepsilon}\, B_{ij}(\underline{\omega}_o,0)\dot{y}_j(\underline{\omega}_o,\tau) + y_i(\underline{\omega}_o,\tau) = 0 \tag{61}$$

Proceeding similarly, and equating the coefficients of ε to zero, we get:

$$[A(\underline{\omega}_o,0)][\nabla\underline{y}(\underline{\omega}_o,\tau)]\ddot{\underline{\omega}}_1 + 2[A(\underline{\omega}_o,0)][\nabla\dot{\underline{y}}(\underline{\omega}_o,\tau)]\dot{\underline{\omega}}_1$$

$$+ \nabla\{[A(\underline{\omega}_o,0)][\ddot{y}(\underline{\omega}_o,\tau)] + y(\underline{\omega}_o,\tau)\}\underline{\omega}_1 = \underline{d}(\underline{\omega}_o,0) \tag{62}$$

Equations (61) and (62) are general second order equations with constant coefficients. Thus, with this time scale, the quantities $\underline{y}(\underline{\omega}_o,\tau)$ and $\underline{\omega}_1(\tau)$ satisfy the equations for damped oscillations.

Let the one term perturbation solutions for the inner and outer boundary layer and the asymptotic time zones be:

$$\underline{y}(\underline{\omega}_o,\tau) + \varepsilon[\nabla\underline{y}(\underline{\omega}_o,\tau)]\underline{\omega}_1 \quad ; \quad 0 \le \tau \le \varepsilon$$

$$\underline{y}(\underline{\omega}_o,\tau) + \varepsilon[\nabla\underline{y}(\underline{\omega}_o,\tau)]\underline{\omega}_1 \quad ; \quad \varepsilon \le \tau \le \sqrt{\varepsilon}$$

and

$$\underline{y}(\underline{\omega}_o,t) + \varepsilon[\nabla\underline{y}(\underline{\omega}_o,t)]\underline{\omega}_1 \quad ; \quad \sqrt{\varepsilon} \le t$$

respectively. The constants are determined by applying continuity conditions at $\tau = \varepsilon$ and $\tau = t = \sqrt{\varepsilon}$. The angular velocities [18] will be continuous throughout these three time zones and subject to control [18] if the amplitude exceeds the nominal values of the angular velocities in any of the zones.

In the large-time asymptotic solutions [4], $\underline{y}(\underline{\omega}_o,t)$ is equal to zero. For a stable satellite, $\underline{\omega}_1(t)$ has the same damped oscillatory form as $\underline{\omega}_o(t)$. As $\tau \to \infty$, the forms of the outer boundary layer solutions and the asymptotic solutions become compatible, unlike that for the inner boundary layer solutions.

STABILITY CRITERIA OF y

Although the solution

$$\underline{y} = \underline{f}(t)$$

is itself a differential equation, it does not necessarily follow that the satellite response will be stable if $\underline{y}$ is stable. But, for the satellite response to be stable, $\underline{y}(t)$ must be bounded.

If either M_1 or M_2 is equal to zero, it has been shown [1] that $\underline{y}(t)$ essentially satisfies Eq. (1). Since Eq. (1) has to be stable in any case, no new conditions are obtained.

If neither M_1 nor M_2 is equal to zero, it is assumed that the matrices A_1, A_3, P_1, and P_3 are positive definite. From Eq. (16) it can be seen that the coefficient of $\ddot{\underline{y}}$ is positive semi-definite. This leads to the necessary condition of the coefficient of $\underline{y}$, $[(P_2A_2^{-1}-P_3A_3^{-1})A_2M_2^{-1}]$, being positive semi-definite. This condition will be satisfied if the following inequalities hold:

(a) If A_2 and P_2 are negative semi-definite, then

$$\|P_1A_1^{-1}\| < \|P_3A_3^{-1}\| < \|P_2A_2^{-1}\|$$

or

$$\|P_1A_1^{-1}\| > \|P_3A_3^{-1}\| > \|P_2A_2^{-1}\| \tag{63}$$

(b) If A_2 and P_2 are positive semi-definite, then

$$\|P_1A_1^{-1}\| > \|P_3A_3^{-1}\| < \|P_2A_2^{-1}\|$$

or

$$\|P_1A_1^{-1}\| < \|P_3A_3^{-1}\| > \|P_2A_2^{-1}\| \tag{64}$$

These inequalities produce an approximate estimate of the conditions of stability of $\underline{y}$.

CONCLUSIONS

In this paper, several important features of the singularly perturbed formulation for a flexible satellite were explored. The procedure yields a method of separating the total response period of a satellite into two boundary layers and a large time zone. This produces a simpler procedure than that encompassing the complete response in only one set of solutions. In each period, the same set of generalized Euler's equations, given by:

$$\underline{y}(\underline{\omega}_o,t) = \underline{f}(t) \tag{65}$$

is to be solved with different forcing functions, f(t). The only limita-

tion in this method is that the determination of the higher order terms of the infinite series for the angular velocities requires complicated evaluation of the coefficients of Taylor's series. A method for obtaining $\underline{\omega}_o$ from equations similar to Eq. (75) was also obtained. The complete solution will be reported in Ref. [18].

ACKNOWLEDGEMENTS

This work was supported in part by the National Aeronautics and Space Administration under Contract No. NAS5-21798 through the Space Science and Engineering Center, University of Wisconsin, Madison, Wisconsin.

REFERENCES

1. Das, A., and Huang, T. C., "Pointing Error Analysis of Geosynchronous Satellites, Parts I-III," Technical Report, Space Science and Engineering Center, Madison, Wisconsin, December 1972; NASA Contract Report No. NAS5-11542.

2. Das, A., and Huang, T. C., "Pointing Error Analysis of Geosynchronous Satellites, Parts IV-VI," Technical Report, Space Science and Engineering Center, Madison, Wisconsin, October 1973; NASA Contract Report No. NAS5-11542.

3. Huang, T. C., and Das, A., "Thermoelastic Flutter Models for Elements of Flexible Satellites," paper presented at the 24th International Astronautical Congress, October 1973, Baku, U.S.S.R.

4. Huang, T. C., and Das, A., "Singular Perturbation Equations for Flexible Satellites," paper presented at the 24th International Astronautical Congress, October 1973, Baku, U.S.S.R.

5. Likins, P. W., "Attitude Stability of Dual-Spin Systems," Space Systems Research Report, Hughes Aircraft Co., SSD 60377R, September 1966.

6. Likins, P. W., and Gale, A. H., "The Analysis of Interactions Between Attitude Control Systems and Flexible Appendages," Paper IAF AD 29, 19th International Astronautical Congress, New York, October 1968.

7. Hale, J. K., Oscillations in Nonlinear Systems, McGraw-Hill, 1963.

8. Cole, J. D., Perturbation Methods in Applied Mathematics, Blaisdell, 1968.

9. Holtzman, J. M., Nonlinear System Theory; A Functional Analysis Approach, Prentice-Hall, Englewood Cliffs, N. J., 1970.

10. Flatto, L., and Levinson, N., "Periodic Solutions of Singularly Perturbed Systems," J. Rational Mech. and Anal., Vol. 4, 1955, pp. 943-950.

11. Levin, J. J., and Levinson, N., "Singular Perturbations of Nonlinear Systems of Differential Equations and Associated Boundary Layer Equations," J. Rational Mech. and Anal., Vol. 3, 1954, pp. 247-270.

12. Pontryagin, L. S., and Rodygin, L. V., "Approximate Solution of a System of Ordinary Differential Equations Involving a Small Parameter in the Derivatives," Soviet Math. Dokl., Vol. 1, 1960, pp. 237-240.

13. Beljaeva, M. A., "Approximate Solution of a System of Ordinary Differential Equations Having a Small Parameter with the Derivatives," Soviet Math. Dokl., Vol. 10, 1969, pp. 1556-1559.

14. Kasymov, K. A., "The Asymptotic Behaviour of the Solution of the Initial Jump Problem for Nonlinear Systems of Differential Equations with a Small Parameter in the Leading Derivative," Soviet Math. Dokl., Vol. 10, 1969, pp. 1531-1535.

15. Coddington, E. A., and Levinson, N., "A Boundary Value Problem for a Nonlinear Differential Equation with a Small Parameter," Proc. Amer. Math. Soc., Vol. 3, 1952, pp. 73-81.

16. Wasow, W., "Singular Perturbations of Boundary Value Problems for Nonlinear Differential Equations of the Second Order," Comm. Pure and Applied Math., Vol. 9, 1956, pp. 93-113.

17. Erdelyi, A., "Singular Perturbation," Bull. Amer. Math. Soc., Vol. 68, 1962, pp. 420-424.

18. Huang, T. C., and Das., A., "Nonlinear Motion Analysis and Control of Flexible Satellites," In preparation.

NONLINEAR MOTION ANALYSIS AND CONTROL OF FLEXIBLE SATELLITES

Aniruddha Das and T. C. Huang

ABSTRACT

Solutions for the angular velocities of a flexible satellite are obtained. The governing equations are derived from the singularly perturbed formulation reported in a previous paper. Deterministic behavior of the disturbing and controlling torques is assumed. The design of an optical control system is also presented.

NOMENCLATURE

A = Generalized mass matrix; Eq. (1).

A_i, i=1-4 = Matrices and vector associated with the equation of motion of flexible elements of the satellite; Eq. (4).

A^* = A composite body of the satellite.

$\underline{a}_n$, i=1,2,3,... = Initial value vectors for $\underline{x}_n$.

B = Generalized damping matrix; Eq. (1).

B_i, i=1-3 = Matrices associated with the perturbation equations for $\underline{x}_n$; Eq. (49).

B^* = A composite body of the satellite.

$\underline{b}_n(T)$ = Specified value of $\underline{x}_n(t)$ at $t = T$.

$\underline{b}'_n$ = Error vector in $\underline{x}_n(T)$; Eq. (71).

$\bar{b}$ = Normalization constant for $\underline{\lambda}$; Eq. (73).

C^1, C^2 = Coefficient matrices; Eqs. (29) and (30).

c_1, c_2 = Real and imaginary parts of p_i; Eq. (82).

$\underline{d}$ = Forcing function; Eq. (1).

$\underline{F}_n(t)$ = Forcing functions; Eqs. (43), (48), (49).

$\underline{F}'_n(t)$, $\underline{F}''(t)$ = Components of $\underline{F}_n(t)$; Eq. (57); Eqs. (94), (95).

$\underline{f}(t)$, $f'(t)$, $f''(t)$ = Forcing functions; Eqs. (3), (33), (35).

$H(T)$ = Minimization functional; Eq. (72).

$\underline{\nabla}H(T)$ = Gradient of H(T); Eq. (75).

$\underline{h}(t)$ = Reaction wheel angular momentum vector

I = Identity matrix.

I_1, I_2 = Integrals; Eqs. (58), (60).

I_A, I_B = Moment of inertia matrices for the composite bodies A* and B*, respectively.

I_A^*, I_B^* = Matrices derived from I_A or I_B; Eq. (14).

$k(t,\tau)$ = Kernel matrix for Duhamel's integrals; Eq. (64).

M = Eigenvector matrix for Eq. (52).

M' = Matrix derived from M; Eq. (54).

N_{Ai}, N_{Bi} = Matrices; Eqs. (99a,b).

n = Order of perturbation.

P_i, i=1-4 = Matrices and vector associated with the generalized Euler's equation; Eq. (5).

P_i = Eigenvalues of Eq. (54).

$\underline{q}$ = Generalized position coordinates of the flexible elements of the satellite; Eqs. (4), (5).

$\underline{r}(t)$ = Eigenfunctions of Eq. (52).

r', r'', r''' = Functions derived from r(t); Eqs. (59), (59a), (77).

S_{Ai} or S_{Bi}, i=1-5 = Matrices associated with the generalized Euler's equations; Eqs. (16), (17).

S'_{A3}, S'_{B3} = Matrices; Eq. (100).

s = Step size for λ.

T = Terminal time.

$\underline{T}_A, \underline{T}_B$ = Forcing function; Eqs. (11), (13).

$\underline{T}_{EB}, \underline{T}_{EA}$ = External disturbing torques; Eq. (13).

$\underline{T}_{Bi}$, i=0,1,2 = Components of $\underline{T}_{EB}$; Eq. (13a).

U = Norm of the control torques; Eqs. (67), (70), (74).

$\underline{u}_n$, n=1,2... = Augmented control torque vectors; Eqs. (42), (47), (49).

$\underline{u}_A, \underline{u}_B$ = Control torque vecotrs.

$\underline{u}_{Ai}, \underline{u}_{Bi}, i=1,2...$ = Components of $\underline{u}_A$, $\underline{u}_B$; Eq. (21).

$\underline{v}_A, \underline{v}_B$ = Forcing functions; Eq. (20).

$\underline{x}_n$, n=1,2,... = Perturbation vectors; Eqs. (44), (46), (49).

$\underline{x}_n^*$ = Uncontrolled component of $\underline{x}_n$; Eq. (63).

$\underline{x}_n'$, $\underline{x}_n''$ = Components of $\underline{x}_n$; Eqs. (92), (93).

$\underline{y}(t)$ = Generalized force for the singularly perturbed formulation; Eqs. (1), (3), (6).

z_1, z_2 = Adjustment factors for s; Eq. (76).

$\delta_{Ai}, \delta_{Bi}, i=1-6$ = Matrices associated with the generalized Euler's equations; Eqs. (7), (11).

$\varepsilon, \varepsilon'$ = Small parameters; Eqs. (1), (20).

$\underline{\eta}$ = Component of $\underline{\omega}_A$ or $\underline{\omega}_B$; Eq. (27).

$\dot{\underline{\theta}}$ = Angular velocity of A* relative to B*, Eq. (19).

$\dot{\underline{\theta}}_i$ = Components of $\underline{\theta}$; Eq. (21).

λ_i = Maximizing parameter; Eq. (68).

μ_i = Relative control vector amplitude; Eq. (69).

Φ = Fundamental matrix of Eq. (52).

Ψ_{Ai}, Ψ_{Bi} = Component functions of $\underline{\omega}_A$, $\underline{\omega}_B$; Eq. (87).

$\underline{\omega}, \underline{\omega}_i, i=0,1,2,...$ = Angular velocity of the composite bodies and its components; Eq. (2).

$\underline{\omega}_A, \underline{\omega}_B$ = Values of $\underline{\omega}_o$ for the bodies A* add B*.

$\underline{\omega}_{Ai}, \underline{\omega}_{Bi}$ = Components of $\underline{\omega}_A$, $\underline{\omega}_B$; Eq. (21).

$\underline{\omega}_{Ai}'$, $\underline{\omega}_{Bi}'$ = Components of $\underline{\omega}_A$, $\underline{\omega}_B$; Eq. (87).

INTRODUCTION

This study is a part of an analysis of the comparative pointing errors of different types of satellites [1,2]. It is the fourth paper of a series; the three previous are Refs. [3,4,5].

It was shown in Refs. [4,5] that it is possible to formulate the response of a flexible satellite in the form of a singularly perturbed equa-

tion given by:

$$\varepsilon A\ddot{\underline{y}} + \varepsilon B\dot{\underline{y}} + \underline{y} = \varepsilon \underline{d} \tag{1}$$

where A, B, $\underline{y}$, and $\underline{d}$ are functions of the angular velocities of the satellite. It was also shown in [4,5], that, taking $\underline{\omega}$ in the form of an infinite series,

$$\underline{\omega} = \underline{\omega}_0 + \varepsilon\underline{\omega}_1 + \varepsilon^2 \underline{\omega}_2 + \cdots \tag{2}$$

$\underline{\omega}_0$ will be given by:

$$\underline{y}(\underline{\omega}_0, t) = \underline{f}(t) \tag{3}$$

where $\underline{f}(t)$ is a known forcing function. For the long term solutions, $\underline{f}(t) = 0$. For the boundary layer solutions near the time $t = 0$, $\underline{f}(t)$ is either a linear function of time, or a damped oscillatory function. After solving $\underline{\omega}_0$ from Eq. (3), $\underline{\omega}_1$, $\underline{\omega}_2$, and other terms of the series can be obtained explicitly in terms of $\underline{\omega}_0(t)$.

Refs. [4,5] mentioned that Eq. (3) represents the generalized Euler's equations where the effects of the flexible elements of the satellite are included. In the present study, explicit expressions for $\underline{y}(\underline{\omega}_0, t)$ will be obtained for both a dual-spin and a single-body satellite. The angular velocity responses will then be obtained with a perturbation procedure assuming that the distrubing and controlling torques are deterministic. A time-optimal control policy will be used to calculate the controlled response of the satellite.

THE EXPLICIT FORM OF $\underline{y}(\underline{\omega}_0, t)$

A considerable amount of literature already exists [6,7,8,9] in which equations of motion of flexible satellites are studied. From these works, as well as from Refs. [1,4,5], it is evident that the following two sets of equations describe the satellite response:

$$A_1\ddot{\underline{q}} + A_2(\underline{\omega}, t)\dot{\underline{q}} + A_3(\underline{\omega}, t)\underline{q} = \underline{A}_4(\underline{\omega}, t) \tag{4}$$

and

$$P_1\ddot{\underline{q}} + P_2(\underline{\omega}, t)\dot{\underline{q}} + P_3(\underline{\omega}, t)\underline{q} = \underline{P}_4(\underline{\omega}, t) \tag{5}$$

Equation (4) governs the motion of the flexible elements of the satellite, while Eq. (5) is essentially the Euler's equation for the conservation of angular momentum of the whole satellite. It has been shown in Refs. [4,5] that eliminating the generalized position vector ($\underline{q}$) from Eqs. (4) and (5) leads to Eq. (1) where ε is a small parameter and is equal to the largest eigenvalue of $[A_1A_3^{-1}]$. It was also shown that the generalized force vector, $\underline{y}(\underline{\omega}, t)$, is given by:

$$\underline{y} = \underline{A}_4 - A_1(A_1+P_1)^{-1}(\underline{A}_4+\underline{P}_4) \tag{6}$$

Consider a dual-spin satellite which consists of two composite bodies (A* and B*) connected by a connector (C*). Let $\underline{\omega}_A$ and $\underline{\omega}_B$ be

the angular velocities of the bodies A* and B* respectively. Let $\underline{\theta}$ be the angular displacement of the body A* with respect to the body B*. It is explained in Refs. [1,6,7,8] that the function, $\underline{A}_4(\underline{\omega},t)$, for the body B* is of the form:

$$\underline{A}_4(\underline{\omega}_B,t) = [\delta_{B1}]\dot{\underline{\omega}}_B + [\delta_{B2}]\hat{\underline{\omega}}_B + [\delta_{B3}]\dot{\underline{\theta}} + [\delta_{B4}]\underline{\theta} \qquad (7)$$

where the vectors $\underline{\omega}_B$ and $\hat{\underline{\omega}}_B$ are given by:

$$\underline{\omega}_B = [\omega_{B,1},\omega_{B,2},\omega_{B,3}]^T \qquad (8)$$

$$\hat{\underline{\omega}}_B = [\omega^2_{B,1},\omega^2_{B,2},\omega^2_{B,3},\omega_{B,1}\omega_{B,2},\omega_{B,2}\omega_{B,3},\omega_{B,3}\omega_{B,1}]^T \qquad (9)$$

The matrices $[\delta_{Bi}]$ are constants. Similar equations also exist for the body A*, with the condition that:

$$[\delta_{B3}] = -[\delta_{A3}]$$

and

$$[\delta_{B4}] = -[\delta_{A4}] \qquad (10)$$

This is true because the terms involving $\underline{\theta}$ and $\dot{\underline{\theta}}$ appear due to the contact forces and torques between the two bodies of the dual-spin configuration under consideration.

The form of the function $\underline{P}_4(\underline{\omega},t)$ for the body B* is given by:

$$\underline{P}_4(\underline{\omega}_B,t) = \underline{T}_B - [I_B]\dot{\underline{\omega}}_B + [\tilde{h}_B]\underline{\omega}_B - \tilde{\omega}_B[I_B]\underline{\omega}_B - [\delta_{B5}]\dot{\underline{\theta}} - [\delta_{B6}]\underline{\theta} \qquad (11)$$

In this equation, $[I_B]$ is the moment of inertia matrix of the composite body B* and $\underline{h}_B$ is the reaction wheel momentum vector. The operator ($\sim$) is defined by:

$$[\tilde{h}] = \begin{bmatrix} 0 & -h_3 & h_2 \\ h_3 & 0 & -h_1 \\ -h_2 & h_1 & 0 \end{bmatrix} \qquad (12)$$

The vector $\underline{T}_B$ is given by:

$$\underline{T}_B = \underline{u}_B - \dot{\underline{h}}_B + \underline{T}_{EB} \qquad (13)$$

where $\underline{u}_B$ is the controlling torque vector and $\underline{T}_{EB}$ is the external distur-

bing torque vector on the body B*. The form of Eq. (11) is explained in Refs. [1,6,7,8]. Let $\underline{T}_{EB}$ be given by:

$$\underline{T}_{EB} = \underline{T}_{BO}(t) + T_{B1}\underline{\omega}_B + T_{B2}\hat{\underline{\omega}}_B \tag{13a}$$

Let the matrix $[I_B^*]$ be defined by:

$$[I_B^*]\hat{\underline{\omega}}_B = \tilde{\omega}_B[I_B]\underline{\omega}_B \tag{14}$$

Let the constant matrix $[\delta_B^*]$ be defined by:

$$[\delta_B^*] = [A_1][A_1+P_1]^{-1} \tag{15}$$

Then substitute Eqs. (7), (11), (14), and (15) into Eq. (6). Equation (3) for the body B* thus becomes:

$$[S_{B1}]\dot{\underline{\omega}}_B + [S_{B2}]\dot{\underline{\theta}} + [S_{B3}]\underline{\omega}_B + [S_{B4}]\underline{\theta} + [S_{B5}]\hat{\underline{\omega}}_B$$

$$- [\delta_B^*][\underline{u}_B - \dot{\underline{h}}_B + \underline{T}_{BO}(t)] = \underline{f}_B(t) \tag{16}$$

where:

$$S_{B1} = (I-\delta_B^*)\delta_{B1} + \delta_B^* I_B$$

$$S_{B2} = (I-\delta_B^*)\delta_{B3} + \delta_B^* \delta_{B5}$$

$$S_{B3} = \delta_B^*[T_{B1} - \tilde{h}_B]$$

$$S_{B4} = (I - \delta_B^*)\delta_{B4} + \delta_B^*\delta_{B6}$$

$$S_{B5} = (I - \delta_B^*)\delta_{B2} + \delta_B^*(I_B^* - T_{B2}) \tag{17}$$

and $\underline{f}_B(t)$ is the function $\underline{f}(t)$ corresponding to the body B*. An equation similar to Eq. (16) holds for the body A* and is given by:

$$[S_{A1}]\dot{\underline{\omega}}_A + [S_{A2}]\dot{\underline{\theta}} + [S_{A3}]\underline{\omega}_A + [S_{A4}]\underline{\theta} + [S_{A5}]\hat{\underline{\omega}}_A$$

$$- [\delta_A^*]\ [\underline{u}_A - \dot{\underline{h}}_A + \underline{T}_{AO}(t)] = \underline{f}_A(t) \tag{18}$$

where the definitions of S_{Ai} and S_{Bi} are analogous for each i. For a dual-spin system, Eqs. (16) and (18) are coupled by the variable θ. This, in turn, must satisfy the relation:

$$\dot{\underline{\theta}} = \underline{\omega}_A - \underline{\omega}_B - \tilde{\omega}_B\underline{\theta} \tag{19}$$

Thus, for a dual-spin system, Eq. (3) implies that Eqs. (16), (18), and (19) must be solved simultaneously. This procedure can be extended easily

to the case of flexible satellites with more than two composite bodies. With a single body satellite, $\underline{\theta}$ does not exist. Hence in this case, only Eq. (16) is to be solved with

$$[S_{B2}] = [S_{B4}] = 0$$

Generally, for a single-body satellite, Eq. (3) contains only three scalar equations corresponding to the three angular velocities. For a dual-spin system, Eq. (3) implies that the nine equations in Eqs. (16), (18), and (19) are to be solved. These numbers can be increased to obtain greater accuracy by transferring some of the structural equations from Eq. (4) to Eq. (5). A more detailed discussion on this aspect is given in Ref. [4].

PERTURBATION SERIES

An approach for solving Eqs. (16), (18), and (21) for the dual-spin case will now be presented. The particular case of a single body system will follow essentially the same procedure. Let

$$\varepsilon' \underline{v}_B(t) = \underline{f}_B(t) + [\delta_B^*](\underline{T}_{BO} - \dot{\underline{h}}_B)$$

and

$$\varepsilon' \underline{v}_A(t) = \underline{f}_A(t) + [\delta_A^*](\underline{T}_{AO} - \dot{\underline{h}}_A) \tag{20}$$

where ε' is the larger magnitude of the terms on the right hand sides of the equations in Eq. (20). In general ε' will be small. Taking ε' as a small parameter, perturbation series are now considered for $\underline{\omega}_A$, $\underline{\omega}_B$, $\underline{\theta}$, $\underline{u}_A$, and $\underline{u}_B$. Let

$$\underline{\omega}_A = \underline{\omega}_{AO} + \varepsilon' \underline{\omega}_{A1} + (\varepsilon')^2 \underline{\omega}_{A2} + \ldots$$

$$\underline{\omega}_B = \underline{\omega}_{BO} + \varepsilon' \underline{\omega}_{B1} + (\varepsilon')^2 \underline{\omega}_{B2} + \ldots$$

$$\underline{\theta} = \underline{\theta}_0 + \varepsilon' \underline{\theta}_1 + (\varepsilon')^2 \underline{\theta}_2 + \ldots$$

$$\underline{u}_A = \varepsilon' \underline{u}_{A1} + (\varepsilon')^2 \underline{u}_{A2} + (\varepsilon')^3 \underline{u}_{A3} + \ldots$$

and

$$\underline{u}_B = \varepsilon' \underline{u}_{B1} + (\varepsilon')^2 \underline{u}_{B2} + (\varepsilon')^3 \underline{u}_{B3} + \ldots \tag{21}$$

where $\underline{\omega}_{AO}$ and $\underline{\omega}_{BO}$ are the constant nominal angular velocities of the bodies A* and B*.

The series for $\underline{\omega}_A$, $\underline{\omega}_B$, and $\underline{\theta}$ are substituted into Eq. (19) and the coefficients of the powers of ε' are separated. This procedure yields the equations:

$$\dot{\underline{\theta}}_0 = \underline{\omega}_{A0} - \underline{\omega}_{B0} - \tilde{\underline{\omega}}_{B0}\underline{\theta}_0 \tag{22}$$

$$\dot{\underline{\theta}}_1 = \underline{\omega}_{A1} - \underline{\omega}_{B1} - \tilde{\underline{\omega}}_{B0}\underline{\theta}_1 + \tilde{\underline{\theta}}_0\underline{\omega}_{B1} \tag{23}$$

Equations for $\dot{\underline{\theta}}_n$ for $n \geq 2$ are similarly obtained. As $\underline{\theta}_0$ is arbitrary, let

$$\underline{\theta}_0 = \underline{0}$$

Hence Eqs. (22) and (23) become

$$\dot{\underline{\theta}}_0 = \underline{\omega}_{A0} - \underline{\omega}_{B0} = \text{a constant} \tag{24}$$

$$\dot{\underline{\theta}}_1 = \underline{\omega}_{A1} - \underline{\omega}_{B1} - \tilde{\underline{\omega}}_{B0}\underline{\theta}_1 \tag{25a}$$

Similarly,

$$\dot{\underline{\theta}}_2 = \underline{\omega}_{A2} - \underline{\omega}_{B2} - \tilde{\underline{\omega}}_{B0}\underline{\theta}_2 - \tilde{\underline{\omega}}_{B1}\underline{\theta}_1 \tag{25b}$$

The nonlinear vector $\hat{\underline{\omega}}_B$ is now expanded in a Taylor's series about $\underline{\omega}_{B0}$. This gives:

$$\hat{\omega}_{B,i} = \hat{\omega}_{B0,i} + \left[\frac{\partial \hat{\omega}_{B,i}}{\partial \omega_{B,j}}\right]_{\underline{\omega} = \underline{\omega}_{B0}} \eta_j + \frac{1}{2}\left[\frac{\partial^2 \hat{\omega}_{B,i}}{\partial \omega_{B,j}\, \partial \omega_{B,k}}\right]_{\underline{\omega} = \underline{\omega}_{B0}} \eta_j \eta_k \tag{26}$$

where

$$\underline{\eta} = \varepsilon' \underline{\omega}_{B1} + (\varepsilon')^2 \underline{\omega}_{B2} + \ldots \tag{27}$$

As $\hat{\underline{\omega}}_B$ is quadratic, the Taylor's series only has three terms. Replacing the value of $\underline{\eta}$ from Eq. (27) into Eq. (26) and separating the coefficients of different powers of ε', the series for $\hat{\underline{\omega}}_B$ is obtained as:

$$\hat{\omega}_{B,i} = \hat{\omega}_{B0,i} + \varepsilon' C^1_{ij}\omega_{B1,j} + (\varepsilon')^2 \left[C^1_{ij}\omega_{B2,j} + \frac{1}{2} C^2_{ijk}\omega_{B1,j}\omega_{B1,k}\right] + \ldots \tag{28}$$

The matrix C^1_{ij} is given by:

$$[C^1] = \begin{bmatrix} 2\omega_{BO,1} & 0 & 0 \\ 0 & 2\omega_{BO,2} & 0 \\ 0 & 0 & 2\omega_{BO,3} \\ \omega_{BO,2} & \omega_{BO,1} & 0 \\ 0 & \omega_{BO,3} & \omega_{BO,2} \\ \omega_{BO,3} & 0 & \omega_{BO,1} \end{bmatrix} \tag{29}$$

The matrix C^2_{ijk} is given by:

$$[C^2] = \begin{array}{c} \\ \\ \\ \\ \\ \\ \end{array} \begin{array}{c} k=1 \quad\quad k=2 \quad\quad k=3 \\ \begin{bmatrix} 2 & 0 & 0 & 0 & 0 & 0 & 0 & 0 & 0 \\ 0 & 0 & 0 & 0 & 2 & 0 & 0 & 0 & 0 \\ 0 & 0 & 0 & 0 & 0 & 0 & 0 & 0 & 2 \\ 0 & 1 & 0 & 1 & 0 & 0 & 0 & 0 & 0 \\ 0 & 0 & 0 & 0 & 0 & 1 & 0 & 1 & 0 \\ 0 & 0 & 1 & 0 & 0 & 0 & 1 & 0 & 0 \end{bmatrix} \end{array} \tag{30}$$

The complete infinite series of Eq. (28) will contain only two constant coefficient matrices, $[C^1]$ and $[C^2]$.

The vector $\underline{v}_B(t)$ is now expanded in a Taylor's series as follows:

$$v_{B,i}(\underline{\omega}_B,t) = v_{B,i}(\underline{\omega}_{BO},t) + \left[\frac{\partial v_{B,i}}{\partial \omega_{B,j}}\right]_{\underline{\omega}_B = \underline{\omega}_{BO}} \cdot \eta_j + \left[\frac{1}{2}\frac{\partial^2 v_{B,i}}{\partial \omega_{B,j}\partial \omega_{B,k}}\right]_{\underline{\omega}_B = \underline{\omega}_{BO}} \cdot \eta_j \eta_k + \cdots$$

or

$$v_{B,i}(\underline{\omega}_B,t) = v_{B,i}(\underline{\omega}_{BO},t) + \varepsilon' \frac{\partial v_{B,i}}{\partial \omega_{B,j}} \omega_{B1,j} + (\varepsilon')^2 \left[\frac{\partial v_{B,i}}{\partial \omega_{B,j}} \omega_{B2,j} + \frac{1}{2}\frac{\partial^2 v_{B,i}}{\partial \omega_{B,j}\partial \omega_{B,k}} \omega_{B1,j}\omega_{B1,k}\right] + \cdots \tag{31}$$

An expansion similar to that given by Eq. (31) exists for $\underline{v}_A(\underline{\omega}_A,t)$.

The series given by Eqs. (21), (28), and (31) is now substituted in Eq. (16), using the definitions from Eq. (13) and (20). The first perturbation equation is obtained by collecting the coefficients of $(\varepsilon')^0$ and ε' from this expanded form of Eq. (16) and equating that sum to zero. Thus, the first perturbation equation becomes

$$\varepsilon'[S_{B1}\dot{\underline{\omega}}_{B1} + S_{B2}\dot{\underline{\theta}}_1 + (S_{B3}+S_{B5}C^1)\underline{\omega}_{B1} + S_{B4}\underline{\theta}_1]$$

$$= \underline{f}'_B(\underline{\omega}_{BO},t) + \varepsilon'[\delta^*_B]\underline{u}_{B1} \tag{32}$$

where

$$\underline{f}'_B(\underline{\omega}_{BO},t) = \underline{f}_B(\underline{\omega}_{BO},t) + [\delta^*_B][\underline{T}_{BO}(\underline{\omega}_{BO},t) - \dot{\underline{h}}_B] - S_{B2}\dot{\underline{\theta}}_0$$

$$- S_{B3}\underline{\omega}_{BO} - S_{B5}\hat{\underline{\omega}}_{BO} \tag{33}$$

The sum of the coefficients of $(\varepsilon')^2$ from the expanded form of Eq. (16) leads to the second peruurbation equation of the system. This second perturbation equation is given by:

$$S_{B1}\dot{\underline{\omega}}_{B2} + S_{B2}\dot{\underline{\theta}}_2 + (S_{B3}+S_{B5}C^1)\underline{\omega}_{B2} + S_{B4}\underline{\theta}_1$$

$$= \underline{f}''_B(\underline{\omega}_{BO},\underline{\omega}_{B1},t) + [\delta^*_B]\underline{u}_{B2} \tag{34}$$

where

$$f''_{B,i} = [\delta^*_B]_{ij}\left\{\left[\frac{\partial T_{BO,j}}{\partial \omega_{B,k}}\right]_{\underline{\omega}_{BO}} \cdot \omega_{B1,k} + \left[\frac{\partial T_{BO,j}}{\partial \dot{\omega}_{B,k}}\right]_{\underline{\omega}_{BO}} \cdot \dot{\omega}_{B1,k}\right\}$$

$$- \frac{1}{2}[S_{B5}]_{ij}[C^2]_{jk\ell}\,\omega_{B1,k}\,\omega_{B1,\ell} \tag{35}$$

Proceeding similarly, the coefficients of $(\varepsilon')^n$, for n = 3,4,..., can be used to generate higher order perturbation equations from Eq. (16). Equation (18) for the body A* also yields the following perturbation equations:

$$\varepsilon'[S_{A1}\dot{\underline{\omega}}_{A1} + S_{A2}\dot{\underline{\theta}}_1 + (S_{A3}+S_{A5}C^1)\underline{\omega}_{A1} + S_{A4}\underline{\theta}_1]$$

$$= \underline{f}'_A(\omega_{AO},t) + \varepsilon[\delta^*_A]\underline{u}_{A1} \tag{36}$$

$$S_{A1}\dot{\underline{\omega}}_{A2} + S_{A2}\dot{\underline{\theta}}_2 + (S_{A3}+S_{A5}C^1)\underline{\omega}_{A2} + S_{A4}\underline{\theta}_1$$

$$= \underline{f}''_A(\underline{\omega}_{AO},\underline{\omega}_{A1},t) + [\delta^*_A]\underline{u}_{A2} \tag{37}$$

in which the vector functions $\underline{f}'_A$ and $\underline{f}''_A$ have forms analogous to $\underline{f}'_B$ and $\underline{f}''_B$, respectively.

Equations (25a), (32), and (36) are now collected to form one augmented set of equations, given by:

$$[B_1]\dot{\underline{x}}_1 + [B_2]\underline{x}_1 = [B_3]\underline{u}_1 + \underline{F}_1(t) \tag{38}$$

where

$$[B_1] = \begin{bmatrix} S_{A1} & 0 & S_{A2} \\ 0 & S_{B1} & S_{B2} \\ 0 & 0 & I \end{bmatrix} \tag{39}$$

$$[B_2] = \begin{bmatrix} (S_{A3}+S_{A5}C^1) & 0 & S_{A4} \\ 0 & (S_{B3}+S_{B5}C^1) & S_{B4} \\ -I & I & \tilde{\omega}_{BO} \end{bmatrix} \tag{40}$$

$$[B_3] = \begin{bmatrix} \delta^*_A & 0 \\ 0 & \delta^*_B \\ 0 & 0 \end{bmatrix} \tag{41}$$

$$\underline{u}_1 = [\varepsilon' \underline{u}_{A1},\ \varepsilon' \underline{u}_{B1}] \tag{42}$$

$$\underline{F}_1 = [\underline{f}'_A,\ \underline{f}'_B,\ \underline{0}]^T \tag{43}$$

and

$$\underline{x}_1 = [\varepsilon'\ \underline{\omega}_{A1},\ \varepsilon' \underline{\omega}_{B1},\ \varepsilon' \underline{\theta}_1]^T \tag{44}$$

Equations (25b), (34) and (37) similarly give rise to an equation of the form

$$[B_1]\dot{\underline{x}}_2 + [B_2]\underline{x}_2 = [B_3]\underline{u}_2 + \underline{F}_2(t) \tag{45}$$

where

$$\underline{x}_2 = [\underline{\omega}_{A2},\ \underline{\omega}_{B2},\ \underline{\theta}_2]^T \tag{46}$$

$$\underline{u}_2 = [\underline{u}_{A2},\ \underline{u}_{B2}]^T \tag{47}$$

and

$$\underline{F}_2 = [\underline{f}''_A,\ \underline{f}''_B,\ -\tilde{\omega}_{B1}\underline{\theta}_1]^T \tag{48}$$

The augmented set of equations corresponding to the coefficients of $(\varepsilon')^n$, for all n, will have the general form given by:

$$[B_1]\dot{\underline{x}}_n + [B_2]\underline{x}_n = [B_3]\underline{u}_n + \underline{F}_n(t) \qquad (49)$$

where the vectors $\underline{x}_n$, $\underline{u}_n$ and $\underline{F}_n$ have to be obtained from the Taylor's expansions, outlined in the first two cases. The solution of Eq. (3) for a dual-spin satellite thus implies the solution of the series of equations of the form of Eq. (49), the first two of which are explicitly given in Eqs. (38-48).

In the case of a single-body satellite the relative angular velocity ($\underline{\theta}$) and the body (B*, for example) do not exist. The perturbation equations for this become merely a special case of the sequence given by Eq. (49).

FORMAL SOLUTIONS

The solutions for the vectors ($\underline{x}_n$) can be obtained from the sequence given by Eq. (49) if the control vectors ($\underline{u}_n$) and the initial value vectors ($\underline{a}_n$) were known. The $\underline{a}_n$ are defined as:

$$\underline{a}_n = \underline{x}_n(0) \qquad (50)$$

The vector function $\underline{F}_n$ contains the vectors $\underline{x}_m$, m = 1,2,..., (n-1). Complementary solutions for all $\underline{x}_n$ satisfy the same fundamental equation. Thus, the solutions of Eq. (49), for $n \geq 2$ will generally contain unbounded secular terms, even though the system given by Eq. (3) is stable. For this reason, the specified initial values of the angular velocities are to be used to define $\underline{a}_1$. The vectors $\underline{a}_n$ and $n \geq 2$ are then to be obtained from the condition that the sum of the secular terms be bounded for each n, $n \neq 1$. Further details of this method are given in Section 6. For the present, assuming that all the $\underline{u}_n$ and $\underline{a}_n$ are known, the formal solutions to Eq. (49) can be obtained as:

$$\underline{x}_n(t) = [\Phi(t)]\underline{a}_n + \int_0^t [\Phi(t-\tau)][B_1]^{-1}[\underline{F}_n(\tau) + B_3\underline{u}_n(\tau)]d\tau \qquad (51)$$

in which $\Phi(t)$ is the fundamental matrix of the homogeneous system given by:

$$\dot{\underline{x}} + [B_1]^{-1}[B_2]\underline{x} = 0 \qquad (52)$$

The vectors $\underline{x}_n(t)$ can, of course, be numerically obtained from a digital computer either from Eq. (49) or Eq. (51). But it will be seen in the next section that these integrations must be repeated several times to determine and optimize the control torque vector ($\underline{u}_n$). For this reason, a semi-analytic algorithm for computing the values of $\underline{x}_n(t)$ is now presented.

Let p_i, i = 1,2,..., be the eigenvalues of $-[B_1^{-1}B_2]$. Let $M = [m_{ij}]$ be a matrix such that

$$m_{nk} = \text{Eigenvector of } -[B_1^{-1}B_2] \text{ for } p_n \text{ if } p_n \text{ is real}$$

and

$$m_{nj} = \text{Re[Eigenvector of } -[B_1^{-1}B_2] \text{ for } p_n \text{ or } p_\ell$$

$$m_{\ell j} = \text{Im[Eigenvector of } -[B_1^{-1}B_2] \text{ for } p_n \text{ or } p_\ell$$

when p_n and p_i are complex conjugate. Let a set of functions $r_i(t)$ be defined corresponding to a p_i for each i, such that

$$r_i(t) = \exp(p_i \cdot t) \quad \text{if } p_i \text{ is real}$$

or

$$r_i(t) = \exp[\text{Re}(p_i) \cdot t]\cos[\text{Im}(p_j)\ t]$$

and

$$r_j(t) = \exp[\text{Re}(p_i) \cdot t]\sin[\text{Im}(p_j)\ t] \tag{53}$$

when p_i and p_j form a pair of complex conjugate roots. A table of values of $r_i(t)$ for each i can be prepared from Eq. (53).

Let a set of matrices $M'_i = [m'_{ijk}]$ be defined corresponding to a p_i for each i, such that

$$m'_{nji} = \begin{cases} m_{ji}, & \text{for all j and } i = n \\ 0, & \text{if } i \neq n \end{cases} \quad \text{if } p_n \text{ is real}$$

or

$$m'_{nji} = \begin{cases} m_{ji}, & \text{for all j and } i = n, \ell \\ 0, & \text{if } i \neq n, \ell \end{cases} \tag{54}$$

$$m'_{\ell ji} = \begin{cases} m_{j\ell}, & \text{for all j and } i = \ell \\ -m_{jn}, & \text{for all j and } i = n \\ 0, & \text{if } i \neq n, \ell \end{cases} \quad \text{if } p_n \text{ and } p_\ell \text{ are complex conjugate.}$$

With the definitions of Eq. (53) and (54),

$$\Phi(t) = \sum_i [(M'M^{-1})_i\ r_i(t)] \tag{55}$$

Hence,

$$\Phi(t)\underline{a}_n = \sum_i [(M'M^{-1}\underline{a}_n)_i\ r_i(t)] \tag{56}$$

Calculating $(M'M^{-1}\underline{a}_n)_i$ just once for each i, the first term of Eq. (51) is obtained for all time from the table of values of $r_i(t)$.

Now, let

$$\underline{F}_n(t) + B_3\ \underline{u}_n(t) + \underline{F}'_n + \underline{F}''_n(t) \tag{57}$$

where $\underline{F}'_n$ is constant and $\underline{F}''_n(t)$ is a non-constant explicit function of time. Then the contribution, (I_1) of $\underline{F}'_n$, in the integral in Eq. (51),

is given by:

$$I_1 = \int_0^t [\Phi(t-\tau)][B_1^{-1}]\underline{F}'_n \, d\tau = \sum_i \{[M'M^{-1}B_1^{-1}F'_n]_i [\int_0^t r_i(t-\tau)d\tau]\}$$

or

$$I_1 = \sum_i \{[M'M^{-1}B_1^{-1}\underline{F}'_n]_i \cdot r'_i(t)\} \tag{58}$$

where

$$r'_i(t) = \int_0^t r_i(t-\tau)d\tau \tag{59}$$

In view of the definition of $r_i(t)$ given in Eq. (53), the functions $r'_i(t)$ can be explicitly integrated from Eq. (59) and its values stored in another table. Thus I_1 is also obtained for all time by forming the vectors $[M'M^{-1}B_1^{-1}\underline{F}'_n]_i$ once for each i.

This method becomes too involved to obtain the contribution I_2 of $\underline{F}''(t)$ in the integral in Eq. (51). For this reason, I_2 is best obtained by a discretized approach.

Let the solution $\underline{x}_n(t)$ be required in an interval [0,T]. Let t_1, t_2, t_3,....t_n be points on the time-axis such that

$$t_1 = \Delta t$$

$$t_i - t_{i-1} = \Delta t, \text{ for all i,}$$

and

$$t_n = T.$$

Let $r''_i(\Delta t)$ be defined by:

$$r''_i(\Delta t) = \int_0^{\Delta t} r_i(\Delta t-\tau)d\tau \tag{59a}$$

Thus r''_i can be obtained from the tables of $r'_i(t)$. Let $I_2(t)$ be the integral

$$I_2(t) = \int_0^t [\Phi(t-\tau)B_1^{-1}\underline{F}''(\tau)]d\tau \tag{60}$$

Then:

$$I_2(0) = 0$$

$$I_2(t_1) = \int_0^{\Delta t} [\Phi(t-\tau)B_1^{-1}\underline{F}''(\tau)]d\tau$$

$$\tilde{=} \int_0^{\Delta t} [\Phi(t-\tau)B_1^{-1}\underline{F}''(0)]d\tau$$

$$= \sum_i [M'M^{-1}B_1^{-1}\underline{F}''(0)]_i r''_i \tag{61}$$

$$I_2(t_2) = I_2(t_1) + \sum_i \{[M'M^{-1}B_1^{-1}\underline{F}_n''(t_1)]_i r_i''\}$$

Hence $I_2(t_m)$ is given by the recurrence relation

$$I_2(t_m) = I_2(t_{m-1}) + \sum_i \{[M'M^{-1}B_1^{-1}\underline{F}_n''(t_{m-1})]_i r_i''\} \qquad (62)$$

Thus $I_2(t)$ can be obtained from Eq. (62) when a table of values of $\underline{F}_n''(t)$ is available.

CONTROL TORQUES

It was seen in the previous section that the solutions ($\underline{x}_n(t)$) can be obtained if the control torques $\underline{u}_n(t)$ are known. The forms of $\underline{u}_n(t)$ are deduced here, along with a brief discussion of the theory. Further theoretical details are given in Refs. [10], [11], and [12]. The control policy chosen here is to find $\underline{u}_n(t)$ such that $\underline{x}_n(T)$ becomes equal to a specified vector ($\underline{b}_n(T)$) in the minimum time ($t = T$).

Let Eq. (51) be regrouped with the definitions

$$\underline{x}_n^*(t) = [\Phi(t)]\underline{a}_n + \int_0^t [\Phi(t-\tau)]B_1^{-1}\underline{F}_n(\tau)\,d\tau \qquad (63)$$

and

$$k(t,\tau) = [\Phi(t-\tau)]B_1^{-1}B_3 \qquad (64)$$

Then Eq. (51) becomes

$$\underline{x}_n(t) = \underline{x}_n^*(t) + \int_0^t k(t,\tau)\underline{u}_n(\tau)\,d\tau \qquad (65)$$

Equation (65) is in the form of a standard control equation discussed in Refs. [10, 11, 12]. For the minimal time policy, $\underline{u}_n(t)$ is a "bang-bang" control given by:

$$u_{n,j}(t) = U \operatorname{sgn}\left[\sum_i \lambda_i k_{ij}(T,t)\right] \qquad (66)$$

where U is the norm of $\underline{u}_n(t)$ given by:

$$U = \|\underline{u}_n\| = \max_i \max_{0\le t\le T} |u_{n,i}(t)| \qquad (67)$$

The parameters λ_i maximize U through the relation

$$U = \max_{\lambda_i} \frac{\sum_i \lambda_i [b_i(T) - x_{n,i}^*(T)]}{\sum_j \int_0^T \left|\sum_i \lambda_i k_{ij}(T,\tau)\right| d\tau} \qquad (68)$$

Equation (67) is interpreted in Refs. [10,11,12] to mean that all the com-

ponents ($u_{n,j}$) of the control vector ($\underline{u}_n$) have the same magnitude U. In the simulated responses of the system given by Eq. (51), it was found that this interpretation leads to large amplitudes of $\underline{x}_n(t)$ when $\underline{b}_n(T)$ is intended to be zero. For a satellite, large amplitudes of $\underline{x}_n(t)$ lead to unsatisfactory pointing accuracy. It was found that this unsatisfactory result arises in the cases where Eq. (51) has one or more eigenvalues which are either at or very close to zero.

It should be mentioned here that the smallest value of the minimum pulse time used in our simulations is 0.01 second. Evidently one method of avoiding large amplitudes of $\underline{x}_n(t)$ is to use a still smaller minimum pulse time. But this may not be applicable in practical situations. For this reason a more flexible interpretation of Eq. (67) was employed. This proved to be entirely successful even with a minimum pulse time as high as 0.05 second.

The modification made is by the introduction of another vector (μ_i) such that Eqs. (66) and (67) are changed to become

$$u_{n,j} = U\, \mu_j \cdot \operatorname{sgn} \left[\sum_i \lambda_i k_{ij}(T,t) \right] \tag{69}$$

where

$$U = \| \underline{u}_n \| \; / \; \| \mu \| \tag{70}$$

The parameters λ_i still satisfy Eq. (68).

Equation (69) essentially means that the amplitudes of $\underline{x}_n(t)$ can be made small when the amplitudes of $u_{n,j}$ are allowed to be different. The comparative values of μ_j also give valuable information on the relative necessity for control on the different axes of a satellite. For example, it was found in our simulations that, for a particular design of a dual-spin satellite, the ratios $\mu_2/\| \mu \|$ and $\mu_3/\| \mu \|$ were of the order of 10^{-4}. This is in cases where μ_2 and μ_3 correspond to the axes of the despun section, μ_2 being perpendicular and μ_3 parallel to the spin-axis of the spinning part. The controls μ_2 and μ_3 can be eliminated in such situations, leading to a simpler system. In our example μ_6 corresponds to the spin-axis of the spinning part and μ_6 equals $\| \mu \|$, which is as it should be.

The effectiveness of the optimization principle given by Eqs. (68), (69), and (70) were checked by comparing the magnitudes of the optimal control $\underline{u}_n(t)$ with that of $\underline{u}_n^*$, where $\underline{u}_n^*$ is a constantly applied torque vector required to obtain the same response $\underline{b}(T)$ for the same T. It was found that, for several different satellite designs, the ratio $\| \underline{u}_n \| \; / \; \| \underline{u}_n^* \|$ was of the order of 10^{-3}. This was quite satisfactory. For a three-axes stabilized design, the control given by Eqs. (66), (67), and (68) led to the value of $\| \underline{x}_1(T) \|$ of the order of 10^{-2} radians per second. The modified control for the same design yielded $\| \underline{x}_1(T) \| \approx 10^{-6}$ rads/second. This is an appreciable increase in the pointing accuracy. In each of these examples, T = 5 seconds.

It is now evident that the critical parameters for the design of a time optimal control for the system of Eq. (65) are λ_i and μ_i.

An algroithm that has proved useful in computer simulations must be explained. Let

$$\underline{b}'_n = \underline{b}_n(T) - \underline{x}^*_n(T) \tag{71}$$

and

$$H(T) = \sum_j \int_0^T \left| \sum_i \lambda_i k_{ij}(T,\tau) \right| d\tau \tag{72}$$

Then λ_i can be found by minimizing H with respect to λ_i with the constraint

$$\sum_i \lambda_i b'_{n,i} = \text{a constant} = \bar{b}(\text{say}), \tag{73}$$

where $\bar{b}$ is arbitrary. This leads to:

$$U = \frac{\bar{b}}{H(T)} \tag{74}$$

and

$$\underline{\nabla}H(T) = \frac{\partial H(T)}{\partial \lambda_i} = \sum_j \int_0^T [\text{sgn} \sum_r \lambda_r k_{rj}(T,\tau)] k_{ij}(T,\tau) d\tau \tag{75}$$

Since H(T), $\underline{\nabla}H(T)$, and $\underline{\nabla}[\underline{\nabla}H(T)]$ are continuous, the conditions for the existence of a local minimum are satisfied [13]. Because closed form expressions of H(T) and $\underline{\nabla}H(T)$ are available, the method of steepest descent with variable step-size [14] is the most suitable in this case. The algorithm follows the computation steps mentioned below.

Step 1: Set the values of T, s, $\underline{\lambda} = \underline{\lambda}_0$, where $\underline{\lambda}_0$ is the initial estimate of $\underline{\lambda}$ and s is the initial step size. Set $\underline{\nabla}H'(T) = H'(T) = 0$. Set the iteration counter, N = 1. Set $z_1 = 0.5$, $z_2 = 0.75$.

Step 2: Compute H(T) and $\underline{\nabla}H(T)$. Set N = N + 1.

If $N > \bar{N}$ or if $|H(T) - H'(T)| < \delta$, go to step 5. Here $\bar{N}$ is the allowable number of iterations and δ is the stop criterion.

Step 3: If $N \neq 2$ go to step 4.

Otherwise, set

$$\underline{\lambda} = \left[\underline{\lambda}_0 - s \cdot \frac{\underline{\nabla}H(T)}{\| \underline{\nabla}H(T) \|}\right]$$

and normalize $\underline{\lambda}$, such that $\sum_i \lambda_i b'_{n,i} = \bar{b}$.

Also, set $H'(T) = H(T)$ and $\underline{\nabla}H'(T) = \underline{\nabla}H(T)$. Go to step 2.

Step 4: Set the new value of s, as

$$s = s \cdot [z_1 + z_2 \cdot \frac{\underline{\nabla H}(T)\ \underline{\nabla H}'(T)}{\| \underline{\nabla H}(T) \| \cdot \| \underline{\nabla H}(T) \|}] \qquad (76)$$

With this new value of s, set

$\lambda = \lambda - s \cdot \frac{\underline{\nabla H}(T)}{\| \underline{\nabla H}(T) \|}$; and normalize $\underline{\lambda}$ such that

$\sum_i \lambda_i b'_{n,i} = \bar{b}$. Also, set $H'(T) = H(T)$ and $\underline{\nabla H}'(T) = \underline{\nabla H}(T)$.

Go to step 2.

Step 5: Exit from the iteration loop. Compute the value of U and store the current value of $\underline{\lambda}$ which is the required value.

The most critical step for quick convergence of this scheme is given by Eq. (76) in Step 4. If $1 > z_2 > z_1 > 0$, the step size decreases rapidly as H(T) starts oscillating about a minimum. A satisfactory pair of values of z_1 and z_2 was found to be 0.5 and 0.75. This pair leads to a 25% reduction of the step size each time the inner product of the two consecutive gradients becomes negative. Normalizing $\underline{\lambda}$ in Steps 3 and 4 maintains the constraint of Eq. (73). Adjusting $\bar{b}$ such that the norm, $\|\lambda\|$, remains close to 1.0 also helps to increase the efficiency of the scheme. A suitable initial choice of the step size (s) was found to be given by:

$$s = \|\underline{\lambda}_0\| / 10.0.$$

This minimization method seeks out the local minimum nearest to the specified initial value of $\underline{\lambda}$. Since the global minimum is required in Eq. (68), a judicious choice of $\underline{\lambda}_0$ is the key to the minimization problem. After numerous trials, a rule of thumb to locate the global minimum was found. The rule is to take the elements of $\underline{\lambda}_0$ as

$$\lambda_{0,i} = \begin{cases} \frac{1}{b'_{n,i}}, & \text{if 'i' corresponds to the spin-axis or a symmetry axis, or the axis of maximum moment of inertia.} \\ 0, & \text{otherwise.} \end{cases}$$

Once the parameters (λ_i) are obtained, the parameters (μ_i) can be determined in the following manner. Using the table of values of either $r'_i(t)$ or $r''_i(\Delta t)$, which are defined by Eqs. (59) or (59a), a table of values of the function $r'''_j(t)$ is to be prepared, in which

$$r'''_j(t) = \text{sgn}\,[\sum_i \lambda_i k_{ij}(T,t)] \qquad (77)$$

Let k_1 be defined as:

$$[k_1]_{ij} = \int_0^T [k(t,\tau)]_{ij} r'''_j(\tau)\, d\tau, \quad \text{(no sum on j)} \qquad (78)$$

Then $\underline{\mu}$ is given by:

$$\underline{\mu} = -\frac{1}{U}\,[k_1]^{-1}\underline{b}'(T) \tag{79}$$

The uniform control torque $\underline{u}_n^*$ is obtained by:

$$\underline{u}_n^* = -[k_2]^{-1}\underline{b}'(T) \tag{80}$$

where

$$[k_2] = \int_0^T [k(t,\tau)]\,d\tau \tag{81}$$

Using these computed values of $\underline{\lambda}$, $\underline{\mu}$, [k], and $\underline{r}'''(t)$, the values of $\underline{u}_n(t)$, and, hence, the integral on the right hand side of Eq. (51) is easily obtained.

Because of the iterative method necessary for the minimization of H(T), the number of scalar equations in Eq. (51) should be small. This requirement underlines the necessity and value of the singular perturbation scheme by which it is possible to reduce the number of degress of freedom of the equations of motion of a flexible satellite.

INITIAL CONDITIONS AND SECULAR TERMS

It was mentioned in the preceeding section that the appearance of secular terms during the integration of the sequence of equations given by Eq. (51) requires an involved method of specifying the initial conditions ($\underline{a}_n$) of the perturbation series $\underline{x}_n(t)$. In fact, this is a classical problem and has been widely studied [15 and 16]. The problem can be understood with a simple example. Let one of the eigenvalues of Eq. (52) be given by:

$$p = c_1 + ic_2 \tag{82}$$

Then the fundamental matrix $\Phi(t)$ of Eq. (52) will contain the function $\exp(c_1 t)\cos(c_2 t)$, as will the solutions $\underline{x}_n(t)$. Now, let it be assumed that $B_1^{-1}\underline{F}_n(t)$ also contains a similar functional term. In that case the contribution (I_3) of $\underline{F}_n(t)$ in the integral in Eq. (51), will be given by:

$$I_3 = \int_0^t \{e^{c_1(t-\tau)}\cos[c_2(t-\tau)]e^{c_1\tau}\cos c_2\tau\}\,d\tau$$

or

$$I_3 = \frac{1}{2}\,t\,e^{c_1 t}\cos c_2 t + \frac{1}{2c_2}\,e^{c_1 t}\sin c_2 t \tag{83}$$

The first term on the right hand side of Eq. (83) is the "secular term," because it is multiplied by the unbounded function (t). If $c_1 < 0$, then

$$\lim_{t \to \infty} \left| t\, e^{c_1 t} \cos c_2 t \right| = \lim_{t \to \infty} \left| t\, e^{c_1 t} \right| = 0$$

If the real parts of the eigenvalues (p_i) of Eq. (52) are negative definite, the secular term becomes bounded because of the modulating exponential function. In this case, the existence of the secular term does not create any problems and the initial values ($\underline{a}_n$) can be chosen as:

$$\underline{a}_1 = \underline{x}_1(0)$$

$$\underline{a}_n = \underline{0} \; ; \; n \neq 1 \tag{84}$$

The integration of Eq. (51) can then be done by the method shown in Section 4 without any further analysis. Another simple solution of the problem occurs if $c_1 > 0$. Here, the satellite is unstable and there is no use for further analysis.

The elimination of the secular term becomes important when at least one of the eigenvalues of Eq. (52) has its real part equal to zero; that is, if $c_1 = 0$.

Let it be assumed that $c_1 = 0$ but $c_2 \neq 0$. In this case, let the forms of sequence $\underline{F}_n(t)$, of which the first two elements are defined by Eqs. (43), (48), (33), and (35), be considered. It is seen from Eq. (83) that the secular terms occur if $\underline{F}_n(t)$ contains functions which are the same as any of those of $\Phi(t)$. There are three ways by which this can happen.

Case 1: Either $\underline{f}_B(\underline{\omega}_{BO},t)$, $\underline{T}_{BO}(\underline{\omega}_{BO},t)$, or $\dot{h}_B$ is non-zero and periodic with "period" c_2. This leads to a resonance and the corresponding loss of the satellite's stability. In this case, the secular terms should be avoided, if possible, by changing the values of either $\underline{\omega}_{AO}$ or $\underline{\omega}_{BO}$.

Case 2: The vector $\underline{T}_{BO}(\underline{\omega},t)$ is a polynomial in $\underline{\omega}(t)$. The constant part of $\underline{T}_{BO}$ does not pose any problems. The terms which are either linear or quadratic in $\underline{\omega}$ have already been separated in Eq. (13a). Thus, $\underline{T}_{BO}(\underline{\omega},t)$ can contain only cubic and higher powers of $\underline{\omega}(t)$. If the magnitude of $\underline{T}_{BO}(\underline{\omega},t)$ is small compared to ε', then $\underline{T}_{BO}(\underline{\omega},t)$ can be expanded by using the series for $\underline{\omega}_A$ or $\underline{\omega}_B$. The problem of the secular terms can then be solved by neglecting the terms involving cubic and higher powers of ω_{Ai} or ω_{Bi} for $i \neq 0$.

Case 3: Both c_1 and c_2 are equal to zero. This leads to a constant eigenfunction for $\underline{x}_n$. The secular terms arising can be avoided by adding this constant part of the solution to $\underline{\omega}_{AO}$ or $\underline{\omega}_{BO}$ as appropriate, and repeating the solution procedure.

If none of the abovementioned methods of avoiding secular terms is applicable, a more general method should be used. Otherwise, Eq. (51) can be integrated directly, using the initial values given by Eq. (84). There is a general method of eliminating secular terms. Similar methods,

valid for systems with only one or two degrees of freedom, have been widely investigated [15,16]. The following method is valid for systems with arbitrarily large degrees of freedom.

Let $\underline{\omega}_A$ and $\underline{\omega}_B$ be given by the doubly perturbed series, given by:

$$\underline{\omega}_A = \underline{\omega}_{AO} + [\Psi_{AO}(t) + \varepsilon' \Psi_{A1}(t) + (\varepsilon')^2 \Psi_{A2}(t) + \ldots]$$
$$\times [\varepsilon' \underline{\omega}'_{A1} + (\varepsilon')^2 \underline{\omega}'_{A2} + (\varepsilon')^3 \underline{\omega}'_{A3} + \ldots] \qquad (85)$$

and

$$\underline{\omega}_B = \underline{\omega}_{BO} + [\Psi_{BO}(t) + \varepsilon' \Psi_{B1}(t) + (\varepsilon')^2 \Psi_{B2}(t) + \ldots]$$
$$\times [\varepsilon' \underline{\omega}'_{B1} + (\varepsilon')^2 \underline{\omega}'_{B2} + (\varepsilon')^3 \underline{\omega}'_{B3} + \ldots] \qquad (86)$$

in which Ψ_{Ai}, Ψ_{Bi}, ω'_{Ai}, and ω'_{Bi} are unknown functions while $\underline{\omega}_{AO}$ and $\underline{\omega}_{BO}$ are the known constant nominal angular velocities of the composite bodies of the satellite.

Expanding Eqs. (85) and (86) in powers of ', we obtain

$$\underline{\omega}_A = \underline{\omega}_{AO} + \varepsilon' \Psi_{AO} \underline{\omega}'_{A1} + (\varepsilon')^2 [\Psi_{AO} \underline{\omega}'_{A2} + \Psi_{A1} \underline{\omega}'_{A1}] + \ldots$$
$$\underline{\omega}_B = \underline{\omega}_{BO} + \varepsilon' \Psi_{BO} \underline{\omega}'_{B1} + (\varepsilon')^2 [\Psi_{BO} \underline{\omega}'_{B2} + \Psi_{B1} \underline{\omega}'_{B1}] + \ldots \qquad (87)$$

Considering the definitions

$$\underline{\omega}_{A1} = \Psi_{AO} \underline{\omega}'_{A1}$$
$$\underline{\omega}_{B1} = \Psi_{BO} \underline{\omega}'_{B1}$$
$$\underline{\omega}_{A2} = \Psi_{AO} \underline{\omega}'_{A2} + \Psi_{A1} \underline{\omega}'_{A1}$$
$$\underline{\omega}_{B2} = \Psi_{BO} \underline{\omega}'_{B2} + \Psi_{B1} \underline{\omega}'_{B1} \qquad (88)$$

and similarly for the coefficients of higher powers of ε', it can be seen that the series given by Eq. (21), (24), and (25a) remain valid. The expression for $\dot{\underline{\theta}}_2$ is now given by:

$$\dot{\underline{\theta}}_2 = \dot{\underline{\theta}}'_2 + \dot{\underline{\theta}}''_2 \qquad (89)$$

where

$$\dot{\underline{\theta}}'_2 = [\Psi_{AO} \underline{\omega}'_{A2} - \Psi_{BO} \underline{\omega}'_{B2} - \tilde{\underline{\omega}}_{BO} \underline{\theta}_2] \qquad (90)$$

and

$$\underline{\dot{\theta}}_2'' = {}^{\Psi}_{A1}\underline{\omega}_{A1}' - {}^{\Psi}_{B1}\underline{\omega}_{B1}' - ({}^{\Psi}_{B0}\underline{\omega}_{B1}')\underline{\theta}_1 \tag{91}$$

Proceeding in the manner shown earlier, the first order perturbation equations given by Eqs. (38) through (44) remain the same.

Let the following definitions be considered:

$$\underline{x}_2' = [{}^{\Psi}_{A0}\underline{\omega}_{A2}' \ , \ {}^{\Psi}_{B0}\underline{\omega}_{B2}' \ , \ \underline{\theta}_2']^T \tag{92}$$

$$\underline{x}_2'' = [{}^{\Psi}_{A1}\underline{\omega}_{A1}' \ , \ {}^{\Psi}_{B1}\underline{\omega}_{B1}' \ , \ \underline{\theta}_2'']^T \tag{93}$$

$$\underline{F}_2' = \begin{Bmatrix} -\frac{1}{2}[S_{A5}]_{ij}[C^2]_{jk\ell}\omega_{A1,k}\omega_{A1,\ell} \\ -\frac{1}{2}[S_{B5}]_{ij}[C^2]_{jk\ell}\omega_{B1,k}\omega_{B1,\ell} \\ -\tilde{\omega}_{B1}\underline{\theta}_1 \end{Bmatrix} \tag{94}$$

$$\underline{F}_2'' = \begin{Bmatrix} [\delta_A^*]_{ij} \left.\frac{\partial T_{A0,j}}{\partial \omega_{A,k}}\right|_{\substack{\omega_{A1,k} \\ \underline{\omega}_{A0}}} + \left.\frac{\partial T_{A0,j}}{\partial \dot{\omega}_{A,k}}\right|_{\substack{\dot{\omega}_{A1,k} \\ \underline{\dot{\omega}}_{A0}}} \\ [\delta_B^*]_{ij} \left.\frac{\partial T_{B0,j}}{\partial \omega_{B,k}}\right|_{\substack{\omega_{B1,k} \\ \underline{\omega}_{B0}}} + \left.\frac{\partial T_{B0,j}}{\partial \dot{\omega}_{B,k}}\right|_{\substack{\dot{\omega}_{B1,k} \\ \underline{\dot{\omega}}_{B0}}} \\ 0 \end{Bmatrix} \tag{95}$$

With these definitions, Eq. (45) reduces to:

$$\{[B_1]\dot{\underline{x}}_2' + [B_2]\underline{x}_2' - [B_3]\underline{u}_2 - \underline{F}_2'(t)\}$$

$$+ \{[B_1]\dot{\underline{x}}_2'' + [B_2]\underline{x}_2'' - \underline{F}_2''(t)\} = 0 \tag{96}$$

Only the second group of terms in Eq. (96) leads to secular terms because $\underline{F}_2'$ can contain the eigenfunctions only if $c_1 = c_2 = 0$. This can be avoided by increasing $\underline{\omega}_{A0}$ or $\underline{\omega}_{B0}$. If it is not possible to change $\underline{\omega}_{A0}$ or $\underline{\omega}_{B0}$, the terms in $\underline{F}_2'$ containing the eigenfunctions can be moved into $\underline{F}_2''(t)$. Thus, the secular terms of Eq. (96) can be avoided by setting

$$B_1\dot{\underline{x}}_2' + B_2\underline{x}_2' = B_3\underline{u}_2 + \underline{F}_2'(t) \tag{97}$$

which can be integrated by the method explained before, and

$$B_1\ddot{\underline{x}}_2'' + B_2\underline{x}_2'' = \underline{F}_2''(t) \tag{98}$$

The elements of $\underline{F}_2''(t)$ corresponding to $\underline{\theta}''(t)$ are equal to zero, seen from Eq. (95). For this reason, only the equations corresponding to $\underline{\omega}_A$ and $\underline{\omega}_B$ in Eq. (98) need be considered now. Equation (98) can be expanded to obtain

$$S_{A1}[\dot{\Psi}_{A1}\underline{\omega}_{A1}' + \Psi_{A1}\dot{\underline{\omega}}_{A1}'] + S_{A3}'\Psi_{A1}\underline{\omega}_{A1}' = N_{A1}\Psi_{A0}\underline{\omega}_{A1}' + N_{A2}[\dot{\Psi}_{A0}\underline{\omega}_{A1}' + \Psi_{A0}\dot{\underline{\omega}}_{A1}'] \tag{99}$$

where

$$N_{A1} = [\delta_A^*]_{ij}\left[\frac{\partial T_{A0,j}}{\partial \omega_{A,k}}\right|_{\underline{\omega}_{A0}} \tag{100a}$$

$$N_{A2} = [\delta_A^*]_{ij}\left[\frac{\partial T_{A0,j}}{\partial \dot{\omega}_{A,k}}\right|_{\dot{\underline{\omega}}_{A0}} \tag{100b}$$

and

$$S_{A3}' = S_{A3} + S_{A5}C^1 \tag{101}$$

An equation similar to Eq. (99) also exists for the body B*. Separating the coefficients of $\underline{\omega}_{A1}'$ and $\dot{\underline{\omega}}_{A1}'$ from Eq. (99), we obtain

$$[S_{A1}\dot{\Psi}_{A1} + S_{A3}'\Psi_{A1} - N_{A1}\Psi_{A0} - N_{A2}\dot{\Psi}_{A0}]\underline{\omega}_{A1}' = 0 \tag{102}$$

and

$$[S_{A1}\Psi_{A1} - N_{A2}\Psi_{A0}]\dot{\underline{\omega}}_{A1}' = 0 \tag{103}$$

Equation (99) can be solved exactly only by writing out each of the scalar equations and then separating the coefficients of each individual eigenfunction. Another solution exists if

$$S_{A1}\Psi_{A1} - N_{A2}\Psi_{A0} = 0 \tag{104}$$

and

$$S_{A1}\dot{\Psi}_{A1} + S_{A3}'\Psi_{A1} - N_{A1}\Psi_{A0} - N_{A2}\dot{\Psi}_{A0} = 0 \tag{105}$$

Equations (104) and (105) are satisfied together if

$$[\dot{N}_{A2} - S_{A3}'S_{A1}^{-1}N_{A2} - N_{A1}] = 0 \tag{106}$$

If Eq. (106) is satisfied, then the exact solutions are

$$\Psi_{A1}\underline{\omega}'_{A1} = S^{-1}_{A1}N_{A2}\underline{\omega}_{A1} \tag{107}$$

and

$$\Psi_{B1}\underline{\omega}'_{B1} = S^{-1}_{B1}N_{B2}\underline{\omega}_{B1} \tag{108}$$

In general, Eq. (106) will not be satisfied and it will be impossible to obtain the Eqs. (107) and (108). Hence an approximate solution is obtained by taking

$$\dot{\underline{\omega}}'_{A1} = \underline{0}$$

$$N_{A2}\dot{\Psi}_{A0} = S_{A1}\dot{\Psi}_{A1}$$

Consequently, from Eq. (102),

$$\Psi_{A1}\underline{\omega}'_{A1} = [S'_{A3}]^{-1}N_{A1}\underline{\omega}_{A1} \tag{109}$$

and

$$\Psi_{B1}\underline{\omega}'_{B1} = [S'_{B3}]^{-1}N_{B1}\underline{\omega}_{B1} \tag{110}$$

Equations (84), (97), (109), and (110) produce the solution $\underline{\omega}_{A2}$ and $\underline{\omega}_{B2}$ defined in Eq. (88). Solutions for the higher order terms of the series given in Eq. (21) can be obtained by a similar procedure.

CONCLUSIONS

The analysis presented in this paper is based on the assumption that all variables and parameters are deterministic. Otherwise, this analysis is almost complete, since the necessary details on the control system and the secular terms have been thoroughly considered. In the next paper [18], the analysis of stochastic equations will be considered. Numerical results are not presented now. Such results will be presented in detail in [19]. In that paper, the response of different classes of satellites will be compared, both for the deterministic and random cases.

REFERENCES

1. Das, A., and Huang, T. C., "Pointing Error Analysis of Geosynchronous Satellites, Parts I-III," Annual Scientific Report, Space Science and Engineering Center, Madison, Wisconsin, December 1972.

2. Das, A., and Huang, T. C., "Pointing Error Analysis of Geosynchronous Satellites, Parts IV-VII," Annual Scientific Report, Space Science and Engineering Center, Madison, Wisconsin, October 1973.

3. Huang, T. C., and Das, A., "Thermoelastic Flutter Models for Elements of Flexible Satellites," Paper presented at the 24th International Astronautical Congress, Baku, U.S.S.R., October 1973.

4. Huang, T. C., and Das, A., "Singular Perturbation Equations for Flexible Satellites," Paper presented at the 24th International Astronautical Congress, Baku, U.S.S.R., October 1973.

5. Huang, T. C., and Das, A., "Analysis of Generalized Forces in the Equations of Motion of Flexible Satellites, " In preparation.

6. Likins, P. W., and Gale, A. H., "The Analysis of the Interactions Between Attitude Control Systems and Flexible Appendages," Paper IAF AD29, 19th International Astronautical Congress, New York, October 1968.

7. Likins, P. W., and Fleischer, G. E., "Results of Flexible Spacecraft Attitude Control Studies Utilizing Hybrid Coordinates," J. of Spacecraft and Rockets, Vol. 8, No. 3, March 1971, pp. 264-272.

8. Grote, P. B., McMunn, J. C., and Gluck, R., "Equations of Motion of Flexible Spacecraft," J. of Spacecraft and Rockets, Vol. 8, No. 6, June 1971, pp. 561-567.

9. Meirovitch, L., and Calico, R. A., "A Comparative Study of Stability Methods for Flexible Satellites, " AIAA Journal, Vol. 11, No. 1, January 1973, pp. 91-98.

10. Saaty, T. L., and Bram, J., Nonlinear Mathematics, McGraw Hill Inc., 1964, pp. 302-306.

11. Hermes, H., and Lasalle, J. P., Fundamental Analysis and Time Optimal Control, Academic Press, 1969.

12. Fan, Liang-Tseng, The Continuous Maximum Principle, John Wiley, 1966, pp. 35-46.

13. Hildebrand, F. B., Methods of Applied Mathematics, Prentice-Hall, Inc., Englewood Cliffs, N. J., 1952, pp. 120-121.

14. Lasdon, L. S., Optimization Theory for Large Systems, McMillan, 1970, pp. 1-5.

15. Gelb, A., and VanderVelde, W. E., Multiple-Input Describing Functions and Nonlinear System Design, McGraw-Hill, 1968, pp. 43-47.

16. Cunningham, W. J., Introduction to Nonlinear Analysis, McGraw-Hill, 1958, pp. 129-135.

17. Krylov, N., and Bogolinbov, N., Introduction to Nonlinear Mechanics, Princeton University Press, Princeton, N. J., Annals of Mathematics Studies, Vol. 11, 1947, pp. 8-28.

18. Huang, T. C., and Das, A., "Random Motion Analysis of Flexible Satellites," In preparation.

19. Huang, T. C., and Das, A., "A Comparative Study on the Pointing Accuracy of Flexible Satellites," In preparation.

RANDOM MOTION ANALYSIS OF FLEXIBLE SATELLITES

Aniruddha Das and T. C. Huang

ABSTRACT

Beginning with a singularly perturbed formulation, the response of a flexible satellite was obtained. This is subjected to random forcing and control torques and to random measurement errors. The method is based on a perturbation technique. Random variables, at different instants of time, were assumed to be uncorrelated.

NOMENCLATURE

A = Generalized mass matrix; Eq. (3).

A^* = Composite body of a satellite.

A_1, A_2, A_3, $\underline{A}_4$ = Matrices and vector associated with the equation for flexible elements of a satellite; Eq. (1).

A_{ij}, A_{ijk}, A'_{ijk} = Components of A_i, i=2,3,4; Eqs. (28), (29), (30).

a_B = Radius of the shell in body B*; Eq. (53).

a_0 = Component of τ_0.

B = Generalized damping matrix; Eq. (3).

B^* = Composite body of a satellite.

$\underline{B}'$ = The earth's magnetic field vector; Eq. (39).

B_1, B_2, B_3 = Coefficients of the deterministic model; Eq. (6).

b_0 = Component of τ_0.

C = Coefficient of the random model; Eq. (17).

C^1 = Component of B_2; Eq. (61).

$\underline{C}_1$, $\underline{C}_2$ = Forced response vectors; Eq. (25).

c^* = The speed of light in vacuum.

c_0 = Component of τ_0.

$\underline{d}$ = Generalized force vector; Eq. (3).

E = Statistical expectation operator.

$\underline{F}_n$ = Disturbing torque function; Eq. (6).

$\underline{f}$ = Generalized force; Eq. (5).

G = Control matrix; Eq. (13).

$\underline{h}$ = Observable function of $\underline{x}_n$; Eq. (8).

I = Identity matrix.

I_B = Moment of inertia matrix of B*.

I_{Bi} = Components of I_B; Eq. (44).

$\underline{J}$ = The volume eddy current density; Eq. (42).

J* = Minimizing functional; Eq. (12).

K_1, K_2, K_3 = Matrices associated with the characteristic equation for dual-spin satellites; Eqs. (67), (68), (69).

ℓ_1 = Length to radius ratio of shells in A* or B*; Eq. (53).

M = Component of $\underline{M}_B$; Eq. (38).

$\underline{M}_B$ = Residual magnetic moment vector of B*.

M_i, i=1-4 = Components of $\Phi(T)$; Eq. (24).

M_x, M_λ = Solutions of Eq. (21).

P_0 = Covariance matrix of $\underline{x}_n(0)$; Eq. (7).

P_1, P_2, P_3, $\underline{P}_4$ = Matrices and vector associated with the generalized Euler's equation; Eq. (2).

P_e = Reflection constant; Eq. (50).

P = Characteristic value; Eqs. (55), (63).

Q = Covariance matrix of $\underline{u}_n(t)$; Eq. (10).

$\underline{q}$ = Generalized position coordinates of the flexible elements; Eq. (1).

$\underline{q}_i$, $\underline{q}_{ij}$ = Components of $\underline{q}$; Eq. (31).

R = Covariance matrix of $\underline{z}(t)$; Eq. (9).

$\underline{r}_c$ = Position vector of a volume element from the center of mass; Eq. (41).

S = Covariance matrix of $\underline{F}_n(t)$; Eq. (11).

S_{Ai}, S_{Bi} = Submatrices of B_1, B_2; Eqs. (60), (61).

T = Terminal time; Eq. (12).

$\underline{u}_n$ = Control torque vector; Eq. (6).

$\underline{X}_n$, n=1,2... = Random state variable; Eq. (14).

$\underline{\bar{x}}_n$ = Deterministic state variable; Eq. (6).

$\underline{y}$ = Generalized force; Eq. (3).

$\underline{z}$ = Observable vector; Eqs. (8), (9).

$\underline{Z}_n$ = Forcing function; Eq. (15).

$\delta(t-\tau)$ = Dirac's delta function.

ε, ε' = Perturbation parameters; Eqs. (3), (7).

ε_1 = Magnitude of B_1' and B_2'; Eq. (39)

θ = Angular measure.

$\underline{\lambda}$, $\underline{\mu}$ = Lagrange's multipliers; Eq. (12).

μ_0 = Permeability of the structural material of the satellite; Eq. (41).

ρ = Average density of the structural material of the satellite; Eq. (45).

ρ', ρ'' = Ratios of the distances of the center of mass from the ends to the radius of the shells of the composite bodies.

σ = Static electrical conductivity of the satellite materials.

σ_i, σ_i' = Real and imaginary parts of the eigenvalues of Eq. (21).

$\underline{\tau}(t)$ = Unit vector directed toward the sun; Eq. (51).

τ_0 = $\tau(0)$.

$\Phi(t)$ = Fundamental matrix of Eq. (21).

ϕ = Scalar potential; Eq. (42).

$\underline{\omega}$ = Angular velocity vector of the satellite.

$\underline{\omega}_i$ = Components of $\underline{\omega}$; Eq. (4).

$\underline{\omega}_B$ = Angular velocity vector of B*.

$\underline{\omega}_{BO}$ = Nominal value of $\underline{\omega}_B$.

OPERATORS

$\dot{(\ )}$ = Time derivative, $\frac{d}{dt}$.

$\bar{(\ )}$ = Deterministic mean value.

$[\ ]^T$ = Transpose

$\tilde{(\ )}$ = Cross product, such that $\underline{u} \times \underline{v} = \tilde{u}\underline{v}$, and hence

$$\tilde{u} = \begin{bmatrix} 0 & -u_3 & u_2 \\ u_3 & 0 & -u_1 \\ -u_2 & u_1 & 0 \end{bmatrix}$$

INTRODUCTION

An analysis of the comparative pointing accuracy of different classes of satellites was reported in Refs. [1,2]. This is part of that study [2].

Equations of motion of flexible satellites have been studied extensively [1,3,4,5,6,7]. These investigations showed that the equation of motion of the flexible elements of a satellite has the form

$$A_1\ddot{q} + A_2(\underline{\omega},t)\dot{q} + A_3(\underline{\omega},t)q = \underline{A}_4(\underline{\omega},t), \qquad (1)$$

where A_1, A_2, and A_3 are square matrices, $\underline{\omega}$ is the angular velocity vector of the satellite, and $q(t)$ is the generalized position coordinates of the flexible elements of the satellite. Also shown, particularly in Ref. [8], was that the generalized Euler's equations for the conservation of angular momentum of the flexible satellite composite bodies can be expressed as

$$P_1\ddot{q} + P_2(\underline{\omega},t)\dot{q} + P_3(\underline{\omega},t)q = \underline{P}_4(\underline{\omega},t). \qquad (2)$$

In general, Eq. (2) has only three scalar equations. Because the number of elements of the vector $q(t)$ is normally much greater than three, the matrices P_1, P_2, and P_3 are usually rectangular.

It was shown in Refs. [8,9] that this large system given by Eqs. (1) and (2) can be considerably reduced to obtain a set of singularly perturbed equations of the form

$$\varepsilon A(\underline{\omega},t)\ddot{\underline{y}}(\underline{\omega},t) + \varepsilon B(\underline{\omega},t)\dot{\underline{y}}(\underline{\omega},t) + \underline{y}(\underline{\omega},t) = \varepsilon \underline{d}(\underline{\omega},t) \qquad (3)$$

In this equation, A and B are square matrices, and the number of scalar equations is the same as that of Eq. (2). Refs. [8,9] demonstrated that, using the small parameter ε to generate the series,

$$\underline{\omega} = \underline{\omega}_0 + \varepsilon\underline{\omega}_1 + \varepsilon^2\underline{\omega}_2 + \text{---}, \qquad (4)$$

Eq. (3) can be solved to obtain

$$\underline{y}(\underline{\omega}_0, t) = \underline{f}(t), \tag{5}$$

where $\underline{f}(t)$ is a known function of time. Solving $\underline{\omega}_0$ from Eq. (5), $\omega_i(\underline{\omega}_0, t)$ for $i \geq 1$ was then explicitly obtained.

The solution of Eq. (5) was treated in detail in Ref. [10] for the case in which all the variables were considered to be deterministic. Equation (5) is nonlinear in $\underline{\omega}_0$. It leads to the Euler's equations when the effects of the flexible elements in this equation are neglected. The explicit form of Eq. (5), as a function of $\underline{\omega}_0$ was derived in Ref. [10]. This was given as a sequence of perturbation equations of the form

$$[B_1]\dot{\underline{x}}_n + [B_2]\underline{x}_n = [B_3]\underline{u}_n + \underline{F}_n(t), \tag{6}$$

where $\underline{u}_n$ are the controlling torques, $\underline{F}_n$ are known functions, and the variables $\underline{x}_n$ were essentially defined by

$$\underline{\omega}_0 = \underline{\bar{x}}_0 + \underline{\bar{x}}_1 + (\varepsilon')^2\underline{\bar{x}}_2 + (\varepsilon')^3\underline{\bar{x}}_3 + \text{---} \tag{7}$$

The variable $\underline{\bar{x}}_0$ in Eq. (7) is a constant and is equal to the nominal angular velocity vector of the satellite.

In the present study, the model given by Eq. (6) will be extended to include the case in which the variables are considered random with certain mean values and variances. The necessity of this extension becomes clear from the following discussion.

The values of the controlling torques ($\underline{u}_n$) are not known, due to probable imperfections of the system. In view of the uncertainty of the errors present, $\underline{u}_n(t)$ are to be considered random variables. The initial values, $(\underline{x}_n(0))$, are also random because they are measured by instruments with inherent error. The initial values, $\underline{q}(0)$ and $\dot{\underline{q}}(0)$, of the structural position coordinates cannot be measured and are unknown. For this reason, the position coordinates $\underline{q}(t)$ must also be considered random variables. Thus, the deterministic solutions of Eq. (6) can be taken as the mean values of the variables involved. But the most likely estimates of these variables can be obtained only by introducing the respective probability distributions. Such an analysis is presented in the following sections.

MAXIMAL PROBABILISTIC FORMULATION

The estimation of the most likely values of $\underline{x}_n(t)$ and $\underline{u}_n(t)$, related by Eq. (6), is known as the "smoothing" problem. Such problems have been treated in detail in Refs. [11, 12]. The present formulation will follow the method shown in [11], and will be given briefly in relation to the system of Eq. (6).

Let it be assumed that the initial values, $\underline{x}_n(0)$, have a Gaussian distribution with a known mean value, $\underline{\bar{x}}_n(0)$, and a known covariance matrix, P_0, given by

$$P_0 = E\{[\underline{x}_n(0) - \overline{\underline{x}}_n(0)][\underline{x}_n(0) - \overline{\underline{x}}_n(0)]^T\} \tag{7}$$

where E denotes statistical expectation. Let $\underline{x}_n(t)$ be measured through a variable $\underline{z}(t)$ where the mean value, $\overline{\underline{z}}(t)$, of $\underline{z}(t)$ is related to $\underline{x}_n$ by

$$\overline{\underline{z}}(t) = \underline{h}(\underline{x}_n). \tag{8}$$

Let it be assumed that the variables $\underline{z}$, $\underline{u}_n$, and $\underline{F}_n$ are also Gaussian with known mean values and covariance matrices, such that

$$E\{[\underline{z}(t) - \overline{\underline{z}}(t)][\underline{z}(\tau) - \overline{\underline{z}}(\tau)]^T\} = R(t)\delta(t-\tau) \tag{9}$$

$$E\{[\underline{u}_n(t) - \overline{\underline{u}}_n(t)][\underline{u}_n(\tau) - \overline{\underline{u}}_n(\tau)]^T\} = Q(t)\delta(t-\tau) \tag{10}$$

$$E\{[\underline{F}_n(t) - \overline{\underline{F}}_n(t)][\underline{F}_n(\tau) - \overline{\underline{F}}_n(\tau)]^T\} = S(t)\delta(t-\tau). \tag{11}$$

Let [0,T] be the time interval in which the maximum-likelihood estimates of the variables are required. These estimates can be obtained by minimizing a functional J*, where J* is given by:

$$\begin{aligned} J^* = {} & [\underline{x}_n(0) - \overline{\underline{x}}_n(0)]^T[P_0]^{-1}[\underline{x}_n(0) - \overline{\underline{x}}_n(0)] \\ & + \int_0^T \{[\underline{z}(t) - \overline{\underline{z}}(t)]^T[R(t)]^{-1}[\underline{z}(t) - \overline{\underline{z}}(t)] \\ & + [\underline{u}_n(t) - \overline{\underline{u}}_n(t)]^T[Q(t)]^{-1}[\underline{u}_n(t) - \overline{\underline{u}}_n(t)] \\ & + [\underline{F}_n(t) - \overline{\underline{F}}_n(t)]^T[S(t)]^{-1}[\underline{F}_n(t) - \overline{\underline{F}}_n(t)]\}dt \\ & + 2\int_0^T \{\underline{\mu}^T[\overline{\underline{z}}(t) - \underline{h}(\underline{x}_n)] \\ & + \underline{\lambda}^T[\dot{\underline{x}}_n + B_1^{-1}\{B_2\underline{x}_n - B_3\underline{u}_n - \underline{F}_n(t)\}]\}dt. \end{aligned} \tag{12}$$

In this equation, $\underline{z}(t)$ is observed. The independent variables are $\underline{x}_n(0)$, $\underline{u}_n(t)$, $\underline{x}_n(t)$, $\overline{\underline{z}}(t)$, and $\underline{F}_n(t)$ along with the Lagrangian multipliers $\underline{\lambda}(t)$ and $\underline{\mu}(t)$.

The minimum in J* can be obtained by solving the variational equations with respect to the independent variables. These variational equations can be reduced to:

$$\dot{\underline{X}}_n = C\overline{\underline{x}}_n + G\overline{\underline{u}}_n + \underline{Z}_n(t). \tag{13}$$

where

$$\underline{X}_n = [\underline{x}_n, \underline{\lambda}]^T \tag{14}$$

$$\underline{Z}_n = [B_1^{-1}\overline{\underline{F}}_n(t), -R^{-1}\underline{z}(t)]^T \tag{15}$$

$$[G] = \begin{bmatrix} B_1^{-1} B_3 \\ 0 \end{bmatrix} \tag{16}$$

and

$$[C] = \begin{bmatrix} -B_1^{-1} B_2 & B_1^{-1}[B_3 Q B_3^T + S][B_1^{-1}]^T \\ R^{-1} & [B_1^{-1} B_2]^T \end{bmatrix} \tag{17}$$

In deriving Eq. (17), it is assumed that the observed variables, $\underline{z}(t)$, are the same as the angular velocities, $\underline{x}_n(t)$, such that

$$\overline{z}(t) = \underline{h}(\underline{x}_n) = \underline{x}_n(t). \tag{18}$$

The boundary conditions associated with Eq. (13) are

$$\underline{\lambda}(T) = 0 \tag{19}$$

and

$$\underline{x}_n(0) = \overline{\underline{x}}_n(0) + [P_0]\underline{\lambda}(0). \tag{20}$$

The most likely values of the random variable $\underline{x}_n$ can be obtained by solving the two point boundary value problem defined by Eqs. (13) through (20). The number of scalar equations in Eq. (13) is exactly twice that of the deterministic set given by Eq. (6). This fact underlines the usefulness of the singularly perturbed formulation introduced in Refs. [8,9].

FORMAL SOLUTIONS FOR $\underline{X}_n$

Two point boundary value problems, similar to that given by Eqs. (13) through (20), have been solved in Refs. [11, 12] after converting them into nonlinear initial value problems. A linear method of solution is also given in Ref. [11] to require particular solutions $\underline{x}_{np}(t)$ and $\underline{\lambda}_p(t)$ of Eq. (13) such that

$$\underline{x}_{np}(0) = \overline{\underline{x}}_n(0) \; ; \; \lambda_p(0) = 0.$$

This linear method of solution also requires the matrix solutions $M_x(t)$ and $M_\lambda(t)$ of the homogeneous equations corresponding to Eq. (13) satisfying

$$\begin{bmatrix} \dot{M}_x \\ \dot{M}_\lambda \end{bmatrix} = [C] \begin{bmatrix} M_x \\ M_\lambda \end{bmatrix}$$

with $M_x(0) = 0$ and $M_\lambda(0) = I$.

Rather than using either of these two methods, a variation of the linear method can be employed. This leads to a simpler algorithm for computer programming.

Let $\Phi(t)$ be the fundamental matrix of the set

$$\dot{\underline{X}} = [C]\underline{X}. \tag{21}$$

An analytic method of determining $\Phi(t)$ has been given in Ref. [10], and this method is to be used. Then the formal solution of Eq. (13) is given by

$$\underline{X}_n(t) = [\Phi(t)]\underline{a}_n + \int_0^t [\Phi(t-\tau)][G\underline{u}_n(\tau) + \underline{Z}_n(\tau)]d , \tag{22}$$

where

$$\underline{a}_n = [\underline{x}_n(0), \underline{\lambda}(0)]^T \tag{23}$$

Let

$$\Phi(T) = \begin{bmatrix} M_1 & M_2 \\ M_3 & M_4 \end{bmatrix} \tag{24}$$

and

$$\begin{Bmatrix} \underline{C}_1(t) \\ \underline{C}_2(t) \end{Bmatrix} = \int_0^t [\Phi(t-\tau)][G\underline{u}_n(\tau) + \underline{Z}_n(\tau)]d\tau, \tag{25}$$

in which the number of rows of $\underline{C}_1$, $\underline{C}_2$, and the square matrices M_1, M_2, M_3, and M_4 are the same as that of $\underline{x}_n(t)$ or $\underline{\lambda}(t)$. Since $\Phi(t)$ is known, $\Phi(T)$ is also known. Methods of computing $C_1(t)$ and $C_2(t)$ using the analytic form of $\Phi(t)$ are also given in Ref. [10]. Hence, from Eq. (22), it can be seen that

$$\begin{bmatrix} \underline{x}_n(T) \\ \underline{\lambda}(T) \end{bmatrix} = \begin{bmatrix} M_1 & M_2 \\ M_3 & M_4 \end{bmatrix} \cdot \begin{bmatrix} \underline{x}_n(0) \\ \lambda(0) \end{bmatrix} + \begin{bmatrix} \underline{C}_1(T) \\ \underline{C}_2(T) \end{bmatrix} .$$

Therefore

$$\underline{\lambda}(T) = M_3\underline{x}_n(0) + M_4\underline{\lambda}(0) + \underline{C}_2(T). \tag{26}$$

Substituting the boundary conditions from Eqs. (19) and (20), Eq. (26) becomes

$$M_3[\bar{x}_n(0) + P_0\lambda(0)] + M_4\lambda(0) + C_2(T) = 0$$

or

$$\lambda(0) = -[M_3P_0 + M_4]^{-1}[C_2(T) + M_3\bar{x}_n(0)]. \qquad (27)$$

Since $\bar{x}_n(0)$ is known, $\lambda(0)$, $x_n(0)$, and, consequently, a_n can be explicitly determined from Eqs. (27), (20), and (23). A method of determining $u_n(t)$ using a time optimal control policy has been given in Ref. [10]. Except for the case when secular terms exist, $x_n(t)$ can thus be directly obtained from Eq. (22), using the methods of Ref. [10].

SECULAR TERMS FOR X_n

The appearance of secular terms is a problem which characterizes all perturbation solutions. The conditions leading to the appearance of such terms in the solution of Eq. (13) must be investigated.

Note that the quantities R(t), Q(t), and S(t) are positive semidefinite. Hence, the off-diagonal blocks of the matrix [C], as defined by Eq. (17), are also positive semidefinite. They also have magnitudes which are small compared to the diagonal blocks. For these reasons, the roots of Eq. (21) will appear in pairs of numbers which are nearly equal in magnitude, but opposite in sign. Thus, the random system given by Eq. (13) will always be asymptotically unstable. In the case of purely imaginary roots, the instability will arise because of the presence of double roots. Because of the inherent unboundedness of X_n, no special effort is required for avoiding the secular terms. The physical reason behind this behavior is that the errors, associated with the system, accumulate with time. This causes the amplitudes of $x_n(t)$ to grow continuously.

SOLUTIONS FOR $q(t)$

Random and deterministic solutions for the structural position coordinates, $q(t)$, must be studied. The generalized coordinates $q(t)$ have to be solved from Eq. (1). Once the vector $\omega(t)$ is determined, Eq. (1) becomes an ordinary linear differential equation with time-varying coefficients. Different numerical and transform methods of solving such equations are available, all of which can consume a large computing effort and time. There is thus the need for an analytic algorithm for solving Eq. (1).

Let the eigenvalues of Eq. (21) be given by $(\sigma_j \pm i\sigma_j')$, $j = 1,2,\ldots,n$. Then, the coefficient matrix $A_2(\omega,t)$ can be expressed as

$$A_2(\omega,t) = A_{20} + [A_{211} + A_{212} + \ldots + A_{21n}] + [A_{221} + A_{222} + A_{223} + \ldots + A_{22m}] + \ldots \qquad (28)$$

where

$$m = n + \frac{1}{2}\, n(n-1) = \frac{1}{2}\, n(n+1)$$

and

$$A_{211} = e^{\sigma_1 t} A'_{211} \; ; \; A_{212} = e^{\sigma_2 t} A'_{212} \; ; \; A_{213} = e^{\sigma_3 t} A'_{213} \; ;$$

$$\ldots \; ; \; A_{21n} = e^{\sigma_n t} A'_{21n} \; ; \; A_{221} = e^{2\sigma_1 t} A'_{221} \; ;$$

$$A_{222} = e^{2\sigma_2 t} A'_{222} \; ; \; \ldots \; ; \; A_{22n} = e^{2\sigma_n t} A'_{22n} \; ;$$

$$A_{22(n+1)} = e^{(\sigma_1+\sigma_2)t} A'_{22(n+1)} \; ;$$

$$A_{22(n+2)} = e^{(\sigma_1+\sigma_3)t} A'_{22(n+2)} \; ; \text{ etc.} \qquad (29)$$

In Eq. (29), the quantities A'_{rst} are periodic and A_{20} is constant. This scheme is designed to separate $A_2(\underline{\omega},t)$ into parts containing $(\underline{\omega})^0$, $\underline{\omega}$, $(\underline{\omega})^2$, etc., and then to separate these again into parts containing the different exponential functions. The second separation is required only for the development of the theory and, as will be seen later, it is not required for actual computation. Using the same procedure, $A_3(\underline{\omega},t)$ and $\underline{A}_4(\underline{\omega},t)$ can also be separated as

$$A_3(\underline{\omega},t) = A_{30} + \sum_j A_{31j} + \sum_k A_{32k} + \ldots$$

$$\underline{A}_4(\underline{\omega},t) = \underline{A}_{40} + \sum_j A_{41j} + \sum_k A_{42k} + \ldots \qquad (30)$$

where A_{30} and $\underline{A}_{40}$ are constants, and $A_{3k\ell}$ and $\underline{A}_{4k\ell}$ are defined in a manner similar to $A_{2k\ell}$. Note that A_1 is a constant.

Let it be assumed that the vector $\underline{q}(t)$ can also be separated as

$$\underline{q}(t) = \underline{q}_0(t) + \sum_j \underline{q}_{1j}(t) + \sum_k \underline{q}_{2k}(t) + \ldots \qquad (31)$$

such that

$$\underline{q}_{1j}(t) = e^{\sigma_j t}\, \underline{q}'_{1j}(t)$$

and

$$\underline{q}_{2j}(t) = e^{(\sigma_k+\sigma_\ell)t}\, \underline{q}'_{2j}(t) \quad \text{etc.}$$

The expressions for A_2, A_3, $\underline{A}_4$, and $\underline{q}(t)$ given by Eqs. (28), (30), and (31) are now substituted into Eq. (1). From the resulting equation, the coefficients of the different exponential functions are separated and set equal to zero. This procedure yields the following equations:

$$A_1 \ddot{\underline{q}}_0 + A_{20} \dot{\underline{q}}_0 + A_{30} \underline{q}_0 = \underline{A}_{40} \qquad (32)$$

$$A_1\ddot{\underline{q}}_{1j} + A_{20}\dot{\underline{q}}_{1j} + A_{30}\underline{q}_{1j} = \underline{A}_{41j} - A_{21j}\underline{q}_0 - A_{31j}\underline{q}_0 \qquad (33)$$

for $j = 1,2,\ldots,n$.

$$A_1\ddot{\underline{q}}_{2k} + A_{20}\dot{\underline{q}}_{2k} + A_{30}\underline{q}_{2k} = \underline{A}_{42k} - A_{22k}\dot{\underline{q}}_0 - A_{32k}\underline{q}_0 - A_{21k}\dot{\underline{q}}_{1k} - A_{31k}\underline{q}_{1k} \qquad (34)$$

for $k = 1,2,\ldots,n$.

Equations corresponding to the terms containing the remaining exponential functions are similarly obtained. Defining

$$\underline{q}_1(t) = \sum_j \underline{q}_{1j}(t) \; ; \; \underline{q}_2(t) = \sum_j \underline{q}_{2j}(t) \; ;$$

$$\underline{A}_{41} = \sum_j \underline{A}_{41j} \; ; \; \underline{A}_{42} = \sum_j \underline{A}_{42j} \; ; \; A_{31} = \sum_j A_{31j} \; ;$$

and so on, Eq. (33) is summed over all j to obtain

$$A_1\ddot{\underline{q}}_1 + A_{20}\dot{\underline{q}}_1 + A_{30}\underline{q}_1 = \underline{A}_{41} - A_{21}\dot{\underline{q}}_0 - A_{31}\underline{q}_0$$

Summing the equations containing $\underline{q}_{2k}(t)$,

$$A_1\ddot{\underline{q}}_2 + A_{20}\dot{\underline{q}}_2 + A_{30}\underline{q}_2 = \underline{A}_{42} - A_{22}\dot{\underline{q}}_0 - A_{32}\underline{q}_0 + A_{21}\dot{\underline{q}}_1 + A_{31}\underline{q}_1$$

In general, the quantities A_2, A_3, and $\underline{A}_4$ do not contain cubic and higher powers of $\underline{\omega}(t)$. Hence, the Eqs. (32), (35), and (36) can be considered as sufficient to obtain the total response, $\underline{q}(t)$. It can be assumed that the eigenvalues of Eq. (32) are not equal to the eigenvalues of Eq. (21) or to their multiples. Eqs. (35) and (36) will not lead to any secular terms because of the existence of the modulating functions A_{21}, A_{22}, A_{31} and A_{32}. Equations (32), (35), and (36) are ordinary differential equations with constant coefficients, and thus are integrated directly with the conditions

$$\dot{\underline{q}}_n(0) = \underline{q}_n(0) = \underline{0} \text{ for all } n. \qquad (37)$$

The deterministic and random solutions of $\underline{q}_n(t)$ are therefore obtained by using the deterministic and random solutions of $\underline{\omega}(t)$ in Eqs. (35) and (36).

EXTERNAL TORQUES

The deterministic and random solutions for the angular velocities, governed by Eqs. (6) and (13) require that the functions $\underline{F}_n(t)$ be known. The dependence of $\underline{F}_n(t)$ on the environmental torques acting on the satel-

lite was explained in Ref. [10]. The mathematical models of the environmental torques will be derived here explicitly. The method of modeling these torques follows that shown in Ref. [13].

Let it be assumed that the satellite consists of two composite bodies, A* and B*. The torque models are now derived for the body B*, while those for the body A* can be obtained similarly. Let $\underline{\omega}_B$ be the angular velocities of the body B*. The composite bodies are assumed to consist of a cylindrical shell with two plates covering the ends.

A. Residual Magnetic Torque

The flow of electric current in the electric circuits inside the spacecraft reacts with the earth's magnetic field to create the torque on it.

Let $\underline{M}_B$ be the residual magnetic moment vector of the body B* in the B*-based coordinates. Let $\underline{B}'$ be the earth's magnetic field vector in the B*-based coordinates. The elements of $\underline{M}_B$ and $\underline{B}'$ are assumed to be of the form

$$\{M_B\} = [M, M, M]^T \tag{38}$$

$$\{\underline{B}'\} = [\varepsilon_1 \cos \omega_{B,3} t, -\varepsilon_1 \sin \omega_{B,3} t, B_3']^T \tag{39}$$

Then the external magnetic torque on the body B* is given by

$$\underline{T}_{EBM} = \underline{M}_B \times \underline{B}' = M \begin{bmatrix} (B_3' + \varepsilon_1 \sin \omega_{B,3} t) \\ (\varepsilon_1 \cos \omega_{B,3} t - B_3') \\ -\varepsilon_1 (\sin \omega_{B,3} t + \cos \omega_{B,3} t) \end{bmatrix} \tag{40}$$

B. Eddy Current Torque

Eddy currents are induced in a satellite spinning in the earth's magnetic field. These eddy currents, in turn, react with the surrounding magnetic field to create a torque on the satellite. The torques on the body B* are given by a volume integral over that body as follows:

$$\underline{T}_{EBC} = \frac{1}{\mu_0 c^*} \int \underline{r}_c \times (\underline{J} \times \underline{B}') dv \tag{41}$$

where

μ_0 = the permeability of structural material of the satellite,

c^* = the speed of light in vacuum,

$\underline{r}_c$ = the position vector of a volume element from the center of mass,

$\underline{J}$ = the volume eddy current density.

All vectors in Eq. (41) are in the B*-based coordinates. The vector $\underline{J}$ is given by

$$\underline{J} = \frac{1}{2\mu_0\sigma}(\underline{\omega}_B \times \underline{B}) \times \underline{r}_c + \underline{\nabla}\phi \tag{42}$$

where σ = the static electrical conductivity of the satellite material,

$\underline{\nabla}$ = the operator for spatial gradient,

and ϕ = a scalar potential for the body such that $\nabla^2\phi = 0$ and $\frac{\partial\phi}{\partial n} = 0$ on the bounding surfaces of the satellite.

In this problem, the field of ϕ is that of the thin plates and shells. Therefore, ϕ is nearly a constant. This reduces Eq. (41) to the following form:

$$\underline{T}_{EBC} = \frac{1}{2\mu_0^2\sigma c^*}\int \underline{r}_c \times \{[(\underline{\omega}_B \times \underline{B}') \times \underline{r}_c] \times \underline{B}'\}dv$$

$$= \frac{1}{2\mu_0^2\sigma c^*}\int \underline{r}_c \times \{[(\omega_{\underline{B}} \cdot \underline{r}_c)\underline{B}' - (\underline{B}' \cdot \underline{r}_c)\underline{\omega}_B] \times B'\}dv$$

$$= \frac{1}{2\mu_0^2\sigma c^*}\int \{(\underline{\omega}_B \cdot \underline{r}_c)[\underline{r}_c \times (\underline{B}' \times \underline{B}')] - (\underline{B} \cdot \underline{r}_c)[\underline{r}_c \times (\underline{\omega}_B \times \underline{B}')]\}dv$$

or

$$\underline{T}_{EBC} = \frac{1}{2\mu_0^2\sigma c^*}\int (\underline{B}' \cdot \underline{r}_c)[(\underline{r}_c \cdot \underline{B}')\underline{\omega}_B - (\underline{r}_c \cdot \underline{\omega}_B)\underline{B}']dv \tag{43}$$

It is now assumed that the moment of inertia matrix of the body B* has the form

$$[I_B] = \begin{bmatrix} I_{B1} & 0 & 0 \\ 0 & I_{B2} & 0 \\ 0 & 0 & I_{B3} \end{bmatrix} \tag{44}$$

Hence Eq. (43) reduces to

$$T_{EBC,1} = -\frac{1}{2\mu_0^2\sigma c^*\rho}[\varepsilon_1^2(\omega_{B,1}\sin^2\omega_{B,3}t + \frac{1}{2}\omega_{B,2}\sin 2\omega_{B,3}t)I_{B2}$$

$$+ (B_3')^2\omega_{B,1}I_{B3} - \varepsilon_1 B_3'\omega_{B,3}I_{B3}\cos(\omega_{B,3}t)] \tag{45}$$

$$T_{EBC,2} = -\frac{1}{2\mu_0^2\sigma c^*\rho}\left[\varepsilon_1^2(\omega_{B,2}\cos^2\omega_{B,3}t + \frac{1}{2}\omega_{B,1}\sin 2\omega_{B,3}t)I_{B1}\right.$$

$$\left. + (B_3')^2\omega_{B,2}I_{B,3} + \varepsilon_1 B_3'\omega_{B,3}I_{B,3}\sin(\omega_{B,3}t)\right] \quad (46)$$

$$T_{EBC,3} = \frac{1}{2\mu_0^2\sigma c^*\rho}\left[(\varepsilon_1^2\omega_{B,3}\cos^2\omega_{B,3}t - B_3'\varepsilon_1\omega_{B,1}\cos\omega_{B,3}t)I_{B1}\right.$$

$$\left. + (\varepsilon_1^2\omega_{B,3}\sin^2\omega_{B,3}t + B_3'\varepsilon_1\omega_{B,2}\sin\omega_{B,3}t)I_{B2}\right] \quad (47)$$

where

$$\underline{T}_{EBC} = [T_{EBC,1}, T_{EBC,2}, T_{EBC,3}]^T \quad (48)$$

and ρ is the average density of the structural materials. If $\omega_{B,1}$ and $\omega_{B,2}$ are small compared to $\omega_{B,3}$, and ε is small compared to B_3, the Eqs. (45), (46), and (47) are simplified to

$$\underline{T}_{EBC} = \frac{1}{2\mu_0^2\sigma c^*\rho}\begin{bmatrix} [B_3'\varepsilon_1\omega_{B,3}\cos\omega_{B,3}t - (B_3')^2\omega_{B,1}]I_{B,3} \\ -[B_3'\varepsilon_1\omega_{B,3}\sin\omega_{B,3}t + (B_3')^2\omega_{B,2}]I_{B,3} \\ 0 \end{bmatrix} \quad (49)$$

C. Solar Radiation Torque

The solar radiation torque arises from the asymmetric pressure distribution which is developed on the surfaces of the satellite due to the electromagnetic radiation from the sun. The formulae used here are taken from Beletskii [14].

The radiation torque vector, $\underline{T}_{EBS}$, on the body B* is given by the following integrals over the surface of that body exposed to the sun.

$$\underline{T}_{EBS} = P_e\{(1-\varepsilon_0)[\underline{\tau} \times \int \underline{r}_c(\underline{n}\cdot\underline{\tau})ds] + \varepsilon_0[2\int \underline{n} \times \underline{r}_c(\underline{n}\cdot\underline{\tau})^2 ds]\} \quad (50)$$

In Eq. (50), all vectors are in the B*-based coordinates and

P_e = a constant = 1×10^{-7} lbs/ft^2 for a surface normal to the sun

ε_0 = the reflection coefficient of the body,

$\underline{n}$ = the unit outward normal to the surface element,

$\underline{\tau}$ = the unit vector directed from the sun,

$\underline{r}_c$ = the position vector of the surface element from the center of the body B*.

It is assumed in this analysis that the angle of incidence of solar radiation is large on the plates which, in turn, are highly reflective. This assumption allows us to consider that the plate surfaces produce negligible torque. Thus, the integrals in Eq. (50) are taken only over the surface of the shell.

Let

$$\underline{\tau}_0 = [a_0,\ b_0,\ c_0]^T$$

be the direction cosines of the sun-vector at the time t = 0. Then

$$\underline{\tau} = \begin{bmatrix} \cos \omega_{B,3}t & \sin \omega_{B,3}t & 0 \\ -\sin \omega_{B,3}t & \cos \omega_{B,3}t & 0 \\ 0 & 0 & 1 \end{bmatrix} \begin{bmatrix} a_0 \\ b_0 \\ c_0 \end{bmatrix}$$

or

$$\underline{\tau} = \begin{bmatrix} (a_0 \cos \omega_{B,3}t + b_0 \sin \omega_{B,3}t) \\ (-a_0 \sin \omega_{B,3}t + b_0 \cos \omega_{B,3}t) \\ c_0 \end{bmatrix} \tag{51}$$

Let the unit outward normal on the shell element be given by

$$n = [\cos\theta,\ \sin\theta,\ 0]^T$$

Then

$$\underline{n} \cdot \underline{\tau} = \cos\theta(a_0 \cos \omega_{B,3}t + b_0 \sin\omega_{B,3}t) + \sin\theta(-a_0 \sin \omega_{B,3}t + b_0 \cos\omega_{B,3}t). \tag{52}$$

Using Eq. (52), Eq. (50) is reduced to

$$T_{EBS} = P_e \cdot a_B^3(1-\varepsilon_0) \begin{bmatrix} \{a_0[(\rho'')^2-(\rho')^2]-\ell_1 c_0 \omega_{B,3}t\}\{-a_0 \sin\omega_{B,3}t + b_0 \cos\omega_{B,3}t\} \\ \{\ell_1 c_0 \omega_{B,3}t - a_0[(\rho'')-(\rho')^2]\}\{a_0 \cos\omega_{B,3}t + b_0 \sin\omega_{B,3}t\} \\ 0 \end{bmatrix}$$

$$- \frac{2}{3} P_e \cdot \varepsilon_0 a_B^3[(\rho'')^2-(\rho')^2](2a_0^2+b_0^2) \begin{bmatrix} \sin\omega_{B,3}t \\ \cos\omega_{B,3}t \\ 0 \end{bmatrix} \tag{53}$$

in which a_B, $a_{B\,1}$, $a_B P'$, and $a_B P''$ are respectively the radius, the length, and the distances from the center of mass to the ends of the shell. The total environmental torque is obtained by summing these individual torques.

STABILITY CRITERIA

It was mentioned in Section 4 that the random system governed by Eq. (13) will always be unstable. Hence, any analysis of stability must be based on the deterministic system given by Eq. (6).

It can be seen from Ref. [10] that Eq. (6) defines a sequence of perturbed equations from the basic system of equations given by Eq. (5). Thus the total deterministic response of a satellite will be stable if each of Eq. (6)'s linearized equations is stable [15] about the point $\underline{x}_n = 0$. This means that the real parts of the eigenvalues of the homogeneous equation

$$B_1\dot{\underline{x}} + B_2\underline{x} = 0 \tag{54}$$

must be negative semi-definite.

For the particular case of a single-body satellite containing three scalar equations in Eq. (54), the corresponding characteristic equation is given by

$$\{\text{Det. } [B_1]\}p^3 + \{\text{Det. } [B_1]\cdot \text{tr}[B_1^{-1}B_2]\}p^2 + \{\text{Det. } [B_2]\ \text{tr}[B_2^{-1}B_1]\}p + \text{Det. } [B_2] = 0 \tag{55}$$

where p is the characteristic root.

The following stability criteria are obtained from the Routh's series [16] corresponding to Eq. (55):

$$\text{Det } [B_1] > 0 \tag{56}$$

$$\text{Det } [B_2] > 0 \tag{57}$$

$$\text{tr } [B_1^{-1}B_2] > 0 \tag{58}$$

$$\{\text{tr } [B_1^{-1}B_2]\}\{\text{tr } [B_2^{-1}B_1]\} > 1 \tag{59}$$

To investigate the case of a dual-spin satellite, the definitions of the matrices B_1 and B_2 given in Eqs. (39) and (40) of Ref. [10] are rewritten:

$$[B_1] = \begin{bmatrix} S_{A1} & 0 & S_{A2} \\ 0 & S_{B1} & S_{B2} \\ 0 & 0 & I \end{bmatrix} \tag{60}$$

and

$$[B_2] = \begin{bmatrix} (S_{A3}+S_{A5}C^1) & 0 & S_{A4} \\ 0 & (S_{B3}+S_{B5}C^1) & S_{B4} \\ -I & I & \tilde{\omega}_{BO} \end{bmatrix} \tag{61}$$

The definitions of S_{Ai}, S_{Bi}, and C^1, corresponding to the bodies A* and B* of a dual-spin satellite, are given in Ref. [10]. The form of $[B_1]^{-1}$ can be deduced from Eq. (60) as given by

$$[B_1]^{-1} = \begin{bmatrix} S_{A1}^{-1} & 0 & -S_{A1}^{-1}S_{A2} \\ 0 & S_{B1}^{-1} & -S_{B1}^{-1}S_{B2} \\ 0 & 0 & I \end{bmatrix} \tag{62}$$

Hence, for dual-spin satellites, the characteristic equation corresponding to Eq. (54) is given by

$$\text{Det.} \begin{bmatrix} \{S_A^{-1}(S_{A3}+S_{A5}C^1+S_{A2})+pI\} & -S_{A1}^{-1}S_{A2} & S_{A1}^{-1}(S_{A4}-S_{A2}\tilde{\omega}_{BO}) \\ S_{B1}^{-1}S_{B2} & \{S_{B1}^{-1}(S_{B3}+S_{B5}C^1-S_{B2})+pI\} & S_{B1}^{-1}(S_{B4}-S_{B2}\tilde{\omega}_{BO}) \\ -I & I & (\tilde{\omega}_{BO}+pI) \end{bmatrix} = 0 \tag{63}$$

This determinant is directly reducible in the special case when S_{Ai} and S_{Bi} are of the same order. The reduced form is given as

$$\text{Det} \quad \{[S_{A1}^{-1}S_{A3}+pI]\,[(S_{B1}^{-1}S'_{B3}+pI)(\tilde{\omega}_{BO}+pI)-S_{B1}^{-1}S_{B2}(S_{B2}^{-1}S_{B4}+pI)] + S_{A1}^{-1}S_{A2}[S_{A2}^{-1}S_{A4}+pI]\,[S_{B1}^{-1}S'_{B3}+pI]\} = 0 \tag{64}$$

where

$$S'_{A3} = S_{A3} + S_{A5}C^1$$

$$S'_{B3} = S_{B3} + S_{B5}C^1 \tag{65}$$

Equation (64) can be reduced further to obtain

$$\text{Det}\,[p^3I + p^2K_1 + pK_2 + K_3] = 0 \tag{66}$$

where

$$K_1 = \tilde{\omega}_{B0} + S_{A1}^{-1}(S'_{A3} + S_{A2}) + S_{B1}^{-1}(S'_{B3} - S_{B2}) \tag{67}$$

$$K_2 = S_{A1}^{-1}S'_{A3}\,[\tilde{\omega}_{B0} + S_{B1}^{-1}(S'_{B3} - S_{B2})] + S_{A1}^{-1}[S_{A2}S_{B1}^{-1}S'_{B3} + S_{A4}] + S_{B1}^{-1}[S'_{B3}\,\tilde{\omega}_{B0} - S_{B4}] \tag{68}$$

$$K_3 = S_{A1}^{-1}S'_{A3}S_{B1}^{-1}[S'_{B3}\,\tilde{\omega}_{B0} - S_{B4}] + S_{A1}^{-1}S_{A4}S_{B1}^{-1}S'_{B3} \tag{69}$$

Equation (66) corresponds to the third order equation given by

$$\dddot{\underline{x}} + K_1\ddot{\underline{x}} + K_2\dot{\underline{x}} + K_3\underline{x} = 0 \tag{70}$$

It is algebraically difficult to obtain specific stability criteria for Eq. (70). But using different time-scales, Eq. (70) can be separated into three simpler equations, valid in different time zones. These three equations are

$$\dddot{\underline{x}} + K_1\ddot{\underline{x}} = 0 \tag{71}$$

$$K_1\ddot{\underline{x}} + K_2\dot{\underline{x}} = 0 \tag{72}$$

$$K_2\dot{\underline{x}} + K_3\underline{x} = 0 \tag{73}$$

The system given by Eq. (70) is dominated by Eq. (71) for short time scales, by Eq. (72) for intermediate time scales, and by Eq. (73) for large time scales. Thus the system will be stable if each of the subsystems given by Eqs. (71), (72), and (73) are stable. For third order systems, the required criteria are easily obtained as

$$\begin{aligned}
&\text{Det } [K_1] > 0\\
&\text{tr } [K_1] > 0\\
&\{\text{tr } [K_1]\}\{\text{tr } [K_1^{-1}]\} > 1\\
&\text{Det } [K_2] > 0\\
&\text{tr } [K_1^{-1}K_2] > 0\\
&\{\text{tr } [K_1^{-1}K_2]\}\{\text{tr } [K_2^{-1}K_1]\} > 1\\
&\text{Det } [K_3] > 0\\
&\text{tr } (K_2^{-1}K_3] > 0\\
&\{\text{tr } [K_2^{-1}K_3]\}\{\text{tr } [K_3^{-1}K_2]\} > 1
\end{aligned} \tag{74}$$

CONCLUSIONS

This analysis considers most of the variables related to the random response of a flexible satellite. In that sense, it is an extension of

the analysis presented in Ref. [10] in which only a deterministic model was considered. It was shown that the random model is always unstable, although the deterministic model is stable. Several stability criteria for the deterministic model were established. Detailed numerical results, and several performance criteria comparing the response of three-axes stabilized, spinning, and dual-spin satellites, for the deterministic and random cases, will be presented in Ref. [16].

REFERENCES

1. Das, A., and Huang, T. C., "Pointing Error Analysis of Geosynchronous Satellites, Parts I-III," Annual Scientific Report, Space Science and Engineering Center, Madison, Wisconsin, December 1972.

2. Das, A., and Huang, T. C., "Pointing Error Analysis of Geosynchronous Satellites, Parts IV-VII," Annual Scientific Report, Space Science and Engineering Center, Madison, Wisconsin, October 1973.

3. Huang, T. C., and Das, A., "Thermoelastic Flutter Models for Elements of Flexible Satellites," Paper presented at the 24th International Astronautical Congress, Baku, U.S.S.R., October 1973.

4. Likins, P. W., and Gale, A. H., "The Analysis of the Interactions Between Attitude Control Systems and Flexible Appendages," Paper IAF AD29, 19th International Aeronautical Congress, New York, October 1968.

5. Likins, P. W., and Fleischer, G. E., "Results of Flexible Spacecraft Attitude Control Studies Utilizing Hybrid Coordinates," J. of Spacecraft and Rockets, Vol. 8, No. 3, March 1971, pp. 264-272.

6. Grote, P. B., McMunn, J. C., and Gluck, R., "Equations of Motion of Flexible Spacecraft," J. of Spacecraft and Rockets, Vol. 8, No. 6 June 1971, pp. 561-567.

7. Meirovitch, L., and Calico, R. A., "A Comparative Study of Stability Methods for Flexible Satellites," AIAA Journal, Vol. 11, No. 1, January 1973, pp. 91-98.

8. Huang, T. C., and Das, A., "Singular Perturbation Equations for Flexible Satellites," Paper presented at the 24th International Astronautical Congress, Baku, U.S.S.R., October 1973.

9. Huang, T. C., and Das, A., "Analysis of Generalized Forces in the Equations of Motion of Flexible Satellites," In preparation.

10. Huang, T. C., and Das, A., "Nonlinear Motion Analysis and Control of Flexible Satellites," In preparation.

11. Saaty, T. L., and Bram, J., Nonlinear Mathematics, McGraw-Hill, 1964, pp. 358-361.

12. Kalman, R. E., and Bucy, R. S., "New Results in Linear Filtering and Prediction Theory," J. Basic Engineering, March 1961, pp. 95-108.

13. Dobrotin, B., et. al., "Mariner Limit Cycle and Self-disturbance Torques," J. of Spacecraft and Rockets, June 1970, pp. 684-689.

14. Beletskii, V. V., "Motions of an Artificial Satellite About Its Center of Mass," NASA TTF-429, 1966.

15. Struble, R. A., Nonlinear Differential Equations, McGraw-Hill, 1962, pp. 129-147.

16. Huang, T. C., and Das, A., "A Comparative Study on the Pointing Accuracy of Flexible Satellites," In preparation.

A COMPARATIVE STUDY OF THE POINTING ACCURACY OF FLEXIBLE SATELLITES

Aniruddha Das and T. C. Huang

ABSTRACT

Numerical results comparing the pointing accuracy of spinning, three-axes stabilized, and dual-spin satellites are presented. The descriptions of the analytical models were reported earlier, and thus are not included. The responses are compared for deterministic and random models with and without external torques. The performance of a uniform control system was compared to a time-optimal control system for the same base-line configurations.

INTRODUCTION

In order to complete our study, we must examine the numerical results of an analysis of the comparative pointing accuracies of different classes of satellites [1,2]. The three classes of satellites previously compared were spinning, three-axes stabilized, and dual-spin satellites. The dynamic model of the dual-spin case is based on a satellite configuration shown in Figure 1. The other classes were obtained from the two composite bodies of this configuration. The analysis is based on the continuously distributed mass models for the beams, plates, and shells shown in Figure 1. Details of this analysis, using Galerkin's method and a singularly perturbed formulation, was given in Refs. [3-5]. Analytical methods used to obtain the deterministic and random responses of the satellites was dealt with in Refs. [6] and [7], respectively.

The present study is primarily directed toward the precession and nutation rates of the three types of satellites. In the presence of an initial disturbance and for a similar control system, the satellite, of which the angular velocity response can be reduced to the nominal angular velocities in the shortest time, is to be considered the most accurate satellite in regard to the maintenance of a fixed angular position in space. For this reason, the two angular velocities transverse to the spin directions were plotted against time in a digital computer simulation corresponding to different situations. Our conclusions are based on these simulations.

THE BASELINE CONFIGURATIONS

Several bits of numerical data were used in a computer simulation for the configuration shown in Figure 1.

Item	Data for the Composite Body	
	A	B
Nominal spin rate, rad./sec.	0.0	6.28
No. of beam-end masses.	4	4
No. of beams.	4	4
No. of spring-mass-damper systems.	4	4
No. of rigid bodies.	2	2
Mass of each s.m.d. system, slugs.	0.0125	0.0125
Each beam-end mass, slugs.	0.0025	0.0025
Mass of each rigid body, slugs.	0.0250	0.0250
Linear mass density of beams, slugs/in.	0.125×10^{-4}	0.125×10^{-4}
Length of each beam, ins.	36.0	10.0
Rad. of gyration of beam-end masses about the junction point, ins.	0.01	0.009
Area density of plates, slugs/in^2.	0.156×10^{-4}	0.156×10^{-4}
Shell radius, ins.	25.0	30.0
Radial distances of s.m.d. systems, ins.	12.5	15.0
Angles of separation of s.m.d. systems	90°	90°
Radial distances of the centres of mass of rigid bodies, ins.	19.0	23.0
Heights of the centres of mass of rigid bodies above plates, ins.	1.0	1.0
Angles subtended by the rigid bodies at the centre, rads.	0.08	0.08
Lengths of the rigid bodies, ins.	6.0	6.0
Total mass of the composite body, slugs.	0.27	0.32
Area density of shell, slugs/in^2.	0.156×10^{-4}	0.156×10^{-4}

Length of shell, ins.	20.0	20.0
Height of the centre of mass above the end of shell, ins.	10.0	10.0
Height of the beam junctions above the centre of total mass on shell, ins.	0.0	0.0
Angles between the spin axis and the beam axes, degrees.	90.0°	90.0°
Angles of separation of beams.	90.0°	90.0°
Principal moments of inertia of the rigid bodies, slugs in^2.	0.025,0.05,0.1	0.025,0.05,0.1
Young's modulus of plates and shell, psi.	$30.0x10^6$	$30.0x10^6$
Thickness of plates and shell, ins.	0.0625	0.0625
Poisson's ratio for plates and shell.	0.3	0.3
Young's modulus of beams, psi.	$30.0x10^6$	$30.0x10^6$
Area moments of inertia of the beam cross-sections, in^4.	$0.1918x10^{-3}$	$0.1918x10^{-3}$
Principal moments of inertia of the composite bodies, slugs in^2.	60.0,77.0,140.0	80.0,95.0,120.0
Principal reaction wheel moments, lbs. in. sec.	1.0,1.0,2.0	0.5,0.5,2.0
Spring constants for s.m.d. systems, lbs/in.	500.0,550.0	200.0,200.0
Plate solar radiation magnitudes, $(in.sec^{-1})$.	$1.0x10^{-4}$	$1.0x10^{-3}$
Angles between plate normals and the Sun, rads.	0.5,0.5	0.5,0.5
Angles between beam normals and the Sun, rads.	0.5,0.5	0.3,0.3
Beam solar radiation magnitudes, $(in.sec^{-1})$.	0.002	0.003
Beam radiation time constant, sec.	0.001	0.001

Damping constant for s.m.d. systems, lbs. sec/in.	0.03	0.03
Plate radiation time constant, sec.	0.001	0.002
Residual magnetic torque, lbs. ins.		
(a) Constant part	10^{-5}	10^{-5}
(b) Rotating part	10^{-5}	10^{-5}
Eddy current torque magnitude, lbs. ins.	10^{-5}	10^{-5}
Reflection coefficient	0.7	0.7
Initial Sun vector	$[1,0,0]^T$	$[1,0,0]^T$
Solar pressure constant, P_e, lbs/in^2.	0.7×10^{-9}	0.7×10^{-9}

The following data were used for the dual-spin configuration only:

Length of the connector = 2.0 ins.

Young's modulus of the connector = 3.0×10^7 psi.

Area moment of inertia of the cross-section of the connector = 0.08 in^4.

Cross-sectional area of the connector = 0.7854 in^2.

Frictional torque per unit relative angular velocity in the bearing = 0.001 lbs. in^2/rad.

Ratio between the imaginary part and the real part of the Young's modulus of the connector = 10^{-4}.

In the simulations for the random cases, the covariance matrices were taken as scalar matrices. The scalar magnitudes of these matrices are as follows:

Initial value matrix - 1.0×10^{-4}.

Measured value matrix - 1.0×10^{-10}.

Control and external torque matrices - 1.0×10^{-10}.

THE SATELLITE RESPONSE

In each of the different cases considered, the satellite was taken to have an initial disturbance, such that the initial angular velocities were $[0.001, 0.0, \Omega]^T$, where the nominal velocities were $[0.0, 0.0, \Omega]^T$. Tables 2, 3 and 4 indicate the manner in which the plotted response given in Figures 2-91 was obtained.

Table 2. Responses Without Environmental Torques

Type of Satellite	Type of Response	Without Control Fig. No.	Control Policy	
			Uniform Fig. No.	Optimal Fig. No.
Three-axes stabilized	(a) Deterministic	2	3	4
	(b) Random	5	6	7
	(c) Difference of (a) & (b)	8	8	9
	(d) The multiplier, $\underline{\lambda}$, Ref. [7]	10	11	12
Spinner	(a) As above.	13	14	15
	(b)	16	17	18
	(c)	19	19	20
	(d)	21	22	23
Dual-spin	(a)	24	25	26
	(b)	27	28	29
	(c)	30	30	31
	(d)	32	33	34

Table 3. Responses with Environmental Torques

Type of Satellite	Type of Response	Without Control Fig. No.	Control Policy	
			Uniform Fig. No.	Optimal Fig. No.
Three-axes stabilized	(a) Deterministic	35	36	37
	(b) Random	38	39	40
	(c) Difference of (a) & (b)	41	41	42
	(d) The multiplier, λ, Ref. [7]	43	44	45
Spinner	(a) As above	46	47	48
	(b)	49	50	51
	(c)	52	52	53
	(d)	54	55	56
Dual-spin	(a)	57	58	59
	(b)	60	61	62
	(c)	63	63	64
	(d)	65	66	67

The responses shown in Figures 2-67 correspond to the long time first order expansions mentioned in Refs. [6,7]. The second and third order responses are similar in nature.

Table 4. Long Time Second Order and Boundary Layer Deterministic Responses

Type of Response	Type of Satellite	Without Control; Fig. No.	With Optimal Control; Fig. No.
Long time;	Spinner	68	69
Second order	Dual-spin	70	71
Outer boundary layer;	Three-axes stab.	72	73
First order	Spinner	74	75
	Dual-spin	76	77
Outer boundary layer;	Spinner	78	79
Second order	Dual-spin	80	81
Inner boundary layer;	Three-axes stab.	82	83
First order	Spinner	84	85
	Dual-spin	86	87
Inner boundary layer;	Spinner	88	89
Second order	Dual-spin	90	91

A comparison of the performances of the satellites can be made on the basis of the long time first order responses. Except for the differential responses plotted in Figs. [8,19,30,41,52,63], the curves marked 1 and 2 are the angular velocity responses about the body-fixed axes No. 1 and 2. These axes are transverse to the axes of symmetry. Axis No. 1 passes through the nominal axis of the beam No. 1, shown in Figure 1. The difference between the deterministic and random responses was plotted as the response type (c). In Figures [8,19,30,41,52,63], the curves marked 1 and 2 comprise the differential response for the uncontrolled case, and those marked 3 and 4 are for the uniformly controlled case for the transverse angular velocities of the satellite. The uniform control is obtained by applying a constant torque to the satellite. The optimal control torques are based on the theory given in Ref. [6].

CONCLUSIONS

The responses given in Figures [2-67] show that, despite the stability of the individual composite bodies, the dual-spin configuration is unstable when the deterministic models are considered. All the random models are necessarily unstable. In the deterministic case, a spinning satellite is the most ideally controllable, while the three-axes stabilized satellite

exhibits an uncontrollable band near the origin. In the random case, the spinning satellite undergoes large deviations while the three-axes stabilized satellite is perfectly controllable. Note that this expected deviation of the spinning satellite in the random case can be reduced considerably by choosing a much smaller control time interval. Also, a spinning satellite is more suitable for uniform control while a three-axes stabilized satellite needs a "bang-bang" type optimal control. In this configuration, the dual-spin satellite presents a compromise between the advantages and disadvantages of the spinning satellite and the three-axes stabilized satellite. This was due to the comparability of the mass and inertia properties of the two composite bodies. From these considerations, it appears that the configuration with the greatest pointing accuracy is a spinning satellite with uniform control and a very small interval between two angular position measurements. The deterministic responses obtained in Figures [68-91] present essentially the same characteristics as those seen in Figures [2-67].

REFERENCES

1. Das, A., and Huang, T. C., "Pointing Error Analysis of Geosynchronous Satellites, Parts I-III," Annual Scientific Report, Space Science and Engineering Center, Madison, Wisconsin, December 1972.

2. Das, A., and Huang, T. C., "Pointing Error Analysis of Geosynchronous Satellites, Parts IV-VI," Annual Scientific Report, Space Science and Engineering Center, Madison, Wisconsin, October 1973.

3. Huang, T. C., and Das, A., "Thermoelastic Flutter Models for Elements of Flexible Satellites," Paper presented at the 24th International Astronautical Congress, Baku, U.S.S.R., October 1973.

4. Huang, T. C., and Das, A., "Singular Perturbation Equations for Flexible Satellites," Paper presented at the 24th International Astronautical Congress, Baku, U.S.S.R., October 1973.

5. Huang, T. C., and Das, A., "Analysis of Generalized Forces in the Equations of Motion of Flexible Satellites," In preparation.

6. Huang, T. C., and Das, A., "Nonlinear Motion Analysis and Control of Flexible Satellites," In preparation.

7. Huang, T. C., and Das, A., "Random Motion Analysis of Flexible Satellites," In preparation.

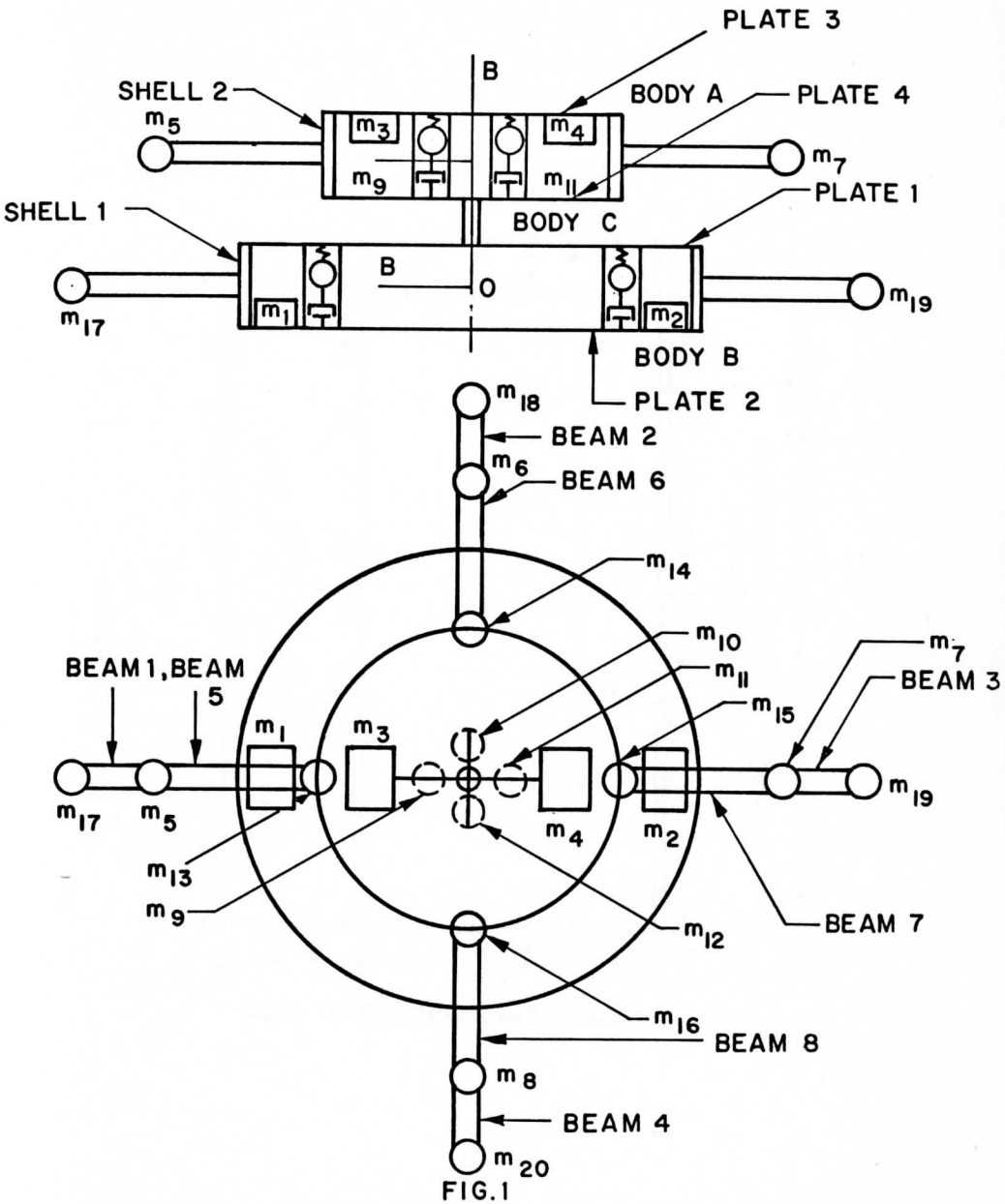

FIG.1

ASSUMED CONFIGURATION OF THE FLEXIBLE SATELLITE

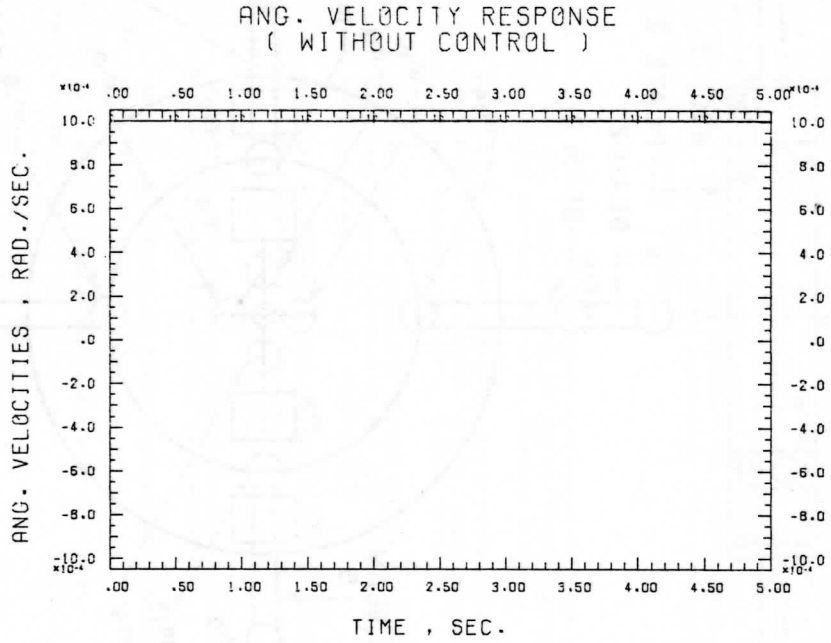
ANG. VELOCITY RESPONSE
(WITHOUT CONTROL)
ANG. VELOCITIES , RAD./SEC.
TIME , SEC.
x10-4
10.0
8.0
6.0
4.0
2.0
.0
-2.0
-4.0
-6.0
-8.0
-10.0
.00
.50
1.00
1.50
2.00
2.50
3.00
3.50
4.00
4.50
5.00

Figure 2

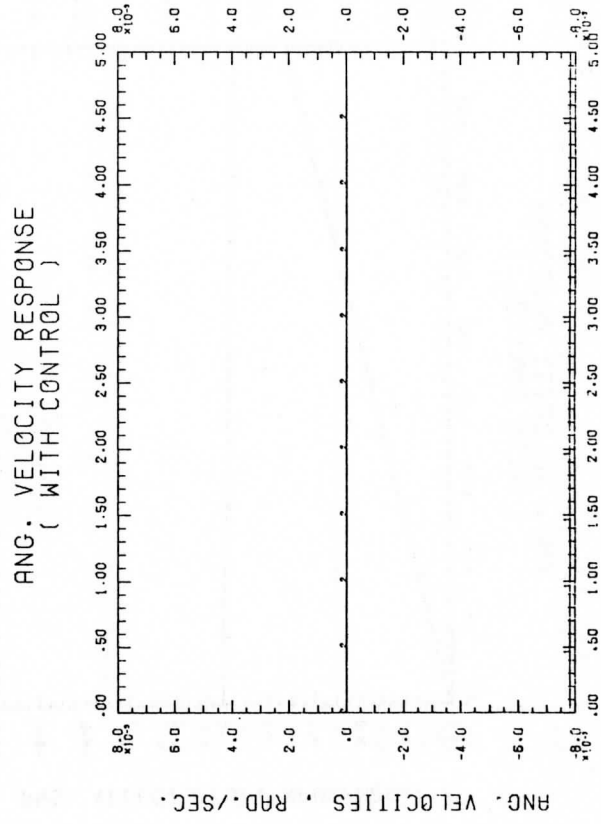
ANG. VELOCITY RESPONSE
(WITH CONTROL)
ANG. VELOCITIES , RAD./SEC.
TIME , SEC.
.00
.50
1.00
1.50
2.00
2.50
3.00
3.50
4.00
4.50
5.00
8.0
6.0
4.0
2.0
.0
-2.0
-4.0
-6.0
-8.0
x10⁻³

Figure 3

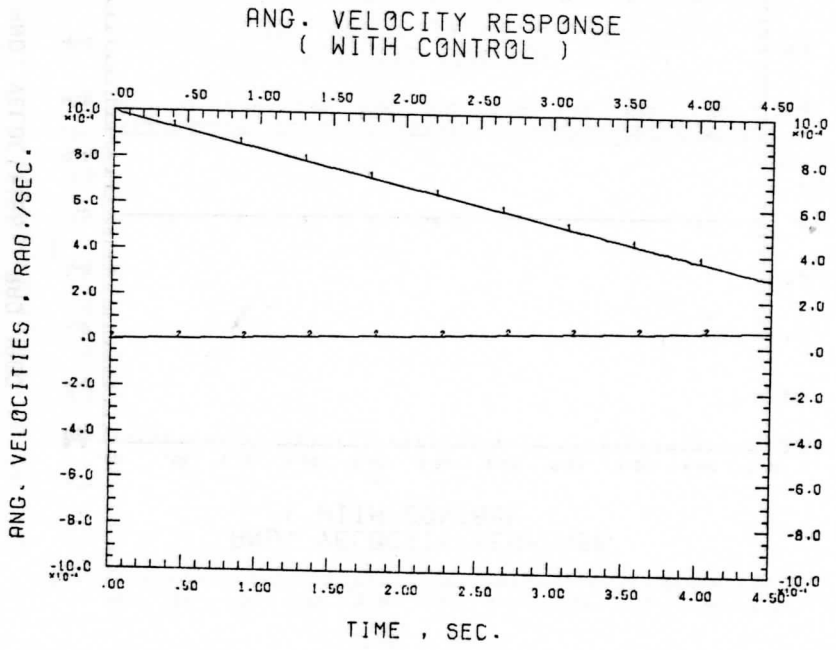
ANG. VELOCITY RESPONSE
(WITH CONTROL)
ANG. VELOCITIES , RAD./SEC.
TIME , SEC.
.00
.50
1.00
1.50
2.00
2.50
3.00
3.50
4.00
4.50
10.0
8.0
6.0
4.0
2.0
.0
-2.0
-4.0
-6.0
-8.0
-10.0

Figure 4

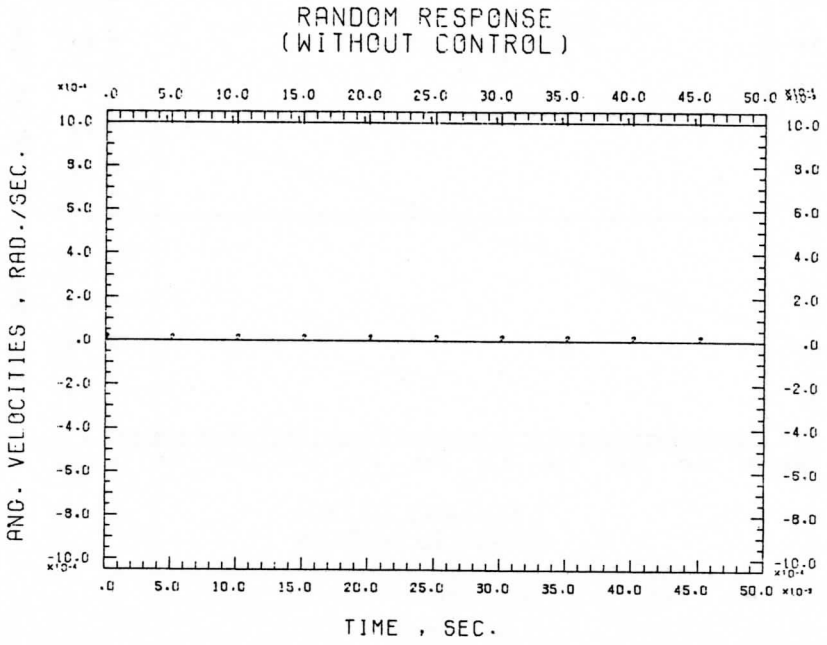
RANDOM RESPONSE
(WITHOUT CONTROL)
ANG. VELOCITIES , RAD./SEC.
TIME , SEC.
.0
5.0
10.0
15.0
20.0
25.0
30.0
35.0
40.0
45.0
50.0
10.0
8.0
6.0
4.0
2.0
-2.0
-4.0
-6.0
-8.0
-10.0

Figure 5

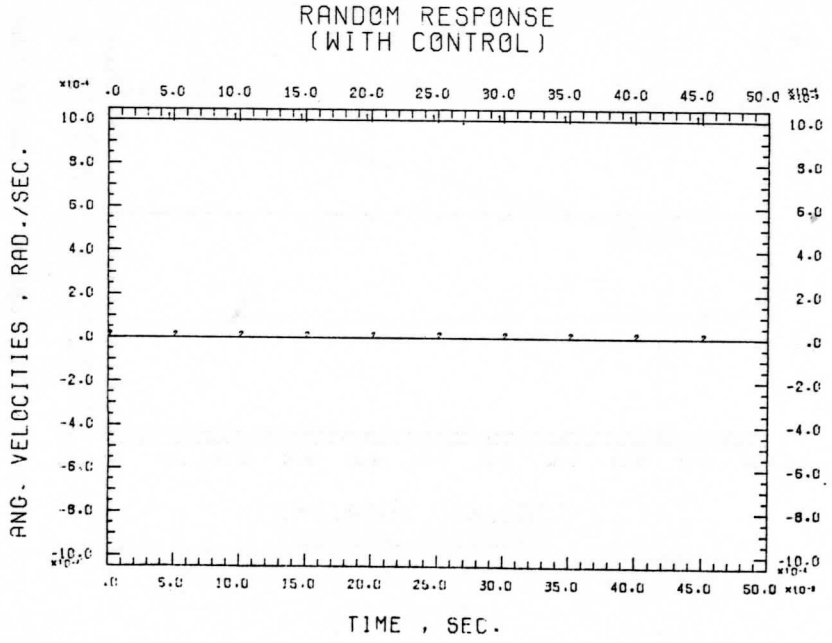
RANDOM RESPONSE
(WITH CONTROL)
ANG. VELOCITIES , RAD./SEC.
TIME , SEC.
.0
5.0
10.0
15.0
20.0
25.0
30.0
35.0
40.0
45.0
50.0
10.0
8.0
6.0
4.0
2.0
-2.0
-4.0
-6.0
-8.0
-10.0

Figure 6

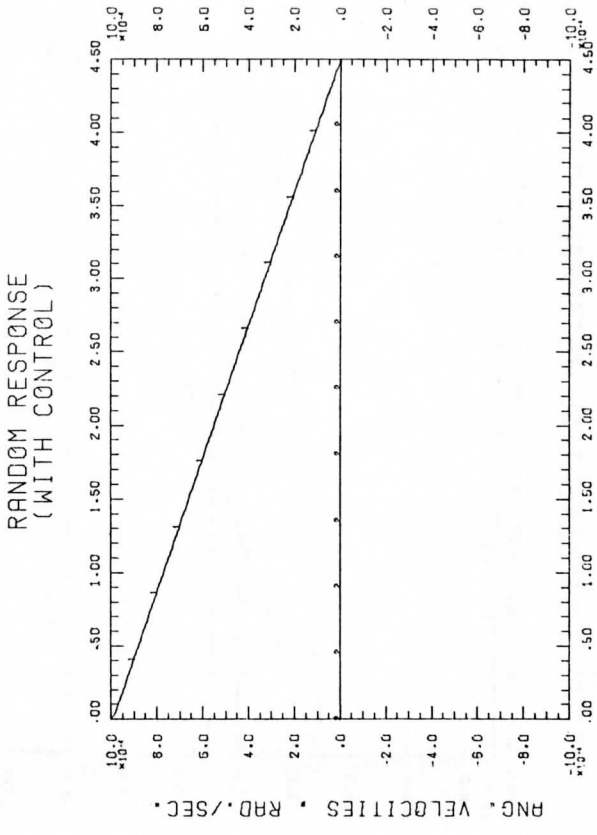
RANDOM RESPONSE
(WITH CONTROL)
RNG. VELOCITIES , RAD./SEC.
TIME , SEC.

Figure 7

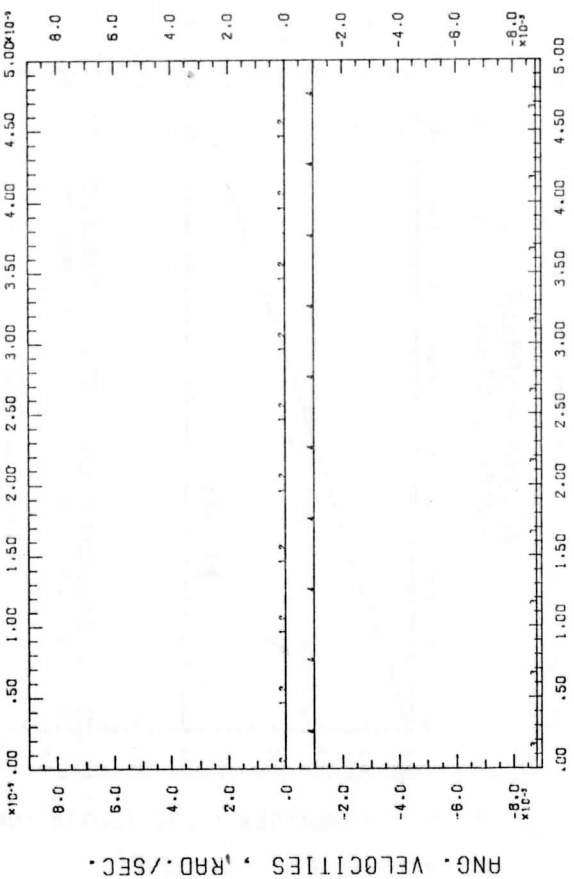

Figure 8

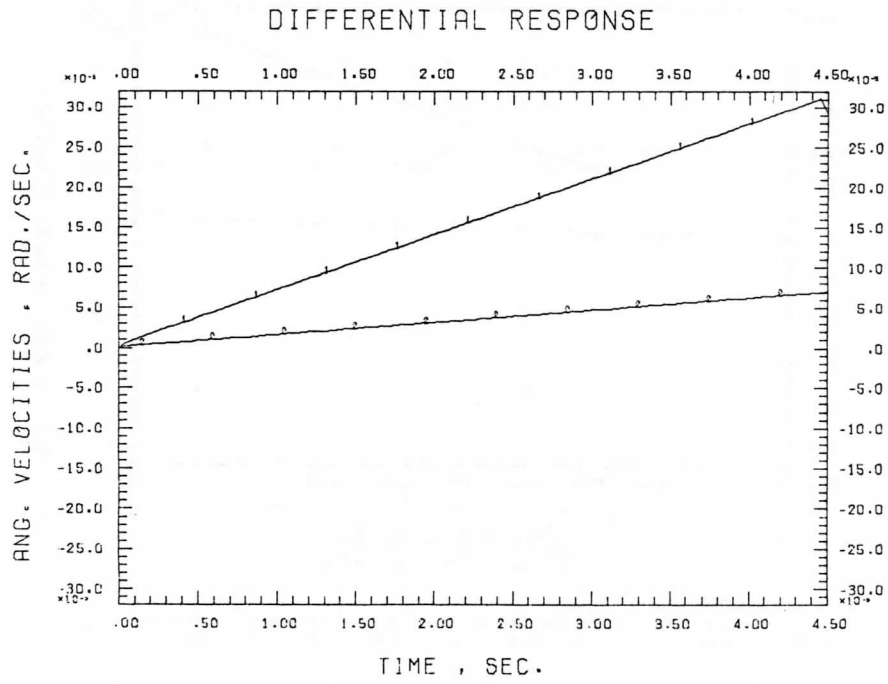
DIFFERENTIAL RESPONSE
ANG. VELOCITIES , RAD./SEC.
TIME , SEC.
×10⁻⁴
.00
.50
1.00
1.50
2.00
2.50
3.00
3.50
4.00
4.50
30.0
25.0
20.0
15.0
10.0
5.0
.0
-5.0
-10.0
-15.0
-20.0
-25.0
-30.0

Figure 9

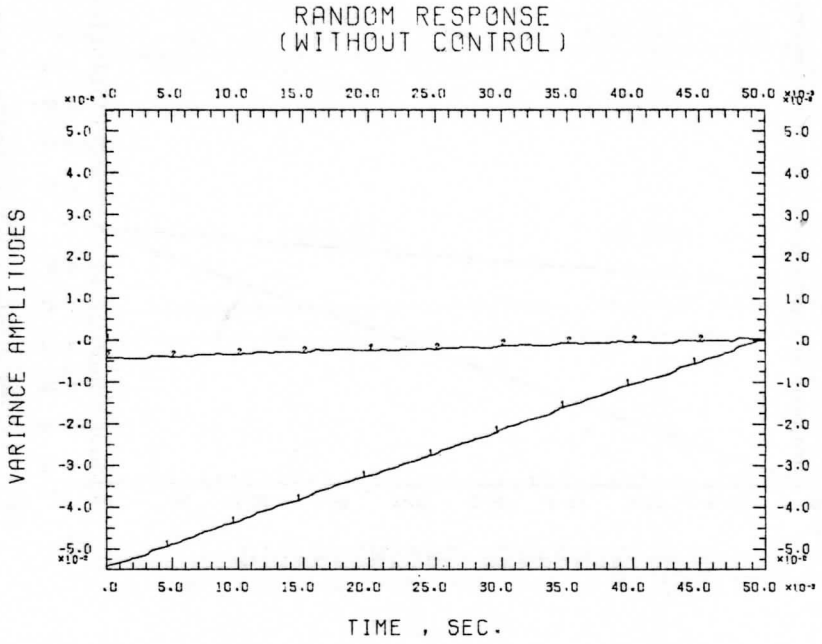
RANDOM RESPONSE
(WITHOUT CONTROL)
VARIANCE AMPLITUDES
TIME , SEC.
.0
5.0
10.0
15.0
20.0
25.0
30.0
35.0
40.0
45.0
50.0
5.0
4.0
3.0
2.0
1.0
.0
-1.0
-2.0
-3.0
-4.0
-5.0

Figure 10

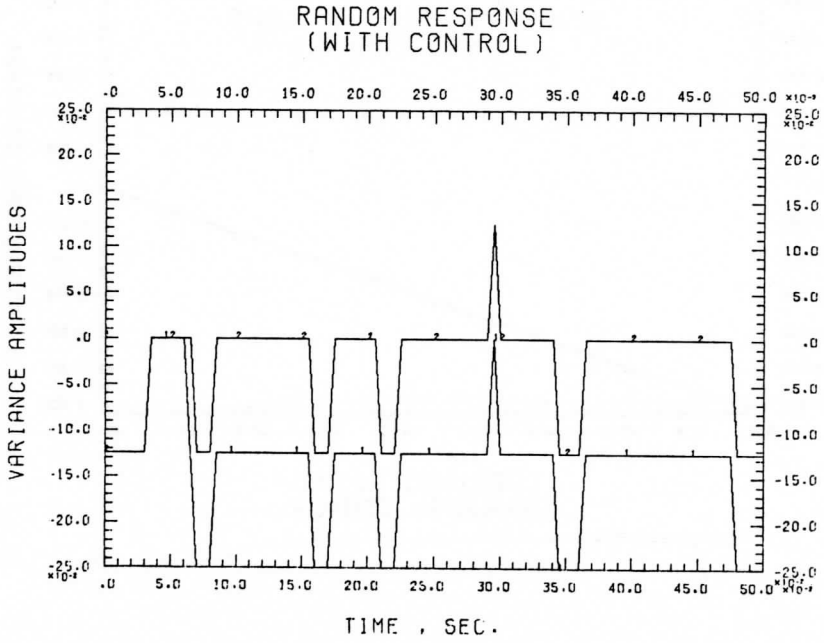
RANDOM RESPONSE
(WITH CONTROL)
VARIANCE AMPLITUDES
TIME , SEC.
.0
5.0
10.0
15.0
20.0
25.0
30.0
35.0
40.0
45.0
50.0
25.0
20.0
15.0
10.0
5.0
-5.0
-10.0
-15.0
-20.0
-25.0

Figure 11

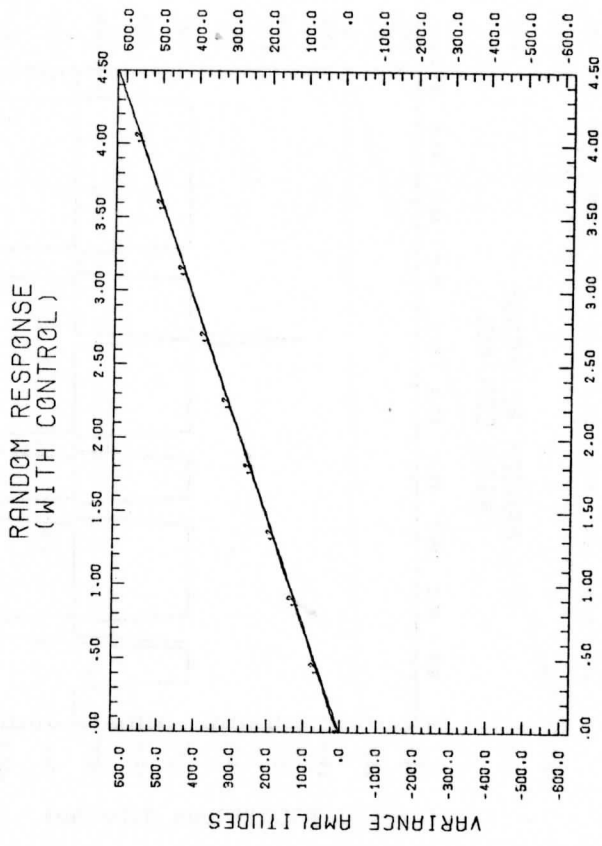
RANDOM RESPONSE
(WITH CONTROL)
VARIANCE AMPLITUDES
TIME , SEC.
600.0
500.0
400.0
300.0
200.0
100.0
.0
-100.0
-200.0
-300.0
-400.0
-500.0
-600.0
.00
.50
1.00
1.50
2.00
2.50
3.00
3.50
4.00
4.50

Figure 12

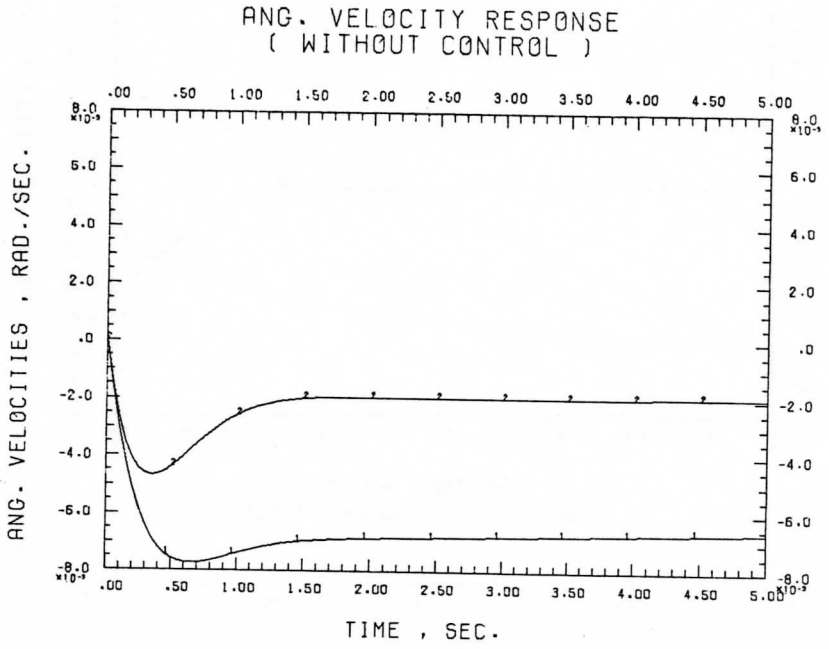
ANG. VELOCITY RESPONSE
(WITHOUT CONTROL)
ANG. VELOCITIES , RAD./SEC.
TIME , SEC.
.00
.50
1.00
1.50
2.00
2.50
3.00
3.50
4.00
4.50
5.00
8.0
6.0
4.0
2.0
.0
-2.0
-4.0
-6.0
-8.0
x10-3

Figure 13

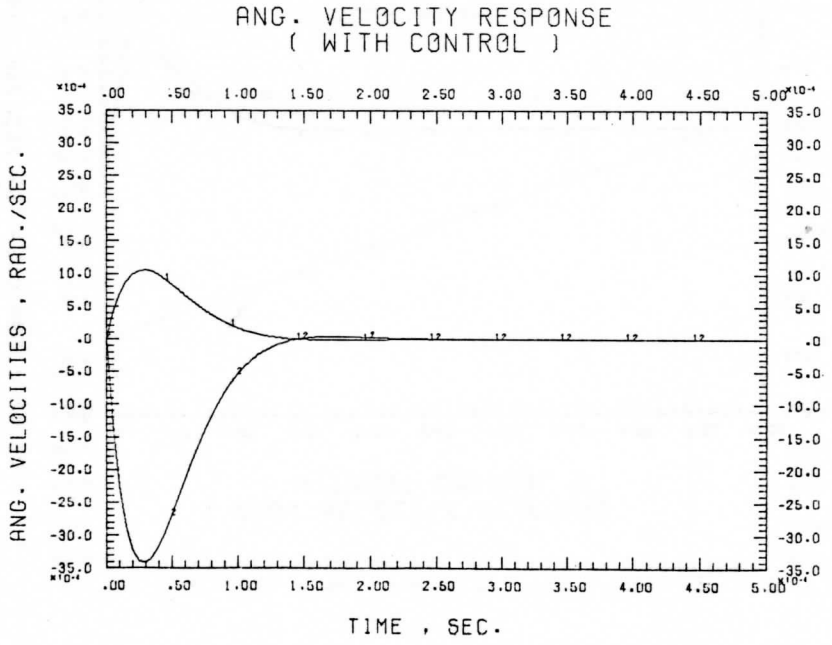
ANG. VELOCITY RESPONSE
(WITH CONTROL)
ANG. VELOCITIES , RAD./SEC.
TIME , SEC.
×10-4
35.0
30.0
25.0
20.0
15.0
10.0
5.0
.0
-5.0
-10.0
-15.0
-20.0
-25.0
-30.0
-35.0
.00
.50
1.00
1.50
2.00
2.50
3.00
3.50
4.00
4.50
5.00

Figure 14

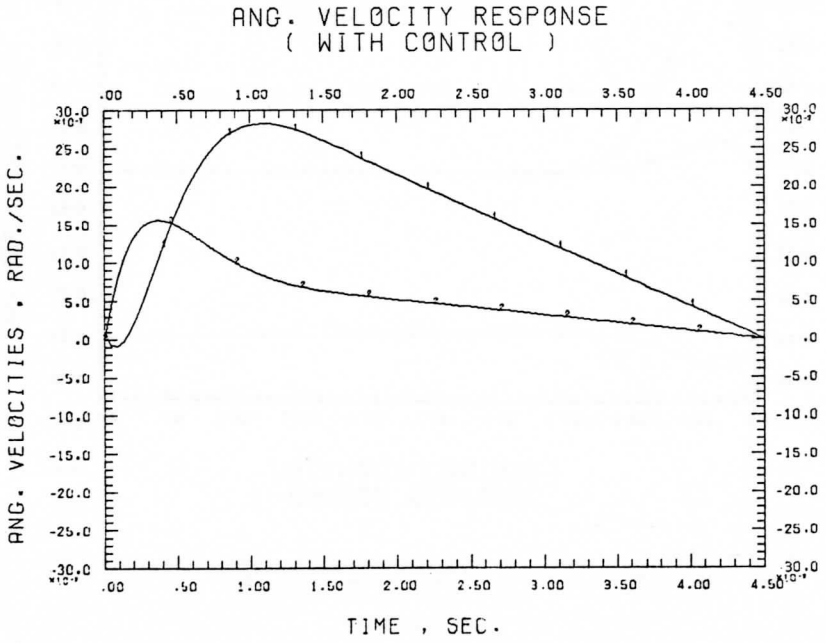
ANG. VELOCITY RESPONSE
(WITH CONTROL)
ANG. VELOCITIES , RAD./SEC.
TIME , SEC.
.00
.50
1.00
1.50
2.00
2.50
3.00
3.50
4.00
4.50
30.0
25.0
20.0
15.0
10.0
5.0
.0
-5.0
-10.0
-15.0
-20.0
-25.0
-30.0

Figure 15

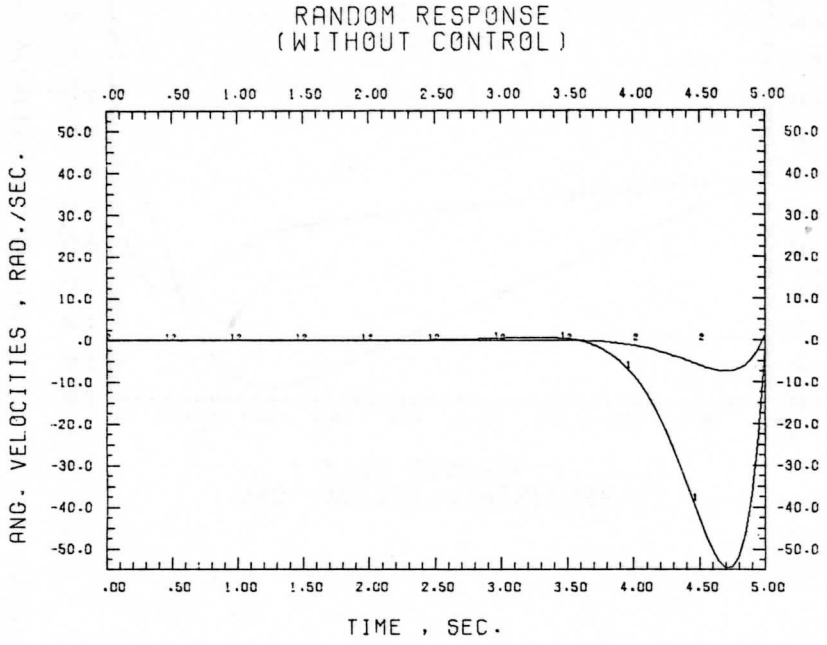
RANDOM RESPONSE
(WITHOUT CONTROL)
ANG. VELOCITIES , RAD./SEC.
TIME , SEC.
.00
.50
1.00
1.50
2.00
2.50
3.00
3.50
4.00
4.50
5.00
50.0
40.0
30.0
20.0
10.0
.0
-10.0
-20.0
-30.0
-40.0
-50.0

Figure 16

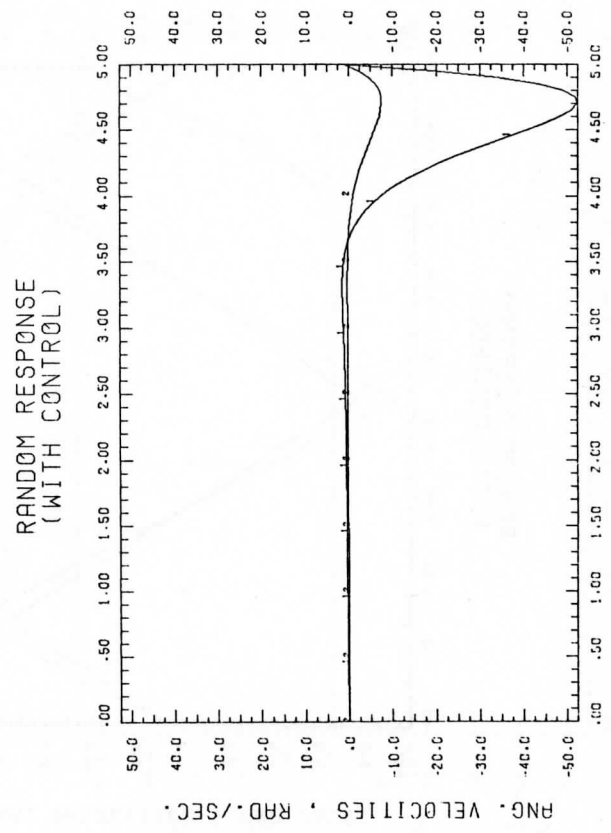
RANDOM RESPONSE
(WITH CONTROL)
RNG. VELOCITIES , RAD./SEC.
TIME , SEC.
50.0
40.0
30.0
20.0
10.0
0.
-10.0
-20.0
-30.0
-40.0
-50.0
.00
.50
1.00
1.50
2.00
2.50
3.00
3.50
4.00
4.50
5.00

Figure 17

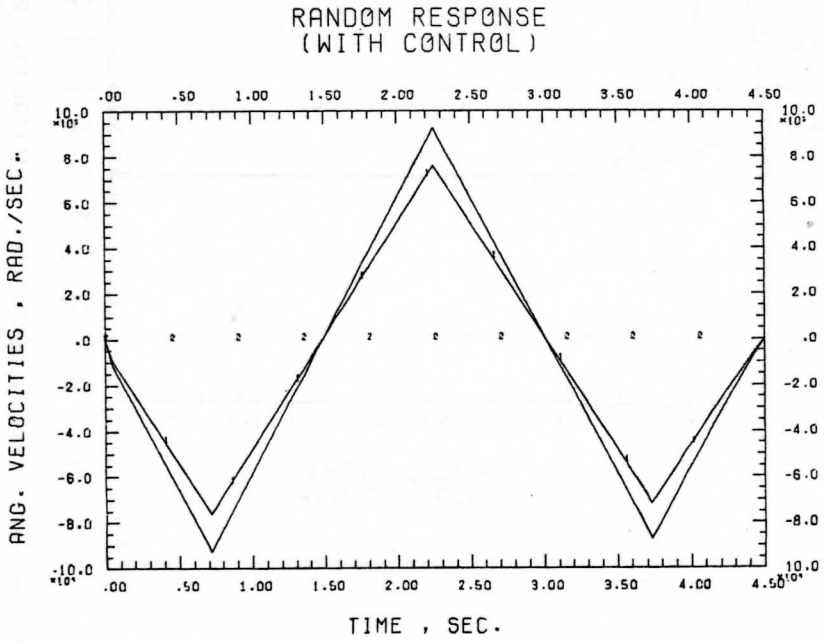
RANDOM RESPONSE
(WITH CONTROL)
ANG. VELOCITIES , RAD./SEC.
TIME , SEC.
.00
.50
1.00
1.50
2.00
2.50
3.00
3.50
4.00
4.50
10.0
8.0
6.0
4.0
2.0
.0
-2.0
-4.0
-6.0
-8.0
-10.0

Figure 18

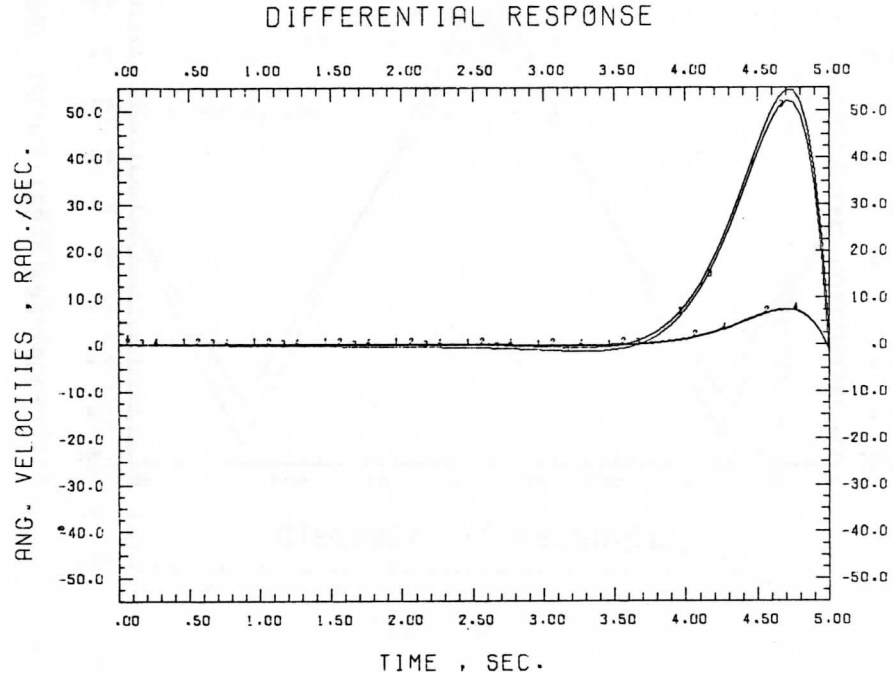
DIFFERENTIAL RESPONSE
ANG. VELOCITIES , RAD./SEC.
TIME , SEC.
.00
.50
1.00
1.50
2.00
2.50
3.00
3.50
4.00
4.50
5.00
50.0
40.0
30.0
20.0
10.0
.0
-10.0
-20.0
-30.0
-40.0
-50.0

Figure 19

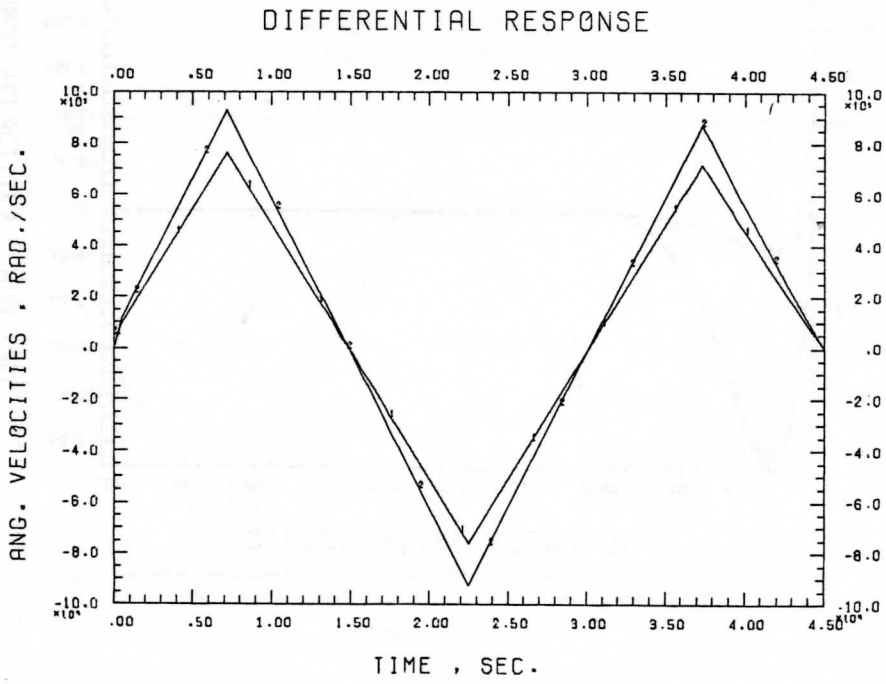
DIFFERENTIAL RESPØNSE
ANG. VELØCITIES , RAD./SEC.
TIME , SEC.
.00
.50
1.00
1.50
2.00
2.50
3.00
3.50
4.00
4.50
10.0
8.0
6.0
4.0
2.0
.0
-2.0
-4.0
-6.0
-8.0
-10.0

Figure 20

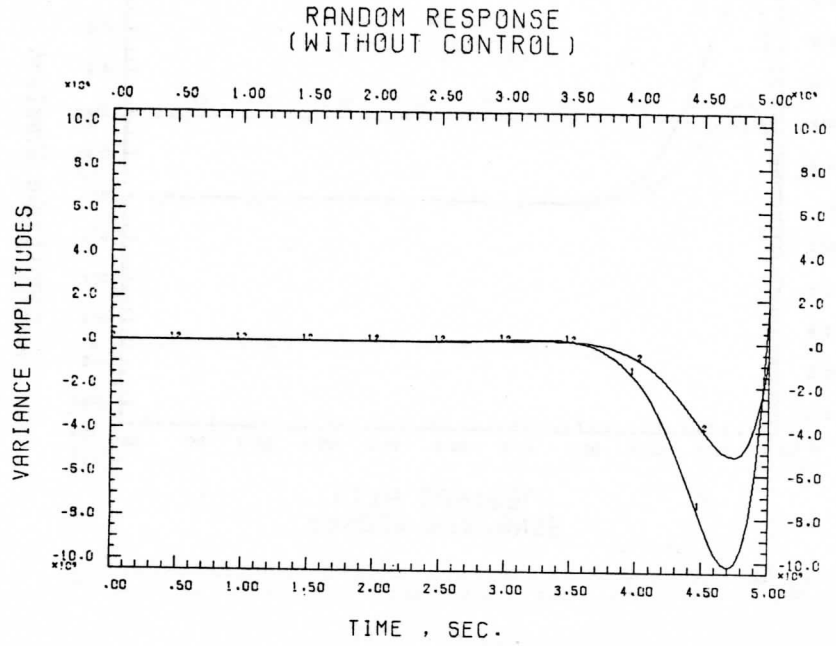
RANDOM RESPONSE
(WITHOUT CONTROL)
VARIANCE AMPLITUDES
TIME , SEC.
.00
.50
1.00
1.50
2.00
2.50
3.00
3.50
4.00
4.50
5.00
10.0
8.0
6.0
4.0
2.0
.0
-2.0
-4.0
-6.0
-8.0
-10.0

Figure 21

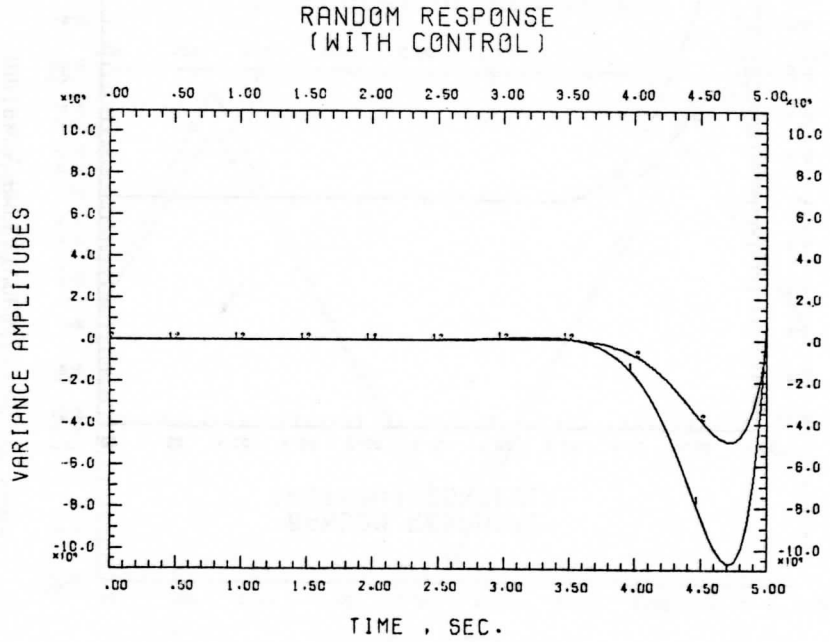
RANDOM RESPONSE
(WITH CONTROL)
VARIANCE AMPLITUDES
TIME , SEC.
.00
.50
1.00
1.50
2.00
2.50
3.00
3.50
4.00
4.50
5.00
10.0
8.0
6.0
4.0
2.0
.0
-2.0
-4.0
-6.0
-8.0
-10.0

Figure 22

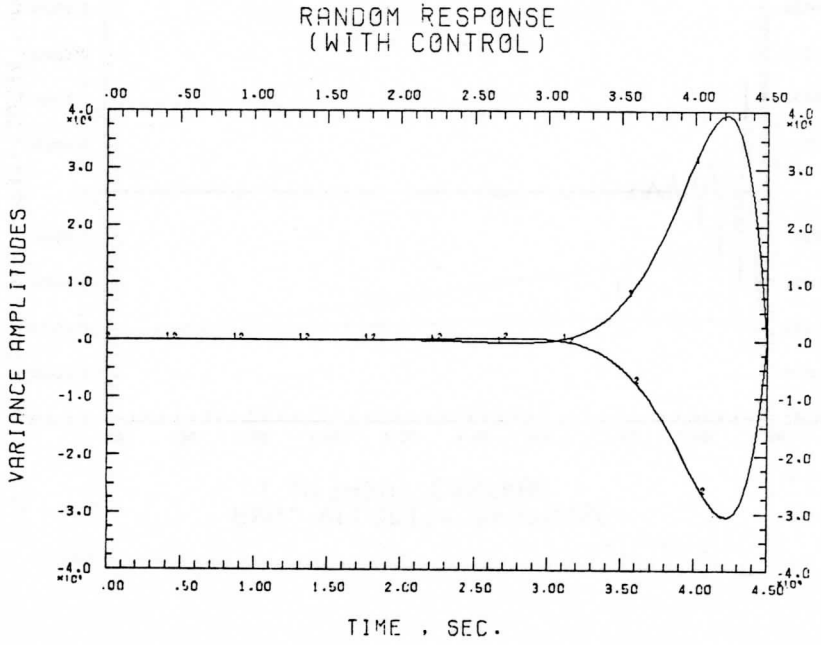
RANDOM RESPONSE
(WITH CONTROL)
VARIANCE AMPLITUDES
TIME , SEC.
.00
.50
1.00
1.50
2.00
2.50
3.00
3.50
4.00
4.50
4.0
3.0
2.0
1.0
.0
-1.0
-2.0
-3.0
-4.0

Figure 23

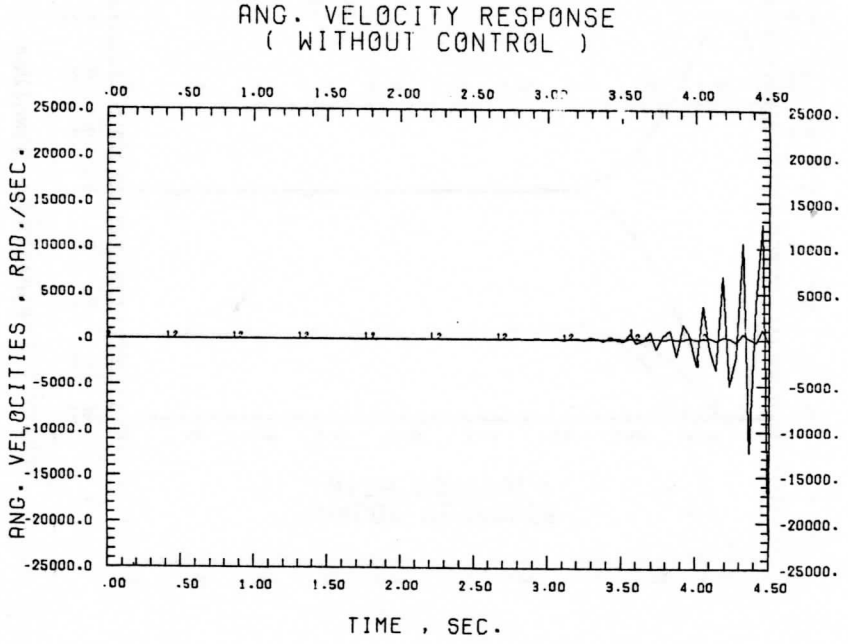
ANG. VELOCITY RESPONSE
(WITHOUT CONTROL)
ANG. VELOCITIES , RAD./SEC.
25000.0
20000.0
15000.0
10000.0
5000.0
.0
-5000.0
-10000.0
-15000.0
-20000.0
-25000.0
.00
.50
1.00
1.50
2.00
2.50
3.00
3.50
4.00
4.50
TIME , SEC.

Figure 24

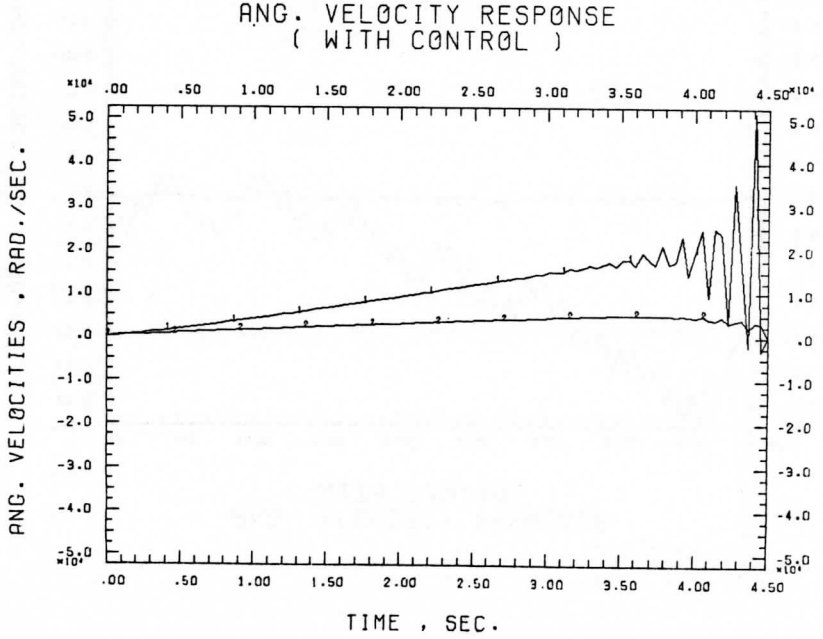
ANG. VELOCITY RESPONSE
(WITH CONTROL)
ANG. VELOCITIES , RAD./SEC.
TIME , SEC.
×10⁴
5.0
4.0
3.0
2.0
1.0
.0
-1.0
-2.0
-3.0
-4.0
-5.0
.00
.50
1.00
1.50
2.00
2.50
3.00
3.50
4.00
4.50

Figure 25

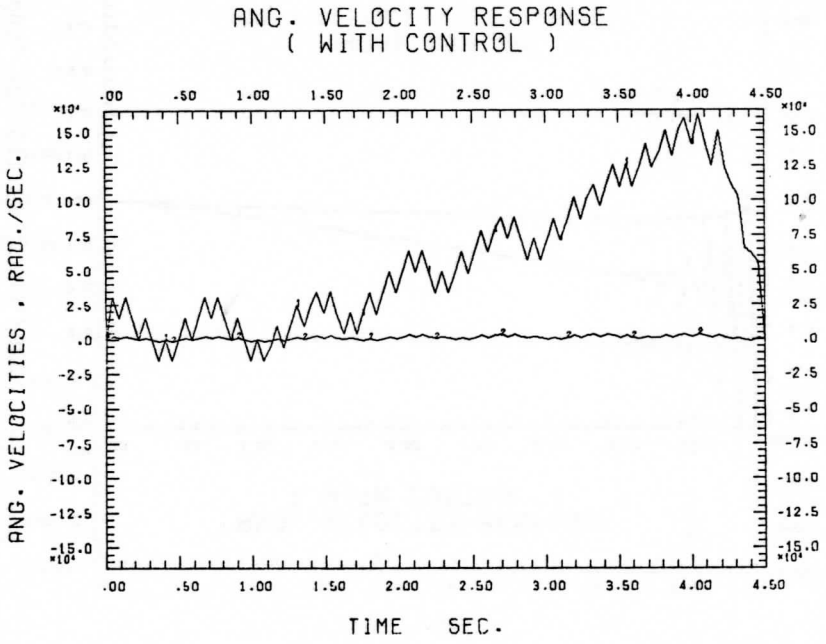
ANG. VELOCITY RESPONSE
(WITH CONTROL)
ANG. VELOCITIES , RAD./SEC.
TIME SEC.
×10⁴
15.0
12.5
10.0
7.5
5.0
2.5
.0
-2.5
-5.0
-7.5
-10.0
-12.5
-15.0
.00
.50
1.00
1.50
2.00
2.50
3.00
3.50
4.00
4.50

Figure 26

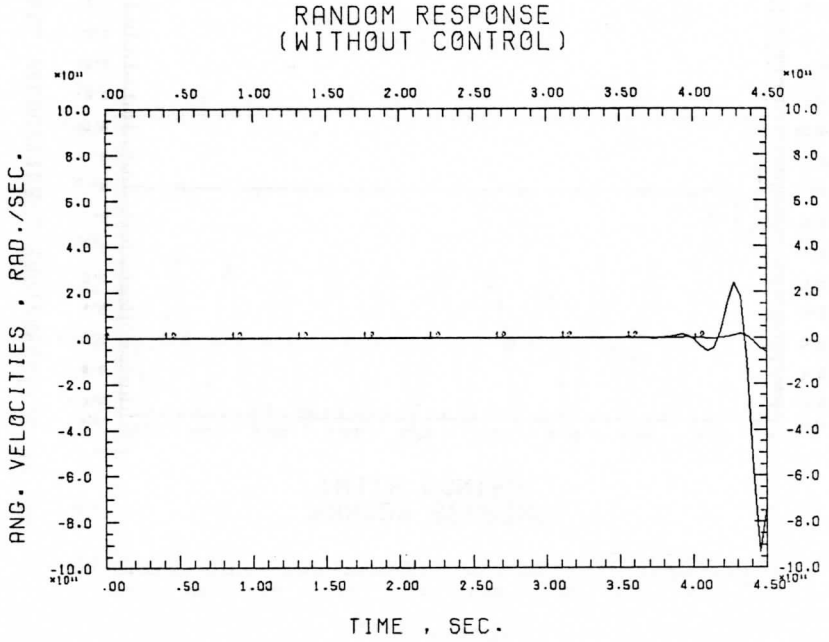
RANDOM RESPONSE
(WITHOUT CONTROL)
ANG. VELOCITIES , RAD./SEC.
TIME , SEC.
×10¹¹
10.0
8.0
6.0
4.0
2.0
.0
-2.0
-4.0
-6.0
-8.0
-10.0
.00
.50
1.00
1.50
2.00
2.50
3.00
3.50
4.00
4.50

Figure 27

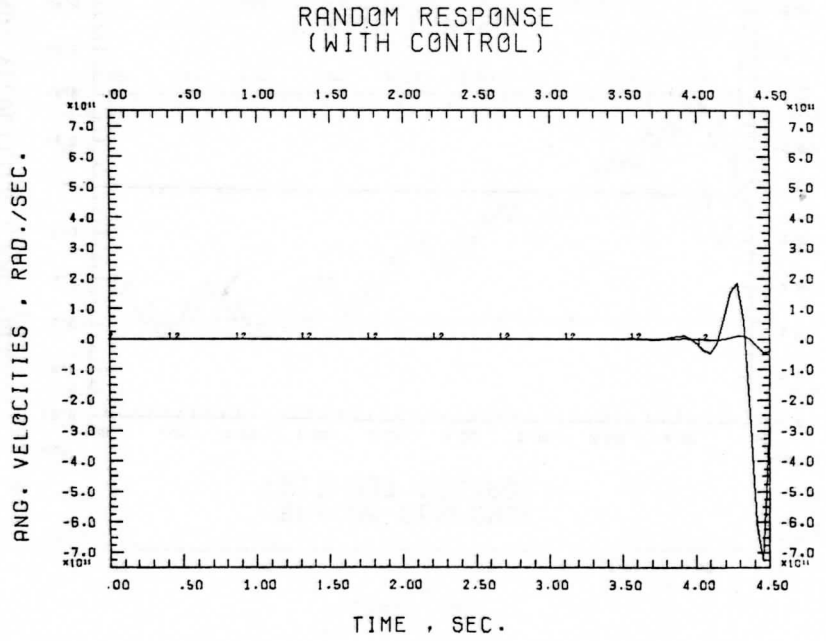
RANDOM RESPONSE
(WITH CONTROL)
ANG. VELOCITIES , RAD./SEC.
TIME , SEC.
.00
.50
1.00
1.50
2.00
2.50
3.00
3.50
4.00
4.50
7.0
6.0
5.0
4.0
3.0
2.0
1.0
.0
-1.0
-2.0
-3.0
-4.0
-5.0
-6.0
-7.0

Figure 28

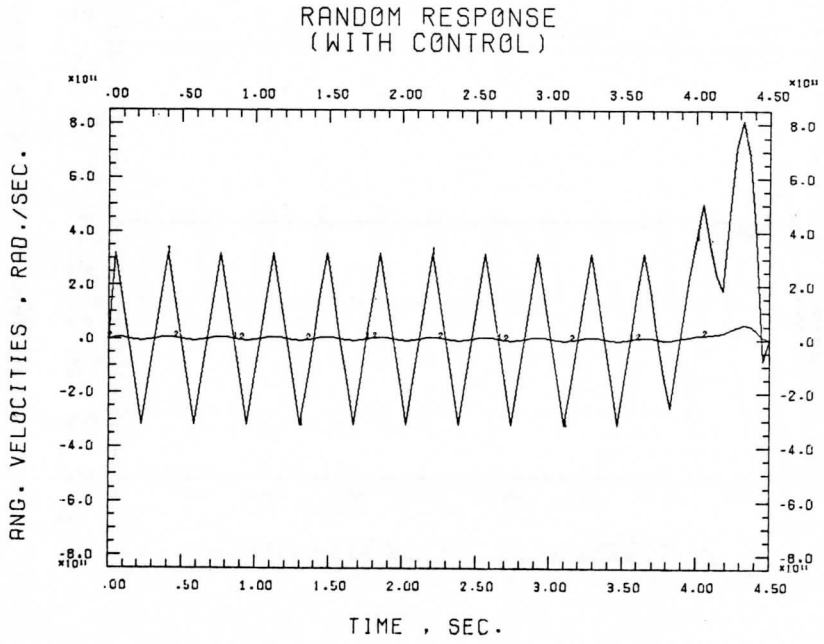
RANDOM RESPONSE
(WITH CONTROL)
ANG. VELOCITIES , RAD./SEC.
TIME , SEC.
x10^11
.00
.50
1.00
1.50
2.00
2.50
3.00
3.50
4.00
4.50
8.0
6.0
4.0
2.0
.0
-2.0
-4.0
-6.0
-8.0

Figure 29

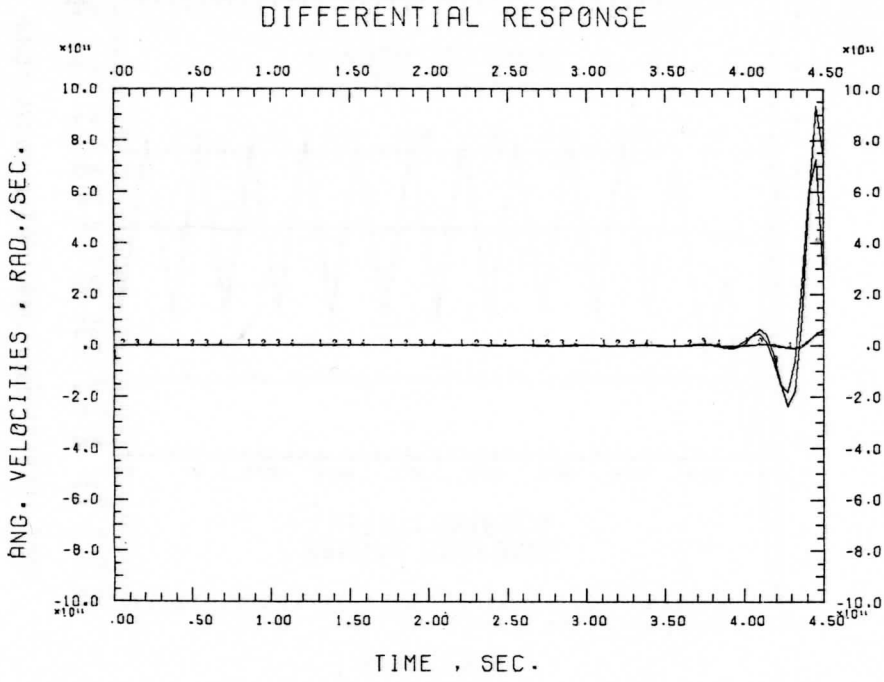
DIFFERENTIAL RESPØNSE
×10¹¹
.00
.50
1.00
1.50
2.00
2.50
3.00
3.50
4.00
4.50
10.0
8.0
6.0
4.0
2.0
.0
-2.0
-4.0
-6.0
-8.0
-10.0
ANG. VELØCITIES , RAD./SEC.
TIME , SEC.

Figure 30

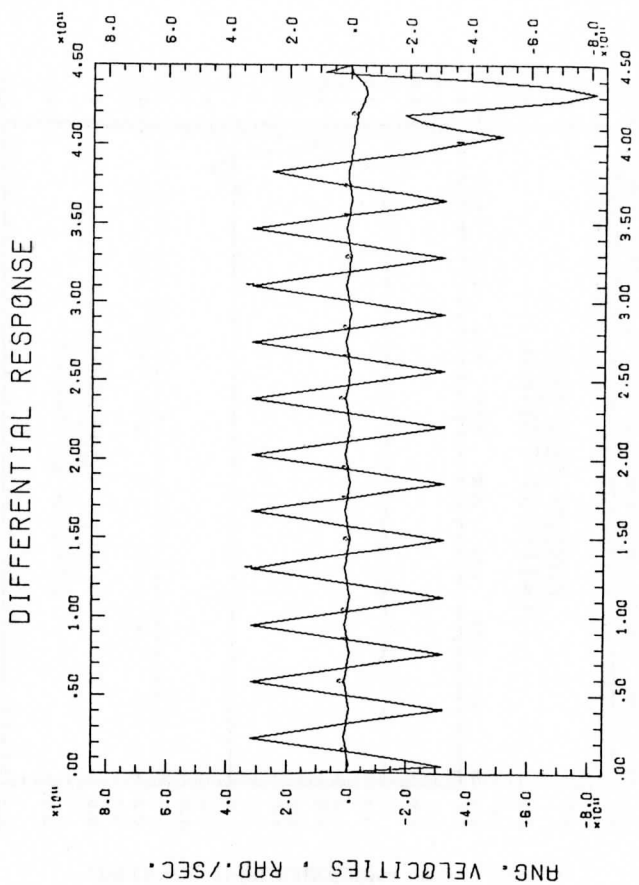
DIFFERENTIAL RESPØNSE
ANG. VELOCITIES , RAD./SEC.
TIME , SEC.
×10¹¹
8.0
6.0
4.0
2.0
.0
-2.0
-4.0
-6.0
-8.0
.00
.50
1.00
1.50
2.00
2.50
3.00
3.50
4.00
4.50

Figure 31

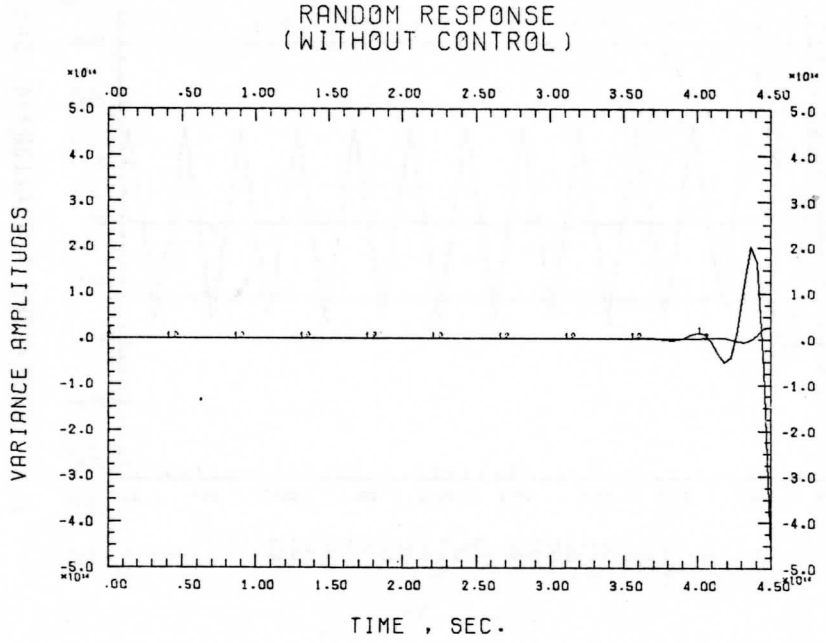
RANDOM RESPONSE
(WITHOUT CONTROL)
VARIANCE AMPLITUDES
TIME , SEC.
×10¹⁴
5.0
4.0
3.0
2.0
1.0
.0
-1.0
-2.0
-3.0
-4.0
-5.0
.00
.50
1.00
1.50
2.00
2.50
3.00
3.50
4.00
4.50

Figure 32

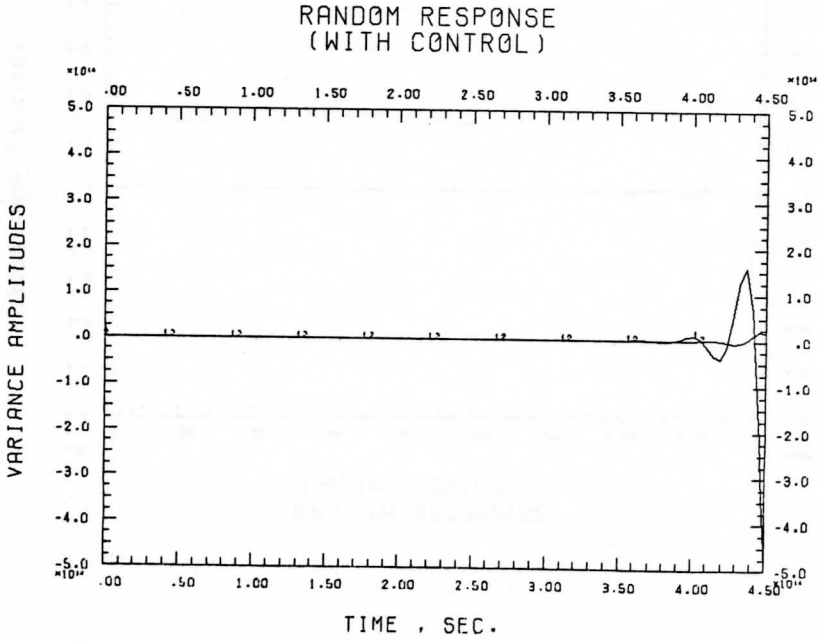
RANDOM RESPONSE
(WITH CONTROL)
VARIANCE AMPLITUDES
TIME , SEC.
×10¹⁴
5.0
4.0
3.0
2.0
1.0
.0
-1.0
-2.0
-3.0
-4.0
-5.0
.00
.50
1.00
1.50
2.00
2.50
3.00
3.50
4.00
4.50

Figure 33

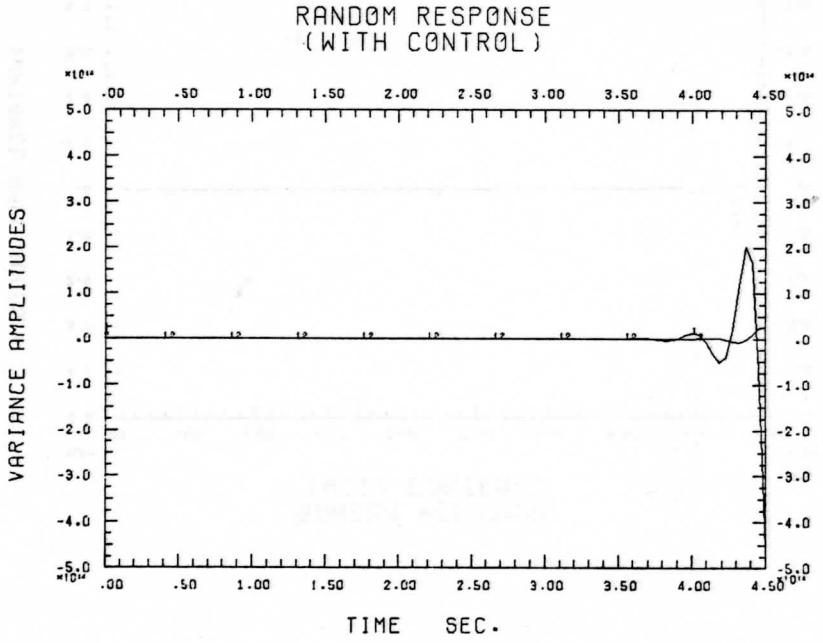
RANDOM RESPONSE
(WITH CONTROL)
VARIANCE AMPLITUDES
TIME SEC.
×10¹⁴
.00
.50
1.00
1.50
2.00
2.50
3.00
3.50
4.00
4.50
5.0
4.0
3.0
2.0
1.0
.0
-1.0
-2.0
-3.0
-4.0
-5.0

Figure 34

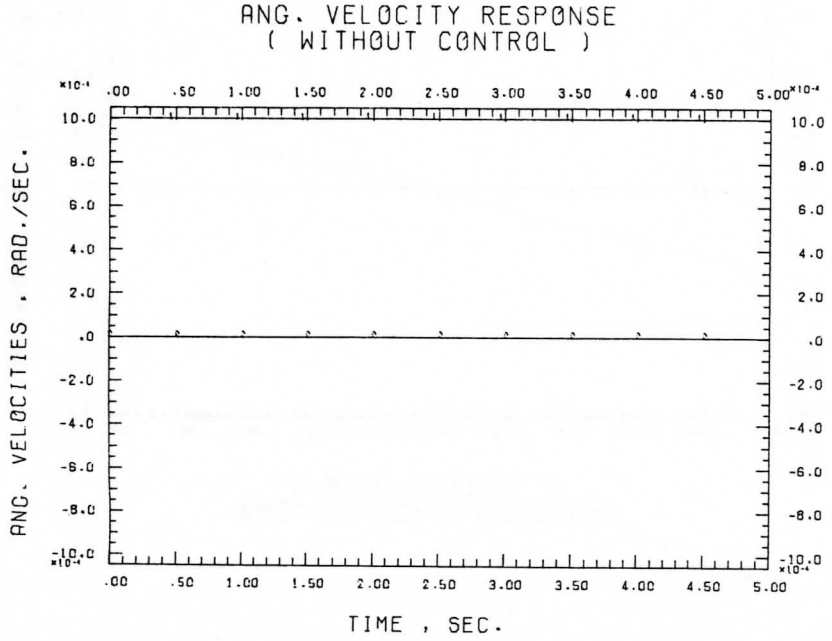
ANG. VELOCITY RESPONSE
(WITHOUT CONTROL)
ANG. VELOCITIES , RAD./SEC.
TIME , SEC.
×10⁻⁴
10.0
8.0
6.0
4.0
2.0
.0
-2.0
-4.0
-6.0
-8.0
-10.0
.00
.50
1.00
1.50
2.00
2.50
3.00
3.50
4.00
4.50
5.00

Figure 35

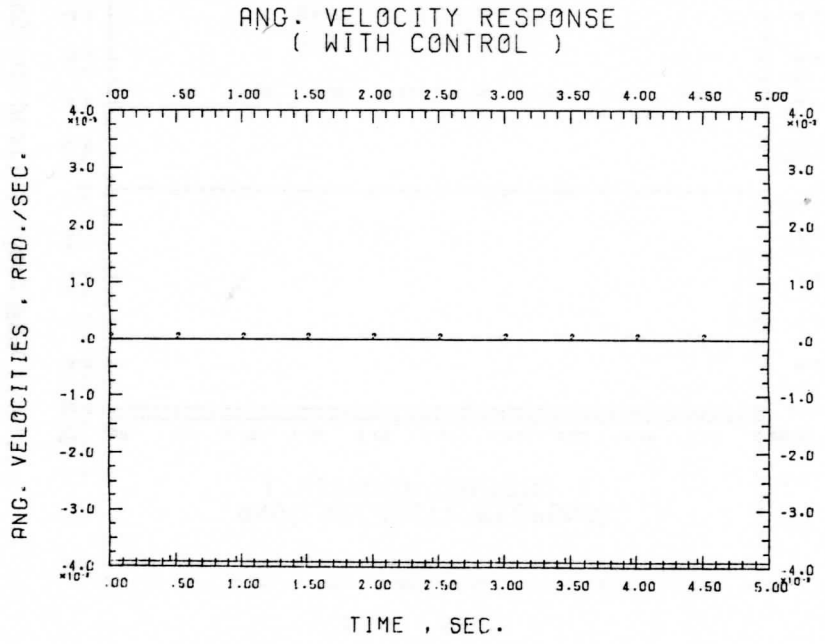
ANG. VELOCITY RESPONSE
(WITH CONTROL)
ANG. VELOCITIES , RAD./SEC.
TIME , SEC.
.00
.50
1.00
1.50
2.00
2.50
3.00
3.50
4.00
4.50
5.00
4.0
3.0
2.0
1.0
.0
-1.0
-2.0
-3.0
-4.0

Figure 36

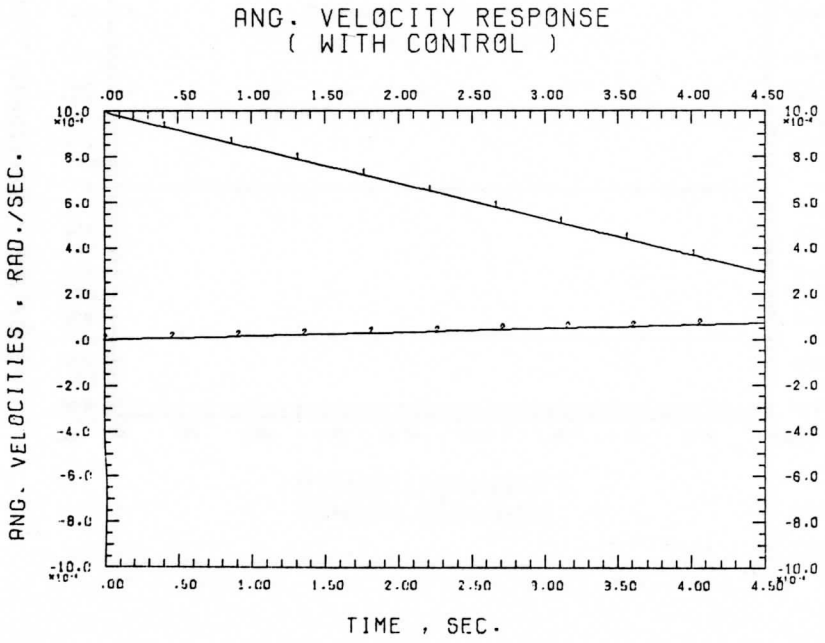
ANG. VELOCITY RESPONSE
(WITH CONTROL)
ANG. VELOCITIES , RAD./SEC.
TIME , SEC.
.00
.50
1.00
1.50
2.00
2.50
3.00
3.50
4.00
4.50
10.0
8.0
6.0
5.0
4.0
2.0
.0
-2.0
-4.0
-6.0
-8.0
-10.0

Figure 37

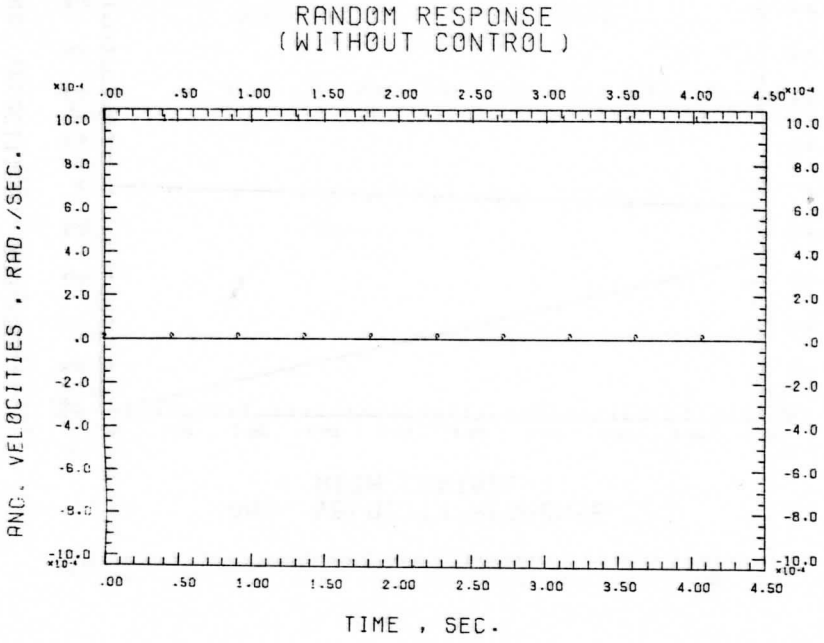
RANDOM RESPONSE
(WITHOUT CONTROL)
ANG. VELOCITIES , RAD./SEC.
TIME , SEC.
×10⁻⁴
.00
.50
1.00
1.50
2.00
2.50
3.00
3.50
4.00
4.50
10.0
8.0
6.0
4.0
2.0
.0
-2.0
-4.0
-6.0
-8.0
-10.0

Figure 38

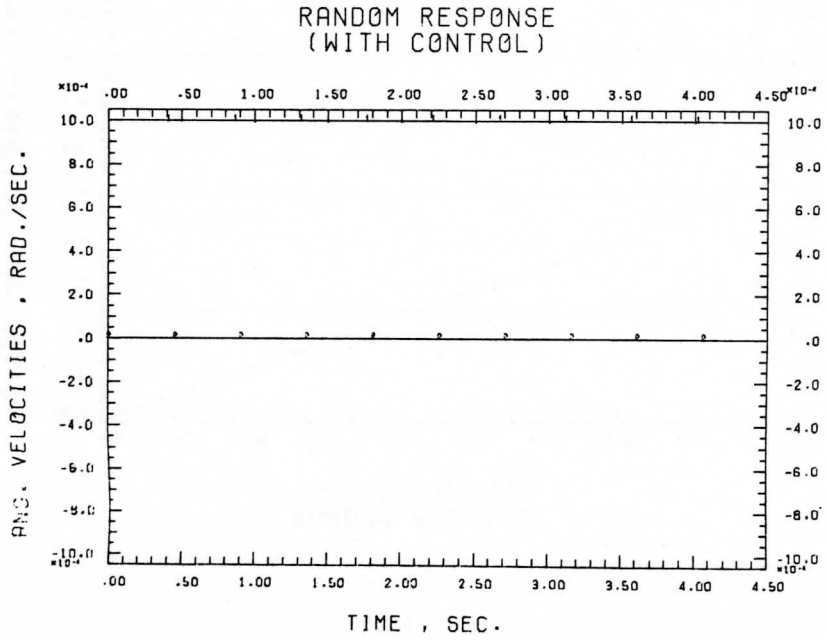
RANDOM RESPONSE
(WITH CONTROL)
ANG. VELOCITIES , RAD./SEC.
TIME , SEC.
×10⁻⁴
.00
.50
1.00
1.50
2.00
2.50
3.00
3.50
4.00
4.50
10.0
8.0
6.0
4.0
2.0
.0
-2.0
-4.0
-6.0
-8.0
-10.0

Figure 39

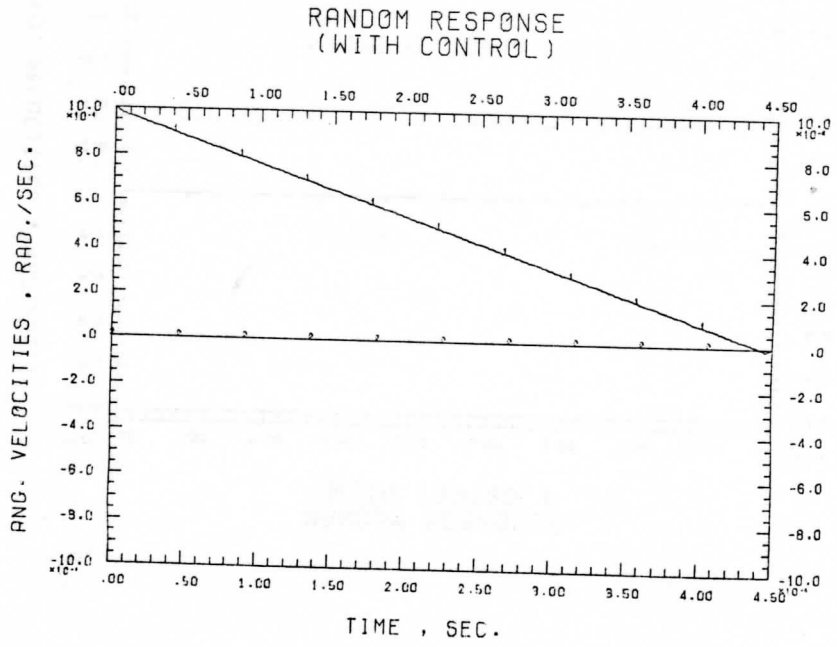
RANDOM RESPONSE
(WITH CONTROL)
ANG. VELOCITIES , RAD./SEC.
TIME , SEC.
.00
.50
1.00
1.50
2.00
2.50
3.00
3.50
4.00
4.50
10.0
8.0
6.0
4.0
2.0
.0
-2.0
-4.0
-6.0
-8.0
-10.0

Figure 40

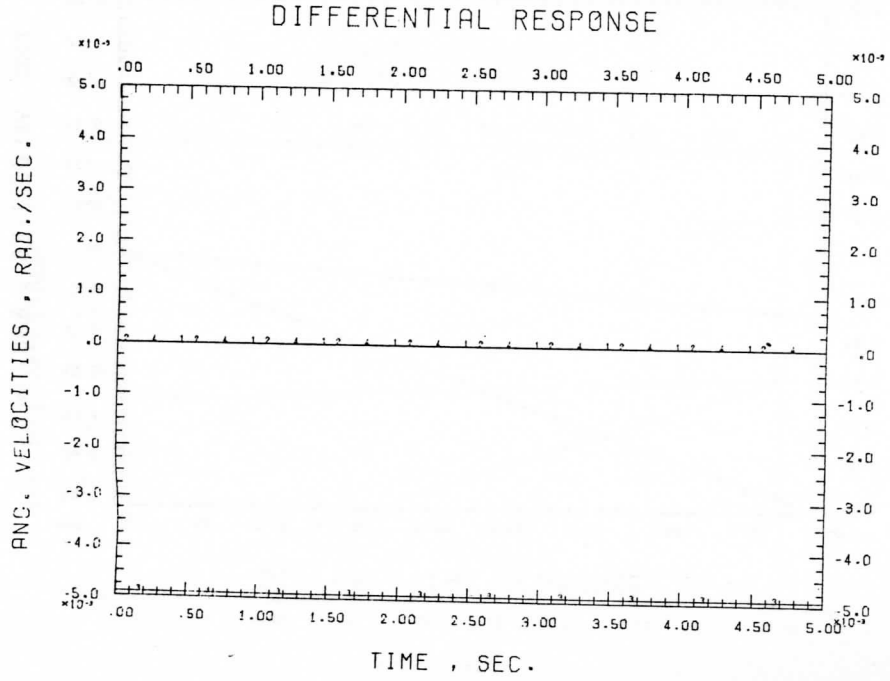
DIFFERENTIAL RESPONSE
ANG. VELOCITIES , RAD./SEC.
TIME , SEC.
×10-3
5.0
4.0
3.0
2.0
1.0
.0
-1.0
-2.0
-3.0
-4.0
-5.0
.00
.50
1.00
1.50
2.00
2.50
3.00
3.50
4.00
4.50
5.00

Figure 41

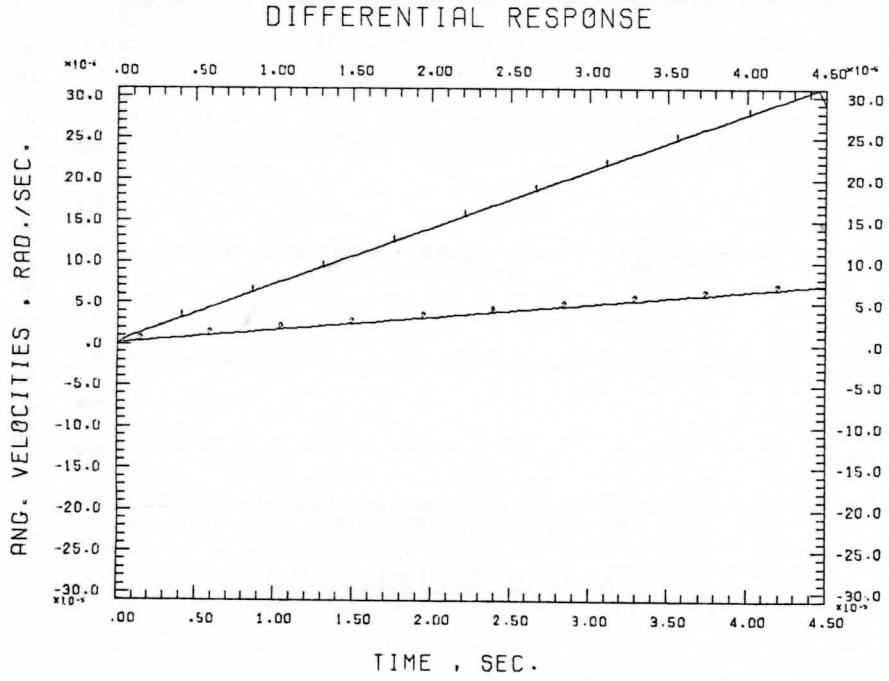
DIFFERENTIAL RESPONSE
ANG. VELOCITIES , RAD./SEC.
TIME , SEC.
×10⁻⁴
30.0
25.0
20.0
15.0
10.0
5.0
.0
-5.0
-10.0
-15.0
-20.0
-25.0
-30.0
.00
.50
1.00
1.50
2.00
2.50
3.00
3.50
4.00
4.50

Figure 42

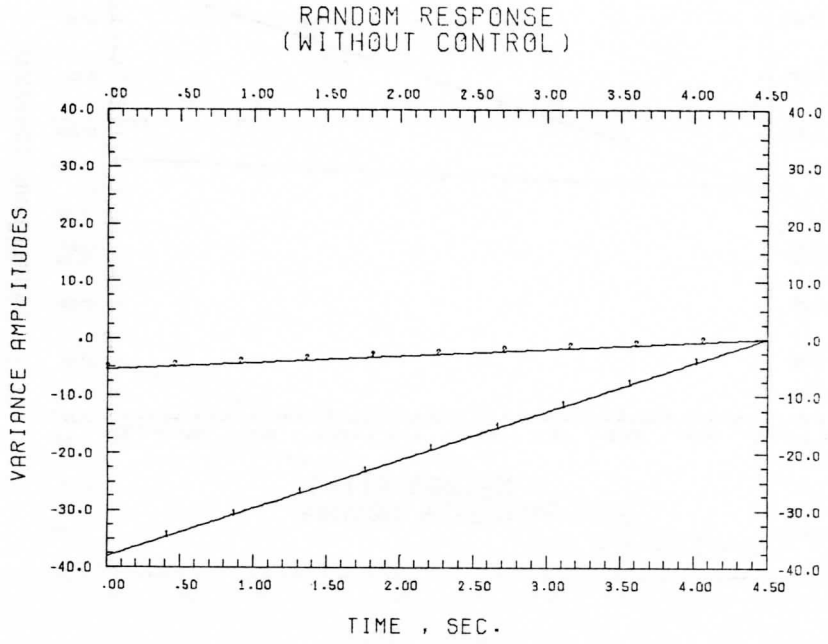
RANDOM RESPONSE
(WITHOUT CONTROL)
VARIANCE AMPLITUDES
TIME , SEC.
.00
.50
1.00
1.50
2.00
2.50
3.00
3.50
4.00
4.50
40.0
30.0
20.0
10.0
.0
-10.0
-20.0
-30.0
-40.0

Figure 43

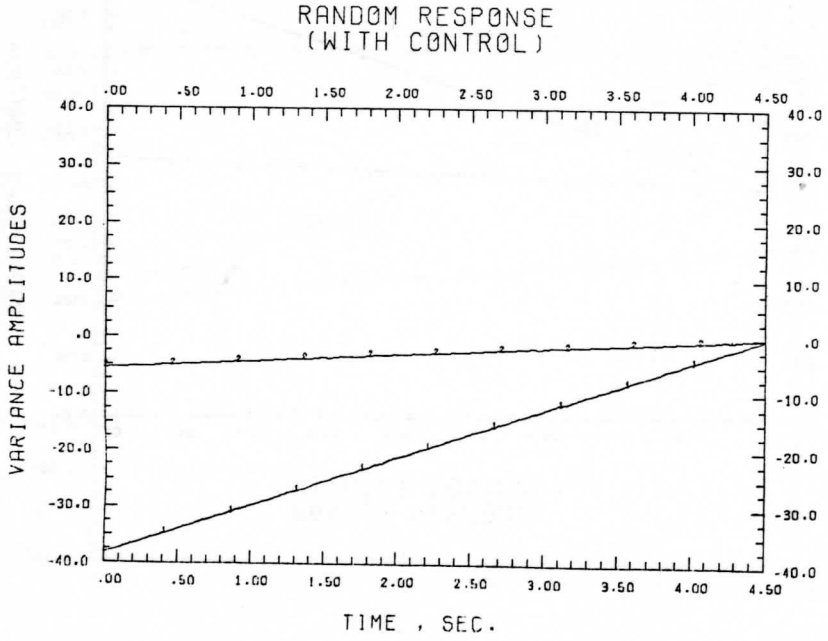
RANDOM RESPONSE
(WITH CONTROL)
VARIANCE AMPLITUDES
TIME , SEC.
.00
.50
1.00
1.50
2.00
2.50
3.00
3.50
4.00
4.50
40.0
30.0
20.0
10.0
.0
-10.0
-20.0
-30.0
-40.0

Figure 44

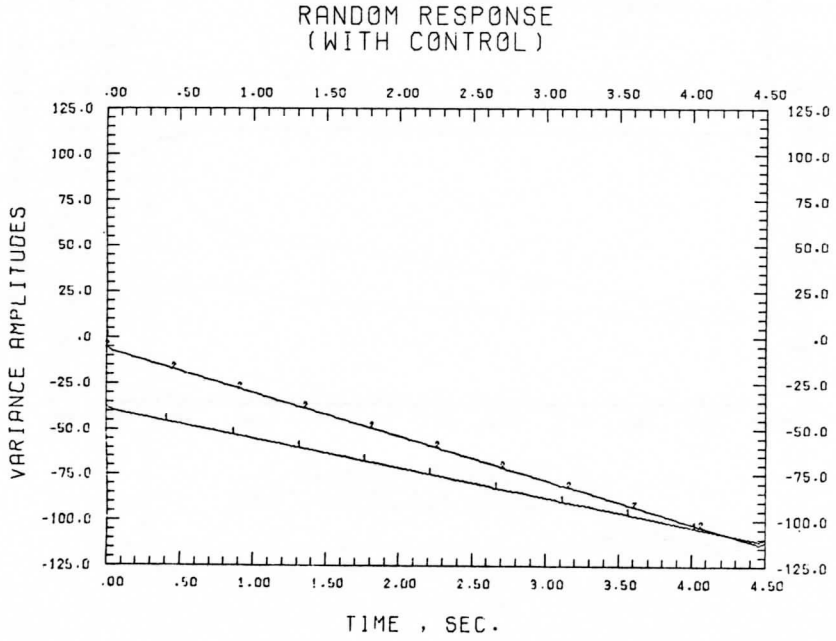
RANDOM RESPONSE
(WITH CONTROL)
VARIANCE AMPLITUDES
TIME , SEC.
.00
.50
1.00
1.50
2.00
2.50
3.00
3.50
4.00
4.50
125.0
100.0
75.0
50.0
25.0
.0
-25.0
-50.0
-75.0
-100.0
-125.0

Figure 45

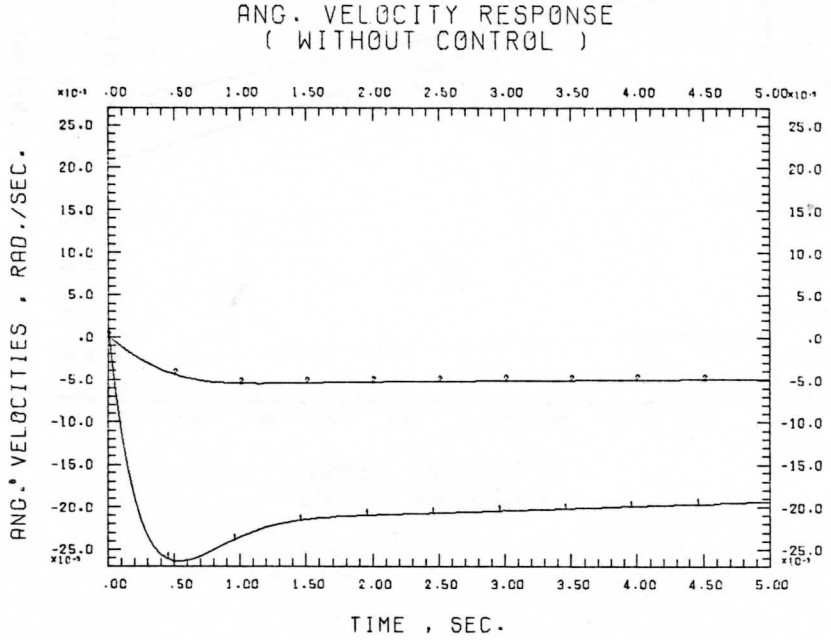
ANG. VELOCITY RESPONSE
(WITHOUT CONTROL)
ANG.' VELOCITIES , RAD./SEC.
TIME , SEC.
.00
.50
1.00
1.50
2.00
2.50
3.00
3.50
4.00
4.50
5.00
25.0
20.0
15.0
10.0
5.0
.0
-5.0
-10.0
-15.0
-20.0
-25.0

Figure 46

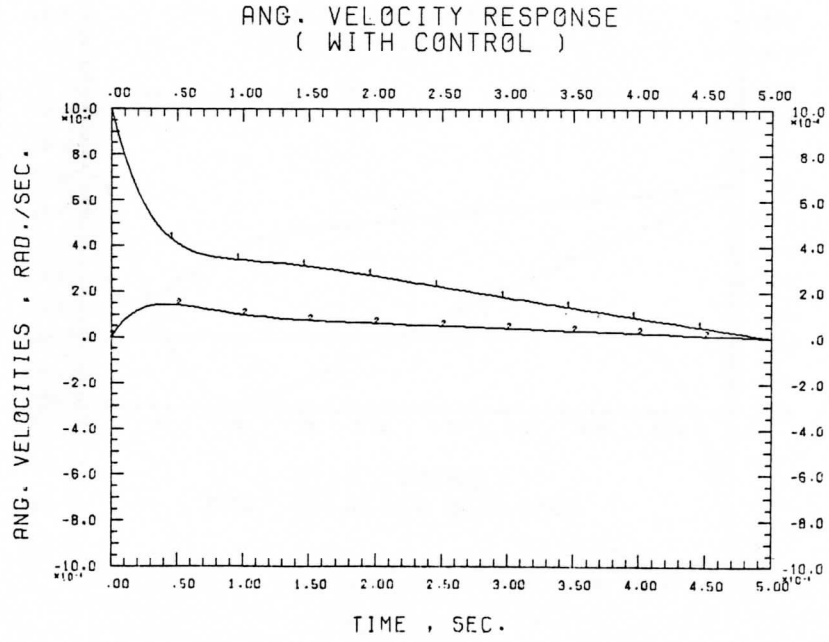
ANG. VELOCITY RESPONSE
(WITH CONTROL)
ANG. VELOCITIES , RAD./SEC.
TIME , SEC.
.00
.50
1.00
1.50
2.00
2.50
3.00
3.50
4.00
4.50
5.00
10.0
8.0
6.0
4.0
2.0
.0
-2.0
-4.0
-6.0
-8.0
-10.0

Figure 47

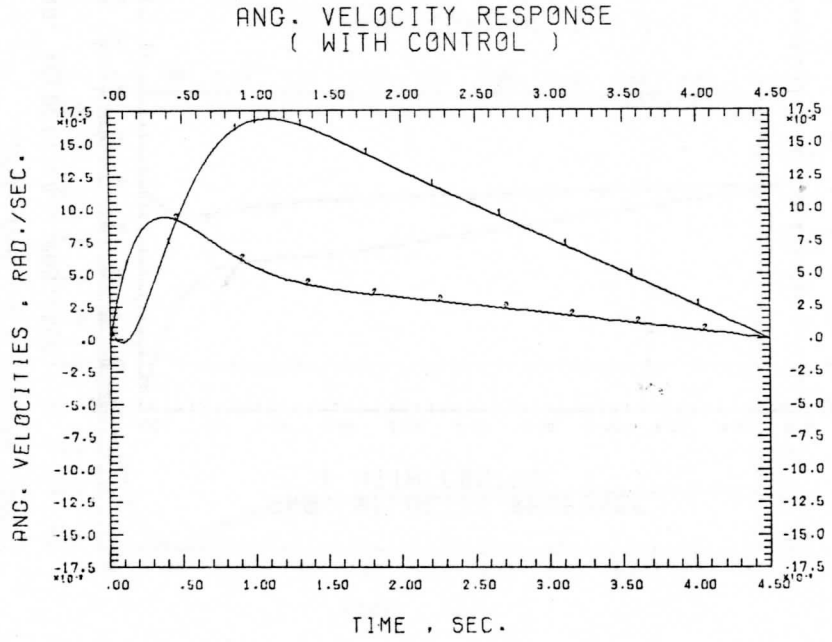
ANG. VELOCITY RESPONSE
(WITH CONTROL)
ANG. VELOCITIES , RAD./SEC.
TIME , SEC.
.00
.50
1.00
1.50
2.00
2.50
3.00
3.50
4.00
4.50
17.5
15.0
12.5
10.0
7.5
5.0
2.5
.0
-2.5
-5.0
-7.5
-10.0
-12.5
-15.0
-17.5

Figure 48

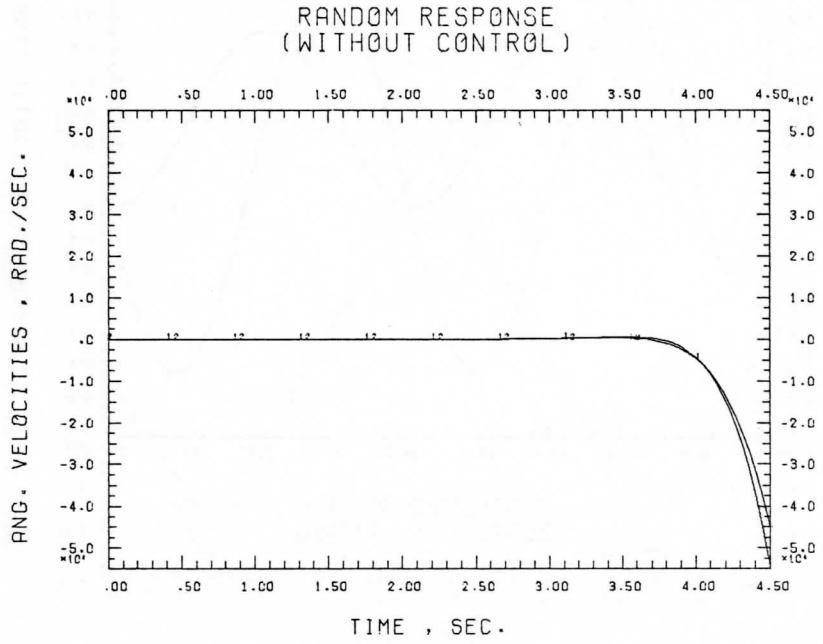
RANDOM RESPONSE
(WITHOUT CONTROL)
ANG. VELOCITIES , RAD./SEC.
TIME , SEC.
.00
.50
1.00
1.50
2.00
2.50
3.00
3.50
4.00
4.50
5.0
4.0
3.0
2.0
1.0
.0
-1.0
-2.0
-3.0
-4.0
-5.0

Figure 49

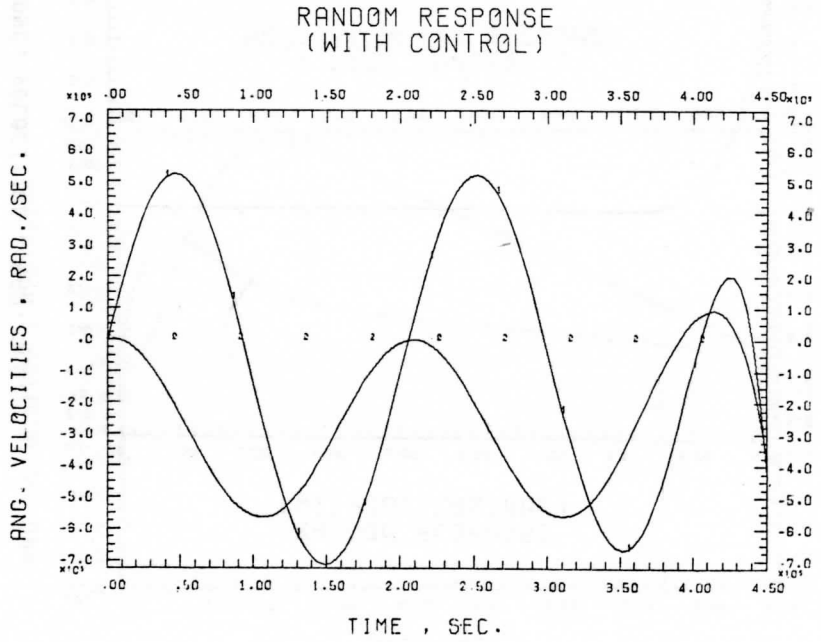
RANDOM RESPONSE
(WITH CONTROL)
ANG. VELOCITIES , RAD./SEC.
TIME , SEC.
x10³
7.0
6.0
5.0
4.0
3.0
2.0
1.0
.0
-1.0
-2.0
-3.0
-4.0
-5.0
-6.0
-7.0
.00
.50
1.00
1.50
2.00
2.50
3.00
3.50
4.00
4.50

Figure 50

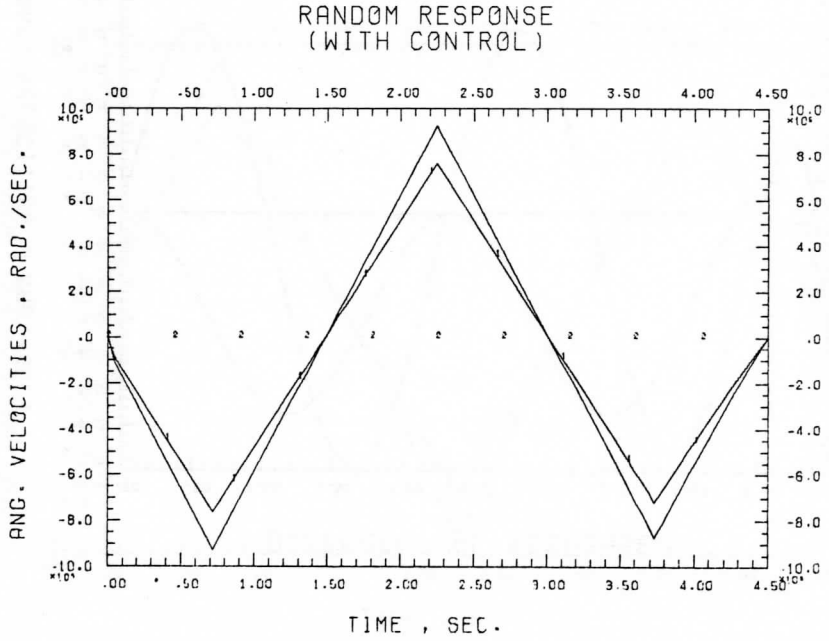
RANDOM RESPONSE
(WITH CONTROL)
ANG. VELOCITIES , RAD./SEC.
TIME , SEC.
.00
.50
1.00
1.50
2.00
2.50
3.00
3.50
4.00
4.50
10.0
8.0
6.0
4.0
2.0
.0
-2.0
-4.0
-6.0
-8.0
-10.0

Figure 51

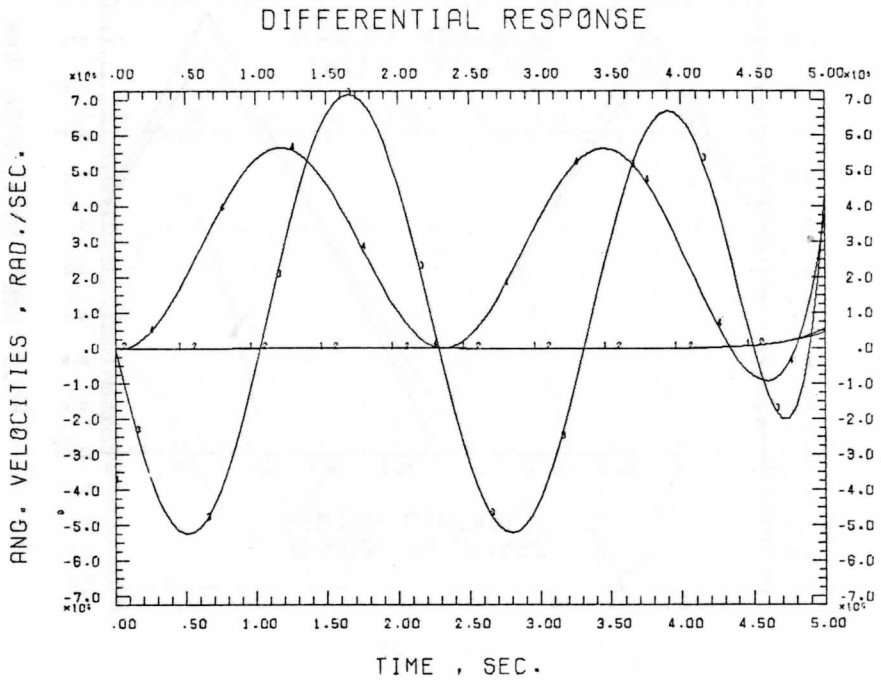
DIFFERENTIAL RESPONSE
ANG. VELOCITIES , RAD./SEC.
TIME , SEC.
x10³ .00 .50 1.00 1.50 2.00 2.50 3.00 3.50 4.00 4.50 5.00x10³
7.0 6.0 5.0 4.0 3.0 2.0 1.0 .0 -1.0 -2.0 -3.0 -4.0 -5.0 -6.0 -7.0
x10³

Figure 52

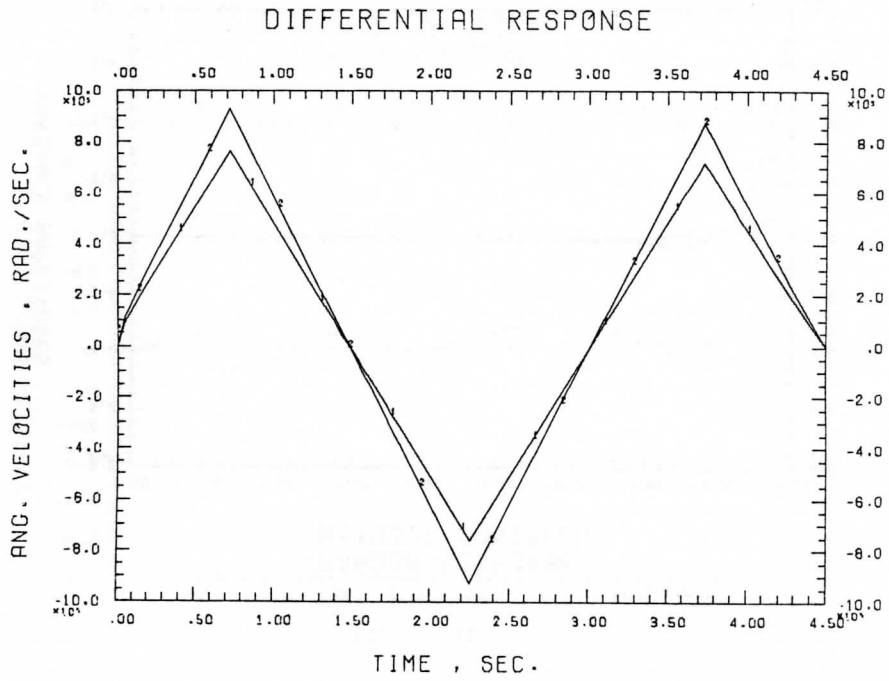
DIFFERENTIAL RESPONSE
ANG. VELOCITIES , RAD./SEC.
TIME , SEC.
.00
.50
1.00
1.50
2.00
2.50
3.00
3.50
4.00
4.50
10.0
8.0
6.0
4.0
2.0
.0
-2.0
-4.0
-6.0
-8.0
-10.0

Figure 53

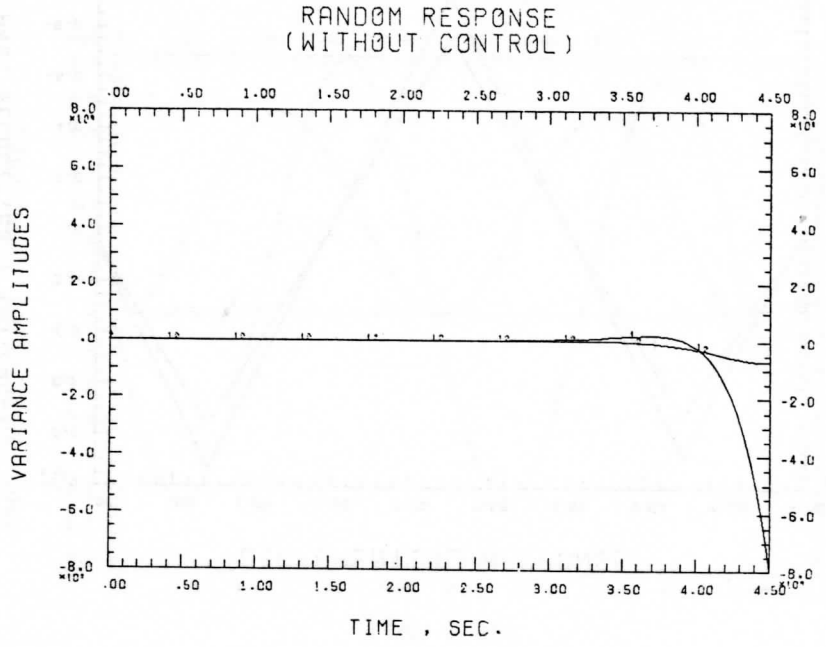
RANDOM RESPONSE
(WITHOUT CONTROL)
VARIANCE AMPLITUDES
TIME , SEC.
.00
.50
1.00
1.50
2.00
2.50
3.00
3.50
4.00
4.50
8.0
6.0
4.0
2.0
.0
-2.0
-4.0
-6.0
-8.0

Figure 54

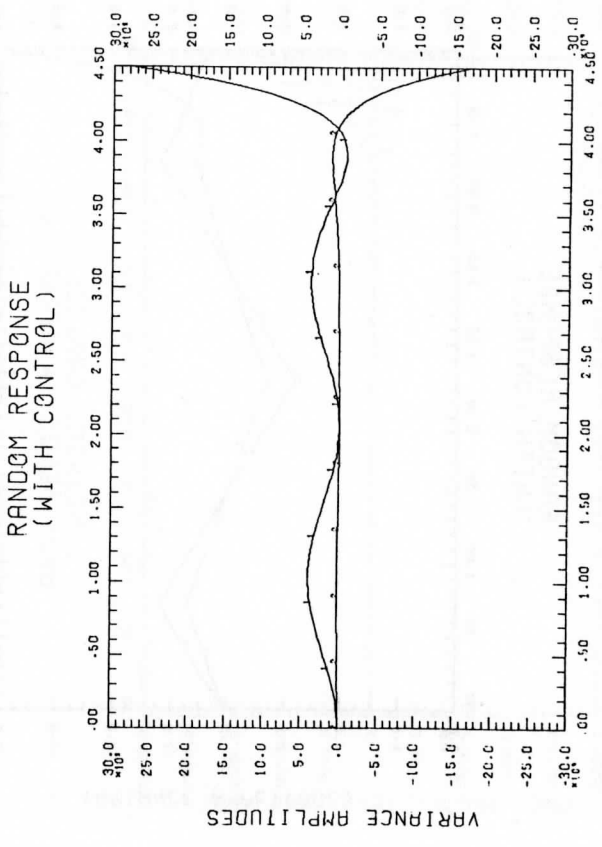
RANDOM RESPONSE
(WITH CONTROL)
VARIANCE AMPLITUDES
TIME , SEC.

Figure 55

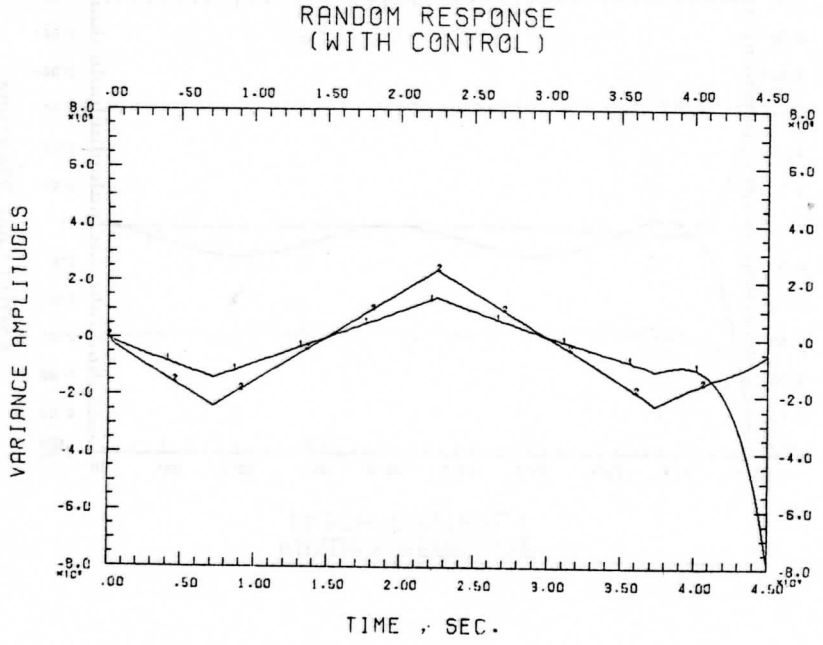
RANDOM RESPONSE
(WITH CONTROL)
VARIANCE AMPLITUDES
TIME , SEC.
.00
.50
1.00
1.50
2.00
2.50
3.00
3.50
4.00
4.50
8.0
6.0
4.0
2.0
.0
-2.0
-4.0
-6.0
-8.0

Figure 56

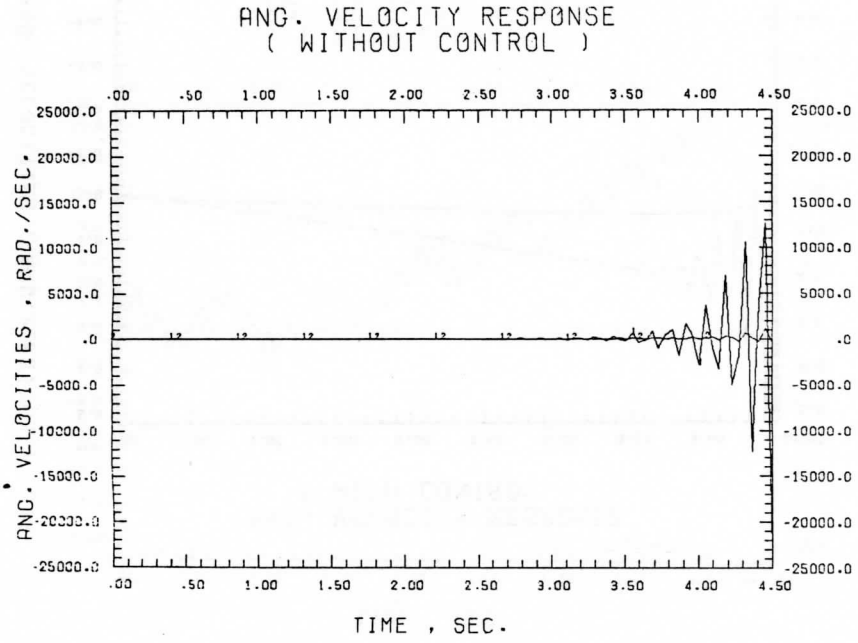
ANG. VELOCITY RESPONSE
(WITHOUT CONTROL)
ANG. VELOCITIES , RAD./SEC.
TIME , SEC.
.00
.50
1.00
1.50
2.00
2.50
3.00
3.50
4.00
4.50
25000.0
20000.0
15000.0
10000.0
5000.0
.0
-5000.0
-10000.0
-15000.0
-20000.0
-25000.0

Figure 57

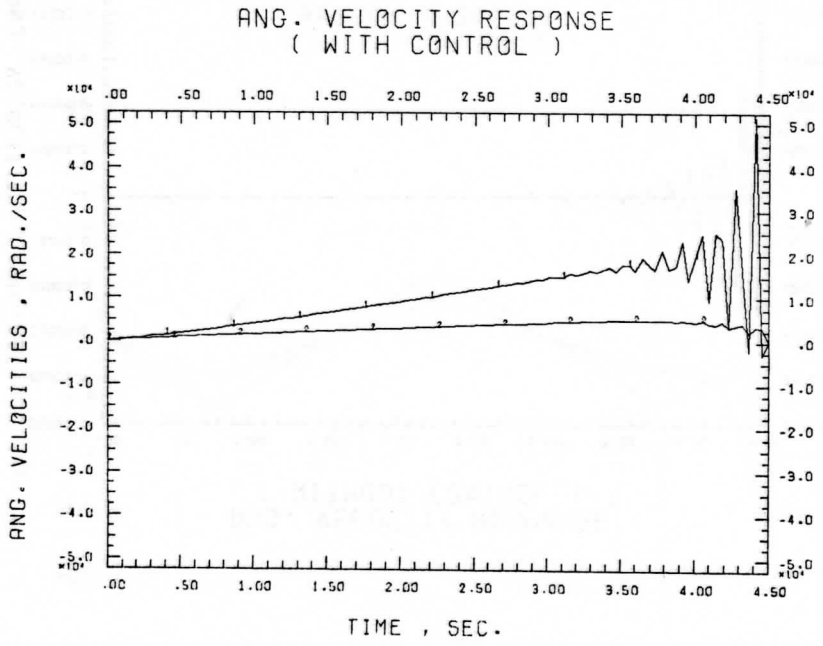
ANG. VELOCITY RESPONSE
(WITH CONTROL)
ANG. VELOCITIES , RAD./SEC.
TIME , SEC.
×10⁴
.00
.50
1.00
1.50
2.00
2.50
3.00
3.50
4.00
4.50
5.0
4.0
3.0
2.0
1.0
.0
-1.0
-2.0
-3.0
-4.0
-5.0

Figure 58

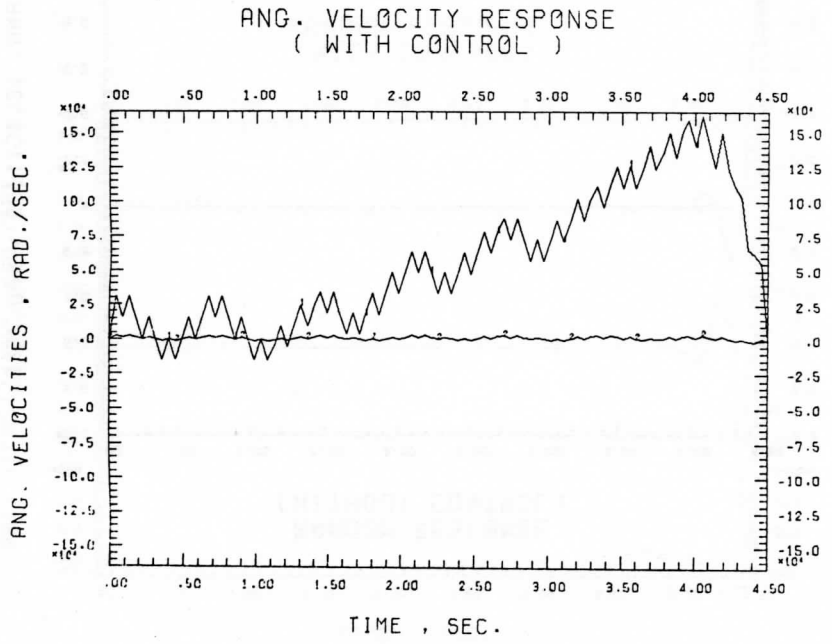
ANG. VELOCITY RESPONSE
(WITH CONTROL)
ANG. VELOCITIES , RAD./SEC.
TIME , SEC.
.00
.50
1.00
1.50
2.00
2.50
3.00
3.50
4.00
4.50
15.0
12.5
10.0
7.5
5.0
2.5
.0
-2.5
-5.0
-7.5
-10.0
-12.5
-15.0

Figure 59

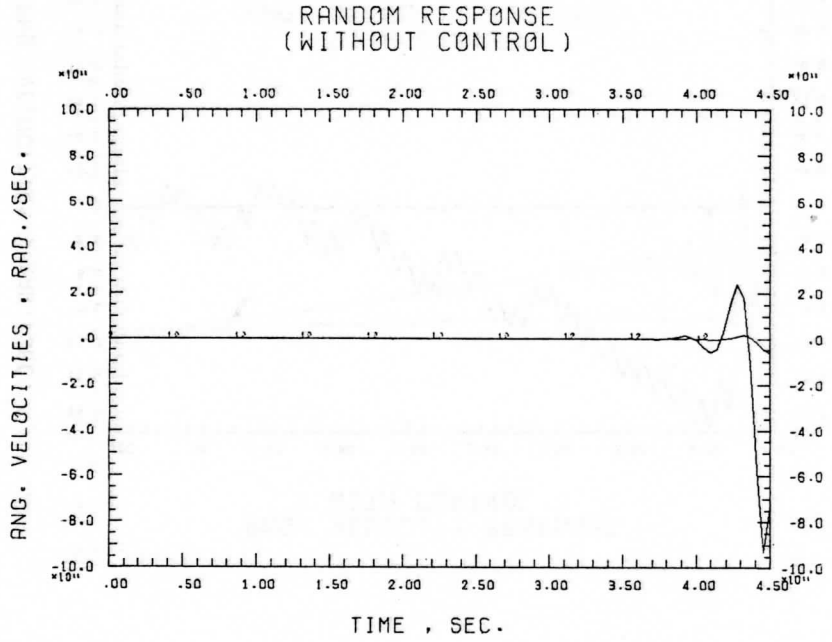
RANDOM RESPONSE
(WITHOUT CONTROL)
ANG. VELOCITIES , RAD./SEC.
TIME , SEC.
×10¹¹
10.0
8.0
6.0
4.0
2.0
.0
-2.0
-4.0
-6.0
-8.0
-10.0
.00
.50
1.00
1.50
2.00
2.50
3.00
3.50
4.00
4.50

Figure 60

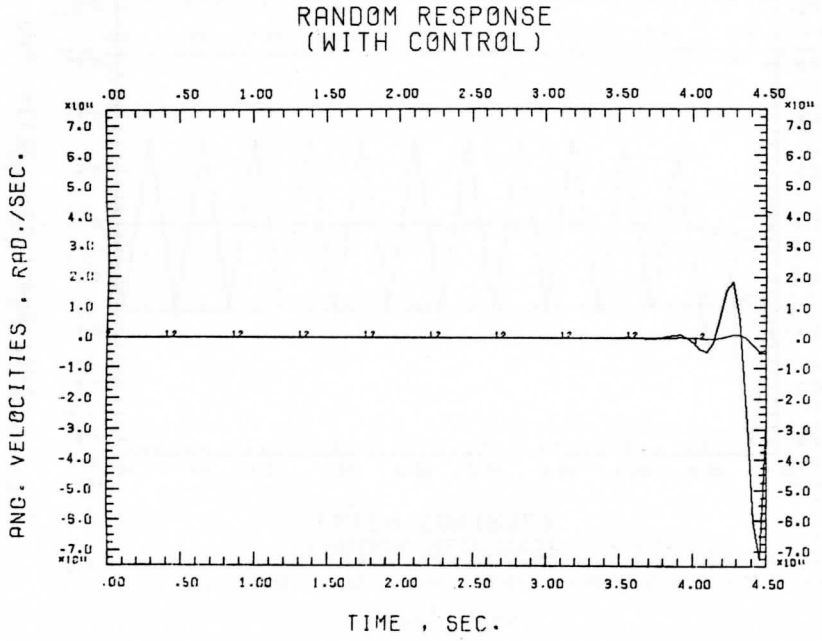
RANDOM RESPONSE
(WITH CONTROL)
ANG. VELOCITIES , RAD./SEC.
TIME , SEC.
.00
.50
1.00
1.50
2.00
2.50
3.00
3.50
4.00
4.50
7.0
6.0
5.0
4.0
3.0
2.0
1.0
.0
-1.0
-2.0
-3.0
-4.0
-5.0
-6.0
-7.0

Figure 61

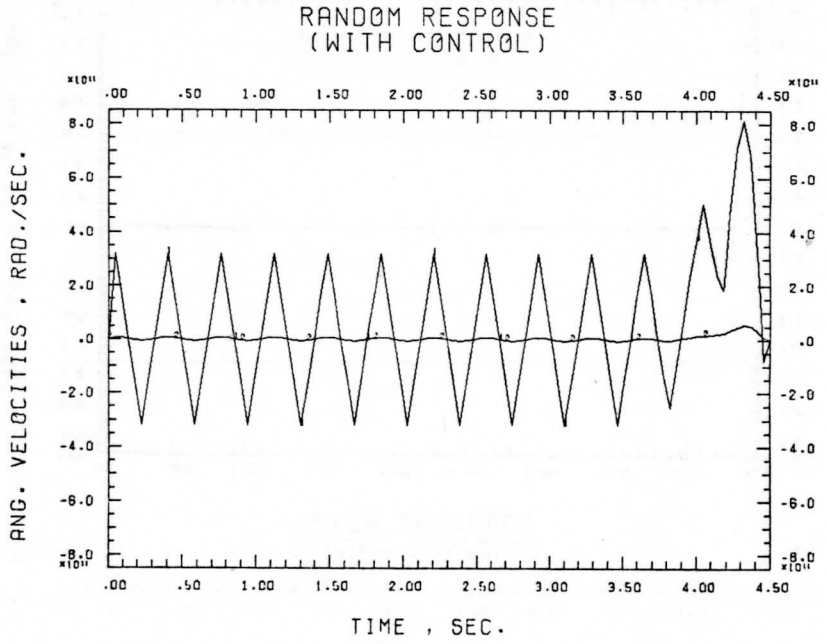
RANDOM RESPONSE
(WITH CONTROL)
ANG. VELOCITIES , RAD./SEC.
TIME , SEC.
x10^11
.00
.50
1.00
1.50
2.00
2.50
3.00
3.50
4.00
4.50
8.0
6.0
4.0
2.0
.0
-2.0
-4.0
-6.0
-8.0

Figure 62

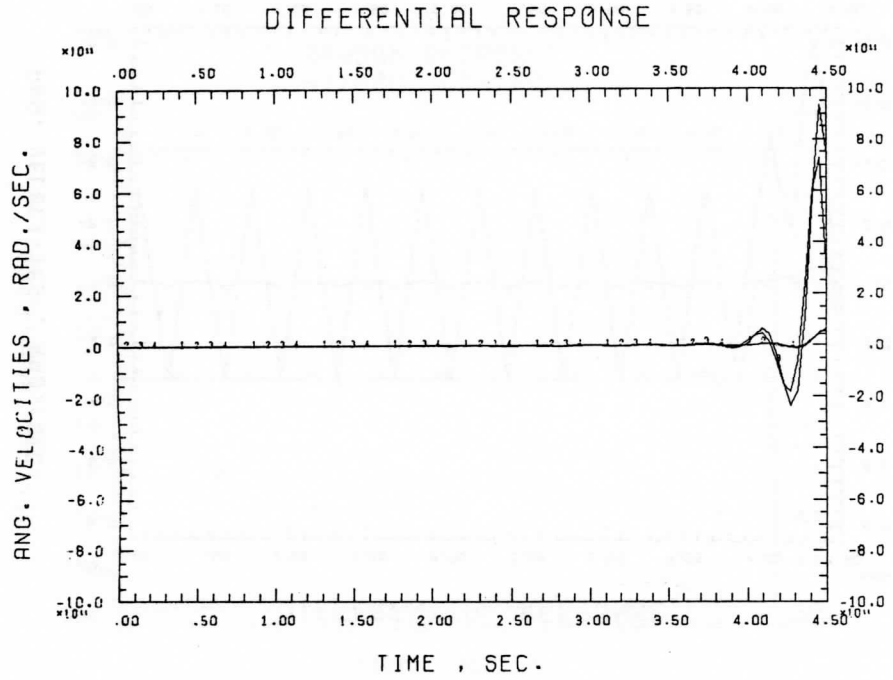
DIFFERENTIAL RESPONSE
×10¹¹
.00
.50
1.00
1.50
2.00
2.50
3.00
3.50
4.00
4.50
10.0
8.0
6.0
4.0
2.0
.0
-2.0
-4.0
-6.0
-8.0
-10.0
ANG. VELOCITIES , RAD./SEC.
TIME , SEC.

Figure 63

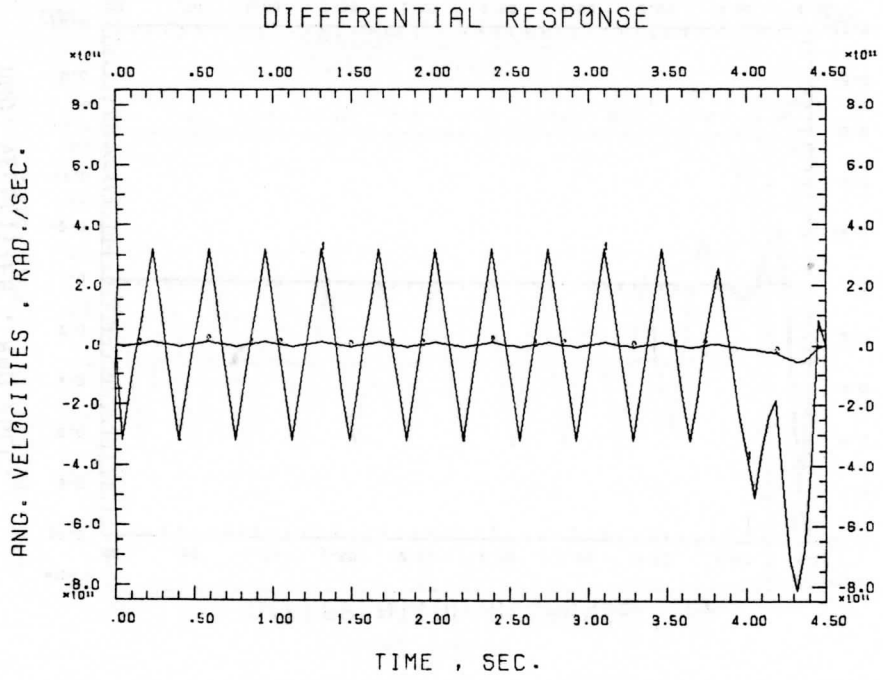
DIFFERENTIAL RESPØNSE
ANG. VELØCITIES , RAD./SEC.
TIME , SEC.
×10¹¹
.00
.50
1.00
1.50
2.00
2.50
3.00
3.50
4.00
4.50
9.0
6.0
4.0
2.0
.0
-2.0
-4.0
-6.0
-8.0

Figure 64

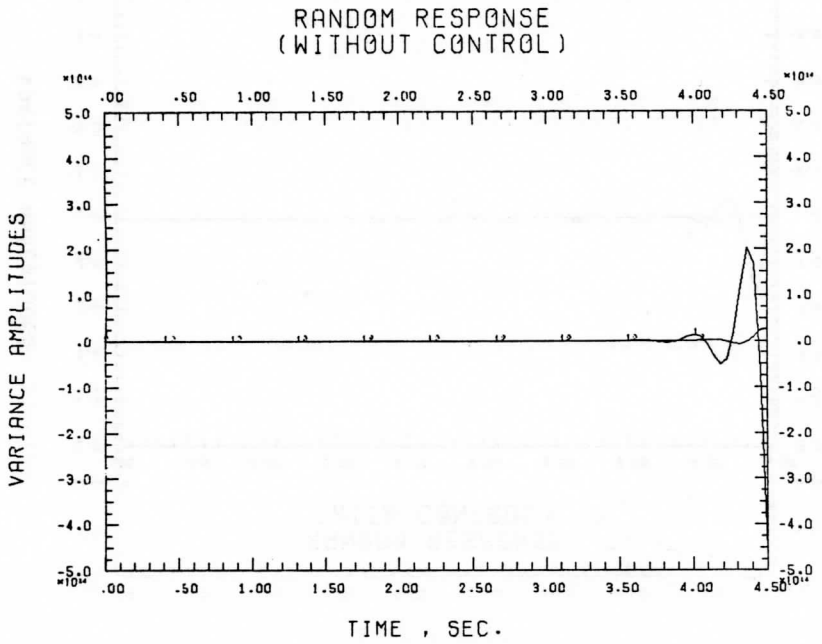
RANDOM RESPONSE
(WITHOUT CONTROL)
VARIANCE AMPLITUDES
TIME , SEC.
.00
.50
1.00
1.50
2.00
2.50
3.00
3.50
4.00
4.50
5.0
4.0
3.0
2.0
1.0
.0
-1.0
-2.0
-3.0
-4.0
-5.0

Figure 65

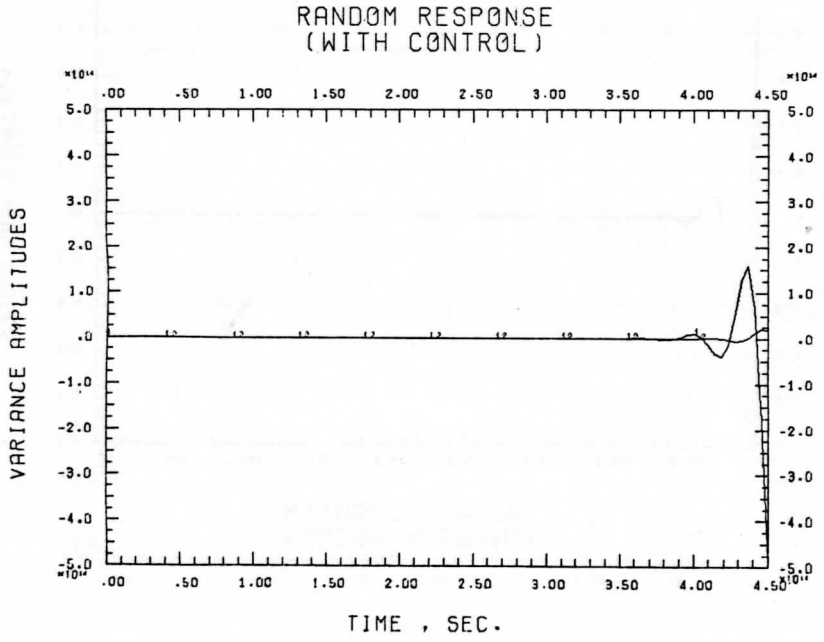
RANDOM RESPONSE
(WITH CONTROL)
VARIANCE AMPLITUDES
TIME , SEC.
.00
.50
1.00
1.50
2.00
2.50
3.00
3.50
4.00
4.50
5.0
4.0
3.0
2.0
1.0
.0
-1.0
-2.0
-3.0
-4.0
-5.0

Figure 66

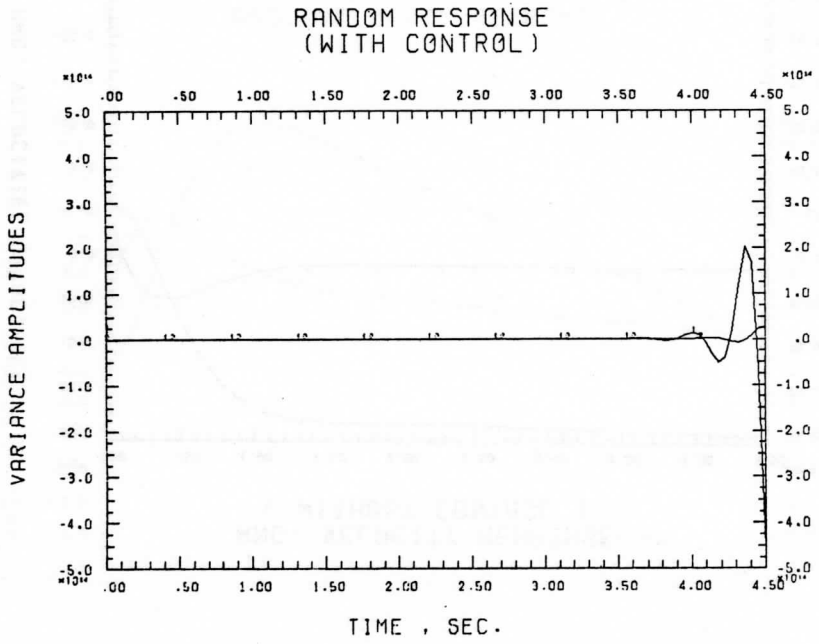
RANDOM RESPONSE
(WITH CONTROL)
VARIANCE AMPLITUDES
TIME , SEC.
×10¹⁴
5.0
4.0
3.0
2.0
1.0
.0
-1.0
-2.0
-3.0
-4.0
-5.0
.00
.50
1.00
1.50
2.00
2.50
3.00
3.50
4.00
4.50

Figure 67

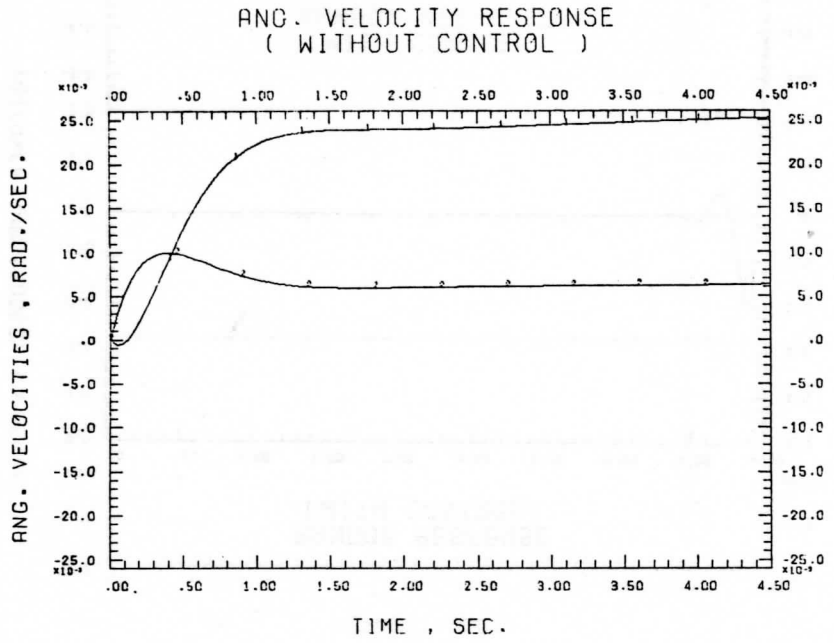
ANG. VELOCITY RESPONSE
(WITHOUT CONTROL)
ANG. VELOCITIES , RAD./SEC.
TIME , SEC.
x10-3
.00
.50
1.00
1.50
2.00
2.50
3.00
3.50
4.00
4.50
25.0
20.0
15.0
10.0
5.0
.0
-5.0
-10.0
-15.0
-20.0
-25.0

Figure 68

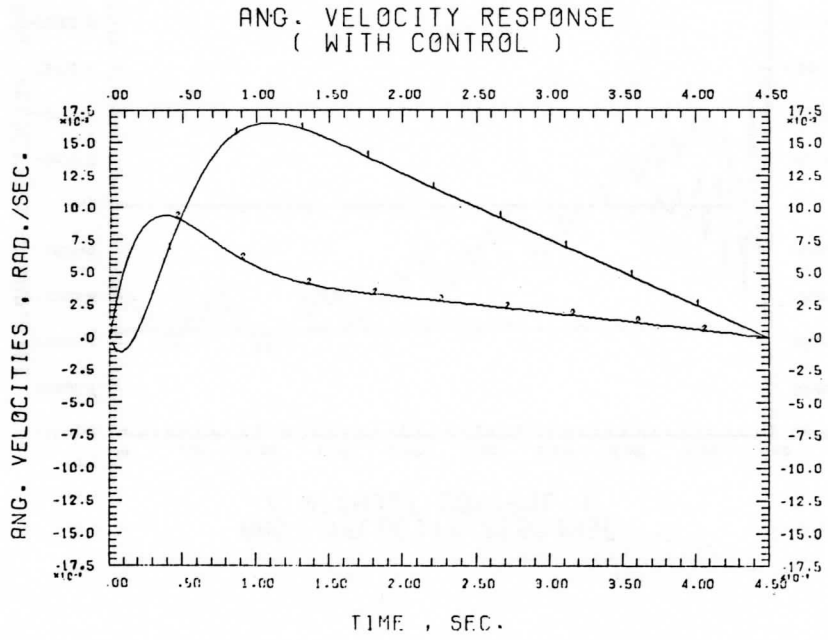
ANG. VELOCITY RESPONSE
(WITH CONTROL)
ANG. VELOCITIES , RAD./SEC.
TIME , SEC.
.00
.50
1.00
1.50
2.00
2.50
3.00
3.50
4.00
4.50
17.5
15.0
12.5
10.0
7.5
5.0
2.5
.0
-2.5
-5.0
-7.5
-10.0
-12.5
-15.0
-17.5

Figure 69

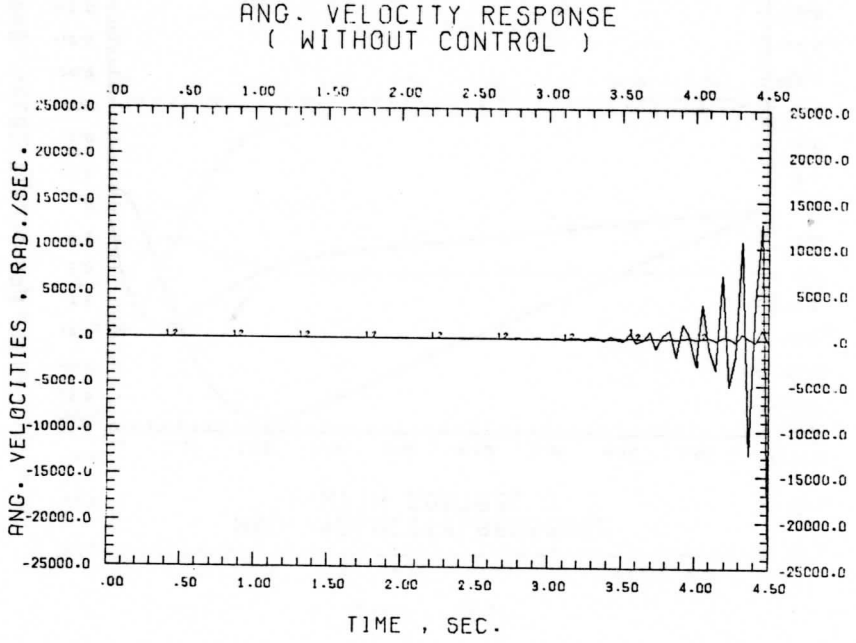
ANG. VELOCITY RESPONSE
(WITHOUT CONTROL)
ANG. VELOCITIES , RAD./SEC.
25000.0
20000.0
15000.0
10000.0
5000.0
.0
-5000.0
-10000.0
-15000.0
-20000.0
-25000.0
.00
.50
1.00
1.50
2.00
2.50
3.00
3.50
4.00
4.50
TIME , SEC.

Figure 70

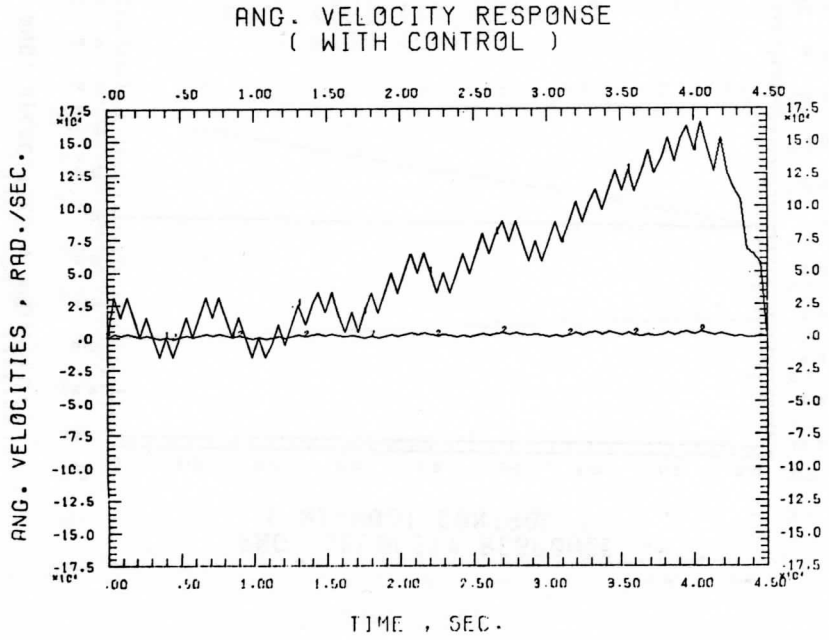
ANG. VELOCITY RESPONSE
(WITH CONTROL)
ANG. VELOCITIES , RAD./SEC.
TIME , SEC.
.00
.50
1.00
1.50
2.00
2.50
3.00
3.50
4.00
4.50
17.5
15.0
12.5
10.0
7.5
5.0
2.5
.0
-2.5
-5.0
-7.5
-10.0
-12.5
-15.0
-17.5

Figure 71

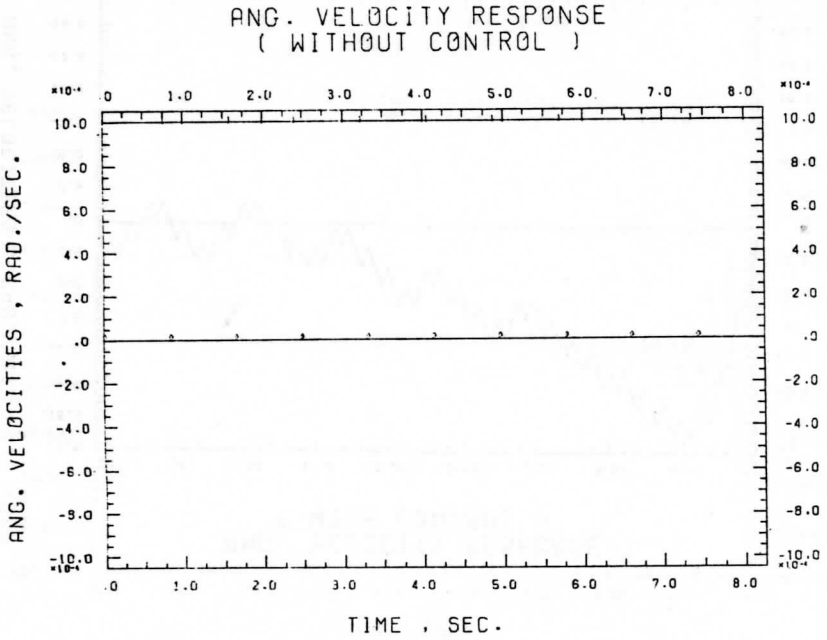
ANG. VELOCITY RESPONSE
(WITHOUT CONTROL)
ANG. VELOCITIES , RAD./SEC.
TIME , SEC.
10.0
8.0
6.0
4.0
2.0
.0
-2.0
-4.0
-6.0
-8.0
-10.0
1.0
2.0
3.0
4.0
5.0
6.0
7.0
8.0

Figure 72

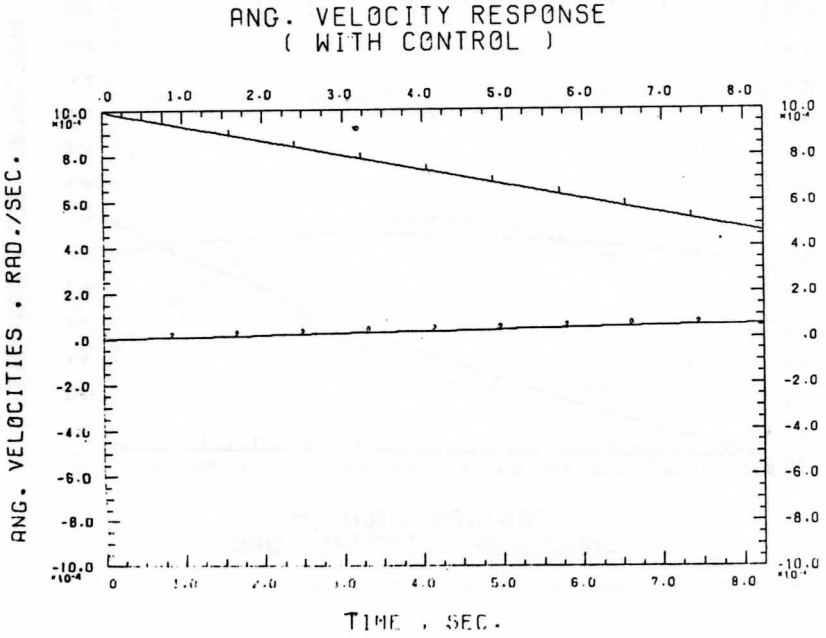
ANG. VELOCITY RESPONSE
(WITH CONTROL)
ANG. VELOCITIES • RAD./SEC.
TIME , SEC.
10.0
8.0
6.0
4.0
2.0
.0
-2.0
-4.0
-6.0
-8.0
-10.0
1.0
2.0
3.0
4.0
5.0
6.0
7.0
8.0

Figure 73

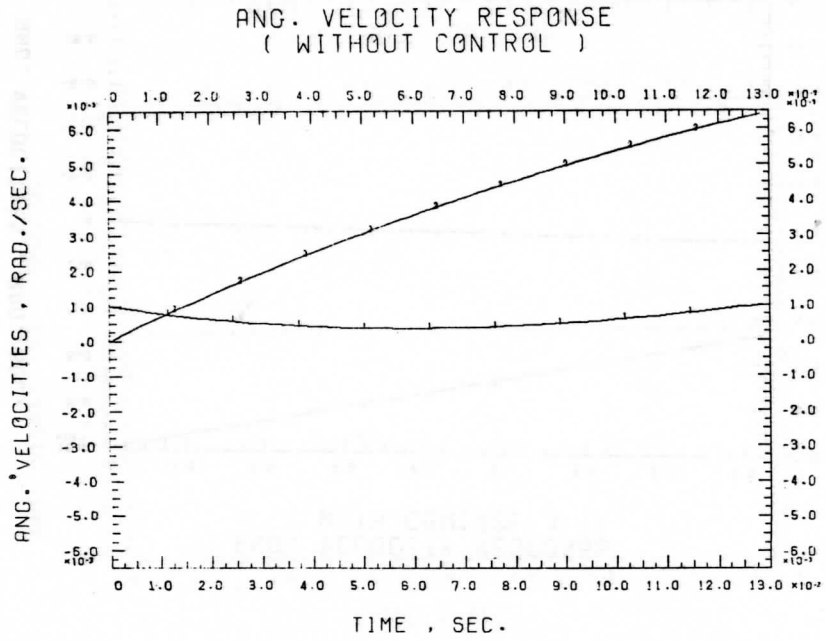
ANG. VELOCITY RESPONSE
(WITHOUT CONTROL)
ANG. VELOCITIES , RAD./SEC.
TIME , SEC.
0 1.0 2.0 3.0 4.0 5.0 6.0 7.0 8.0 9.0 10.0 11.0 12.0 13.0
6.0 5.0 4.0 3.0 2.0 1.0 .0 -1.0 -2.0 -3.0 -4.0 -5.0 -6.0

Figure 74

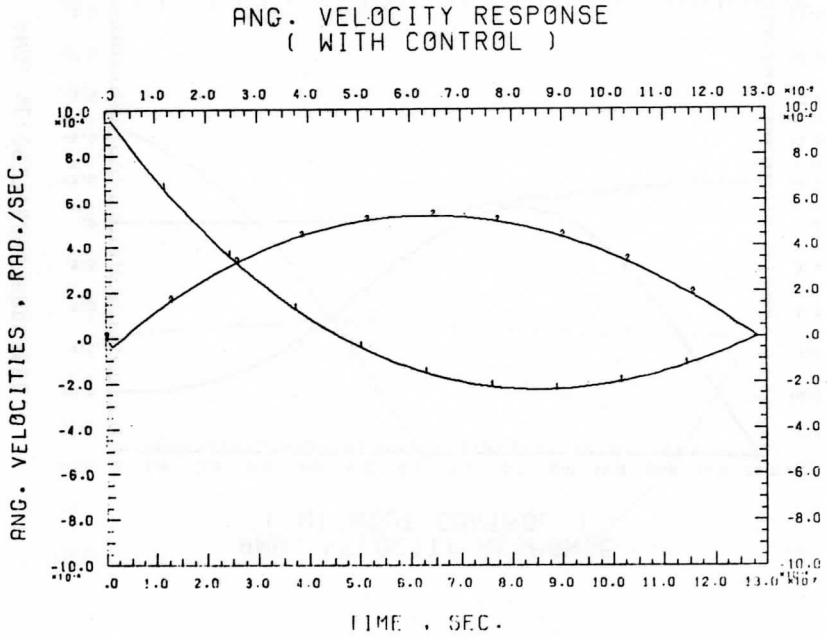
ANG. VELOCITY RESPONSE
(WITH CONTROL)
ANG. VELOCITIES , RAD./SEC.
TIME , SEC.
10.0
8.0
6.0
4.0
2.0
.0
-2.0
-4.0
-6.0
-8.0
-10.0
1.0
2.0
3.0
4.0
5.0
6.0
7.0
8.0
9.0
10.0
11.0
12.0
13.0

Figure 75

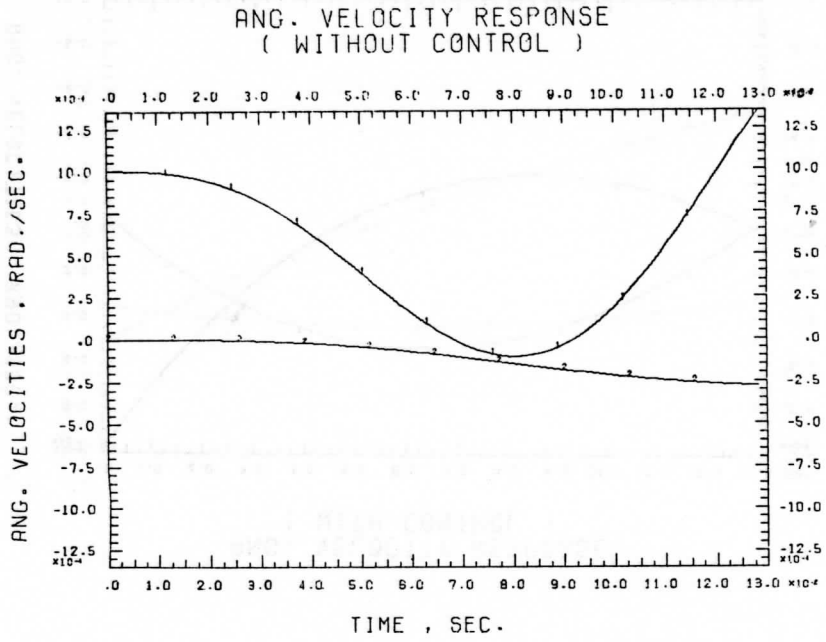
ANG. VELOCITY RESPONSE
(WITHOUT CONTROL)
ANG. VELOCITIES , RAD./SEC.
TIME , SEC.
12.5
10.0
7.5
5.0
2.5
.0
-2.5
-5.0
-7.5
-10.0
-12.5
1.0
2.0
3.0
4.0
5.0
6.0
7.0
8.0
9.0
10.0
11.0
12.0
13.0

Figure 76

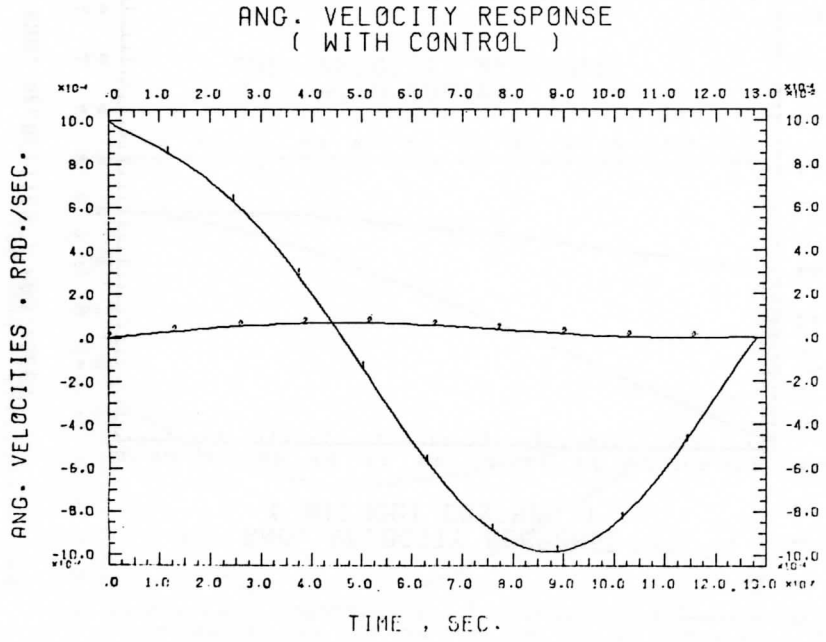
ANG. VELOCITY RESPONSE
(WITH CONTROL)
ANG. VELOCITIES . RAD./SEC.
TIME , SEC.
10.0
8.0
6.0
4.0
2.0
.0
-2.0
-4.0
-6.0
-8.0
-10.0
1.0
2.0
3.0
4.0
5.0
6.0
7.0
8.0
9.0
10.0
11.0
12.0
13.0

Figure 77

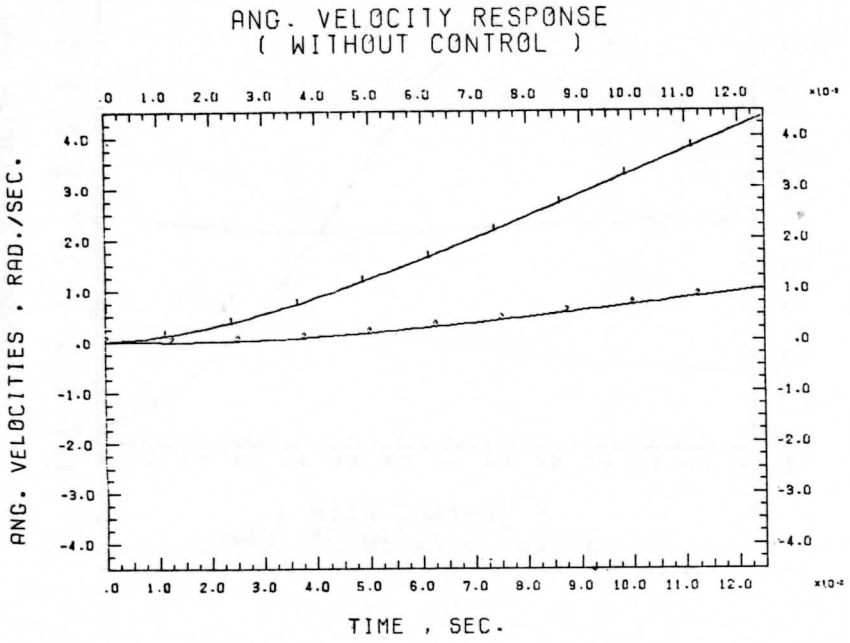
ANG. VELOCITY RESPONSE
(WITHOUT CONTROL)
ANG. VELOCITIES , RAD./SEC.
TIME , SEC.
.0 1.0 2.0 3.0 4.0 5.0 6.0 7.0 8.0 9.0 10.0 11.0 12.0
4.0 3.0 2.0 1.0 .0 -1.0 -2.0 -3.0 -4.0

Figure 78

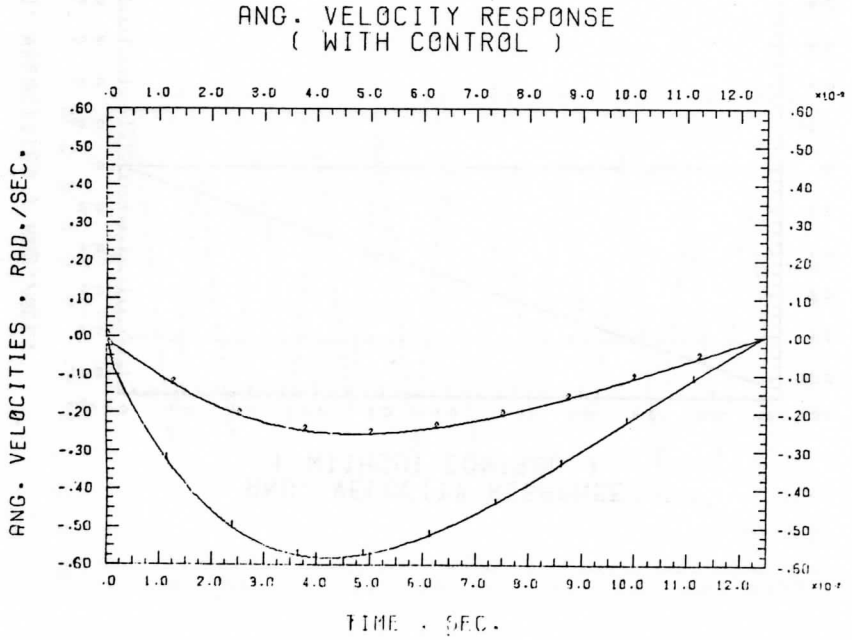
ANG. VELOCITY RESPONSE
(WITH CONTROL)
ANG. VELOCITIES • RAD./SEC.
TIME . SEC.
.0 1.0 2.0 3.0 4.0 5.0 6.0 7.0 8.0 9.0 10.0 11.0 12.0
.60 .50 .40 .30 .20 .10 .00 -.10 -.20 -.30 -.40 -.50 -.60

Figure 79

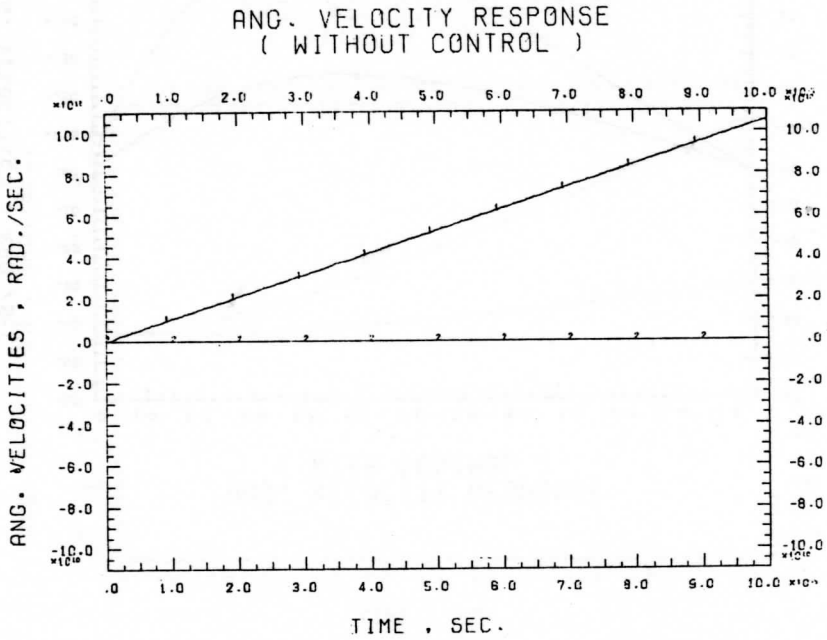
ANG. VELOCITY RESPONSE
(WITHOUT CONTROL)
ANG. VELOCITIES , RAD./SEC.
TIME , SEC.
.0
1.0
2.0
3.0
4.0
5.0
6.0
7.0
8.0
9.0
10.0
-2.0
-4.0
-6.0
-8.0

Figure 80

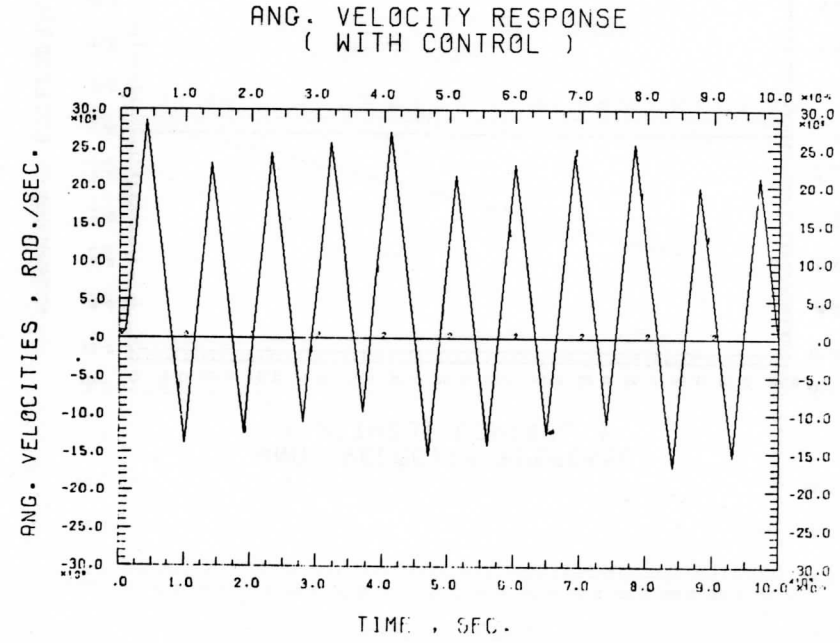
ANG. VELOCITY RESPONSE
(WITH CONTROL)
ANG. VELOCITIES , RAD./SEC.
TIME , SEC.
.0
1.0
2.0
3.0
4.0
5.0
6.0
7.0
8.0
9.0
10.0
30.0
25.0
20.0
15.0
10.0
5.0
-5.0
-10.0
-15.0
-20.0
-25.0
-30.0

Figure 81

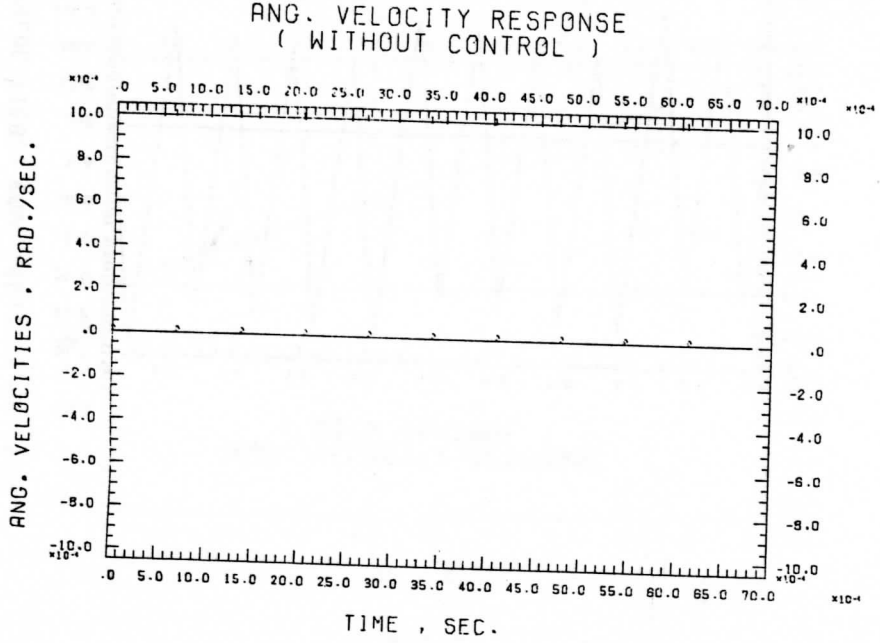
ANG. VELOCITY RESPONSE
(WITHOUT CONTROL)
ANG. VELOCITIES , RAD./SEC.
TIME , SEC.
10.0
8.0
6.0
4.0
2.0
.0
-2.0
-4.0
-6.0
-8.0
-10.0
5.0
10.0
15.0
20.0
25.0
30.0
35.0
40.0
45.0
50.0
55.0
60.0
65.0
70.0

Figure 82

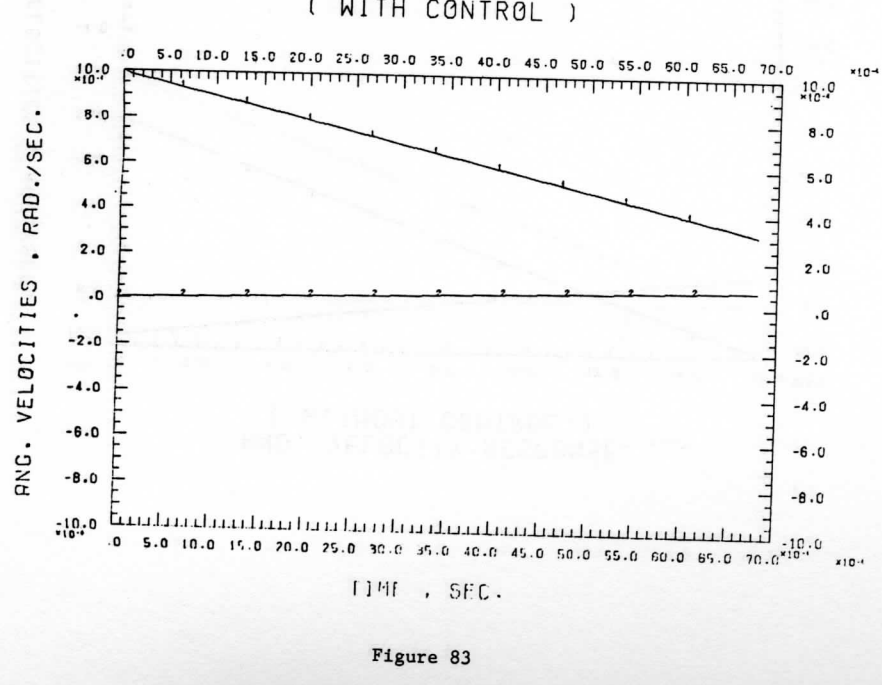
ANG. VELOCITY RESPONSE
(WITH CONTROL)
ANG. VELOCITIES , RAD./SEC.
TIME , SEC.
.0 5.0 10.0 15.0 20.0 25.0 30.0 35.0 40.0 45.0 50.0 55.0 60.0 65.0 70.0
10.0 8.0 6.0 4.0 2.0 .0 -2.0 -4.0 -6.0 -8.0 -10.0
×10⁻⁴

Figure 83

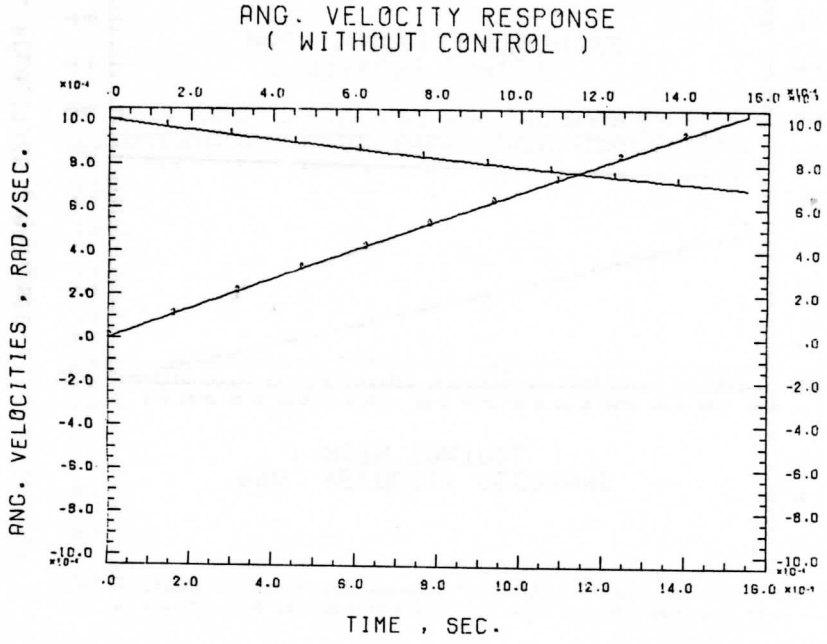
ANG. VELOCITY RESPONSE
(WITHOUT CONTROL)
ANG. VELOCITIES , RAD./SEC.
TIME , SEC.
10.0
8.0
6.0
4.0
2.0
.0
-2.0
-4.0
-6.0
-8.0
-10.0
2.0
4.0
6.0
8.0
10.0
12.0
14.0
16.0

Figure 84

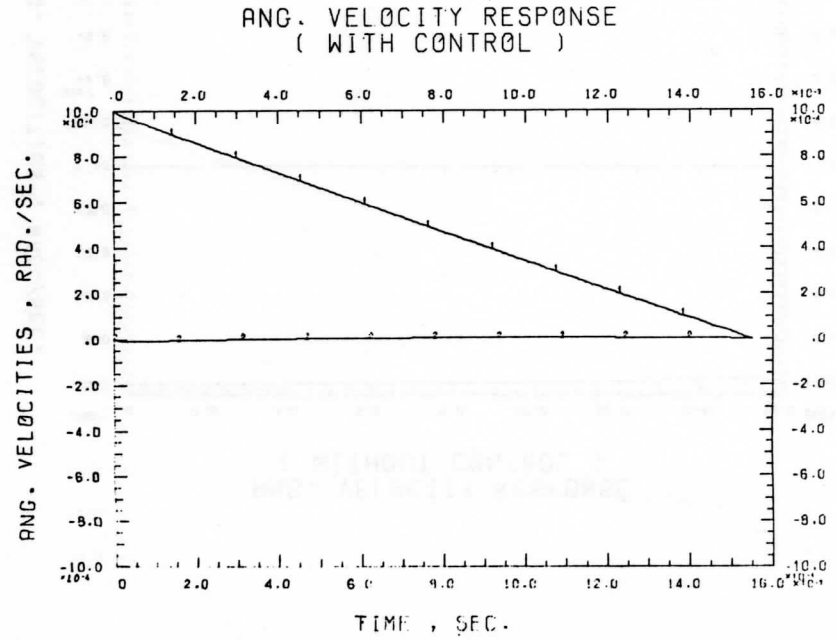
ANG. VELOCITY RESPONSE
(WITH CONTROL)
ANG. VELOCITIES , RAD./SEC.
TIME , SEC.
.0
2.0
4.0
6.0
8.0
10.0
12.0
14.0
16.0
10.0
8.0
5.0
4.0
2.0
.0
-2.0
-4.0
-6.0
-8.0
-10.0

Figure 85

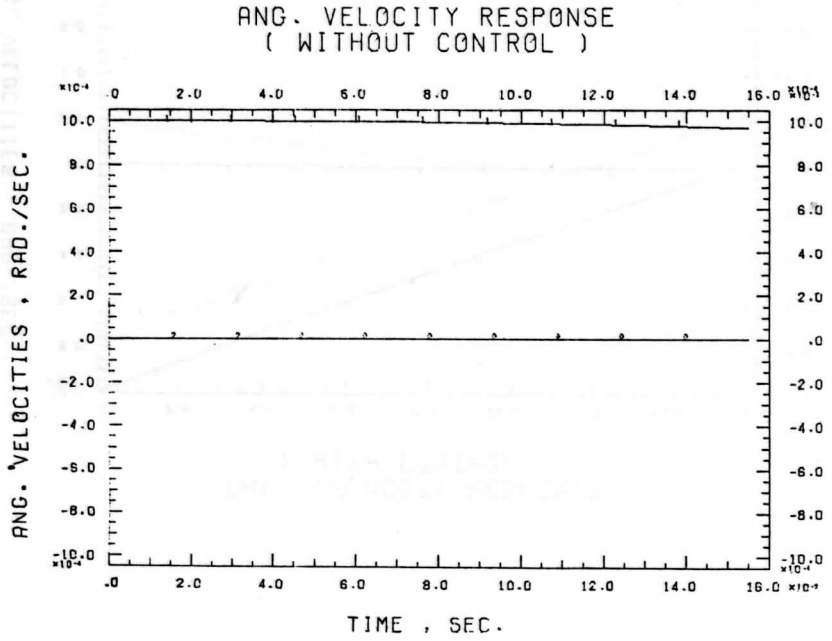
ANG. VELOCITY RESPONSE
(WITHOUT CONTROL)
ANG. VELOCITIES , RAD./SEC.
TIME , SEC.
.0
2.0
4.0
6.0
8.0
10.0
12.0
14.0
16.0
10.0
8.0
6.0
4.0
2.0
-2.0
-4.0
-6.0
-8.0
-10.0

Figure 86

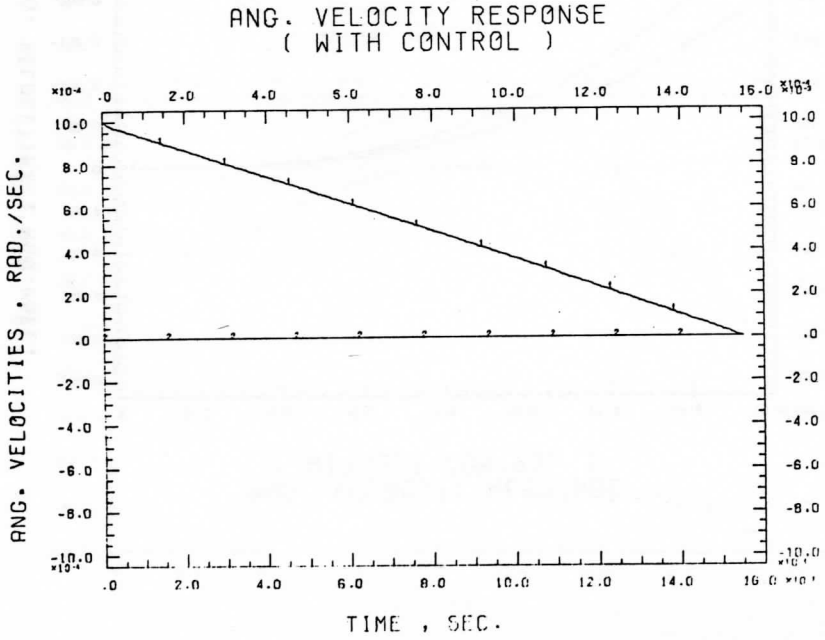
ANG. VELOCITY RESPONSE
(WITH CONTROL)
ANG. VELOCITIES , RAD./SEC.
TIME , SEC.
×10-4
×10-3
.0
2.0
4.0
6.0
8.0
10.0
12.0
14.0
16.0
10.0
9.0
8.0
6.0
4.0
2.0
.0
-2.0
-4.0
-6.0
-8.0
-10.0

Figure 87

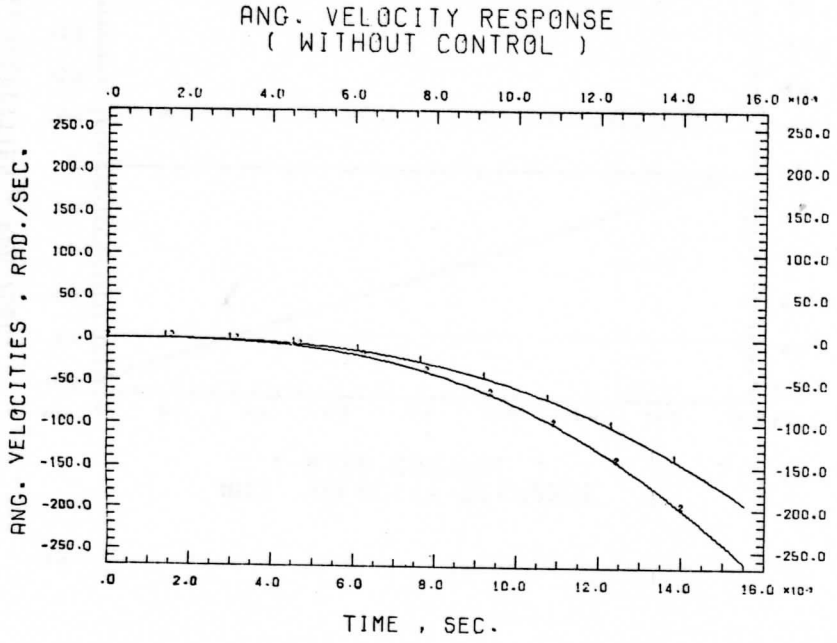
ANG. VELOCITY RESPONSE
(WITHOUT CONTROL)
ANG. VELOCITIES , RAD./SEC.
250.0
200.0
150.0
100.0
50.0
.0
-50.0
-100.0
-150.0
-200.0
-250.0
.0
2.0
4.0
6.0
8.0
10.0
12.0
14.0
16.0
TIME , SEC.

Figure 88

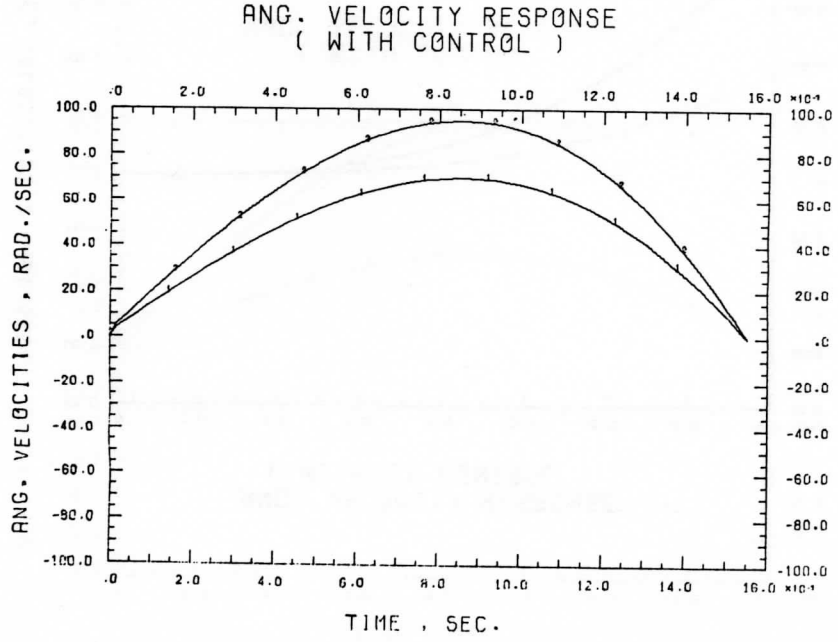
ANG. VELOCITY RESPONSE
(WITH CONTROL)
ANG. VELOCITIES , RAD./SEC.
TIME , SEC.
100.0
80.0
60.0
40.0
20.0
.0
-20.0
-40.0
-60.0
-80.0
-100.0
2.0
4.0
6.0
8.0
10.0
12.0
14.0
16.0

Figure 89

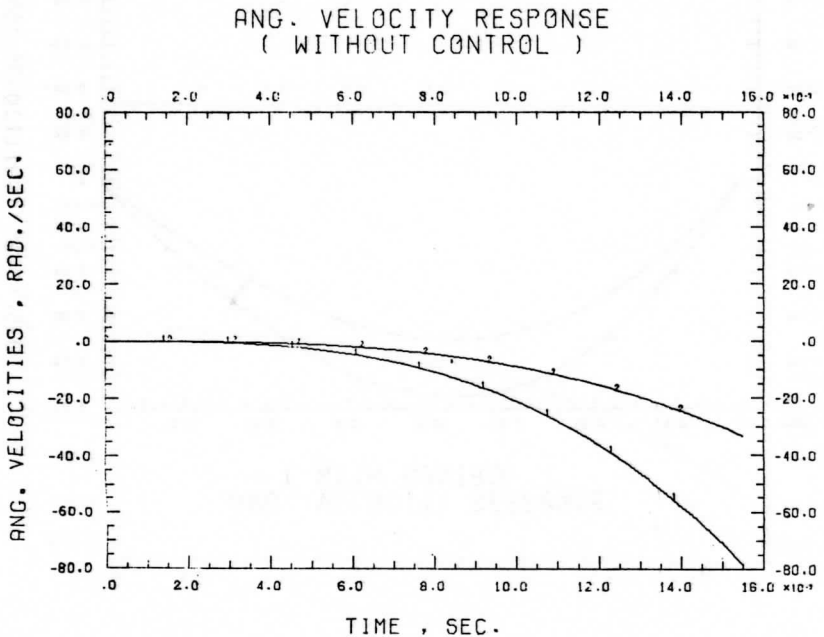
ANG. VELOCITY RESPONSE
(WITHOUT CONTROL)
ANG. VELOCITIES , RAD./SEC.
TIME , SEC.
80.0
60.0
40.0
20.0
.0
-20.0
-40.0
-60.0
-80.0
2.0
4.0
6.0
8.0
10.0
12.0
14.0
16.0

Figure 90

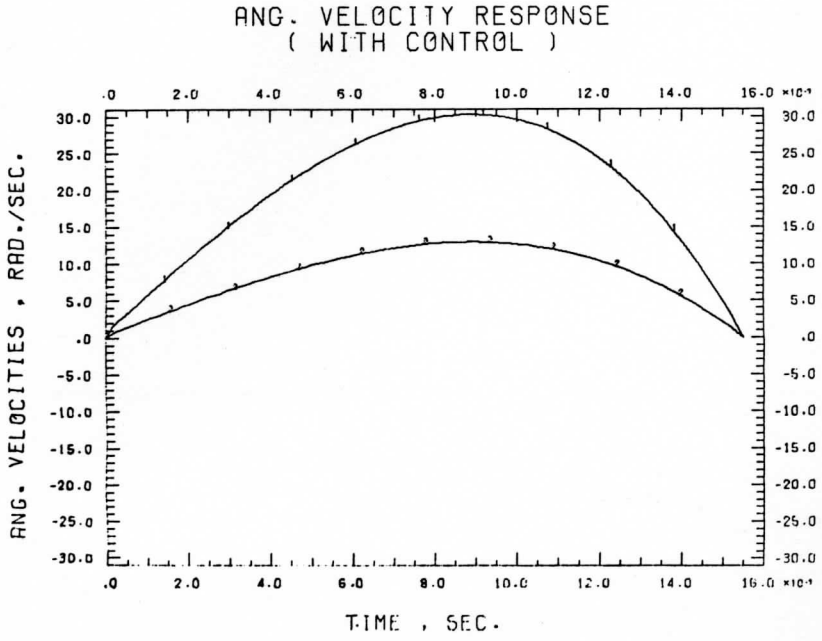
ANG. VELOCITY RESPONSE
(WITH CONTROL)
ANG. VELOCITIES , RAD./SEC.
TIME , SEC.
.0
2.0
4.0
6.0
8.0
10.0
12.0
14.0
16.0 ×10-1
30.0
25.0
20.0
15.0
10.0
5.0
.0
-5.0
-10.0
-15.0
-20.0
-25.0
-30.0

Figure 91

REPORTS AVAILABLE FROM

THE UNIVERSITY OF WISCONSIN PRESS, BOX 1379, MADISON, WISCONSIN 53701

97024. Studies in Atmospheric Energetics Based on Aerospace Probings: Annual Report, 1966. 129 pages. 1967. $5.00

97026. Studies in Atmospheric Energetics Based on Aerospace Probings: Annual Report, 1968. 162 pages. 1969. $5.00

97027. Radiation Experiment in the Vicinity of Barbados: Final Report, NSF Grant Ga. 12603. 100 pages. 1970. $5.00

97028. The Study of Radiation in a Tropical Atmosphere: Final Report. 100 pages. 1970. $5.00

97029. The Educational and Social Uses of Communications Satellites: A Bibliography. 42 pages. 1970. $3.50

97030. Measurements from Satellite Platforms: Annual Scientific Report on NAS5-11542, 1968-69. 388 pages. 1970. $10.00

97031. A Pilot Study on the Application of Geosynchronous Meteorological Satellite Data to Very Short Range Terminal Forecasting. 113 pages. 1970. $5.00

97032. Studies of the Atmosphere Using Aerospace Probings: Annual Report, 1969. 243 pages. 1970. $7.50

97033. Teleconferencing: A Bibliography. 1971. $3.50

97034. Legal and Political Aspects of Satellite Telecommunication: An Annotated Bibliography. 126 pages. 1971. $7.50

97035. Multidisciplinary Studies of the Social, Economic, and Political Impact Resulting from Recent Advances in Satellite Meteorology: An Interim Report, Vol. 1. 459 pages. 1971. $15.00

97036. Multidisciplinary Studies of the Social, Economic, and Political Impact Resulting from Recent Advances in Satellite Meteorology: An Interim Report, Vol. 2. 431 pages. 1971. $15.00

97037. Measurements from Satellite Platforms: Annual Scientific Report on NAS5-11542, 1969-70. 180 pages. 1971. $7.50

97038. Studies of the Atmosphere Using Aerospace Probings: Annual Report, 1970. 69 pages. 1971. $5.00

97039. Legal Aspects of Satellite Teleconferencing. 213 pages. 1971. $7.50

REPORTS AVAILABLE FROM

THE UNIVERSITY OF WISCONSIN PRESS, BOX 1379, MADISON, WISCONSIN 53701

(continued from inside back cover)

97040. Teleconferencing in Wisconsin. 240 pages. 1971. $10.00

97041. Measurements from Satellite Platforms: Annual Scientific Report on NAS5-11542, 1970-71. 270 pages. 1972. $10.00

97042. Experiments in Medical Communications via the ATS-1 Satellite. 136 pages. 1972. $7.50

97043. Specifications for a Vertical Temperature and Moisture Sounder for the Synchronous Meteorological Satellites. 82 pages. 1972. $5.00

97044. Scientific Requirements of Sea Surface Measurements for the GARP Tropical Experiment. 18 pages. 1972. $2.50

97045. Studies of the Atmosphere Using Aerospace Probings: Annual Report, 1971, Vol. II: Application Studies. 104 pages. 1972. $5.00

97046. Multidisciplinary Studies of the Social, Economic, and Political Impact Resulting from Recent Advances in Satellite Meteorology: An Interim Report, Vol. 3. 252 pages. 1972. $10.00

97047. Multidisciplinary Studies of the Social, Economic, and Political Impact Resulting from Recent Advances in Satellite Meteorology: An Interim Report, Vol. 4. 199 pages. 1972. $10.00

97048. Satellite Teleconferencing: An Annotated Bibliography. 130 pages. 1972. $7.50

97049. Measurements from Satellite Platforms: Annual Scientific Report on NAS5-11542, 1971-72. 228 pages. 1972. $7.50

97050. Synchronous Meteorological Satellite Sounder Specification: Final Report Under NASA Contract NAS5-21607. 73 pages. $5.00

97051. Multidisciplinary Studies of the Social, Economic, and Political Impact Resulting from Recent Advances in Satellite Meteorology: An Interim Report, Vol. 5. 290 pages. 1973. $10.00

97052. Measurements from Satellite Platforms: Annual Scientific Report on NAS5-21798, 1972-73. 331 pages. 1974. $10.00